Surface modification of bioceramics: chemically enhanced laser surface microstructuring of hydroxyapatite

Norton, Judy A. M.

Surface modification of Bioceramics:

Chemically enhanced laser surface microstructuring of hydroxyapatite

Judy A.M. Norton

A thesis submitted for the degree of Doctor of Philosophy
at the University of London

Supervised by Dr. I.U. Rehman

January 2008

Interdisciplinary Research Centre in Biomedical Materials (IRC),
Queen Mary, University of London,
Mile End Road, London, E1 4NS, UK.

Queen Mary
University of London

Declaration

I declare that the work presented within this thesis is my own.

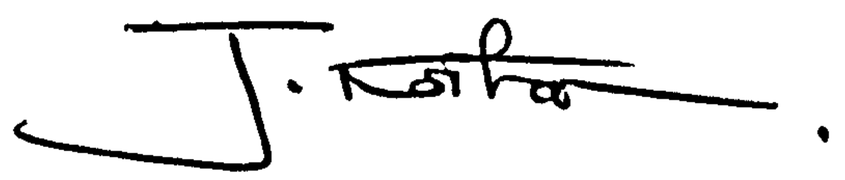

Abstract

Bioceramics have been developed for implants to repair damaged tissues of the human musculo-skeletal system. The clinical success of a bioceramic implant depends largely on the chemical response at the implant interface in addition to the sufficiency of the mechanical properties for the application. The present study combines the developments in the fields of bioceramic materials and laser surface microstructuring of materials.

Bioceramic hydroxyapatite powders (HA, Formula: $Ca_{10}(PO_4)_6(OH)_2$) have been produced by emulsion technology and freeze-drying methods exhibiting BET specific surface areas >148 m^2/g and particle sizes <13 nm prior to thermal treatment. The powder yield has been doubled using an increased reaction temperature of 25 °C from 17 °C, with a small increase (< 4nm) in the average particle size. HA discs that were >95.5 % dense have been achieved after isostatic pressing with pressure of 0.59 MPa and pressureless sintering at 1200 °C for 2 hours. No chemical decomposition was detected using X-ray Diffraction analysis (XRD).

Methods of chemically enhanced laser-assisted etching have been developed to produce microstructural features on the surface of bioceramic HA discs that were 78.5 % dense (2482.95 kg/m^3 measured density). The use of 10 MPa SF_6 at laser fluencies in the range of 14.50-15.20 kJ/m^2 produced a columnar topography with individual structures featuring 10-20 μm height and 8-12 μm width as characterised by Scanning Electron Microscopy (SEM). Chemical characterisation by X-ray microdiffraction, Energy Dispsersive X-ray analysis (SEM-EDS), Fourier Transformed Infrared spectroscopy (FTIR) and Raman spectroscopy (Raman) found the microtopography to be composed of fluorine-substituted HA (FHA). Alternatively the use of 80 MPa NH_3 at laser fluencies in the range of 17.17-18.50 kJ/m^2 produced an irregular surface of scattered porous hillocks that remained chemically unchanged in composition but exhibited four times as many surface hydroxyl groups. In both cases the mechanical and chemical stability of the bulk composition is maintained and the surface of increased surface area, in addition to the presence of concavities and pores is likely to be of enhanced osteoconductivity.

Acknowledgements

I am especially grateful to Dr. I.U. Rehman for his supervision, continued support and tuition (FTIR and Raman) amidst friendship over the past 4 years. Many thanks to Dr. K.W. Kolasinksi for his advice, tuition (XeCl Laser) and inspiring enthusiasm during my project.

Thank you to Dr. D. Mills (Centre of Materials Research, Queen Mary) for the invaluable input in the laser surface modification development and continued technical support throughout my project. I would also like to thank Dr. M.J. Phillips (Centre of Materials Research, Queen Mary) for tuition (XRD, BET and FTIR), equipment, advice and encouragement delivered with many interesting discussions (and always a smile) throughout my PhD. I am very grateful to Dr. G. Cressey (Dept. of Mineralogy, Natural History Museum, London) for his invaluable assistance and X-ray microdiffraction characterisation. Similar thanks are extended to Mr. Z. Movasaghi for FTIR and Raman characterisation and also, Prof. J.Elliott & Dr. S. Dowker for advice and assistance with FTIR analysis. Many thanks to Mr. S. Murray (Plasmabiotol Ltd, UK) for the supply of HA. Thank you to Prof. K.E. Tanner, Dr. R.M. Wilson, Dr. K. Hing and Dr. J.A. Darr for guidance and encouragement during my study.

For all of technical support, I would like to thank: Dr. Z. Luklinska & Mr. M. Willis (SEM and SEM-EDS analysis), Mr. Z. Movasaghi (FTIR and Raman), Mr. V. Ford (production of die moulds), Dr. P. Anderson (use of diamond saw), Dr. M.J. Wang (FTIR-FPA analysis), Dr. A. Spary (use of freeze-dryer), Dr. T. Buckland & Mr. C. Campion (supply of hydroxyapatite, 'Apatec'). For administrative support I would like to thank Mrs. C. Jones.

Thanks for the friendship and support of Mr. R. Twycross-Lewis, Mr. Y. Hernandez, Dr. J. Enuwimide, Dr. D. Ateh, Dr. S. Mellon, Dr. K.E. Baria, Miss. M. Schloenleger, Dr. S. Haque, Miss. N. Rashid, Mr. C. Christophe and all those that I have had the opportunity to share an office with. Special thanks go to Miss. O.O. Akanji & Miss. N. Vaughan for their unconditional comradeship, acceptance, patience and kindness (and

sharing the sniggers, sins, sounds, sun and sorrow), without which I would have most certainly lost inspiration or sanity.

Thanks to Miss. S. Vango, Miss. K. Howard, Miss. M. Davies, Miss. T. Malia, Miss. E. High, Miss. E. Tyson and Mr. A. Sood, for their invaluable friendship and tremendous understanding over the past years (plus many drinks along the way).

I would especially like to thank Mr. R. Clewes-Garner for his companionship and support during the last annum (so much is owed for what seems such a short time – thank you).

Most of all I would like to thank my family: Mr. R. C. Norton & Mrs. R. R. Norton (Mum & Dad) for their unconditional love, support and encouragement, without which I would never have got this far (it has been in the darkest moments and absence that I have felt your wisdom the most).

Finally, I would like to gratefully acknowledge the opportunity for this study and the financial support of Dr. I.U. Rehman and the IRC in Biomaterials.

Contents

List of Tables

List of Figures

Abbreviations

AOT	Dioctylsulfosuccinate
AnalaR	Analytical grade
ATR	Attenuated total reflectance
BET	Brunauer-Emmett-Teller (surface area analysis technique)
ECM	Extracellular matrix
FA	Fluoroapatite
FHA	Fluoride substituted-hydroxyapatite
FTIR	Fourier Transformed Infrared
GPR	General purpose grade
GR-HA	Glass-reinforced hydroxyapatite
HA	Hydroxyapatite
HCl	Hydrochloric acid
HDPE	High density poly ethylene
HIPing	Hot isostatic pressing
HPLC	High performance liquid chromatography
Na-AOT	Sodium salt of dioctylsulfosuccinate
NH_3	Ammonia
PLA	Pulsed laser ablation
PLD	Pulsed laser deposition
PS	Polysulphone
PU	Polyurethane
SBF	Simulated body fluid
SEM	Scanning electron microscopy
SEM-EDS	Energy dispersive X-ray spectroscopy
SF_6	Sulphur hexafluoride
TCP	Tricalcium phosphate
TEM	Transmission electron microscopy
XRD	X-Ray Diffraction
YAG	Yttrium aluminium garnet

Chapter 1 Introduction

The osseous tissues within the human body are often limited in the ability to remodel or repair completely when subjected to trauma, disease, ageing or congenital deformity. Natural tissue repair of bone by means of grafting replacement tissue to the defective site is not without disadvantage or potential risk and further complications. Additionally, the reduction in the number of potential tissue donors with the increased requirement for tissue as human lifespan lengthens through improved medical technology has led to the need for synthetic bone replacement materials. The materials used for orthopaedic implants in bone replacement and repair, include a variety of metals, polymers and ceramics. With advanced surgical techniques and the advantage of tailored implant materials being manufactured to high purity in mass scale, synthetic materials have been successfully used in dental implantation, bone and joint replacement or fixation, maxillofacial fixation and reconstruction and vascular grafting.

Currently, constructed bone grafts in load bearing applications such as hip joint endoprostheses consist primarily of metallic materials that do not match the mechanical properties of natural bone tissue. Complications therefore arise from the greater compressive and tensile strength of the metallic counterpart promoting the resorption and remodelling of the surrounding bone that can result in implant failure. Occurring over a period of time this development is often referred to as stress-shielding. To avoid stress-shielding the implant would ideally be comprised of material with mechanical properties that are similar to those of natural bone. Furthermore, synthetic materials for bone grafting that can be gradually resorbed and replaced at a suitable rate by new healthy bone reduce the risk of implant failure and further surgical repair or revision, that often involve the removal of further healthy osseous tissue. In order to achieve the synthesis of such materials it is necessary to understand the structure and properties of bone as a living tissue.

1.1 Natural Hard Tissue Composition

The hard tissues of the human body (i.e., bones and teeth) are ceramic-organic composites with complex microstructures that have been studied and reviewed extensively in past literature (B.D.Ratner *et al.*, 1996c; D.Siva Rama Krishna *et al.*, 2002; L.J.Jha *et al.*, 1997; W.Suchanek *et al.*, 1998). The organic phase constitutes approximately 20 % of material and consists of mainly type I collagen shown in Figure 1.1 (D.Siva Rama Krishna *et al.*, 2002; W.Suchanek *et al.*, 1998). The inorganic mineral phase accounts for approximately 69 % of the dry mass and is largely carbonated hydroxyapatite (CO_3- $Ca_{10}(PO_4)_6(OH)_2$) in addition to a small amount of ions such as fluoride, magnesium and sodium(L.J.Jha *et al.*, 1997). The remainder comprises water in addition to trace amounts of proteins, lipids and polysaccharides. Dental enamel differs in that the mineral phase is a much greater 97 % of the dry material and contains a larger amount of fluoride incorporated into the inorganic mineral apatite, known as fluoroapatite. It contains less water and is believed to be the hardest substance in the body(W.Suchanek *et al.*, 1998).

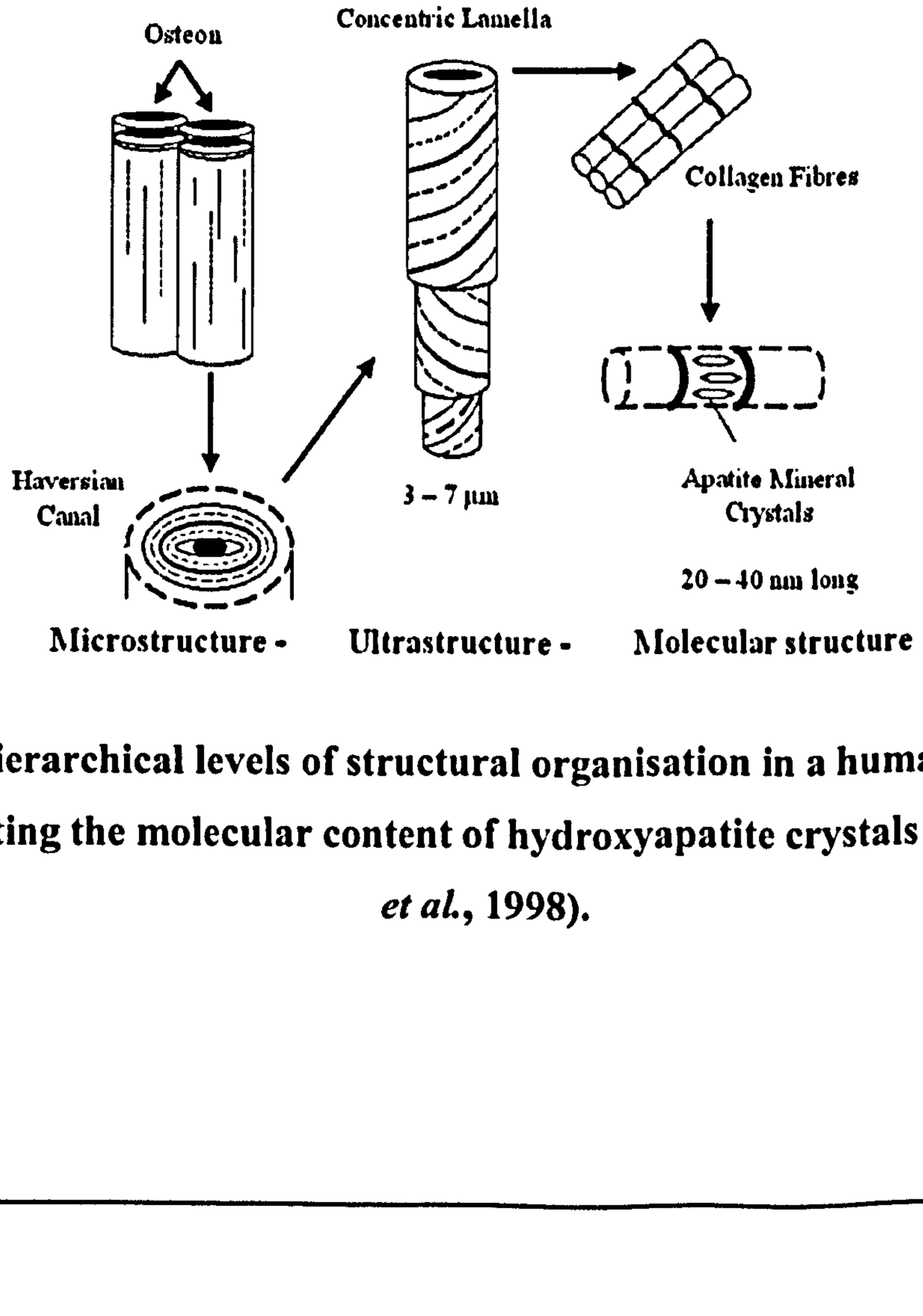

Figure 1.1: Hierarchical levels of structural organisation in a human long bone demonstrating the molecular content of hydroxyapatite crystals (W.Suchanek *et al.*, 1998).

Previous detailed structural descriptions of human bone portray various levels of hierarchical structural organisation (see Figure 1.1) with mechanical properties differing for each component phase whilst contributing to the overall mechanical performance of the material (B.Ji *et al.*, 2004; V.Rusu *et al.*, 2005). The individual levels and their structures include the following; (1) the macrostructure of cancellous and cortical bone, (2) the microstructure (from 10 to 500 μm) i.e, Haversian systems, osteons, single trabeculae, (3) the sub-microstructure or ultrastructure (1-10 μm), i.e. lamellae, (4) the nanostructure (from a few hundred nanometers to 1 μm) i.e. fibrillar collagen and embedded mineral; and (5) the sub-nanostructure or molecular structure (below a few hundred nanometers): molecular structure of constituent elements including minerals, collagen and non-collagenous organic proteins (J.Rho *et al.*, 1998). Bone tissue is a composite in which nanosized crystals of apatite are deposited on collagen fibres and skillfully woven into a three-dimensional hierarchically organised structure that has an irregular, yet optimised, arrangement and orientation of the components with the result that bone is a heterogenous and anisotropic material. The significance of the amorphous arrangement of HA crystals reinforcing a collagen fibre matrix can be reflected not only by the strength of the natural material but also the solubility and dissolution rate. Within the microstructural trabeculae of cancellous bone, osteoclasts degrade regions of existing structure whilst conversely, osteoblasts build new sections of bone and throughout the remodelling process osteocytes serve to maintain the bone matrix. Subsequently, clinical success of the manufactured bone graft is governed not only by the match of the mechanical performance of the replaced hard tissue upon creation of a stable interface, but by the ability to undergo biodegradation and stimulate replacement with natural host tissue over an appropriate recovery period (W.Suchanek *et al.*, 1998).

1.2 Bioceramics

The term 'bioceramics' applies to the specially formulated ceramic compositions selected upon the ability to form a stable interface of biological compatibility with surrounding osseous tissues (T.V.Thamaraiselvi *et al.*, 2004). Individual biocompatible formulations as reported by Hench (1998) may be bioinert (e.g., alumina and zirconia), resorbable (e.g., tricalcium phosphate), bioactive (e.g., hydroxyapatite, bioactive glasses and glass-ceramics), or porous for tissue ingrowth (e.g., hydroxyapatite-coated metals) (L.L.Hench, 1998). 'Biocompatibility' refers to the ability of a material to perform with

an appropriate host response whilst being structurally suitable for the particular application within the body. 'Bioinert' refers to material resistance to further oxidation upon placement within the body with no cytotoxic effect. 'Resorbable' describes the material potential for dissolution via the biological process of bone resorption and subsequent remodelling. Finally the term 'bioactive' implies that the material provides an interface that elicits a specific biological response that results in the formation of a direct physico-chemical bond with the surrounding tissue (B.D.Ratner *et al.*, 1996c). Synthetic bioceramic hydroxyapatite (HA) $Ca_{10}(PO_4)_6(OH)_2$, has bioactive and resorbable properties in addition to chemical similarity with the mineral component of bone tissue (B.M.Tracy *et al.*, 1984). Manufactured by a variety of routes, HA is used widely for bone replacement applications despite mechanical limitations inherent to ceramic materials. Despite sufficient compressive strength values (500-1000 MPa), low values of tensile strength, toughness, fatigue resistance coupled with brittle behaviour impedes usage of the material for load bearing applications at this present time. Whilst the biological HA crystals are of nanometer scale, synthetic HA produced by wet conventional methods is often comprised of large primary particles, with wide particle size distributions and relatively low surface areas that subsequently lower the comparative solubility and furthermore, the mechanical strength resultant of poor sintering behaviour. Therefore the production of high-surface area, un-agglomerated nano-sized HA particles are of great interest in order to improve the dissolution and mechanical properties of the applied product with the additional benefit of enhancing cell-material interaction and relevant bioactivity.

1.3 Surface Microstructuring

Further to the bioactivity of an implant permitting the development of a stable physico-chemical interface with surrounding tissue, studies have demonstrated that surface characteristics such as topography and chemistry are important factors for promoting tissue growth at the interface (M.J.Dalby *et al.*, 2000). Upon implantation extracellular matrix proteins localise on site promoting a cellular response through orientation and conformation that will govern whether the implant is encapsulated in fibrous tissue or direct tissue growth occurs (K.Chittur, 1998). In the case of bioceramics it is the initial interaction of bone cells that influence all subsequent responses relating to cell adhesion, spreading, proliferation and subsequent extra-cellular matrix synthesis and

mineralisation. Surface topography defined as the morphology at the surface can be further subdivided into the macro topography that concerns the physical configuration of the implant, and micro topography resulting from surface roughness or texture. Whilst roughness is attributed to hills or pits or random size and distribution possibly caused by manufacture, texture denotes the micro-configuration of a surface with pillars, cones, pores or grooves (M.J.Dalby *et al.*, 2000). Curtis *et. al.* (1997) discussed extensively the topographical influence of cell behaviour reported through a vast array of studies. As this realisation has become more widely accepted, advances in technology have permitted the development of surface modification techniques that encourage the integration of cells and tissue with implanted biomaterials. The chief methods employed as reported by Flemming *et. al.* (1999) include photolithography, electron beam lithography, sandblasting, electropolishing and etching with reactive ions or acid (A.Hart *et al.*, 2007). Recent studies reported by Kolansinski *et. al.* (2004) suggest the use of laser-assisted etching in the presence of reactive gas for chemical enhancement of laser ablation producing mesoscopic pillars on silicon substrates with partial content of the gas species. In the biomedical area, surface topographical features such as pillars are functional for biomineralisation, drug and cellular delivery in addition to surface interactions with cells, and fundamental studies employing silicon pillars as a model system have developed interest in employing similar methods for the formation of structures on other materials (K.W.Kolasinski, 2004). Successful laser ablation resulting in the development of conical structures on ceramic substrates has already been reported (X.Y.Chen *et al.*, 1999). Whilst previous work with surface topography on silicon has been shown to exert a large influence over osteoblasts, corresponding studies on bioceramic HA with similar laser fabricated topography is yet to be undertaken (M.J.Dalby *et al.*, 2000).

1.4 Project aims

The aim of this project is to attempt to use laser-assisted etching in the presence of reactive gas for chemical enhancement of laser microstructuring of nanocrystalline bioceramic HA. The main objectives include reviewing the initial manufacture of HA powder and with an interest in improving the mechanical properties of the processed HA product, before establishing a suitable method of laser-assisted etching that will fabricate a surface topography of uniform size and distribution to promote cellular

interaction and tissue growth. Fabrication of a surface with improved bioactivity from chemical substitution of HA is also of importance, hence the view to analyse the use of reactive gas in the laser processing step with the hypothesis that the plume chemistry may result in certain reactive species chemically substituting into the HA surface to produce a topography composed of a more bioactive counterpart.

Chapter 2 Apatite Materials

Overview

Research concerning hydroxyapatite ($Ca_{10}(PO_4)_6(OH)_2$) in both naturally occurring and chemically prepared phases is expanding rapidly. Various applications and properties are described in this section with relevant advantages and disadvantages. Variations in the chemistry and structure of the compound are introduced with any relevant reported effects on biological and/or mechanical properties. Limitations of the material in certain applications are discussed along with current manufacturing advances offered as solutions to provide the required properties.

2.1 Ceramic Materials

2.1.1 Background

Ceramic materials describe the group of solid inorganic compounds formed by varying degrees of ionic and/or covalent interatomic bonding. The word is derived from the Greek term *keramos* meaning "pottery" (E.W.Washburn *et al.*, 1920). Material properties such as brittleness, thermal resistance and non conductivity are the result of the bonding requirements of the tightly packed unit cells giving rise to complex crystal structures. Generally, ionically bonded solids must have charge neutrality within each unit cell therefore providing overall an electrically neutral solid and covalently bonded solids must have fourfold co-ordination throughout the structure, such as the diamond cubic structure of Carbon and the crystalline structure of Silica (B.D.Ratner *et al.*, 1996c). In addition to the crystalline form, ceramic materials can also exist in an amorphous or glassy state consisting of a short range ordered network of compounds very similar to the liquid state. The structure is metastable has a tendency over a period of time to transform into the lower free energy crystalline form by a process known as devitrification. Crystalline and glassy phases are often both present in the microstructure of a ceramic material. Controlled devitrification of a glass by thermal processing can produce a glass ceramic, a polycrystalline material with little porosity and mechanical properties that are intermediate of glass and crystalline ceramic materials. Selection of the ceramic composition is governed by the availability of a

large number of nuclei for crystallisation during devitrification (J.C.Anderson *et al.*, 1991).

2.1.2 Applications of Ceramics and bioceramics in the body

At present, ceramic, glass and glass-ceramic provides a description for a substantial range of materials with a variety of intricate applications in addition to the commonplace examples of pottery, ovenware and house bricks. Dental ceramics include the restorative materials featured in gold porcelain crowns, glass-filled ionomer cements and dentures serving to improve the quality of oral hygiene (L.L.Hench, 1998). Within the medical and healthcare industry, the development of ceramic materials has facilitated applications for eyeglasses, diagnostic instruments, chemical ware, thermometers, tissue culture flasks and fibre optics for endoscopy as documented by Hench (1996, 1998). Further applications include the use of insoluble porous glasses as carriers for enzymes, antibodies and antigens due to the outstanding resistance to microbial attack, pH changes, solvent conditions, temperature and damage through packaging under high pressure required for rapid flow circumstances (B.D.Ratner *et al.*, 1996c).

Developments within the last four decades have facilitated the use of bioceramic materials within the human body to repair and reconstruct hard tissue damage within the musculo-skeletal system. Examples of such applications include implant replacement for femoral or knee arthroplasty, maxillofacial reconstruction, dental implants and reconstruction for periodontal disease, ossicular bone prostheses and bone repair after surgery, trauma or damage from disease(B.Kundu *et al.*, 2004; W.Suchanek *et al.*, 1998). The prerequisite for artificial hard tissue replacement material arose from the limited supply of endogenous bone in correlation with the additional surgery for supply, as well as the risk of rejection and disease transmission with the use of exogenous bone (B.D.Ratner *et al.*, 1996c; W.Suchanek *et al.*, 1998).

Advantageous mechanical properties of certain bioceramics include high stiffness, low friction and good wear resistance (T.V.Thamaraiselvi *et al.*, 2004). Whilst these

properties contribute to the suitability for application at articulating surfaces, the poor reliability under tensile loads and brittle catastrophic failure that ceramics are subject to, limits their application as load bearing implants (W.Suchanek *et al.*, 1998). Even in applications as small unloaded implants, powders, coatings and low-loaded porous implants the material must function as efficiently as the replaced tissue for the remaining years of the patient's life. Improved technology and lifestyle have increased the average life span and the bioceramic implant may need to perform for a period greater than 20-25 years providing a need for further improvement in the mechanical properties and performance of bioceramic materials (L.L.Hench, 1998). The mechanical properties of human cortical and cancellous bones in addition to the main types of bioactive ceramics, are shown in Table 2.1, amended from T. Kokubo *et. al.* (2003).

Table 2.1 Mechanical properties of human cortical and cancellous bones and bioactive ceramics

		Strength /MPa		Young's Modulus /GPa	Fracture toughness K_{IC} /MPam^{½}
		Compressive	Bending		
Bone	Cortical	100-230	50-150	7-30	2-12
	Cancellous	2-12	N/a	0.05-0.5	N/a
Hydroxyapatite		500-1000	115-200	80-110	1.0
Glass-ceramic A-W		1080	220	118	2.0
Bioglass® (45S5)		N/a	42	35	N/a

2.1.3 Limitations of bioceramics

Implant failure can result from a number of issues dependant on the application and site of the implant such as cement and/or acetabular cup liner dislodgement of total hip arthroplasty and replacement, periprosthetic fracture of joint replacements (knee, elbow, hip and shoulder) and calcification of vascular prosthesis, grafts or heart valves (J.Wang *et al.*, 2000; M.Park *et al.*, 2003). Intraoperative factors including the use of cement and host factors such as osteoporosis, can also influence periprosthetic fracture. Failure of cement bondage or extensive resorption around the prosthesis due to stress shielding in addition to wear related osteolysis (permitted by wear debris stimulating phagocytic

action of macrophages) contribute to mechanical loosening at the implant-host tissue interface terminating rigid fixation. In addition to pain experienced by the patient the improper placement and fixation of the implant components can facilitate unusual stress conditions that may subsequently reduce the life of the implant (C.Nelson, 2002; D.Fang *et al.*, 1990). Periarticular calcification or ossification can result in femoral impingement and an inadequate range of motion which through other complications, can result in implant failure. This type of surface calcification is undesirable as opposed to that resultant in biological fixation of the femoral stem employing a porous coating of titanium beads covered in hydroxyapatite (which encourage bone ingrowth and ossification) which provide a permanent interface between the bone and the implant. Wear debris released from HA coated metallic implants have been shown to activate monocytic cells and facilitate osteolysis, a common cause of failure in hip replacements. In contrast when HA is used as a macroporous ceramic (such as in oral maxillofacial surgery) with the intention of invasion by healing bone tissue within a bony defect, degradation and resorption of the ceramic by osteoclasts and macrophages is welcome, prior to replacement with new bone. Performance, requirement and failure are shown to be relevant to application and implant site (D.Hirsch *et al.*, 1992; H.Benhayounne *et al.*, 2000; P.Laquerriere *et al.*, 2003).

2.2 Synthetic Ceramic Hydroxyapatite

Synthesised ceramic hydroxyapatite (HA) $Ca_{10}(PO_4)_6(OH)_2$, evokes no cytotoxic effects when implanted and demonstrates excellent biocompatibility and bioactivity with human tissue and is commonly the choice of ceramic for hard tissue replacement. The powder form has reportedly been used in surgery since 1920 (R.Petit, 2007). Natural biological bone mineral differs from processed HA in that the former contains additional ions such as carbonate (CO_3^{2-}) and water (H_2O), in addition to possessing variable Ca/P ratios between 1.6 and 1.7 (HA is 1.67) (J.C.Elliott *et al.*, 2002). Furthermore, biological apatite is nonstoichiometric and poorly crystalline with crystals of submicron dimensions (M.Bohner, 2000). The HA crystals in bone and dentine were reported by Elliott (2002) to be approximately 15 x 40 nm, whilst in dental enamel they were measured at 40 x 100 nm (J.C.Elliott *et al.*, 2002; L.Yubao *et al.*, 1994).

Matching the resorption rates of the material with the tissue replacement and repair rates of the host tissue is vitally important but complex to achieve in that the repair rates of the human body vary significantly and are subject to the type of tissue, tissue health and also age. The ability of an HA implant to be degraded *in vivo* by osteoclasts is largely denoted by the material solubility and dissolution rate at low pH. During bone resorption osteoclasts localise at a chosen site and form a ruffled border reducing the pH to approximately 5.5 immediately beneath the border and the tissue begins to dissolve (E.Y.Kawachi *et al.*, 1998; Y.Miyamoto *et al.*, 2001). Therefore, if the solubility of the implant is less than the solubility of the mineral content of bone, then degradation occurs at a very slow rate, if at all. Similarly, if the solubility of the ceramic implant is greater than the mineral part of the host bone tissue, then degradation occurs. However, if the two solubility values are largely different, biodegradation may proceed too quickly to allow sufficient replacement by natural tissue, and the possibility of void formation arises. Specific properties such as density, crystallinity and presence of micropores have been shown to influence solubility and dissolution. Micropores with diameters of less than 5 μm have particular importance in dissolution properties (C.M.Muller-Mai *et al.*, 1995).

Conventional thermally processed synthetic HA is prepared at around 1100 °C– 1200 °C and is therefore crystalline and stoichiometric with a lower solubility than bone mineral, with the result of very slow (layer by layer) degradation *in vivo* for the former (M.Bohner, 2000). Biological dissolution of apatite ceramics is hypothesised to occur at grain boundaries and dislocations (I.R.Gibson *et al.*, 1999). Unlike the natural platelike bone mineral crystals, polycrystalline synthetic HA consists largely of polygonal sintered coarse particles (C.M.Muller-Mai *et al.*, 1995). Apatite cements set to form HA *in vivo* at the physiological temperature of 37 °C, are less crystalline, have greater solubility and show a faster dissolution rate than sintered HA (Y.Miyamoto *et al.*, 2001). Other implanted calcium phosphates such as dicalciumphosphate (DCPD), cause a pH drop in simulated body fluid (SBF) because of dissolution which serves to further increase the solubility of the material. The pH value is dependent on solubility of HA, wherein the pH decrease as the solubility increases (C.M.Muller-Mai *et al.*, 1995; R.Murugan *et al.*, 2005).

Various complications have surfaced regarding the development of successful resorbable bioceramics including the maintenance of interface, in both strength and stability during biodegradation, in addition to providing only metabolically acceptable substances in the implant material to prevent chronic inflammation and pain occurring upon degradation (L.L.Hench, 1998). Resultantly the substitution of certain chemical species into bioceramic HA has been researched and developed over past years with the intent of improving both the material physical and chemical properties.

2.3 Substituted Apatites

2.3.1 Background

Various chemical substitutions can be made within the ceramic HA lattice without causing adverse reactions upon implantation. There are several inorganic elements present in the chemical composition of the mineral content within hard tissue. Small but significant amounts of sodium (Na^+), magnesium (Mg^{2+}), potassium (K^+), fluoride (F^-), chloride (Cl^-), carbonate (CO_3^{2-}) and water (H_2O) are present amongst the major mineral content of calcium (Ca^{2+}) and phosphate (PO_4^{3-}). The surrounding tissue of the implanted material tolerates appropriate amounts of these species within ceramic apatite (W.Suchanek *et al.*, 1998). The ionic substitutions affect the surface structure and surface charge of the apatite, which plays an influential role in the response of the biological environment to the material. The advantages of the use of substituted apatites for hard tissue replacement have been previously established and several methods have been studied for preparation of such materials (F.Balas *et al.*, 2003).

2.3.2 Carbonated Apatite

Increasing the carbonate content of apatitic materials has several advantages and has been studied largely using cement systems that precipitate HA (E.Fernandez *et al.*, 1999; I.R.Gibson *et al.*, 2002). Increasing the carbonate content of HA (to produce carbonated HA) has been found to increase the material solubility or dissolution rate, without significantly altering the crystallinity. Osteoclasts are therefore able to resorb the material faster during the bone replacement process (Y.Miyamoto *et al.*, 2001). Carbonated HA forms *in vitro* and closely resembles the natural apatite of bone and exhibits a better tissue response and enhanced osteoconductive properties (D.Tadic *et*

al., 2003; E.Fernandez *et al.*, 1999). Carbonate is the most abundant species of the additional ions contained within the natural mineral apatite of human bone and is present at approximately 8 wt % (J.Barralet *et al.*, 1998).

2.3.3 Fluorinated Apatite

The mineral component of tooth enamel is fluoroapatite, an apatite material containing 0.04 wt% to 0.07 wt% of fluoride and is known to be more acid resistant than HA. Apatite is the only type of calcium phosphate material with the ability to incorporate fluoride ions that subsequently improve the physical, chemical and biological properties of the compound (D.Siva Rama Krishna *et al.*, 2002). Previous findings have shown that the addition of fluoride ions to solutions containing calcium and phosphate ions promotes apatite formation by enhancing the rate of hydrolysis of the phase intermediates. The fluoride-containing phase precipitates out of the supersaturated solution thus affecting the magnitude of the driving force for precipitation and assisting crystallisation. The conversion of HA to fluoroapatite requires amounts of fluoride that increase with corresponding pH. A surface layer of fluoroapatite is formed by deposition when the preceding surface is in equilibrium with the bulk solution (L.J.Jha *et al.*, 1997).

2.3.4 Magnesium-substituted Apatite

The magnesium content within biological apatite has been found to be high during the initial stages of calcification, decreasing in amount as the process progresses and calcification increases (E.Bertoni *et al.*, 1998). This Group 2 cation has also been associated as a factor governing bone fragility as a result of qualitative changes of the bone matrix. All stages of skeletal metabolism are adversely affected by depletion of the ion, with common results including decreased osteoblastic and osteoclastic activity that hinders the bone remodelling process and contributes to fragile bones, osteopenia and lack of bone growth (S.R.Kim *et al.*, 2003). Magnesium is also reported by a number of researchers including Bertoni (1998), to inhibit apatite crystallisation in solution, destabilise the structure of HA whilst favouring the thermal conversion into β-tricalcium phosphate (β-TCP) (E.Bertoni *et al.*, 1998).

2.3.5 Silicon-substituted Apatite

Silicon is accepted to be essential to growth and development of biological hard tissue (N.Patel *et al.*, 2003; S.R.Kim *et al.*, 2003). During bone formation and calcification,the osteoid and active growth areas can contain silicon levels of up to 0.5 wt% (E.M.Carlisle, 1970). Silicon content has been shown to improve bioactivity by the stimulation of apatite formation on the surface of bioactive silicate containing glass ceramics (e.g., Bioglass and Cerabone A-W) upon immersion in simulated body fluid (S.R.Kim *et al.*, 2003). The silanol groups (Si-OH) within the materials have been suggested catalysts of apatite nucleation preceding surface layer formation. The breaking of the bonds and subsequent loss of soluble silica precedes the formation of Si-OH bonds and the associated condensation to form SiO_2, which upon polymerisation produces a SiO_2 rich layer upon the glass ceramic surface (L.L.Hench, 1991). The formation of a calcium phosphate layer on top of the SiO_2 rich layer facilitates the growth of apatite crystals and the following cell adhesion, collagen formation and protein formation giving rise to the interfacial bonding between the host tissue and the implanted bioactive glass ceramic (I.R.Gibson *et al.*, 1999). However, whereas pure hydroxyapatite is thermally stable up to temperatures of approximately 1200 °C before it begins to decompose into α or β tricalcium phosphate, the introduction of silicon in greater quantity than 1.97 wt %, results in the formation of α-TCP and calcium phosphate silicate at temperatures above 1100 °C. Thermal stability at temperatures around 1200 °C can be achieved when substituting with amounts below 1.97 wt % (I.R.Gibson *et al.*, 1999; S.R.Kim *et al.*, 2003).

Interestingly, unlike magnesium and silicon, the substitution of fluoride into HA has no significant affect on the thermal stability of the HA structure at temperatures up to 1300 °C (E.Bertoni *et al.*, 1998).

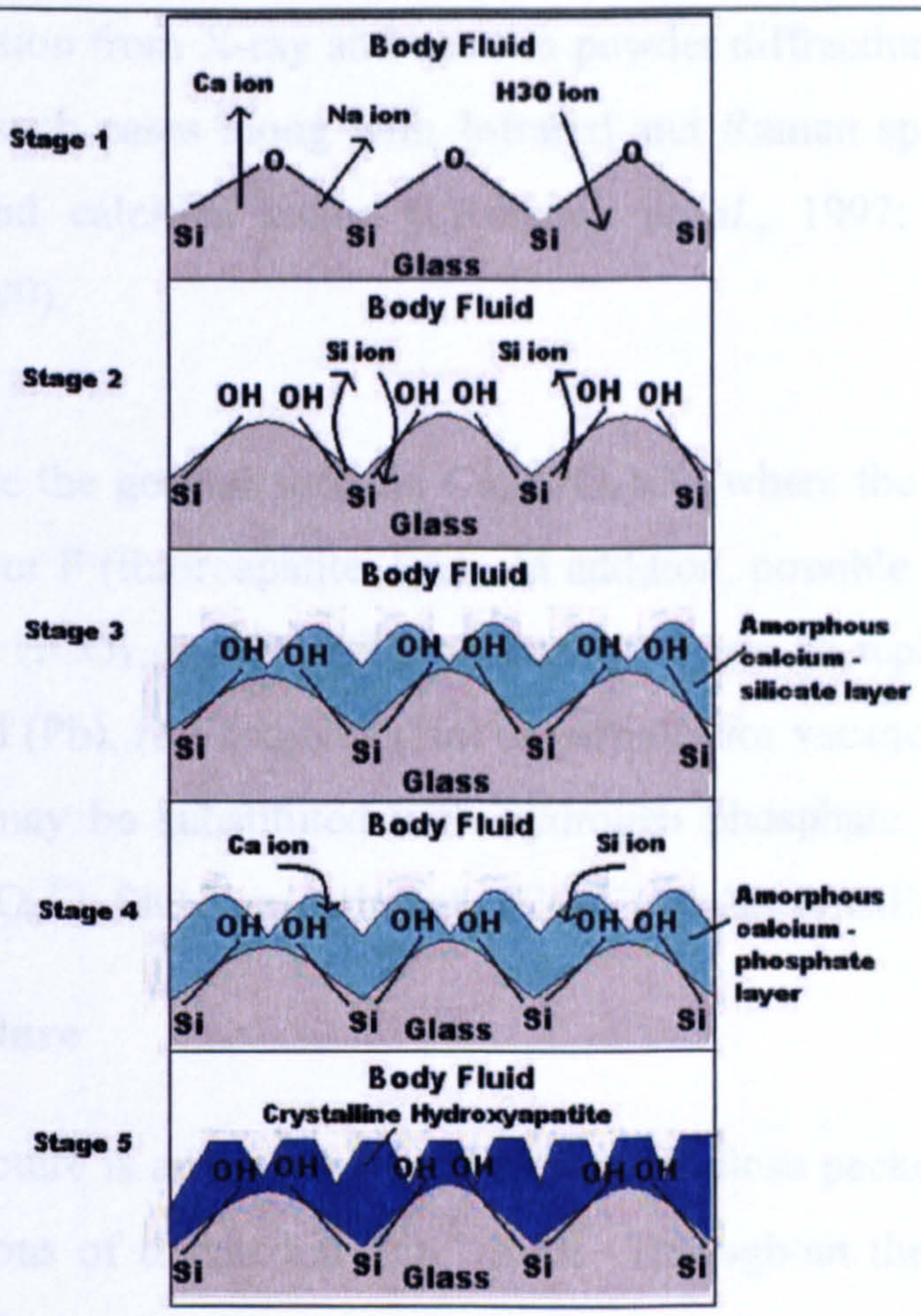

Figure 2.1: Five step mechanism of hydroxyapatite formation on traditional melt-derived bioactive glass.

2.4 Structural Properties

2.4.1 Background

It can be concluded that substituted apatites play an important role in the mineralisation process of biological hard tissue in addition to the fabrication, stability and enhanced bioactivity of HA. The ability of the apatite lattice to accept a large variety of substitutional ions in addition to vacancies and solid solutions has added complexity to determining the structure and chemistry of apatite compounds. Although the basic apatite structure was determined in 1930, it has largely been the past forty years that success has been found in identifying the structural properties of the majority of apatitic compounds. Analytical methods involving single crystal X-ray diffraction studies have provided the majority of the structural detail and crystal chemistry although for many precipitated, biological and mineral apatites where suitable single crystals are unobtainable other methods have been applied (J.C.Elliott, 1994). The Rietveld method

of structure determination from X-ray and neutron powder diffraction patterns has been increasingly used in such cases along with Infrared and Raman spectroscopy for the study of minerals and calcified tissue (I.Rehman *et al.*, 1997; J.C.Elliott, 1984; R.M.Wilson *et al.*, 1999).

Apatitic ceramics have the general formula $Ca_{10}(PO_4)_6X_2$ where the X is typically OH (hydroxyapatite, HA) or F (fluoroapatite, FA). In addition, possible substitutions for X include chlorine (Cl), $½CO_3$ or ½O whilst calcium (Ca) can be replaced by strontium (Sr), barium (Ba), lead (Pb), two sodiums (Na) or partially for vacancies. The phosphate (PO_4^{3-}) components may be substituted with hydrogen phosphate (HPO_4^{2-}), arsenate (AsO_4^{3-}), vanadate (VO_4^{3-}), SiO_4^{4-} or carbonate (CO_3^{2-}) groups (J.C.Elliott, 1994).

2.4.2 Apatite Structure

The basic apatite structure is an approximated hexagonal close packed (HCP) lattice of spherical representations of tetrahedral PO_4^{3-} ions. Throughout the lattice octahedral interstitial sites give rise to channels that run parallel to the hexagonal axis. The apatite unit cell contains six PO_4^{3-} ions and six octahedral interstitial sites, described by three HCP cells in both volume and parameter. The first published reports of this structure were almost in unison in 1930 by Naray-Szabo and Mehmel in Germany (J.C.Elliott *et al.*, 2002; M.Mehmel, 1930; S.Naray-Szabo, 1930). The lattice parameters are approximately a=0.94 and c= 6.9 Å and can deviate slightly along with refractive indices and calculated densities depending on the preparation and processing methodology which can frequently introduce nonstoichiometry.

Within a portion of the channels, linear columns of fluoride ions (F^-) are located with individual ions each surrounded by three calcium ions (Ca^{2+}) forming additional columns accounting for $^6/_{10}$ of the calcium content. Similar columns are comprised of the residual Ca^{2+} ions that run through the remaining channels (J.C.Elliott *et al.*, 2002). It has been reported that the hexagonal packing of the PO_4^{3-} ions determines the stability of the lattice, which may be altered by ionic substitutions contributing to the complexity of studying many of the apatites. Pure hydroxyapatite for example, is pseudohexagonal shown in Figure 2.2 with a doubled b-axis relating to an ordered arrangement of the

hydroxyl ions (OH^-) in columnar formation when successive hydroxyl linkages so (-OH-OH-OH-) integrity is maintained (V.P.Orlovskii *et al.*, 2002).

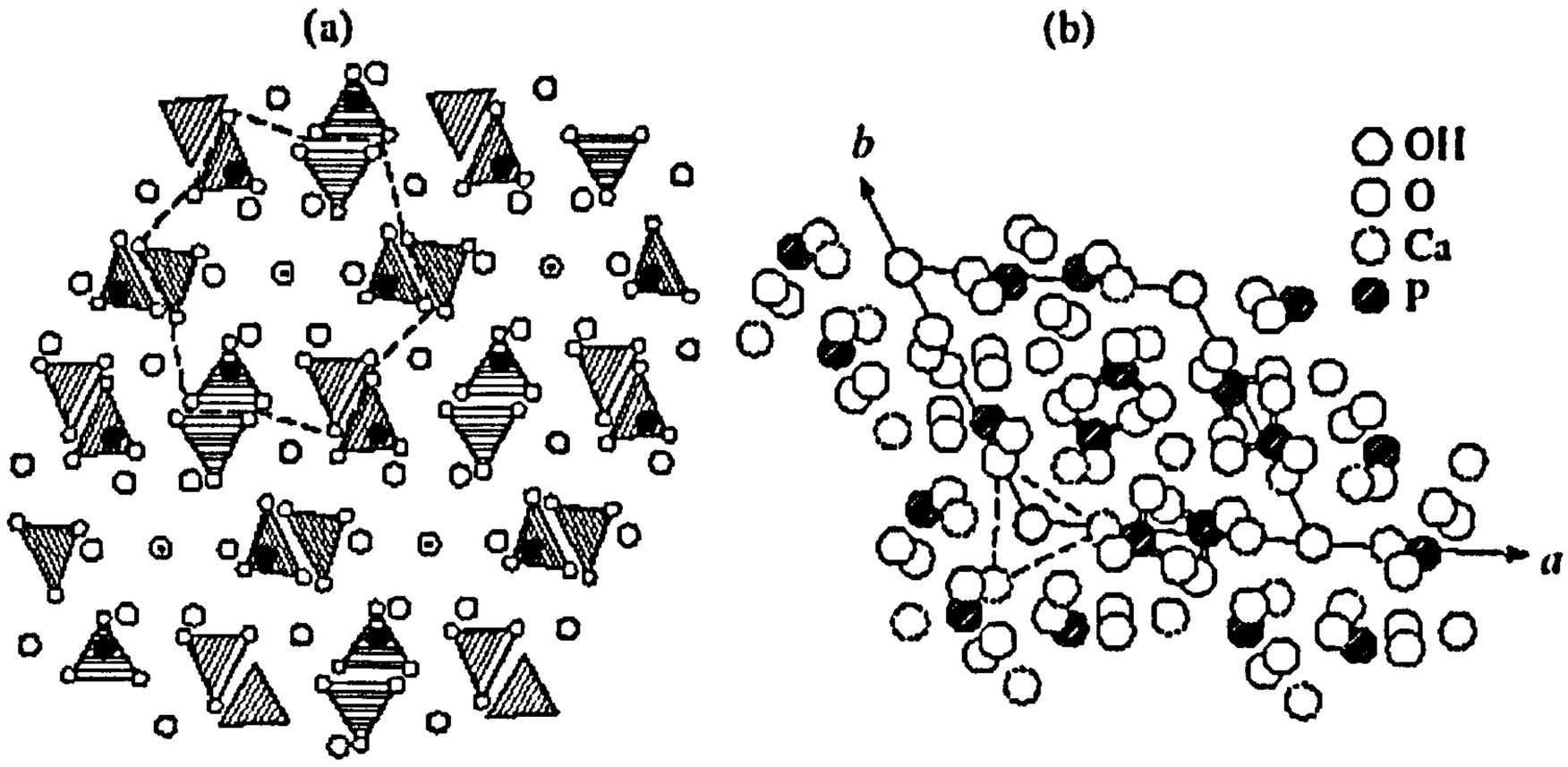

Figure 2.2: (a) Atomic structure of HA and (b) its projection along the *c* axis (V.P.Orlovskii *et al.*, 2002).

Approximate lattice parameters (Å) of a=9.421, b=2a, c=6.881 were reported for the HA structure that demonstrates monoclinic spacing. The structure becomes hexagonal if 10% of the OH^- ions are replaced with F^- ions and it is therefore reasoned that biological apatites tend to be hexagonal due to their natural impurities disrupting the (-OH-OH-OH-) columnar integrity and varying the OH^- direction (J.C.Elliott, 1997). The ionic radius of the fluoride group is also larger than that of the hydroxyl group and, therefore, upon increasing F^- substitution into the HA structure, a significant increase in the $Ca_{(2)}$-OH bond length and marked decrease in the a-axis dimension is observed (L.J.Jha *et al.*, 1997; W.T.Lee *et al.*, 2000).

Precipitated apatites share similar XRD patterns to poorly crystalline and biological HA irrespective of the variation in Ca/P molar ratios which ranges from approximately 1.5 to greater than 1.67. Reported structural differences between precipitated HA and thermally processed HA include a larger a-axis by 0.01-0.02 Å. This is also seen upon decreasing Ca/P ratio, in addition to a decrease in the c-axis parameter (J.C.Elliott, 1994; J.C.Elliott, 1997).

2.5 Structural and Chemical effects of Substitutions

2.5.1 Magnesium

Magnesium can be substituted for calcium and incorporated into the crystalline structure by up to about 10 wt % according to Bertoni *et. al.*. (1998) although the amount of magnesium found associated to biological HA by chemical analysis is significantly higher as a result of the majority of the compound being adsorbed to the crystal surface or present in an amorphous phase (E.Bertoni *et al.*, 1998). The magnesium ion (Mg^{2+}) is of limited acceptance within the HA lattice due to the ionic radius (0.72 Å) being much smaller than that of Ca^{2+} (1.00 Å). Changes in structure that correlate with the substitution include an increase in the *a*-axis parameter along with a decrease in the *c*-axis parameter, with an increase in the Mg^{2+} content (J.C.Elliott, 1997). The inhibiting effect on the crystallisation of HA has been suggested due to the structural mismatch created by the Mg^{2+} ions when incorporated into prenucleated HA structures (E.Bertoni *et al.*, 1998).

2.5.2 Silicon

The substitution sites within the HA structure are largely determined by the ionic radii of the ions to be incorporated. Substitution of silicon into hydroxyapatite follows the formula; $Ca_{10}(PO_4)_{6-x}(SiO_4)_x(OH)_{2-y}$ and is admitted as a silicate ion substituting for phosphate at its P site due to the similarity between the respective ionic sizes. To compensate for the extra negativity of the silicate ion there is a reduction in the amount of hydroxyl groups. The ionic radius of the Si^{4+} ion at 0.42 Å is larger than the radius of the P^{5+} ion of 0.35 Å resulting in a slight corresponding increase in the *a* and *c* lattice constants upon replacement. The change in lattice constants confirms incorporation into the structure as opposed to surface attachment. Corresponding to the change in the unit cell parameters, the theoretical density of silicon-substituted hydroxyapatite is less than that of pure HA (S.M.Best *et al.*, 2003; S.R.Kim *et al.*, 2003) Prior to this establishment there was concern over whether the silicon ion substituted completely for the phosphate within the lattice, or whether partial replacement took place or whether the ionic species remained as an independent phase (F.Balas *et al.*, 2003).

2.5.3 Silicon Co-substitution

Substitution of Mg^{2+} by Ca^{2+} is limited to less than 1 wt % in synthesised HA partially due to the difference between the hydrated properties of both ions. The tightly bound hydration layer of the Mg^{2+} ion resultant of its smaller ionic radius when compared to the Ca^{2+} ion, provokes much slower dehydration of the aqueous ions, a prerequisite for incorporation into the crystalline structure. However it has been established by Kim *et. al.* (2003) that when the Mg^{2+} ion is co-substituted with the silicate ion it can be incorporated into the HA lattice at levels equal to 1 wt %.(S.R.Kim *et al.*, 2003) The improved bioactivity of the substituted apatite has been a suggested result of the increased negative surface charge from substitution of PO_4^{3-} groups with SiO_4^{4-} groups (J.Vandiver *et al.*, 2005).

2.5.4 Carbonate

Carbonate ion substitution into the HA structure is unique in that there are two possible atomic sites for the substitution with distinct synthesis techniques reported to produce them.(I.R.Gibson *et al.*, 2002) A-type substitution of CO_3^{2-} occurs at the hydroxyl (OH) position whereas B-type substitution occurs at the phosphate PO_4^{3-} position.(J.Barralet *et al.*, 1998) The following equation (2.1) describes the simple A-type substitution mechanism where a substitution ratio of one carbonate group replacing two hydroxyl groups exists allowing the production of a neutrally charged material with controlled chemical composition.

$$Ca_{10}(PO_4)_6(OH)_2+CO_2 \rightarrow Ca_{10}(PO_4)_6(OH)_{2-x}(CO_3)_xH_2O$$

(Equation 2.1)

However, Gibson and Bonfield (2002) suggested that the documented production method is ill suited for the synthesis of biomedical materials due to the lengthy reaction times and the lack of control over the level of carbonate substitution which will proceed more readily at the material surface than in the bulk composition. The resultant material is unlikely to be replicative of the carbonated mineral phase of natural bone as analysis demonstrates that the carbonate ions observed in natural tissue are not located solely on the A site of the hydroxyl groups (I.R.Gibson *et al.*, 2002).

The production of B-type carbonated hydroxyapatite (CHA) is often by methods of controlled precipitation from solutions containing calcium, phosphate and carbonate ions at high pH. Substituting a carbonate group in the phosphate ion site serves to reduce the crystallinity and precipitate size of the material providing difficulty in the characterisation of substitution mechanism. The problem of maintaining charge balance by replacing PO_4^{3-} with less negative CO_3^{2-} has been resolved by a variety of mechanism models describing B-type carbonate substitution (J.Barralet *et al.*, 1998). Coupled or co-substitution where the additional substitution of a monovalent ion (such as sodium from sodium carbonate solution used for the source of carbonate ions during precipitation) for a calcium ion balances the negative charge caused by carbonate substitution is described by Equation 2.2 (A.Antonakos *et al.*, 2007).

$$Ca_{10-x}Na_x(PO_4)_{6-x}(CO_3)_x(OH)_2 \text{ or}$$
$$Na^+ + CO_3^{2-} \leftrightarrow Ca^{2+} + PO_4^{3-}$$

(Equation 2.2)

Problems with purity could be encountered due to the incorporation of sodium ions from the reactants into the structure and so alternative methods have been researched. Further suggestions of vacancy formation (usually calcium) within the unit cell were put forward to explain the charge balance in addition to a combination of the two mechanisms (I.R.Gibson *et al.*, 2002; J.C.Elliott, 1994).

Structurally it has been identified within a number of studies that the lattice parameters change linearly by a decrease in the a-axis from approximately 9.44 to 9.3 Å and an increase in the c-axis from approximately 6.88 to 6.93 Å as the carbonate content is increased from 0 to 22 wt %. The theoretical maximum carbonate content that can be incorporated into the HA lattice is 22.27 wt % assuming that water is absent. When prepared in aqueous systems it has been commonly observed that carbonate is incorporated in such quantities when sodium (Na^+) ions are present and that significantly less than 20 wt % is incorporated when absent (J.C.Elliott, 1994).

Both A and B types substitution can occur simultaneously resulting in AB type substitution with a more complex mechanism. Produced largely by aqueous precipitation the co-substitution of sodium or ammonium ions from the reactants occurs to maintain charge balance. This type of substitution is considered common to the

apatite that constitutes natural bone mineral and has therefore been of great interest during the recent few years (I.R.Gibson *et al.*, 2002).

2.6 Limitations of Bioceramic HA

Although artificially prepared bioceramic HA with resemblance to the structure of natural bone has good compatibility within the human body that can be enhanced by various substitutions, wide usage in medical application is limited due to poor mechanical properties which result from poor sintering properties of the materials (S.Bose *et al.*, 2003; V.A.Dubok, 2000).

Load bearing applications require high mechanical strength materials provided by high densification during conventional pressureless sintering of fine ceramic powder. Microstructural features such as sintered density, the average grain size in addition to the distribution of the grain size and any microstructural defects largely determine the mechanical properties. Many of these strength-limiting microstructural properties stem from the powder itself. Therefore the preparation of fine agglomerate-free powder with a uniform grain size and high surface area that will sinter or thermally consolidate favourably is of primary importance during the fabrication of a bioceramic HA implant with high sintered density and a desirable microstructure (G.C.Koumoulidis *et al.*, 2003).

The conventional powder processing methods can lead to the formation of hard particle agglomerates that can exhibit a higher green density than the surrounding material and are virtually impossible to eliminate using the conventional compaction techniques such as die-pressing and isostatic (hot or cold) pressing. These powder compacts containing agglomerates undergo differential sintering at the sintering temperature giving rise to the strength limiting microstructural flaws which may facilitate crack formation and propagation (M.G.S.Murray *et al.*, 1995). Within the starting powder, high aspect ratio morphology can lead to poor packing of the particles subsequently causes exaggerated grain growth during thermal densification treatments (S.Bose *et al.*, 2003).

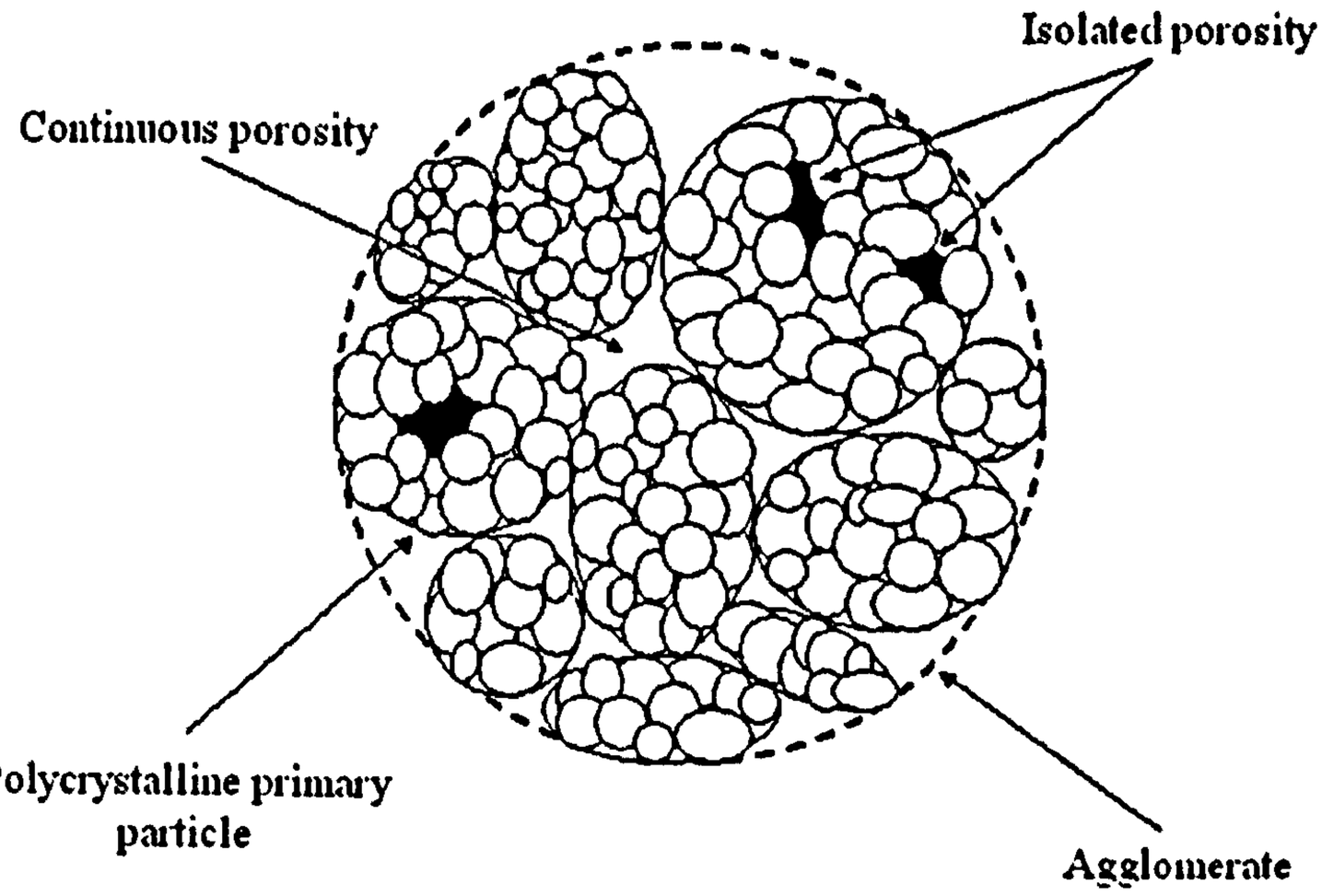

Figure 2.3: Schematic diagram of an agglomerate consisting of dense, polycrystalline primary particles (M.N.Rahaman, 2003).

2.7 Nanoceramics

Nanostructure processing of HA bioceramic allows chemical homogeneity and microstructural uniformity to be achieved facilitating the generation of fully dense bioceramics at low sintering temperature with a significant reduction in flaw size. If the grain size is reduced to the nanometer range (1-100 nm) particularly the lower end, then the normally brittle bioceramic can be made more easily deformable. In addition, the high volume fraction of grain boundaries provides for increased ductility and superplasticity for net-shape forming at low temperatures. Significantly enhanced sinterability is experienced due to the excellent compositional homogeneity and phase purity associated with nanocrystalline HA provides stability against decomposition at high temperatures (1200-1300 °C), achieving dense products with superior mechanical integrity without the undesirable secondary phases (A.S.Edward *et al.*, 2001). To sinter HA above 1300 °C without decomposition into tetra calcium phosphate or TCP, requires the process to be performed under moisture (L.B.Kong *et al.*, 2002).

Human bone is a natural nanocomposite (consists of two or more phases obtaining properties that are unavailable in individual phases or components) with impressive toughness and strength resultant of the composition largely of nanoscale platelike crystals of HA which are dispersed in a matrix of collagen fibres. The superior strength arises from the enormous surface area available for interaction i.e. the number of interfaces between the two phases due to the nanoparticle composition.

The engineering of HA with a grain size reduced to nano-level would result in a number of improved functional properties due to the reduced grain size, large surface area to volume ratio and ultra fine structure resembling that of natural apatite. The implant-cell interaction in the biological environment would be enhanced and furthermore, the osteoconductivity, solubility, sinterability and mechanical reliability of the material could be promoted by controlling the particle size and structural morphology at the nano-level. Previous study has demonstrated the increased solubility and superior bioresorption of nanocrystalline HA which has been attributed to the high surface area to volume ratio (R.Murugan *et al.*, 2005).

It has been concluded that the ionic dissolution of nanocrystalline HA is similar to that of natural bone mineral due to the amount of calcium release corroborating well with the calcium release pattern of biological apatite and being significantly greater in amount than that released from conventional HA.

Summary

Hydroxyapatite is a bioactive ceramic material found naturally in the mineral portion of human bones and teeth. Chemically synthesised it may be medically applied as a bone substituting material within the human body to correct bony defects. Various inorganic ions are found in naturally occurring apatite and similar additions and substitutions may be incorporated into the lattice of chemically prepared apatite also. Such incorporations vary properties of the material such as mechanical (compressive) strength and bioactivity. However, large and inconsistent particle sizes in addition to processing flaws limit the material strength of chemically synthesised hydroxyapatite preventing usage in load bearing applications. The production of nanocrystalline hydroxyapatite similar to the particle size found in human tissue provides an improvement in the material properties, such as thermal stability, mechanical properties and solubility.

Chapter 3 Processing of hydroxyapatite

Overview

Introductions to hydroxyapatite manufacture by conventional wet precipitation and emulsion technology are provided in this chapter with respective advantages and drawbacks. Much research has been carried out in the processing area in order to improve the chemical and structural properties of HA products. Previous research is used to report physical properties of HA synthesised using emulsion systems. Further processing treatments after chemical synthesis are mentioned in addition to the consequential effects on the HA product. The main experimental outline is provided for material synthesis carried out within this particular study.

3.1 Main Processing Methods

Many different chemical processing routes have been employed in order to prepare fine HA powder, including precipitation and co-precipitation, hydrothermal reactions (H.S.Liu *et al.*, 1997; J.Hu *et al.*, 2001; L.Yubao *et al.*, 1994; T.Hattori *et al.*, 1990; X.Deng *et al.*, 2001), sol-gel synthesis (B.Melde *et al.*, 2002; C.S.Chai *et al.*, 1999; L.L.Hench *et al.*, 1990; M.Hsieh *et al.*, 2001), mechanochemical synthesis (R.E.Riman *et al.*, 2002; W.Suchanek *et al.*, 2002), pyrolysis of aerosols (K.Okuyama *et al.*, 2003; M.Vallet-Regi *et al.*, 1994) and recently supercritical fluid (G.Demazeau, 1998; J.Liu *et al.*, 2001; M.M.Hoffman *et al.*, 2000; R.Marr *et al.*, 2000; R.Noyori, 1999) and emulsion synthesis (G.C.Koumoulidis *et al.*, 2003).

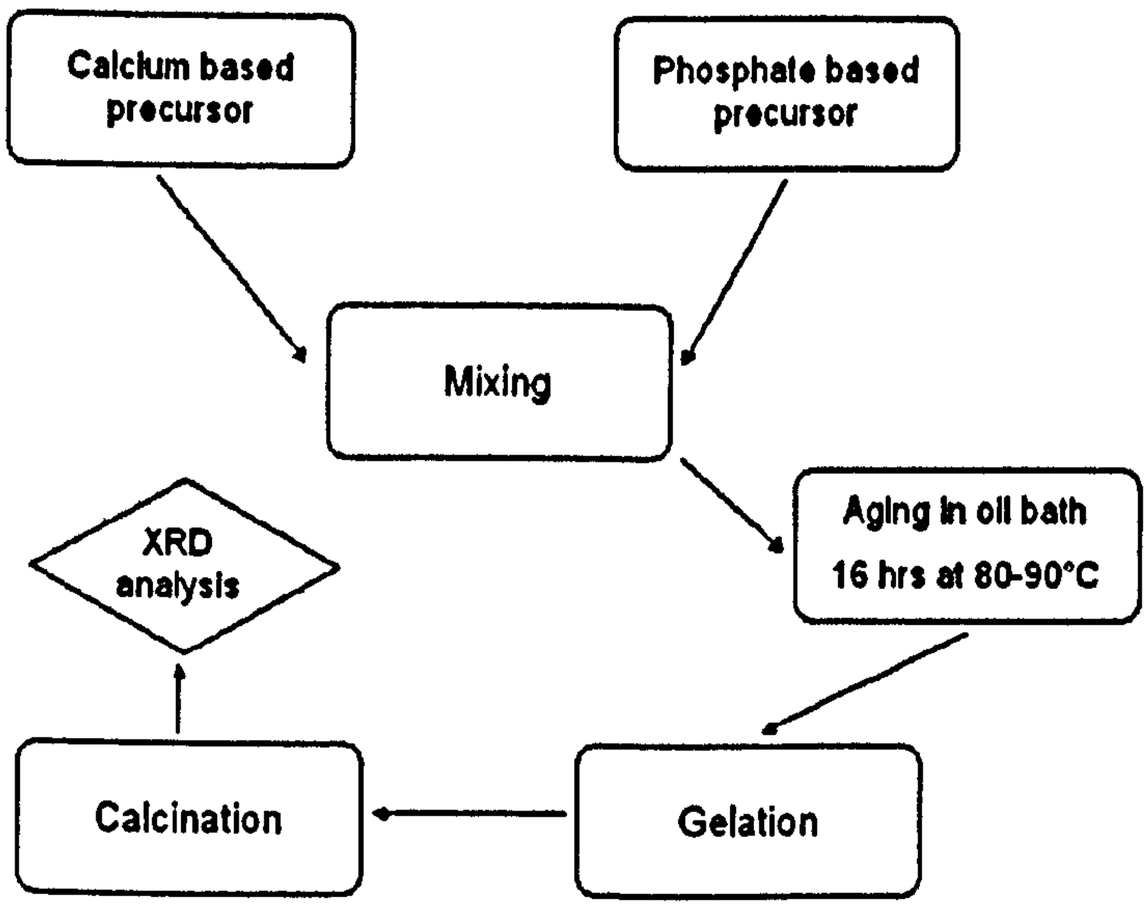

Figure 3.1: Schematic diagram of sol-gel synthesis of HA. Second to conventional precipitation, it is the most widely used manufacturing route.

3.2 Conventional Precipitation

Wet chemical synthesis or "bulk" precipitation is one of the most commonly used techniques providing a high production yield but of generally large primary particles with wide particle distributions due to the inability to control the flocculation of particles during formation and as a result ball-milling is required during the final stages to produce less agglomerated particles (J.Gomez-Morales *et al.*, 2001; L.M.Rodriguez-Lorenzo *et al.*, 2000; M.J.Phillips *et al.*, 2003). The main formulae used involve calcium hydroxide ($CaOH_2$) and orthophosphoric acid (H_3PO_4) or calcium nitrate ($Ca(NO_3)_2$), diammonium hydrogen phosphate ($(NH_4)_2HPO_4$) and ammonium hydroxide (NH_4OH) which result in a faster production rate (H.Gilman *et al.*, 1991; H.Gilman *et al.*, 1994; L.Chow *et al.*, 2004). Previous work has obtained HA from reactions (3.1) and (3.2):

$$5Ca(NO_3)_2 + 3NH_4H_2PO_4 + 7NH_4OH \rightarrow Ca_5(PO_4)_3OH + 10NH_4NO_3 + 6H_2O$$

(Equation 3.1)

$$5Ca(OH)_2 + 3H_3PO_4 \rightarrow Ca_5(PO_4)_3OH + 9H_2O$$

(Equation 3.2)

Precipitation of HA is a two-step process involving nucleation and grain growth. Nucleation involves the random assembly of molecules in solution to form aggregates that are lacking in size required for precipitation. When the nuclei become bigger, grain growth occurs. A supersaturated solution occurs when a solution contains more solute than should be present at equilibrium and the more solute that is dissolved, the greater the supersaturation. The rate of nucleation is affected more by the relative super-saturation than the rate of grain growth, proceeding at a much faster rate in a highly supersaturated solution. This results in a suspension of fine particles that give rise to a very small final size of the precipitate. HA precipitation involves Ca^{2+} and PO_4^{3+} simultaneously, with concentrated amounts required in order to facilitate a high rate of nucleation.

Conventional precipitation does not possess high enough concentrations of phosphorous and calcium to obtain a high rate of nucleation and resultant fine particle size as the procedure follows the addition of either a calcium or phosphorous solution into the other. However a modification by Kong and Boey (2002) allowed the production of nanosized HA by a simple precipitation process with high concentration of both ions (L.B.Kong *et al.*, 2002). Crystallinity and particle size are also affected by preparatory solution temperature in addition to carbonate incorporation (M.M.Seckler *et al.*, 1999; Y.X.Pang *et al.*, 2003).

3.3 Emulsion Technology

In order to synthesise nanosized HA powder research has led to the modification of certain well-established conventional processing routes including the use of emulsion technology (M.P.Pileni, 1997). Although this has been studied extensively over the past twenty-five years, the potential for use as a refinement measure for preparing fine, agglomerate-free ceramic powders has only been recently discovered (M.G.S.Murray *et al.*, 1995). Applications have included powder production for electronic, magnetic and optical materials with the potential use for the synthesis of nanoparticle calcium phosphates and HA only being realised within the last decade (M.J.Phillips *et al.*, 2003).

3.3.1 Macroemulsion

The traditional definition of a macroemulsion is a heterogeneous system consisting of at least one immiscible liquid dispersed in another in the form of droplets with the individual diameter usually larger than 0.1 μm. It demonstrates limited stability with a cloudy or milky appearance before the suspended droplets will eventually agglomerate and the dispersed phase will separate. The stability of the dispersed system can be accentuated by additives such as ambiphilic surface-active agents or surfactants (A.Graciaa *et al.*, 1988). These compounds serve to lower the surface tension of liquids, or reduce the interfacial tension between two liquids or a liquid and a solid (G.K.Lim *et al.*, 1999a; T.Stoebe *et al.*, 1997).

3.3.2 Microemulsion

Alternatively, a microemulsion is a thermodynamically stable, isotropic dispersion of two immiscible liquids stabilised by an interfacial film of surfactant (H.Wennerstrom *et al.*, 1997). The dispersion may be either "oil-in-water" or "water-in-oil" and is typically transparent. The dispersed phase is confined in the nanometer range of spherical droplets or continuous channel. The delivery of nanosized particles of organic and inorganic composition is due to the chemical reaction being confined to within the nanosized domains or reactors when the droplets containing the desirable reactants collide with each other (G.K.Lim *et al.*, 1996). Within the dynamic structure of the microemulsion the nanosized droplets are in constant coalescence, breakdown and deformation.

Generally a "water-in-oil" composition is prepared where the water phase (formulated with corresponding hydroxide) subject to a high dielectric constant is dispersed within an oil phase of low dielectric constant, such as the organic solvent, iso-octane (2,2,4-trimethylpentane), petroleum ether/PE or cyclohexane (G.K.Lim *et al.*, 1997; I.Lisiecki *et al.*, 1999; K.Kandori *et al.*, 1988). The nanosized droplet reactors produced are in the form of reverse micelles where the colloidal aggregate of amphipathic surfactant molecules interact with the Ca^{2+} and/or PO_4^{3-} ions within the central aqueous solution using the hydrophilic portion of the molecule and giving rise to a "cagelike" structure with the exterior created by the hydrophobic portion of the surfactant molecule

interacting with the surrounding oil phase, an apolar solvent (see Figure 3.2) (J.J.Silber *et al.*, 1999). The formation of HA results from the confined reaction of the calcium and phosphate ions(A.Filankembo *et al.*, 2000; G.K.Lim *et al.*, 1999a; J.J.Silber *et al.*, 1999).

The shape and spontaneous curvature for reverse micelles corresponds to the energetically favourable packing configuration of the surfactant molecules at the interface governed largely by the molecular geometry. Although there is no clear definition, certain researcher's only term the surfactant aggregates reverse micelles if the water to surfactant ratio within the core is less than 15, regarding microemulsions to be associated with "droplets" corresponding to larger core water content with water/surfactant ratio being above 15. Regardless of this there are many reports of their use as microreactors to produce well-defined nanosized crystallites or chemically modified enzymes and they have also been formed in critical and supercritical fluids. Much of the geometric modelling has been based on reverse/inverse microemulsions utilising sodium bis(2-ethylhexyl)sulfosuccinate or Na-AOT as the surfactant facilitating reverse micelles in "water-in-oil" microemulsions (E.M.Carlisle, 1970).

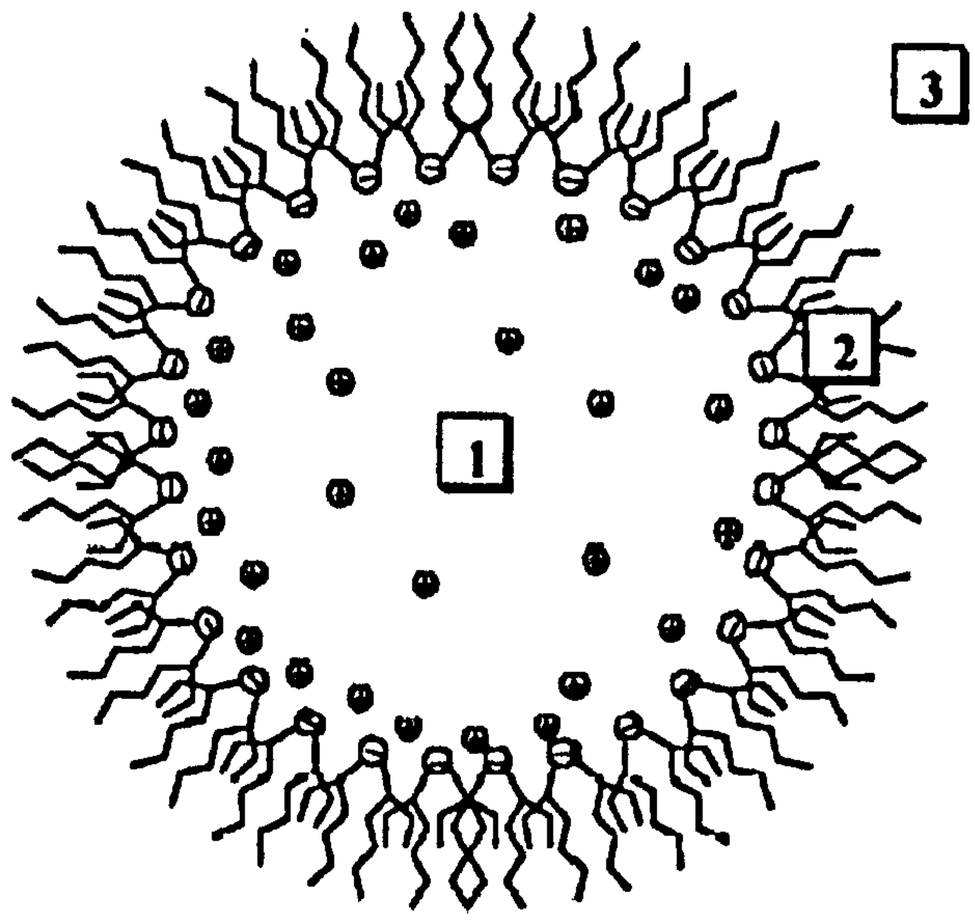

Figure 3.2: Schematic of the different regions of the micellar solution: (1) Water pool; (2) Interface; and (3) Organic pseudophase (J.J.Silber *et al.*, 1999).

This surfactant is one of the most widely employed surfactants in reverse micellar systems or "water-in-oil" emulsions, due to the ability to form well characterised micelles over a wide range of water/surfactant mole ratios and low solute concentrations (J.J.Silber *et al.*, 1999). The association of Na-AOT surfactant in such apolar solvents is resultant of the dipole-dipole and ion pair interactions between amphiphiles as opposed to the hydrophobic attractions-electrostatic repulsion responsible for micellisation in water. The thermodynamics of the process add confirmation by the entropies of micellisation of AOT in polar solvents to give direct micelles are positive, whilst entropies of micellisation to form reverse micelles are negative (J.J.Silber *et al.*, 1999; M.P.Pileni, 1993).

From the large amount of research placed into microemulsion synthesis it has been identified that the main disadvantage associated with the "water-in-oil" reverse microemulsion processing is the large requirements for oil and surfactant phases with a relatively low production yield if the chemicals are not recycled in addition to the problem of disposal of nonbiodegradable surfactants (G.K.Lim *et al.*, 1999b). Alternatively, the use of "oil-in-water" microemulsions offers the advantage of a high production yield at the expense of a small amount of oil and surfactant phases creating a micellar system facilitating the synthesis of nanocrystalline HA. The surfactant molecules in micelles interact with calcium ions in the exterior aqueous environment whilst the oil phase residing in the hydrophobic cores of oil-swollen micelles creates an expansion in the dimensions thus forming microemulsion droplets as seen in Figure 3.3 (G.K.Lim *et al.*, 1999a). The expansion increases the number of calcium-rich domains that act as reaction sites on the droplet exterior that facilitate HA formation upon contact with the phosphate ions present in the aqueous phase (or during collision). The reaction is rapid due to the concentrated surface calcium being localised and spontaneous nucleation of forming HA proceeds simultaneously as the nucleation sites are formed due to the continuous aqueous phase providing a constant supply to the reaction sites and growth of HA crystallites (G.K.Lim *et al.*, 1999a; K.Sonoda *et al.*, 2002).

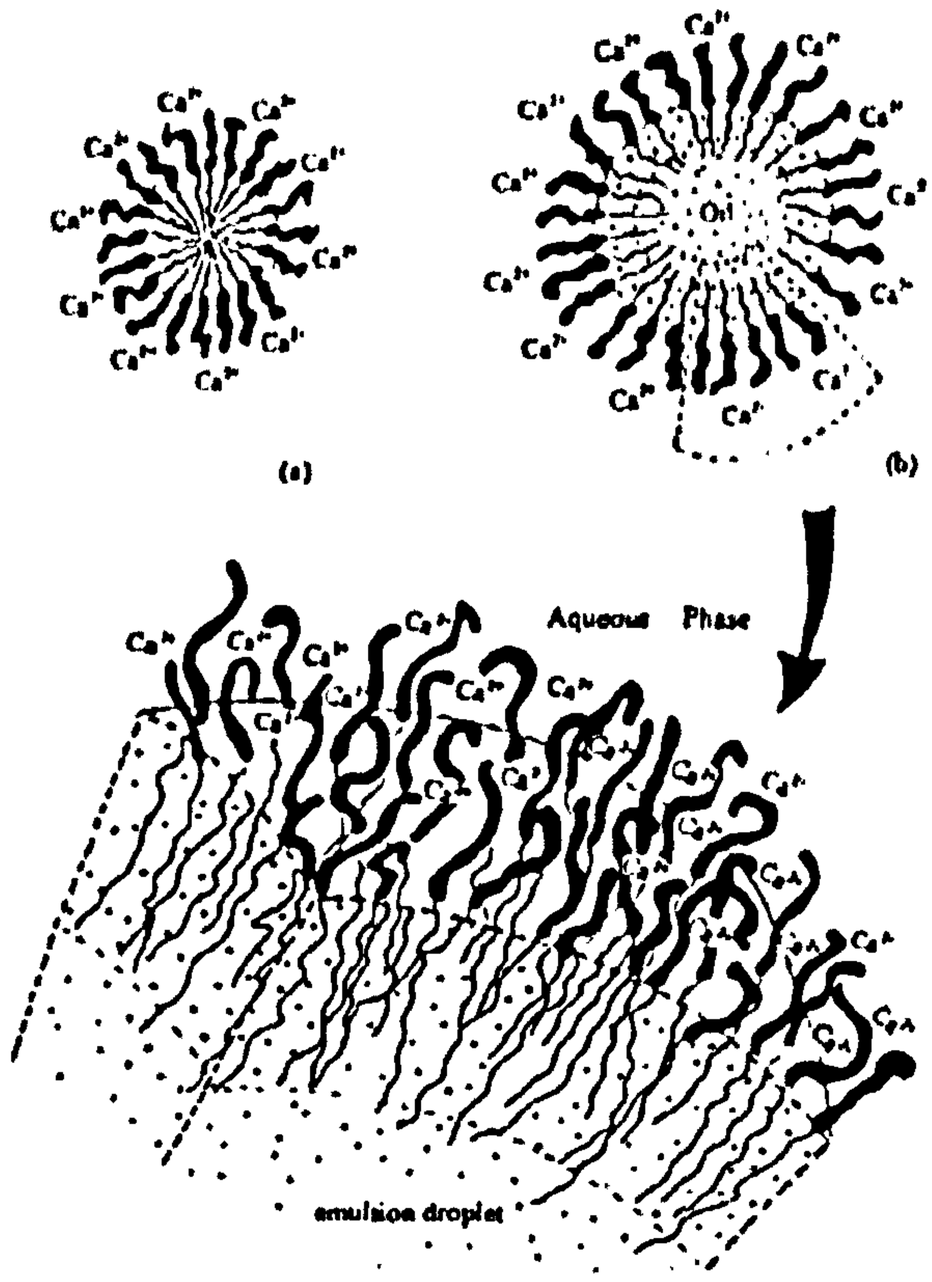

Figure 3.3: Schematic representation of (a) micelle and (b) emulsion droplets (G.K.Lim *et al.*, 1999a).

The larger emulsion droplets are reported to be more stable than surfactant micelles that are typically less than 10 nm in size. The larger droplets also have a longer average life span resultant from the interaction between the hydrophobic portion of the surfactant molecules and the oil in droplet cores that possess viscoelasticity hindering the rapid disintegration and coalescence. Solid HA particle formation on the droplet surface strengthen the droplet integrity further and add to the advantages of an emulsion system as opposed to a micellar system for nanocrystalline HA production. The consistent and uniform size of the nanocrystals prevents extensive growth of crystallite and particle size during calcination above temperatures of 650 °C (G.K.Lim *et al.*, 1999a; S.Bose *et al.*, 2003).

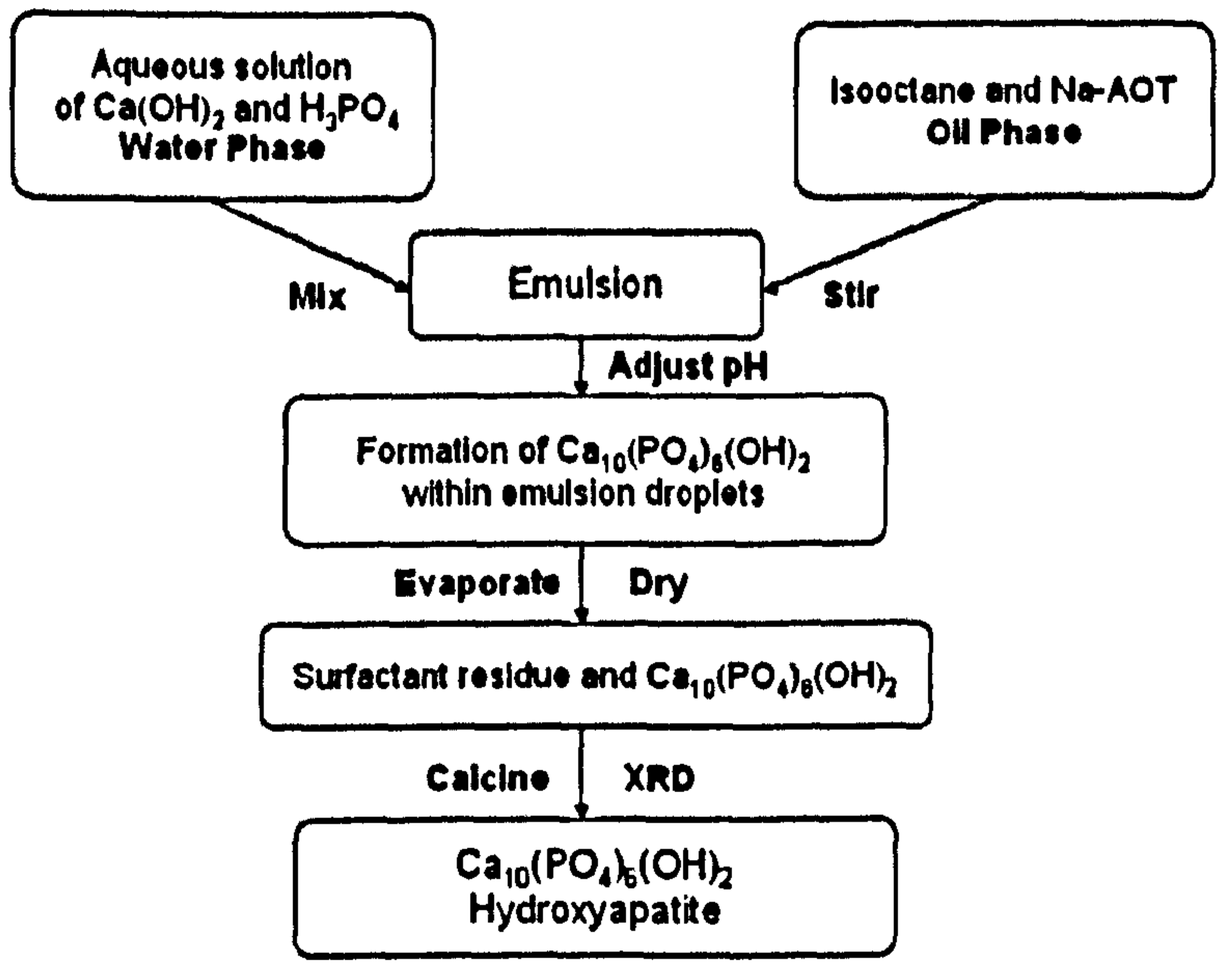

Figure 3.4: Flowchart for emulsion synthesis of HA (S.Bose *et al.*, 2003).

The methodology employed within this study is similar to that depicted in Figure 3.4 based on the previous reasearch described and can be found in Sections 5.1 and 5.2.

3.3.3 Freeze-drying

Heat-dried or oven-dried powders often contain large agglomerates that give rise to weak sintered HA ceramic products with inhomogeneous pores resulting in an inefficient performance during application. Freeze-drying of powders has been previously shown to be a promising technique for preparing uniform fine-grained powders which can be sintered to very high densities. Earlier methods have been established that have successfully produced homogeneous, fine-grained and highly reactive Al_2O_3 and Fe_2O_3 powders (H.Lu *et al.*, 1998).

Since this realisation other methods have been developed for the synthesis of hydroxyapatite powder that employ freeze-drying of the powdered product as opposed to oven-drying (H.Lu *et al.*, 1998; P.Shuk *et al.*, 2001). The freeze-dried HA powders

maintained high thermal stability and suggested that the drying method had significant influence over the properties over the HA ceramic products as well as the powder by the improved and superior mechanical properties over the conventionally heat-dried HA ceramic products (T.Hattori *et al.*, 1987). The sintered freeze-dried ceramics had much higher density, flexural strength and hardness (Vickers) than the corresponding sintered oven-dried products (H.Lu *et al.*, 1998; T.Hattori *et al.*, 1988).

3.3.4 Powder Morphology

The morphology of HA crystallites synthesised by microemulsion processing has been reported by several research groups and has been of interest for HA plasma spraying applications which require the HA fed powder to have not only a narrow particle size distribution but also preferably a spherical morphology. Whilst a narrow particle size range ensures that a constant physical state is maintained by all of the species within the plasma spray, the flowability of the powder feedstock from the powder hopper to the plasma spray gun preceding spraying, is enhanced by spherical morphology (T.Hirai *et al.*, 2000). Reconstruction of bone and dental defects such as periodontal pockets and surgical bone defects is attempted with the packing of ceramic porous and dense HA granules into the area to achieve enhanced repair and growth of the defected part. For such applications the size and shape of the ceramic particles is important in addition to a narrow distribution. Particles with a smaller diameter are fully resorbed and cannot act as a substrate for the uptake of mesenchymal cells. Previous fabrication of smaller particles has involved ball milling before fractioning the product according to size. Despite the simple methodology, the particles posed acute problems because of the irregular shape. Particles of irregular shape packed poorly in columns and created large voids that made the treatment inefficient. The sharp edges of the particles fractured easily which could clog the implanted system. The use of spherical particles avoids such problems further to the benefit that more spherical shaped powders pack with greater efficiency than angular shaped powders and can therefore improve further consolidation and processing (E.C.Abdullah *et al.*, 1999; M.Sunny *et al.*, 2002).

Identification of these optimal powder characteristics led to the preparation of fine calcium phosphate particles by an emulsion liquid membrane system (ELM, water-in-

oil-in-water (W/O/W) emulsion) utilising the internal water phase consisting of micron-sized water droplets which provide a restricted reaction area capable of controlling size and morphology of produced particles (T.Hirai *et al.*, 2000). Spherical microspheres of HA have also been produced by a water-in-oil emulsion to produce small, uniform and spherical particles and a cross-linking technique with chitosan (employed as a combustable binder) to produce HA microspheres (M.Sunny *et al.*, 2002).

Rod-like HA particles of nanometer size have also been obtained by microemulsion-mediated routes that demonstrated a significant modification in size and shape during calcination (at 600 °C) resulting in agglomerated irregular-rod-shaped particles that were large in size although still within the nanometer range (L.Qi *et al.*, 1997). It has also been demonstrated that the reaction temperature employed during microemulsion synthesis of HA nanoparticles has a strong influence on the size and shape of the produced crystals. A reaction temperature of 25 °C has been found to produce spherical to irregular-rod shaped particles of sizes between 30-60 nm. However at a reaction temperature of 50 °C the resultant HA particles have been truncated rod shape with distinct bevelled corners at the apex and generally of a larger size (T.Furuzono *et al.*, 2001).

Whilst the mechanism controlling these differences has yet to be explained in detail, it is likely that HA crystal growth proceeds significantly faster at the higher reaction temperature due to the faster reaction rate and the available nucleation sites, resulting in larger crystals at the end of the processing time (G.Chen *et al.*, 2001). Compositional changes such as surfactant concentration and the molar ratio of water to surfactant have also been shown to influence the size and shape of particle products (K.Wei *et al.*, 2005).

3.4 Calcination and Sintering

3.4.1 Calcination

Calcination is a heat treatment process used to modify the raw powder to improve processing properties (H.Juang *et al.*, 1996). It constitutes a necessary step of HA powder preparation when wet chemical methods are used for production and facilitates particle growth corresponding with surface area reduction of the powder. The temperature and the atmosphere of the treatment are the most important parameters responsible for the surface area reduction of ceramic powders. Water vapour within the atmosphere is known to affect the behaviour of numerous oxides and hydroxides causing partial dehydration and/or decomposition (D.Bernache-Assollant *et al.*, 2003).

Various studies into the mechanisms and elementary processes responsible for the reduction of surface area during HA powder calcination have agreed with a model established for several other ceramic oxides. Below 850 °C, superficial diffusion and gaseous phase transport is predominant leading to a reduction of surface area without densification of the material. The adsorption-desorption of water vapour on the surface of the HA powder controls this diffusion. At a temperature of 850 °C, densification of the material begins and although surface area reduction could result from gaseous phase transport it can also be resultant from mechanisms that are effective in the densification of the material such as, volume diffusion and grain boundary diffusion (D.Bernache-Assollant *et al.*, 2003).

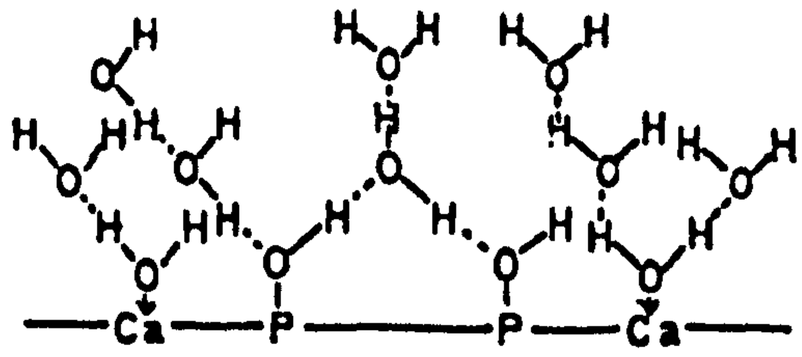

Figure 3.5: Adsorption of water to HA.

Calcination under the correct conditions changes the particle size distribution of HA powder from multi-modal to uni-modal due to coalescence of finer particles during the thermal treatment without any phase transformation. Research demonstrates that treatment below 700 °C does not affect the sintering behaviour significantly. In contrast, calcination above 800 °C delays the initiation of sintering and the subsequent shrinkage proceeds in a wider temperature range that may result in a decrease of grain growth during sintering. Finer powder in uncalcined HA bioceramic powder provides greater surface area as the driving force of sintering but complications including van der Waal forces become more significant and retard the packing of the HA powder. Generally calcination increases the efficiency of powder packing compromising the driving force of sintering.

The process of calcination not only improves the properties of sintered HA powder/material but has proved beneficial for forming processes like injection moulding and slip casting in addition to various kinds of practical applications because of better packing and fluidity capability. It has been previously established that HA powder calcined at 900 °C and then sintered at 1150 °C provides a finer grain size in the resultant material with good mechanical properties (about 55 MPa) (H.Juang *et al.*, 1996).

3.4.2 Sintering

Sintering is a complex process due to the change of many different parameters such as surface area, chemical content, vacancy concentration, grain size, pore size and connectivity (D.Tadic *et al.*, 2004; P.Habibovic *et al.*, 2005). It is well known that the mechanical properties of a polycrystalline ceramic are highly dependent on grain size and porosity with optimal mechanical strength attained at zero porosity and minimal grain size (A.J.Ruys *et al.*, 1995). Carbonated HA similar to the biological mineral content found in bone has been found to sinter to full density in a wet CO_2 atmosphere. This is useful as few HA powders are completely free of carbonate due to the presence of carbon dioxide in the reaction solutions when precautions are not undertaken to remove it. It has also been established that full density may be achieved over a very

narrow range of sintering times demonstrating the importance of sintering time as a parameter to control (J.Barralet *et al.*, 2000).

Solid-state sintering of powder compacts is usually the process used for manufacture of dense HA bioceramics and alumina. Atoms diffuse to contacting areas between particles under the driving force of the surface energy gradients. Material transport can take place by grain boundary diffusion, diffusion, volume diffusion, creep or a combination of these methods depending on the temperature or material involved. Sintering temperatures are usually in excess of one-half of the melting point of the material as long-range migration of atoms is required (B.D.Ratner *et al.*, 1996a).

At sintering temperatures above 1200 °C, HA bioceramic tends to become unstable and eliminates OH groups before forming decomposition products such as α–TCP and β–TCP. Decomposition to β–TCP is accompanied with a considerable molecular volume increase that is detrimental to mechanical properties (A.Tampieri *et al.*, 1997).

During sintering the movement of atoms serve to fill up pores and open channels between the grains of the powder. A small increase in density is observed before the onset of densification corresponding to the first stage of sintering, where necks form between powder particles shown in Figure 3.6. The second stage of sintering corresponds to densification and the removal of most of the sample porosity. The crystals become tightly bonded together as the pores and open channels are closed, improving greatly the density, strength and fatigue resistance of the material structure (N.Y.Mostafa, 2005). The sintered microstructure consists of crystals bonded together by ionic-covalent bonds with little (if any) remaining porosity. It is an essential treatment required to obtain bioceramics with high purity and uniform fine-grained microstructure (B.D.Ratner *et al.*, 1996a).

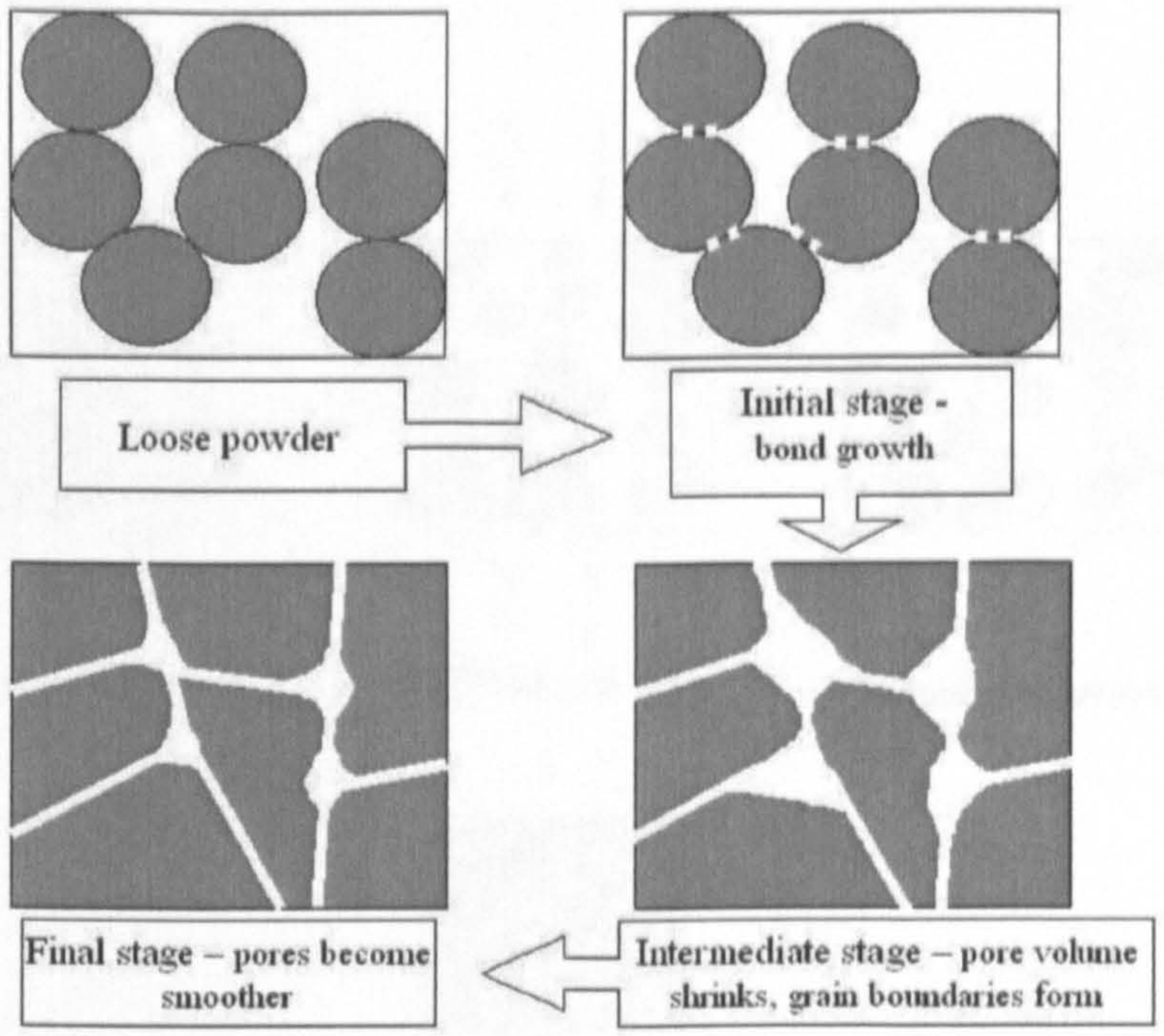

Figure 3.6: Schematic diagram of particle fusion and pore size reduction during stages of sintering.

The start of densification of HA depends on the chemical composition of the precursor powder governed by the Ca/P ratio. However the final sintered density is governed by the homogeneity and particle size distribution of the precursor powder. Powders of fine or nanocrystalline particle size and improved packing homogeneity have much higher surface area, which is the driving force for solid state sintering (Figure 3.6). The amount of surface free energy decrease is proportional to the free energy decrease for the sintering reaction (N.Y.Mostafa, 2005; Y.Sung *et al.*, 2004).

Hot isostatic pressing (HIPing) can be applied to pre-sintered powder to eliminate voids and closed porosity to further improve structural homogeneity and material properties. Densification is achieved by temperature and pressure improving the tensile and fatigue strengths as well as overall mechanical properties plus polishability (useful for when low friction and wear resistant surfaces are required). Elevated temperatures are used during the process and a very high vacuum to remove air and moisture from the material prior to application of high inert gas pressures (21 MPa) and further heat (1200 ˚C) to achieve a uniform fine grain size and near 100 % density.

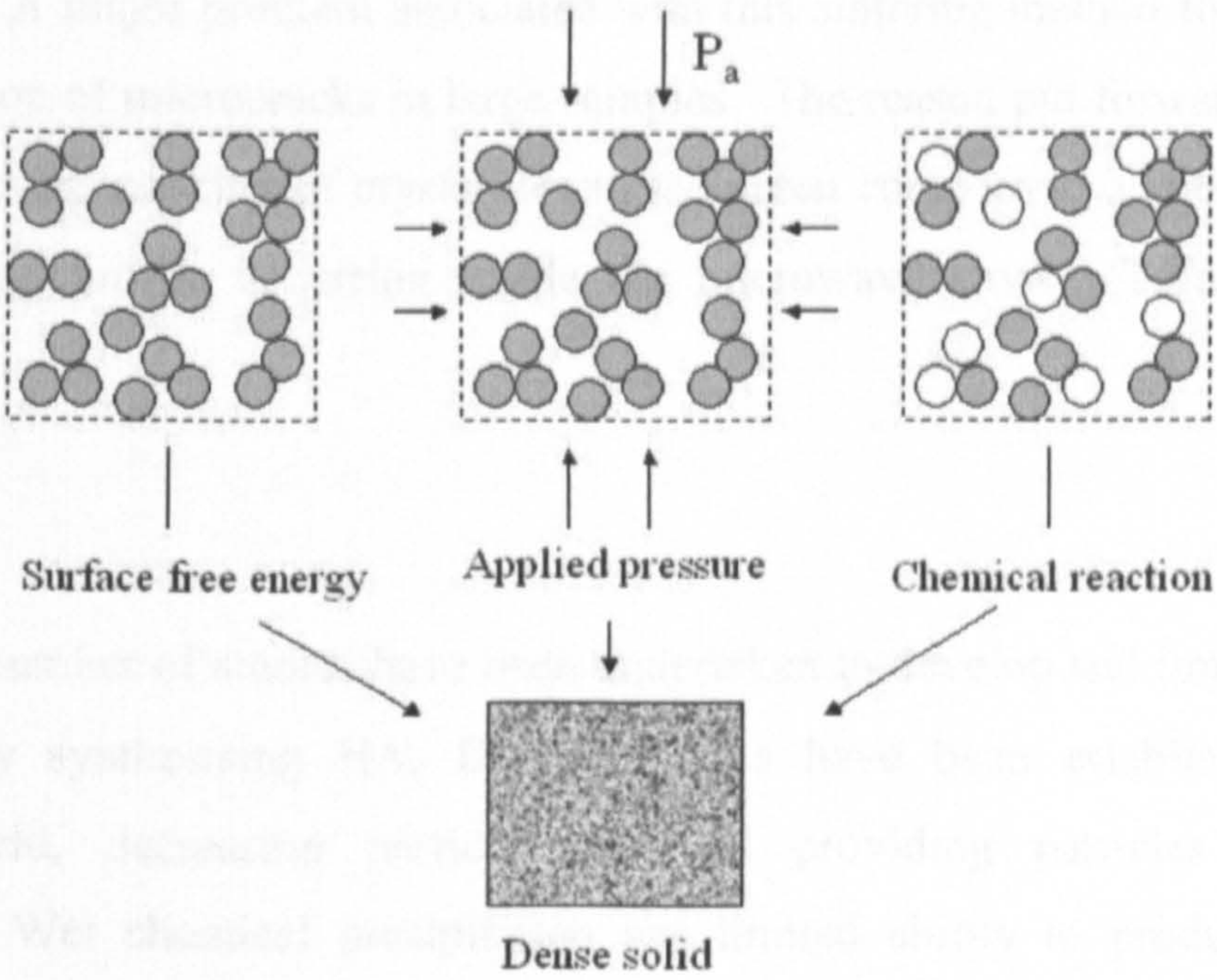

Figure 3.7: Schematic diagram illustrating three main driving forces for sintering: surface free energy, applied pressure and chemical reaction (M.N.Rahaman, 2003).

Microwave heating has been studied for the past two decades for providing an alternative faster route for the sintering of various ceramic systems (S.Vijayan *et al.*, 2002). Research demonstrates that microwave couples effectively with certain materials generating heat within the object depending largely on dielectric constant and dielectric loss factor properties. Reported advantages over conventional solid-state sintering include a shorter time of processing in addition to better physical and mechanical properties to the final sintered ceramic (T.Furuzono *et al.*, 2001). Microwave synthesis of materials such as carbonated HA has been advantageously described to heat throughout the volume with a very efficient transformation of energy requiring shorter reaction times than conventionally needed to produce samples having comparable X-ray powder patterns (T.S Sampath Kumar *et al.*, 2000).

The nature of powders has a significant influence on the microwave-assisted sintering of HA powders. A major problem associated with this sintering method for densification is the production of microcracks in large samples. The reason put forward corresponds to the non-uniform packing of crystallites in the green compact in addition to the non-uniform heating profile occurring inside the microwave cavity (T.Furuzono *et al.*, 2001).

Summary

A significant number of studies have been undertaken to develop and improve methods for chemically synthesising HA. Different aims have been established including increasing yield, decreasing particle size and providing particles of spherical morphology. Wet chemical precipitation has limited ability to produce fine, free-flowing HA powder and research into alternative methods has led to the use of emulsion synthesis. Micro/macroemulsion systems can be inverse/reverse systems if based on "water in oil" formulations as opposed to "oil in water" formulations. A very small product particle size is achieved due to the restriction on reaction space within the droplets/micelles present where the chemistry takes place. Freeze drying the HA product permits significant benefits in comparison to oven drying before further thermal post-processing treatments such as calcination and sintering enhance the chemical and mechanical stability of the HA product.

Chapter 4 HA Surface Microstructuring

Overview

Within this section, the role of the biomaterial surface is discussed with significance to the physical and chemical properties and how they affect interfacial cellular reactions. The initial part considers chemical properties and surface functional groups with respect to previously established findings and the view to improve the bioactivity of HA. The subject area of surface topography is introduced with reported cellular reactions to type of topographical feature before methods of fabrication are discussed. The latter section with significance to this particular study describes the use of laser technology to fabricate surface microstructure and documents previous methodology which could be of great benefit if possible, to the creation of surface microstructures on bioceramic HA.

4.1 Background

The significant role of surface micro- and nanostructure in biological phenomena such as protein adsorption and bone cell adhesion to implanted bioceramics has only recently been put forward and highlights that the capability to process materials with tailored structure at the micro- and nanoscale level may provide the possibility to elicit specific responses from cells in addition to optimising the *in vivo* response and subsequent success of the material. General alterations to the surface can be made by adsorption of ions or molecules, dissolution/ reprecipitation, encapsulation or surface reactions (L.Borum-Nicholas *et al.*, 2003). Nanostructure processing allows for the design of structural and surface features that are inspired by the architecture of bone improving biological acceptability and affinity of the bioceramic with other materials (M.P.Ginebra *et al.*, 2004). In addition to which, nanoparticles and nanostructured surfaces have a larger surface area for adhesion that increases the interactions between the particles or substrate surface and the surrounding environment (G.Chen *et al.*, 2001).

4.2 Surface Interactions and Chemistry

The interactions between the material surface and the surrounding tissue or biomaterial have proved to be important factors in governing the application of the implant as well

as the clinical success. It has recently been understood that the interactions relate to surface structure and properties of the HA including surface functional groups, surface charge, acidity and basicity, hydrophobicity and porosity (H.Tanaka *et al.*, 1997b; J.Vandiver *et al.*, 2005). However, investigations into the surface of HA bioceramic are far fewer than those on the preparation, chemical and crystal structure characterisation of the material (Z.Cheng *et al.*, 1998). It has been established however, that biological molecules interact with the crystallite surface of implanted HA by exposing a certain section of their structure against the material surface to arrange their conformations most suitable for the adsorption (G.Yin *et al.*, 2002; P.Ducheyne *et al.*, 1999).

There are three kinds of P-OH groups on the surface in bioceramic HA which are hydrophilic and act as adsorption sites for various molecules such as H_2O, CH_3OH, CH_3I and CO_2 (G.M.S.El Shafei *et al.*, 2001; T.Ishikawa *et al.*, 1989). In addition n-butylamine, pyridine, acetic acid are adsorbed onto HA by hydrogen bonding to several of the surface P-OH groups. On nonstoichiometric HA these surface groups occur in numbers of 2.6 groups nm^{-2} (H.Tanaka *et al.*, 2004). Protein amino acids similarly attach to the surface P-OH groups on bioceramic HA. The configuration and structure of functional groups such as these participates in determining the mode of adsorption that takes place to the substrate surface (B.D.Boyan *et al.*, 1996; G.Shafei *et al.*, 2001). Because the number of the P-OH groups determines many of the surface properties, regulation of the number of these surface groups will result in surface modifications of the bioceramic (H.Tanaka *et al.*, 1997a; T.Ishikawa *et al.*, 2000). These can change a number of the material properties including acidity and basicity, affinity and reactivity to molecules and catalytic activity. It has been suggested that increasing the number of the surface P-OH groups serves to increase the electrophoretic mobility of HA and that the control of this property may improve the adsorption property of proteins (H.Tanaka *et al.*, 2004). The significance of protein adsorption corresponds to the monolayer of protein that is observed on biomaterial surfaces within seconds of implantation. Serum and extracellular matrix proteins adsorb quickly after contact with an inorganic material surface (I.Degasne *et al.*, 1999). Cells respond specifically to proteins and so the interfacial film could influence subsequent reactions to the implanted bioceramic HA (K.Anselme, 2000; P.J.ter Brugge *et al.*, 2002). When the cells arrive at the implant

surface after protein adsorption they can adhere to the implant via cell surface receptors and their ligands, release active compounds, recruit other cells or grow/proliferate. The protein layer adsorbed onto the implant surface governs the type of cellular response and subsequent biological events (A.Pierres *et al.*, 2002; B.D.Ratner *et al.*, 1996c). In other words, the cell-surface interactions mediated by proteins occuring at the interface between biomaterial substrates and tissue influence cell function, development and subsequent tissue morphogenesis determining largely the long term effectiveness and function of the material (B.Kasemo, 2002) (A.Andersson *et al.*, 2003a). The fate of the implanted material is significantly mediated by regulating inflammatory reactions and strength of connection to surrounding tissues (A.Pierres *et al.*, 2002).

The hydrophobicity, electric potential and other surface properties of the adsorbed proteins influence sequential interfacial events including bacterial adhesion. The surface free energy is known to affect protein adsorption to calcium phosphate materials such as HA including the specific serum glycoproteins that affect bone cell attachment and spreading on the biomaterial (J.D.de Bruijn *et al.*, 1992; M.Ball *et al.*, 2001). Fibronectin and vitronectin are major extracellular matrix proteins found in abundance in blood plasma and known to be involved in cell adhesion (A.Rosa *et al.*, 2003). They contain the specific RGD sequence (arginine-glycine-aspartic acid-serine), an adhesive peptide that is recognised by specific cell membrane receptors such as integrins (P.A.Ramires *et al.*, 2001). Integrins are transmembrane (α-β) heterodimers, the intracellular part of which is linked to the actin microfilament network through talin and/or vinculin, tensin and α-actinin cytoskeletal proteins. Fibronectin and vitronectin are ligands for several integrins (I.Degasne *et al.*, 1999). Cell binding to extracellular proteins generates an intracellular signal that affects the cytoskeleton status initiating actin microfilament assembly and focal adhesion plates, which consequently influences cell spreading (R.Lange *et al.*, 2002).

A number of researchers have reported that negatively charged surfaces are consistently favourable for the heterogeneous nucleation of HA in supersaturated solutions of 'simulated body fluid' (SBF). The offered explanation corresponds to the accumulation

of Ca^{2+} ions due to the electrostatic interaction resulting in an increase in supersaturation near the negative surface that preferentially triggers the initial nucleation (A.S.Posner *et al.*, 1975; D.N.Misra, 2005; E.Y.Kawachi *et al.*, 1998; P.Zhu *et al.*, 2004). This could be useful knowledge when considering that ideally, implanted HA should be recognised as host tissue and facilitate if not promote resorption, replacement and further nucleation of the natural mineral.

Hydrophobicity is an important surface property playing a dominant role in physical interactions between components in an aqueous environment and influence of adhesion or adsorption of biological components on a pre-adsorbed protein layer (K.Kawasaki *et al.*, 2003). When bioceramic HA is implanted as a bone substitute material, a bone injury is created and filled with the bioactive material known to favour osteointegration. After the protein monolayer is formed, the surface is then colonised by adherent bone cells creating a very close bone-ceramic contact with little if any fibrous interface. Reports have demonstrated that osteoblastic cells have a hydrophobic character allowing them to specifically attach onto hydrophobic surfaces such as the protein matrices found covering HA bone implants. It has therefore been proposed that the relationship between hydrophobicity induced by the presence of the polysaccharide layer on the implant surface could create a selective adsorption of osteoblast cells and macromolecules resultantly enhancing osteointegration and bone healing (P.Zanchetta *et al.*, 2001). Another study however, suggests that the hydrophilicity of the material surface itself is not a major factor in the attachment and growth of cells (B.A.Scheven *et al.*, 2002).

4.3 Surface Topography

Past literature establishes that cellular responses to an implanted material depend upon the physical and chemical characteristics of the substrate, particularly upon its chemical composition, crystallinity, particle size and surface structure (D.R.Villarreal *et al.*, 1998; J.Sun *et al.*, 1997; Y.Shin *et al.*, 1997). Additionally, variations in surface texture, structure or topography may affect the cellular response through strong effects on the cell cytoskeleton and shape. Research has demonstrated that cells may react to the type of topography (D.Deligianni *et al.*, 2001). The creation of surface nano or

micro-features correspond to the functional domains present upon cell membranes being in the order of nanometers although the dimensions of the cell may be around 10-20 μm (R.Barbucci *et al.*, 2003).

An advantage of micro- or nanosized materials is the possibility of producing novel compositions or designs on the surface of materials. Several of the characteristics such as the biological activity and control of cellular behaviour, i.e. adhesion, proliferation, differentiation, migration etc. depend largely on the dimensions of the different domains that may be of the same order of magnitude as those of the biological moeities they have to interact with under normal physiological conditions. Surface control of cellular behaviour plays an important role in the formation of tissues and organs as well as the realisation of functional biomaterials that can manipulate two fundamental external signals: the cell-substrate and cell-cell interactions allowing adhesion and growth of specific cells that are orientated in the three dimensional space allowing regeneration and specific placement of specific biological tissues (R.Barbucci *et al.*, 2002). With regard to osteoblastic cells it has been established that the substratum surface topography alters cell shape and modulates fibronectin at the transcriptional and post-transcriptional levels in addition to the amount of fibronectin assembly into the extracellular matrix which will promote cell attachment and spreading (I.Degasne *et al.*, 1999; K.Dee *et al.*, 1996).

It is suggested that at the nanoscale level chemistry and topography converge. Mediated by this suggestion an approach to creating topographical features that mimic chemical species has been viewed with previous study establishing a method of nano-scale patterning of solid substrates using proteins as templates. The results identified that proteins will adsorb more readily to a surface if the surface is patterned with the 'imprint' of that protein and should as a result produce a more biologically compatible implant substrate (H.G.Craighead *et al.*, 2001).

Surfaces provide accessibility for reactions and can be created in geometries of high surface area in order to enhance reaction turnover rates. Special affinities and reactions may be enhanced by specific organic microenvironments. Minimising the surface energy at a material interface can be utilised to orient specific structures or molecules to the surface whilst self-assembly in the plane of the interface can be used to provide precise spacing and orientation (D.Castner *et al.*, 2002). Self-assembly utilises large oligomers to create supramolecular constituent units of a highly regular nanostructure that can be amphiphilic (having both hydrophobic and hydrophilic regions) and multilayered for modification of biomaterial surfaces (M.Tirrell *et al.*, 2002).

Biomimetic modification of a material surface aims to promote selective interaction with a specific cell type through biomolecular recognition events. Biomaterial surfaces or three-dimensional matrices are modified with active peptides that mimic part of the extra cellular matrix (ECM) responsible for cell attachment to the material in order to induce tissue formation conforming to the cell type seeded on the material. Extensive research has been undertaken into the attachment and incorporation of adhesion promoting oligopeptides or domains of ECM proteins into base materials used in the biomaterial industry (D.A.Smith *et al.*, 2003; D.Castner *et al.*, 2002; M.Tirrell *et al.*, 2002).

Various types of surface topography (such as pits, cliffs, grooves, ridges, spikes, hills and tunnels with different features such as sloping edges or vertical edges) and their subsequent effect on different cell types have been investigated. Brief examples of research findings include; (i) orientation of fibroblasts along 3 and 10 μm deep grooves but insert obliquely into 22 μm grooves with resultant better osteointegration and induction of mineralised tissue from surface microtexture (Y.Ito, 1999); (ii) macrophages in direct contrast to fibroblasts, accumulate preferentially on roughened and hydrophobic surfaces; (iii) substrate roughness enhances fusion of osteoclast precursors (preceding differentiation) as opposed to chondrocytes which maintain their differentiation when established on roughened surfaces; (iv) epithelial tissue outgrowth is inhibited by pores when the diameter exceeds 0.9 μm and depth exceeds 100 nm but

may bridge or span over pores when the diameter is less than 35 µm (J.H.Fitton *et al.*, 1998); (v) dimensions of features can vary endothelial cell morphology (R.Barbucci *et al.*, 2002). The tendency of osteoblastic cells to attach more rapidly to surfaces with a rougher microtopography has been described to increase the bone apposition which is a desirable result for any bone substituting material (P.A.Ramires *et al.*, 2001).

The dimensions of the topographical features have been shown to influence the degree of cell behaviour with certain cell types being more sensitive than others. Macrophage-like cells can react to dimensions at least as small as 44 nm and epitena, epithelia, fibroblasts and endothelia react to depths as shallow as 70 nm (A.Curtis *et al.*, 1997). Nanostructured surfaces have attracted much attention recently motivated by the existence of many nanoscale structures within natural tissues such as bone (A.Andersson *et al.*, 2003a).

Substrates with parallel repeating step edges can impose directional constraints on cells (orientation and shape) and affect the rate and direction of cell migration by the phenomena of contact guidance. The parameters such as groove/ridge width and groove depth have been systematically varied to determine which of the controls topographically induce contact guidance. Cellular parameters such as cell type and cell density also influence the degree of contact guidance. Cell alignment is often reduced when the repeat spacing of ridges and grooves is increased and when the repeat spacing is much larger than the breadth of the cell, alignment is diminished. Moreover, deeper grooves induce alignment more potently than by shallower ones (A.Andersson *et al.*, 2003b). As discussed, the ability to control and guide cells is beneficial in biomaterial and tissue engineering applications in order to create more advanced products with increased biological compatibility but the exact mechanism behind the cell guidance ability remains unclear, in particular whether it is the topography and/or the chemistry that causes the guidance (A.Andersson *et al.*, 2003b).

No conclusion has been offered as to whether the effect of surface features on cells may result from the surface features themselves or be the result of the reaction that occurs as the media and serum condition the material surface although it is readily understood that the two responses are related. In terms of topographical studies of HA substrates it has been understood that regular and uniform surface morphology of HA are important factors that affect cell proliferation and differentiation. An offered explanation describes how the physicochemical properties of the ceramic surface can affect the reorganisation of proteins on ceramic specimens and subsequently change the profile of adsorbed proteins. The type of substrate determines which integrins and extracellular matrix proteins are expressed by osteoblasts providing information about how implant materials may effect osteoblast differentiation. The previously mentioned fibronectin plays an important role in osteoblast differentiation (A.Rosa *et al.*, 2003). Chemically there are conflicting findings in the compositional influence of HA on cell behaviour with reports suggesting that calcium ions are advantageous to cell growth,(H.Cheung *et al.*, 1985) but high phosphate concentration within ceramics has been inhibitory to cell activity (C.Knabe *et al.*, 1997; M.Ball *et al.*, 2001).

4.4 Fabrication of Topography

Precise fabrication of topography has been performed in a variety of ways including polymer demixing, injection molding, micro-printing, photoimmobilisation, photo- and electron beam lithography plus wet chemical etching. Laser ablation can be used to remove materials either on a point-to-point basis with a moving beam, or through a mask. All serial methods of manufacture creating surface topography point-by-point are intrinsically slower than those in which the whole pattern is transferred at the time, such as in photolithography or casting (A.Curtis *et al.*, 1997). Most recently, photo- and electron beam lithography with/without wet chemical etching were the general processes used to create micro and nanostructured surfaces, utilising the same technology used in production of integrated circuit boards where a silicon wafer is processed with a precise pattern of metal lines, holes and dopant atoms created on or in it (A.Curtis *et al.*, 1997; R.Barbucci *et al.*, 2003). A wide range of biocompatible materials can be patterned in this manner with the most popular choice being silicon or fused silica. The process begins with a pattern being defined in a radiation-sensitive material known as a resist (typically a polymeric thin film) which is then transferred

into or onto the substrate material. The type of radiation used to expose the resist is defined by the resolution required in the final structure. For lateral details of 1 μm or more, the radiation is provided by UV light, while if the features required are of 100 nm or less then electron beam lithography (using a scanning and focused electron beam) is used to expose the resist. The resist is then developed to leave a relief pattern that is then transferred to the substrate by etching. The resist precludes etching in the areas that are covered in resist (Figure 4.1) (R.G.Flemming *et al.*, 1999). It can also be used as a stencil during the addition of material to the substrate (A.Curtis *et al.*, 1997; M.Tirrell *et al.*, 2002).

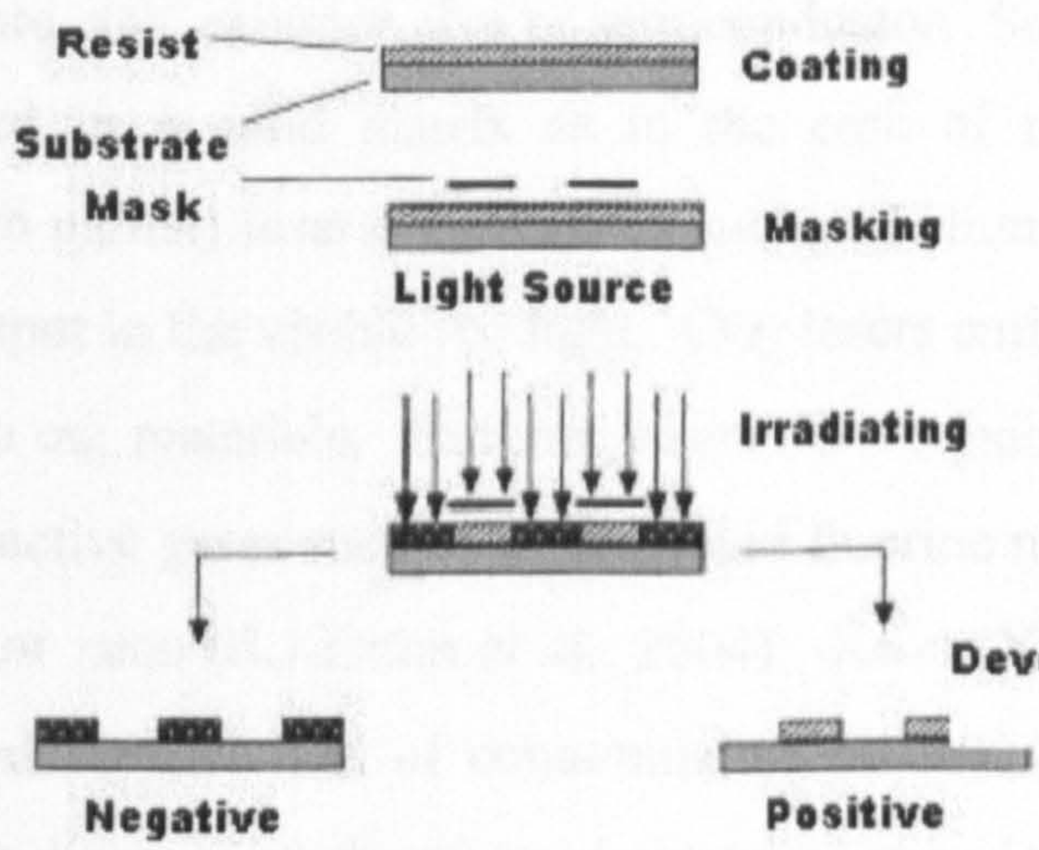

Figure 4.1: Schematic diagram of the photolithographic process (R.G.Flemming *et al.*, 1999).

There are several variations of this process but with the same principles. Resists can be negative or positive depending on whether the exposure to radiation hardens or softens the resist's reaction to the developer. Etching can be performed with hydrofluoric acid that used independently can provide sloping walls in grooves, but with the assistance of reactive ions (F^-) directed vertically by an electric field onto a horizontal substrate under the correct conditions, vertically sided structures can be achieved (A.Curtis *et al.*, 1997). The resists or photomasks can often contain defects which may make the mask unusable depending on size and position. This is a disadvantage due to the expense of manufacturing the resists that are designed to be used repeatedly (N.H.Rizvi, 2003). Polymer demixing is a fairly new method employed to produce nanostructured surfaces and employs different blends of polymers that undergo phase separation during spin

casting onto a glass substrate. Topography is produced by the different shrinkage or surface tension relationships while cooling from the melt. Controlling the concentration and proportions of the polymers defines the type of topography that can be produced including, pits, islands/hills and ribbons of varying height or depth (R.Barbucci *et al.*, 2003).

4.5 Laser Technology

There are many types of lasers (acronym for light amplification by stimulated emission of radiation) that are used in medical (J.L.Arias *et al.*, 2003a), industrial (W.Marine *et al.*, 2000) and commercial fields. They are often described by the lasing medium used such as in solid state, gas, excimer, dye or semiconductor. Solid state lasers have lasing material distributed in a solid matrix as in the case of ruby or neodymium-YAG (yttrium aluminium garnet) lasers. Gas lasers such as helium and helium-neon (HeNe) have a primary output in the visible red light. CO_2 lasers emit energy in the far-infrared and can be used to cut materials. Excimer lasers derive their name from 'excited' and 'dimer' and use reactive gases such as chlorine and fluorine mixed with inert gases such as argon, krypton or xeon (R.J.Exton *et al.*, 2004). Xeon (Xe) is often chosen because of its ease of handling and lack of contamination risk (K.W.Kolasinski, 2006b). A pseudomolecule or dimer is produced upon electrical stimulation that emits light in the ultraviolet range when lased. However although applicable to materials that are often considered difficult to machine such as dielectric materials (e.g. diamond and sapphire), excimer laser processing is associated with expense due to the massive size of the excimer system and poor stability (E.W.Kreutz *et al.*, 2003). Semiconductor lasers, otherwise known as diode lasers are not solid state lasers but very small electrical devices that use low power (P.K.Mudhopadhyay *et al.*, 2005).

4.5.1 Laser Ablation and Deposition

Material surfaces can be modified using a variety of different laser technologies. Different emission durations (pulsed or continuous), wavelengths, power and atmospheric conditions have been used to develop a variety of ways in which lasers can be employed to cut, ablate, remove and deposit material on object surfaces for a number of purposes (N.H.Rizvi, 2003).

Ultrafast lasers can be used to remove thin films, minute particles or contaminants from the surface of materials and has particular applications in the manufacturing side of the semiconductor industry. Within recent years the use of nanosecond lasers to remove silicon dioxide thin films from the surface of silicon has been established. A stronger removal force is provided by ultrashort pulses (pico- and femto-second) creating a faster acceleration of the surface whilst the use of femtosecond pulses allows precise coating removal from a microscopic area (J.Magyar *et al.*, 2003). In addition, by using ultrashort laser pulses, any material can be machined to very high precision including high band gap dielectrics such as SiC (silicon carbide) and diamond as a consequence of the interaction of the ultrashort pulses occurring by largely different mechanisms to those associated with conventional longer pulse lasers. The interaction demonstrates independence from the usual linear absorption properties of the material thus being applicable to materials that are typically transparent to the laser radiation due to the optical properties at the wavelength. The removal of material faster than heat can be conducted to the bulk material facilitates machining to micron scale precision with minimal collateral damage to the remaining material (E.W.Kreutz *et al.*, 2003).

Ultrashort laser pulses are also applied to the field of pulsed laser deposition, where an ultrashort pulse is used to ablate the surface of a material, interacting with a highly localised volume of material. The area of ablation is confined to a focal region of the laser beam interacting with the surface of ablated material. A very high repetition rate of several MHz can provide sufficient energy (at least several hundred nanojoules) to achieve highly efficient ablation producing a continuous stream of material to a target substrate that requires a deposited thin film or coating of close to epitaxial quality (J.M.Fernandez-Pradas *et al.*, 1999; J.M.Fernandez-Pradas *et al.*, 2002). Pulsed laser ablation typically involves an excimer laser and has been applied to various types of HA bioceramic material creating a plume of mixed evaporated and particulate material. The plume material condenses quickly onto the substrate material such as a metal implant for dental or orthopaedic application where the benefit of the HA film or coating can enhance the biocompatibility of the implant combining the excellent mechanical properties of metals with the outstanding bioactivity of HA. The coating can also be

used as an intermediate layer to provide better mechanical compatibility with bone than the pure metal implants due to the closer similarity in mechanical properties of bioceramic HA to natural bone than metallic materials and bone. At the same time as the ablated plume HA material condenses onto the substrate forming a thin film, the attachment of macroparticles onto the film surface takes place (Figure 4.2) (H.Zeng *et al.*, 2000b). The size and distribution of these macroparticles can be controlled by altering the laser fluence allowing the production of apatite ceramic coatings that are firmly attached with a specific crystallinity, morphology and composition (M.Ball *et al.*, 2001).

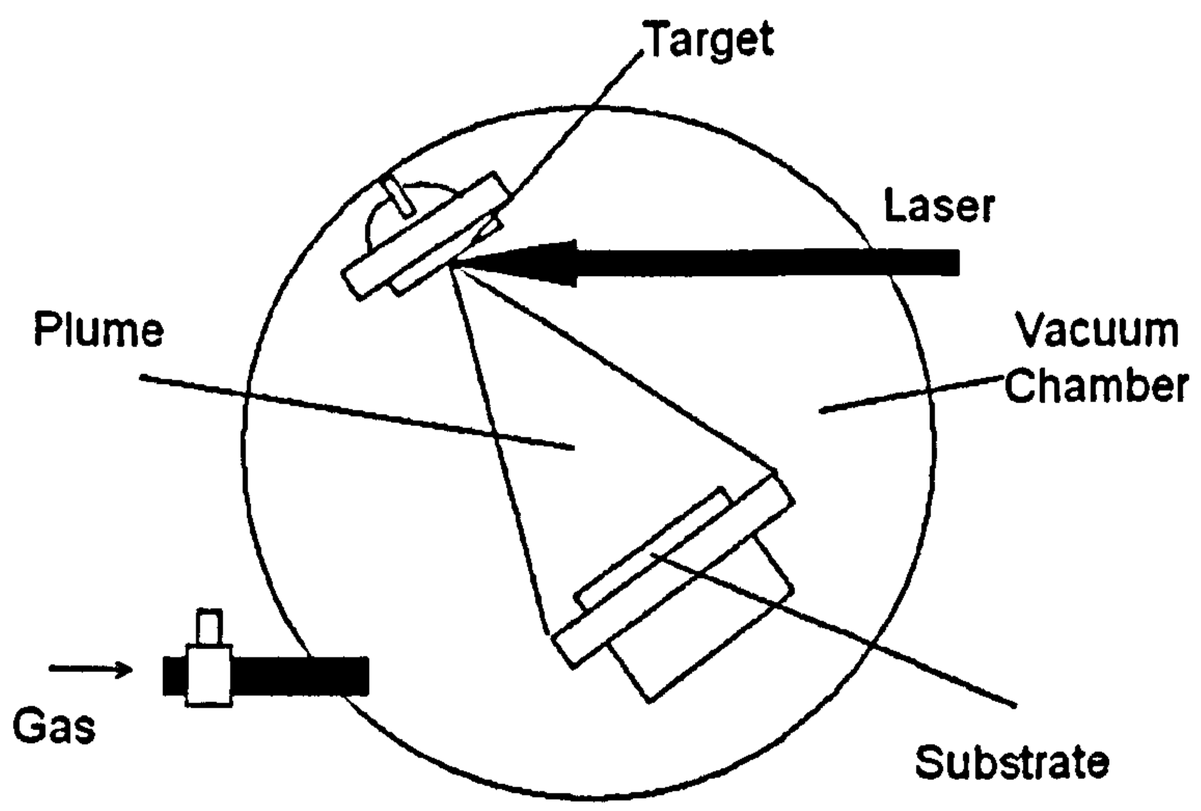

Figure 4.2: Schematic diagram of pulsed laser deposition (H.Zeng *et al.*, 2000b).

Since the mid-1980s the pulsed-laser ablation and deposition technique has been widely used for materials science and processing. Much research has been placed into the two unique characteristics of the transfer of the stoichiometry of a multicomponent system onto a substrate and also the possibility of combining gas-phase chemistry with surface physics (J.C.Conde *et al.*, 2004).

The pulsed laser ablation and deposition methods offer a number of advantages such as:

(1) growth of materials with high melting point and the use of all materials (metals, semiconductors and insulators),

(2) stoichiometry transfer of the target composition with the absence of contamination and

(3) gas phase chemistry can be induced when the target material is ablated in the presence of a low pressure (ambient) of reactive gas leading to the formation of a new compound by the reaction between the reactive atmosphere and the energetic species in the plasma plume. This allows possibilities of film oxygenation amongst other chemical changes (S.Liste *et al.*, 2004).

In spite of these advantages there are drawbacks preventing it emerging as a technology for high-quality thin film deposition and surface modification. The presence of droplets on the film surface and in-homogeneities in the grown film due to the anisotropic expansion of the plasma plume are present restrictions (J.C.Conde *et al.*, 2004).

Since the first reported preparations regarding HA bioceramic coatings in 1992 using an excimer KrF laser at a wavelength of 248 nm followed by synthesis with an ArF laser at a shorter wavelength of 193 nm, many different scientists have explored the main technological conditions required to obtain high crystallinity, high density, low solubility and low permeability properties in the deposited coatings (J.M.Fernandez-Pradas *et al.*, 1998). Success has been achieved in providing deposits with very similar mean composition to the target material after establishment that all of the elements present in the target HA were found in the gaseous phase and should result therefore in transferring the biological properties of the target to the deposits (N.H.Rizvi, 2003). Target property and deposition parameters such as temperature, laser wavelength, gas pressure and composition in atmosphere have been investigated to provide a variety of bulk material and surface properties (H.Zeng *et al.*, 2000b).

The use and importance of controlled gas compositions has been well established with ambient gas providing complex composition, preserving stoichiometry and improving crystal structure by decreasing revaporisation from the film surface. This serves to

preserve the volatile species on a heated substrate in addition to improving the plume quality by moderating the energy of the ablated species (H.Zeng *et al.*, 2000b). Various atmospheres of O_2, H_2O, Ar and Ar+H_2O have been studied and used to establish that the optimum pressure is determined by both the pressure necessary for obtaining the correct composition and the pressure that leads to a well-defined plume and uniform coating thickness. Water vapour or H_2O in the atmosphere is optimal when HA material is involved and utilising a pressure of 50 Pa may enable high purity, highly crystalline HA coatings with the highest degree of hydroxylation to be obtained when using a KrF or ArF laser beam at either wavelength of 193 and 248 nm (H.Zeng *et al.*, 2000b; J.M.Fernandez-Pradas *et al.*, 1998). Other work has observed that in an H_2O processing atmosphere the non-stoichiometric HA target surface becomes a combination of a more stoichiometric HA and calcium oxide upon resolidification after exposure to the same type of laser (J.L.Arias *et al.*, 2003a). When H_2O conditions are ambient, gas phase reactions and film surface reactions are permitted and the formation of different phases from the original HA is likely facilitating tetracalcium phosphate (TTCP) presence within the coating. The rate of ablation is affected as a result (J.M.Fernandez-Pradas *et al.*, 1998) (J.L.Arias *et al.*, 2003a). An Ar/H_2O mixture within the atmosphere can serve to decrease the variation of Ca/P ratio within an HA coating (H.Zeng *et al.*, 2000b).

The ablation rate of HA in different atmospheres depends largely on the backscattering of the ablated particles by molecules of the gas redepositing material onto the surface. Study demonstrates that the ablation rate decreases as the atmospheric pressure increases. This corresponds to the surface unity force created by the impinging gas molecules against the target particles being increased allowing a smaller amount of the target particles to leave the material surface (J.L.Arias *et al.*, 2003a).

The substrate temperature must be sufficient that diffusion and reactions at the surface are permitted but not so high that the coating-substrate interface deteriorates (titanium substrates may undergo titanium oxidation thus breaking down the interface) and losing all mechanical strength. Past literature denotes that a laser wavelength of too large a

magnitude (355 nm) will not permit efficient ablation, depositing larger particulates onto the substrate surface at the expense of the mechanical properties. The smaller wavelength of 193 nm ensures that the ablated material is only constituted by atoms, ions and small molecules (J.L.Arias *et al.*, 2003a; J.M.Fernandez-Pradas *et al.*, 1999). Regarding the pulse repetition rate when ablating HA, the time interval between pulses must be sufficient such that there is enough time for the material to diffuse within the surface and accommodate in the structure before the material from the next pulse arrives. It has been found that as the pulse repetition rate is increased from 20-80 Hz there is a decrease in the structural order of the HA coatings and at 100 Hz the coatings become amorphous and there is a subsequent increase in the rate of deposition (J.L.Arias *et al.*, 2002). Generally the coatings have a columnar structure as a result of growth in size of grain-like particulates. Amorphous coatings demonstrate a surface with small droplets embedded in a continuous matrix (J.M.Fernandez-Pradas *et al.*, 2001; L.D'Alessio *et al.*, 1999).

A recent development to the pulsed laser deposition (PLD) method of HA coating uses a second ultraviolet KrF excimer laser as an 'assist laser' to anneal the substrate. Irradiation with the assist beam improves the adhesion of the coating and helps to control crystallinity (M.Katto *et al.*, 2002; M.Katto *et al.*, 2003).

In addition to various types of surface modification, coating and material removal, laser ablation is also used to remove carious (decayed) dental hard tissue. Although research was initiated over 30 years ago, the relevant authorities only approved the use of infrared laser ablation of dental enamel in 1998 (D.Fried *et al.*, 1998; M.Gonzalez *et al.*, 1999). The use of CO_2 lasers to irradiate and ablate dentine has been reported to induce structural changes converting the dentine into a structure with crystallinity similar to that of enamel (M.Gonzalez *et al.*, 1999). Femtosecond pulsed lasers generate very low mechanical and thermal stress to dental tissues unlike mechanical drills or previous Er:YAG-lasers that generated microcracks in the enamel providing starting points for new carious attacks (H.Lubatschowski *et al.*, 2003).

Conventional PLA is also used to synthesise nanostructures and nanoclusters of silicon. Clusters can be defined as aggregates of atoms with a typical size from some tens up to a few thousand atoms. The small dimensions of these particles determine their properties strongly characterised by quantum effects. Larger clusters of 10-20 nm share properties similar to those of bulk materials. Nanometer sized semiconductor particles have superior properties in modern day technology since quantum confinement in such structures modifies the bulk Si band structure resulting in radiative transitions (W.Marine *et al.*, 2000).

Nanocluster synthesis may result from ablation performed at relatively low gas pressures of inert or reactive gas with respective size controlled by laser parameters such as fluence, wavelength, pulse duration and the ambient gas conditions. Within the laser plume and ablated vapour amidst the process of expansion and cooling, condensation of particles precedes multiple collisions with the ambient gas molecules and stabilise the newly formed nanoclusters prior to arrival at the substrate surface (W.Marine *et al.*, 2000).

4.6 Laser Modification and Microstructuring

Recent developments in the field of surface microstructuring have resulted in the ability to form a variety of structures on the surface of a substrate material such as silicon by exposure of the surface to the multiple pulse irradiation of a high intensity laser (K.W.Kolasinski, 2004). The structures have a typical period comparable with the wavelength of light and a profile dependant on the polarisation, incident energy density and the number of pulses. Structures such as ridges, resonant or large-scale periodic structure (A.B.Brailovsky *et al.*, 1995), cones (A.J.Pedraza *et al.*, 1999; T.Her *et al.*, 1998), or columns (F.Sanchez *et al.*, 1998) have been induced on various target materials by laser radiation in ambient atmospheres with differing laser beam characteristics (E.Gyorgy *et al.*, 2004). Studies regarding surface microstructuring of substrate silicon have employed a number of process gases in addition to alternating between using excimer laser beams (A.J.Pedraza *et al.*, 1999; D.Mills *et al.*, 2004; F.Sanchez *et al.*, 1998; F.Sanchez *et al.*, 1999) and amplified solid-state laser beams (Ti:sapphire) (D.Riedel *et al.*, 2004; T.Her *et al.*, 1998).

As a result of the growing interest in the interaction of laser beams with surfaces under etching conditions, a recent fabrication technique has been used for the formation of pillars above a bulk silicon (Si) substrate/wafer, by laser irradiation of Si in the presence SF_6 gas based on similar previous studies where distributions of conical structures have developed after cumulative radiation (D.Mills *et al.*, 2004; F.Sanchez *et al.*, 1999). Earlier research has established that the ambient gas has an influence on the shape of the conical spikes by the formation of sharp structures in the presence of SF_6 or Cl_2 gas in contrast to rough, disorganised, uneven and scattered structures produced in the presence of N_2, He or vacuum. These observations suggest that the chemical reaction between SF_6 or Cl_2 and silicon contributes to the formation of sharp spikes and that the role of the gas is not purely physical providing influence through heat development or pressure on the developing structure (T.Her *et al.*, 1998). Similarly in a more recent study, when the process gas was changed from SF_6 to NF_3 or 5% HCL/He, distinctly different Si mesostructures were formed by the nanosecond irradiation (D.Mills *et al.*, 2004).

The photochemical etching processes using femtosecond pulsed laser beams produced nanoscale spikes/cones by largely removal of material (similar to ablation as opposed to deposition) demonstrated by the conical base positions laying deep within the substrate and not on the initial surface. Optical parameters such as the laser wavelength and repetition rate govern the size and mean separation of the spikes (D.Riedel *et al.*, 2004). The suggested cone formation from irradiation of a Ti:sapphire laser is related to an array of silicon balls or spherical caps on the rippled surface of silicon observed in the early stages of irradiation. The caps form a grid determining ultimately the position of the cones and one possible mechanism corresponds to these caps being highly reflective due to thermal transitions so that photochemical etching is minimal resulting in eventual cone formation. Another possibility is that their sub-wavelength, spherical shape scatters the radiation rather than absorbing it protecting the structures against further ablation. It is likely that some redeposition occurs from the ejected hot molten Si additionally contributing to cone growth (D.Riedel *et al.*, 2004). The growth of microcolumns produced in an earlier investigation under similar conditions and with the

same type of laser was proposed to occur through a combination of pulsed-laser melting of the tips of the columns and deposition of silicon from the intense flux of silicon-rich vapour produced by the ablation of the surface regions between the columns. The molten tips of the columns are strongly preferred sites for deposition due to a large accommodation coefficient, resulting in a very high axial growth rate aligned along the incident beam direction (A.J.Pedraza *et al.*, 1999).

The structural formation is suggested to occur in two stages:

(i) the development of a small protrusion and

(ii) the evolution into a growing column or cone.

The growth stage can be divided into three separate stages:

(iii) the formation of a silicon-rich vapour,

(iv) the transport of this vapour to the tip of the column and, (v) the liquid-phase silicon-deposition reaction.

Grooves or holes are initially formed where etching is enhanced because laser energy is concentrated as the beam undergoes multiple reflections from the steep walls producing silicon-rich molecules (A.J.Pedraza *et al.*, 1999). Another study resulting in the production of sharp conical spikes on a silicon substrate by the same type of laser irradiation and similar processing conditions could have also been attributed to a vapour phase transport-based mechanism (T.Her *et al.*, 1998).

In general, reports on structural developments after cumulative excimer (e.g. XeCl) laser irradiation suggest that the conical or columnar structures are not formed by a growth process, but by preferential ablation (A.J.Pedraza *et al.*, 1999; F.Sanchez *et al.*, 1998). In contrast however, columnar structures produced by the irradiation of an ArF excimer laser on silicon have been explained as resulting from a real growth process (where the height of some columns can be between one and two orders of magnitude

higher than the crater depth) as opposed to preferential ablation (F.Sanchez *et al.*, 1999). The reported topography appears after a progressive evolution of the surface through hydrodynamic processes, with well-defined steps and with forces to move the liquid silicon originated from gradients in temperature and capillary action in to addition by expansion during solidification. Surface tension forces redistributed the material from the initial hillocks that each contributing laser pulse had melted, into growing columnar structures. Spherical structures had been observed below the spherical tips with the offered explanation that the structures may have originated from the freezing of a melted silicon front climbing the wall of the column, subjected to heat loss via conduction to the substrate. Alternatively, they may have resulted from the melting of the tip by the repeated laser pulse but this occurrence would be likely to accompany a reduction in columnar height (F.Sanchez *et al.*, 1999).

Recent study and development in laser surface modification of silicon has established that the Si pillars formed under irradiation (from either femtosecond or nanosecond) pulsed lasers can be modified post-processing in wet chemical etches thus altering their structure. Stain etching in acidic fluoride solutions leads to porosification with retention of the gross structure, which may be advantageous for drug delivery purposes where the porous layer can provide a reservoir for the delivery molecules. The use of conventional and non-conventional stain etchants creates luminescence under UV illumination for simplified observation of the nanocrystalline coating porous layer (D.Mills *et al.*, 2004).

4.7 Surface Modification of Hydroxyapatite

The realisation that surface treatment of materials (such as silicon) with excimer laser radiation often results in the formation of a rough columnar or cone-shaped surface topography with a considerably increased surface area has inspired the search for a non-porous bioactive material with adequate mechanical properties and a high surface to volume ratio, similar to porous materials that can be applicable for drug delivery in addition to better interfacial properties improving success as an implant material. Disadvantages of the pulsed laser deposition method such as target damage making coatings less homogenous can be put to profit by applying the laser treatment to the

materials surface with the aim of changing the surface morphology instead of depositing ablated material on another target.

Within recent years a research group in Portugal have used a nanosecond KrF excimer laser for surface modification of both dense hydroxyapatite and glass-reinforced hydroxyapatite (GR-HA, has superior mechanical properties to pure HA) employing a 248 nm radiation wavelength and 30 ns pulse duration to obtain a rough disorganised columnar or cone-shaped surface topography. The surface modification was carried out in air using a wide range of radiation fluence and number of pulses. It was determined that the actual surface area doubled in samples treated with 1000 pulses at 10 kJ/m^2 laser fluence. Both SEM and laser profilometry were employed to observe and analyse the surface roughness. X-ray photoelectron spectroscopy (XPS), XRD and FTIR were used to analyse chemical properties of the material and changes in the surface layer constitution. XPS analysis of the laser treated HA sample portrayed formation of other calcium phosphates with displaced Ca and P peaks that appeared similar to peak values of untreated GR-HA. FTIR and XRD analysis confirmed this loss of crystallinity.

The offered explanation of the formation of a cone shaped surface topography is similar to the model previously proposed (D.Riedel *et al.*, 2004), as a result of a combination of shadowing and progressive reduction of the radiation fluence due to the increasing inclination of the surface towards incident radiation combined with a scattering of radiation (A.Queiroz *et al.*, 2004).

The use of gaseous H_2O in the ambient processing atmosphere has been fairly well documented in terms of laser deposition for coatings (H.Zeng *et al.*, 2000b; J.L.Arias *et al.*, 2003a; J.M.Fernandez-Pradas *et al.*, 1998), but in terms of laser ablation as there is little in the literature about surface modification of HA the few existing reports concern the dental application of the modification and removal of dental hard tissue or enamel (containing mostly HA). The use of H_2O is strongly and widely recommended to prevent the accumulation of non-apatite calcium phosphate phases on the irradiated

surface (D.Fried *et al.*, 2002). One study employing the irradiation of artificial HA sample with a CO_2 laser without water present in the processing atmosphere suggested that the decrease in the characteristic peaks of HA in the resultant XRD patterns suggested the decomposition of HA due to the thermal effect of laser irradiation (M.Tanaka, 2000). The temperature of the interacting surface should increase during photo ablation due to the thermal effect with the reaction in Equation (4.1) taking place:

$$Ca_{10}(PO_4)_6(OH)_2 \rightarrow 3Ca_3(PO_4)_2+CaO+H_2O$$

(Equation 4.1)

The product from the reaction of CaO with H_2O is likely to produce tricalcium phosphate and heat. The presence of H_2O molecules in the vapour or gas phase participate in the scattering of the different species as well as controlling the velocity of the emissive components in the plume in addition to the thermal effect preventing the undesirable products (P.Serra *et al.*, 1998).

4.8 Characterisation

4.8.1 FTIR Spectroscopy

Infrared spectroscopy is an analysis technique that provides information on the vibrations of atomic and molecular units and is a standard analytical method employed to reveal information of the specific chemistry and the molecular structure and orientation of a material specimen (B.D.Ratner *et al.*, 1996c). The region of the electromagnetic spectrum that gives rise to infrared radiation promotes transitions in a molecule between vibrational; (from near- and mid-infrared radiation) and rotational (far infrared radiation) energy levels of the lowest electronic energy state (A.Cross, 1969; S.D.Ross, 1972). The molecule can absorb the radiation by increasing its own vibrational energy. IR (infrared) spectrospcopy relates to the ability of the molecule to absorb radiation energy at certain specific frequencies which match the natural vibrational frequencies of the molecule occurring in the IR region of the electromagnetic spectrum, during irradiation with a whole range of infrared frequencies (N.Colthup *et al.*, 1975). Therefore, chemical bonds and groups of bonds within a specimen will vibrate at specific frequencies and upon exposure to IR rays will only absorb the energy at frequencies characteristic to the material. The transmittance and

reflectance of the IR rays by the sample is translated into peaks producing a spectral pattern that can be compared and analysed to identify the material (B.D.Ratner *et al.*, 1996c). The absorption frequency depends on the molecular vibrational frequency but the intensity of the absorption depends on how effectively the IR photon energy can be transferred to the molecule governed largely by the change in the dipole moment resultant of the molecular vibration. In order to absorb infrared radiation a molecular vibration must cause a change in the dipole moment of the molecule (N.Colthup *et al.*, 1975).

A Fourier transformed infrared (FTIR) spectrometer largely improves the signal-to-noise-ratio (S/N) and spectral accuracy but even with the high S/N, the small absorption signal associated with the extremely small mass of material in a surface region can present challenges to the sensitivity of the spectrometer. Surface FTIR studies involve an increase in the intensity of the surface signal and reduce the bulk absorption signal with the three most commonly used methods being; (i) Attenuated total reflectance (ATR) penetrating to a depth of 1-5 μm, (ii) External reflectance mode penetrating to a depth of 0.1-10 nm when the sample is placed on a specular surface and (iii) Diffuse reflectance mode penetrating to a depth of 1-5 μm but the sample must be rough.(B.D.Ratner *et al.*, 1996b) A vacuum is not required for this technique and analysis can be applied to minute quantities of materials in solid, liquid or gaseous state.

4.8.2 Raman Spectroscopy

Raman spectroscopy has been described by Darimont *et. al.* (2003) as a fast method for analysing molecular properties of bulk materials, such as hydroxyapatite, with micron size spatial resolution. The Raman Effect describes a type of scattering first portrayed by C.V. Raman in 1928 and results from the inelastic scattering of light by matter through phonon excitations. The frequency of the shift is analysed and distinct intensity peaks (Stokes lines) at different frequencies occur providing information on the vibrational states of molecules and ions in the solid state. In order for a molecular vibration to be Raman active, the vibration must be accompanied by a change in the polarizability of the molecule. Any parameter modifying the scattering process can

cause a change in position, intensity or shape of the Raman bands (G.L.Darimont *et al.*, 2003; N.Colthup *et al.*, 1975).

4.8.3 SEM Imaging

This widely used and much written about technique functions by focusing and rastering a relatively high-energy electron beam on a material surface. Low-energy electrons are emitted from each impact spot of the focused beam. The intensity of the secondary electron emission is a function of the atomic composition of the sample and the geometry of the features under observation. The surfaces are imaged by spatially reconstructing the intensity of the secondary electron emission on a phosphorus screen. Only the secondary electrons generated near the surface of the bulk material can escape to be detected because of the shallow penetration depth of the low-energy secondary electrons produced by the primary electron beam, permitting surface analysis only (B.D.Ratner *et al.*, 1996b).

4.9 Types of Process Gas

4.9.1 Sulphur hexafluoride (SF_6)

The previous groups that successfully provided a regular and uniform surface topography on silicon investigated a number of parameters including the type of process gas used. The most successful development has involved the use of sulphur hexafluoride (SF_6) on the surface modification of silicon (E.Gogolides *et al.*, 2004). Being one of the most popular insulating gases next to air (due to it being electronegative), the gas is non-flammable and fairly inert and non-corrosive at normal temperatures. At temperatures above 500 °C the decomposition products include highly reactive fluorine. The physical properties of SF_6 are shown in Table 4.1 (V N Maller *et al.*, 1981).

Table 4.1 Physical properties of SF_6

Molecular Weight	146.05
Melting point, °C	-50.8
Sublimation temperature, °C	-63.9
Density (liquid at 50 °C), g/mL^{-1}	1.98
Density (liquid at 25 °C), g/mL^{-1}	1.329

Density (gas at 1 bar and 20 °C), g/L^{-1}	6.164
Critical temperature, °C	45.6
Critical pressure, atm	36.557
Critical density, g/mL^{-1}	0.755
Surface tension (at –50 °C), dyne/cm^{-1}	11.63
Viscosity (gas at 25 °C), poise	1.61E-4
Boiling point, °C	- 63.0
Specific heat (at 30 °C), cal/g^{-1}	0.143
Relative density (air=1)	5.10
Vapour pressure (at 20 °C), bar	10.62

Being an extremely stable gas with unique physical and chemical properties the worldwide dominant use of SF_6 is for gas-insulated equipment for electrical transmission and distribution systems in addition to blanketing or degassing of molten reactive metals such as magnesium and aluminium. It is a very efficient green house gas with a likely atmospheric lifetime of approximately 3200 yr determined solely by atmospheric destruction processes that take place above 60 km (M.Maiss *et al.*, 1998).

4.9.2 Ammonia (NH_3)

Ammonia (NH_3) gas is colourless with a similar sharp, penetrating odour to when in the pressurised liquid form. Generally it is not a flammable gas although a large, intense energy source can cause ignition. The gas can decompose at high temperatures forming very flammable hydrogen and toxic nitrogen dioxide. It is a compressed and corrosive gas that is shipped and stored in a liquefied form under its own vapour pressure (787 kPa at 21.1 °C). Its primary use is in the fertilisation industry where it can be used to manufacture nitrogen fertilisers (urea, ammonium nitrate etc) in addition to being a directly applied fertiliser. Some chemical and physical properties of NH_3 are shown in Table 4.2 (T.A.Czuppon, 1992).

In terms of laser processing NH_3 is used to provide a reactive atmosphere for chemical reaction where a chemical component of the laser plume reacts with the reactive added

medium. Commonly this process is used for the fabrication of nitride thin films by laser ablation of III-IV elements (such as silicon) in a NH_3 atmosphere (Compressed Gas Association, 1990; T.M.Di Palma *et al.*, 1997). When the energetic threshold is in excess of a wavelength of 206 nm the NH_3 molecules start to photodissociate and reports demonstrate that in the ultraviolet band region of 168-217 nm, NH_3 molecules photochemically dissociate into NH_2 and H fragments. Altering the laser fluence (kJ/m^2) has been shown to control the composition of N and Si. When the laser power is decreased from high to low, the nitrogen concentration is increased in the deposited compounds and the amount of adsorbed NH_3 on the surface is greater (C.K.Choo *et al.*, 1999; C.K.Choo *et al.*, 2004).

Table 4.2 Physical properties of NH_3

Molecular weight	17.03
Conversion factor, ppm at 25 °C	1.4
Melting point, °C	FREEZING POINT = - 77.7
Boiling point, °C	- 33.4
Relative density (specific gravity)	0.682 at - 33.4 °C (liquid) 0.707 at 25 °C (gas)
Solubility in water, g/100 ml at 25 °C	52.9 (very soluble)
Solubility in other liquids	Soluble in ethanol, diethyl ether Other organic solvents and mineral acids
pH value	11.6
Surface tension, dyne/cm^{-1} at – 40 °C	44.55
Vapour density, °C	0.597
Vapour pressure (at 40 °C), kPa	~ 2070 (20.4 atm)
Critical temperature, °C	133
Critical pressure, °C	11425

Based on the described findings the experimental set up and conditions for laser surface modification investigated in this study employing both SF_6 and NH_3 process gases can be found in Section 5.

Summary

The importance of biomedical surface science on determining the biological host response to implanted materials and therefore, the subsequent clinical success has been established by many research groups. Surface chemistry including surface functional groups, surface charge, acidity and basicity, hydrophobicity and porosity have a large influence on cell attachment, adhesion and subsequent tissue response. Different types of cells exhibit variations in sensitivity and types of response to a particular type of surface micro/nanostructure such as grooves, ridges, cones or pits. Cellular response may therefore be enhanced by the fabrication of a particular topography upon an implanted biomaterial and the subsequent biocompatibility improved. The main types of methodology employed to create surface structure include; polymer demixing, photoimmobilisation, photo- and electron beam lithography, wet chemical etching laser ablation. The main types of laser are described by the lasing medium used such as in solid state, gas, excimer, dye or semiconductor and can be emitted in a variety of durations (pulsed or continuous), wavelengths and power. Various types of process gases can be used in combination with the lasing conditions to produce surface structures upon a substrate by a combination of ablation and deposition. In this manner, the fabrication of conical structures on silicon substrates has been investigated employing excimer lasers in the presence of SF_6 gas. Similar research employing a different type of excimer laser without processing gas has taken place to modify the surface of HA samples. The resultant increase in material surface area corresponded to the development of a rough, disorganised columnar-like topography that was produced. The aim of this research project is to employ similar lasing conditions to those used to create uniform structures on silicon, for the structural surface modification of nanocrystalline HA.

Chapter 5 Materials and Methods

5.1 Hydroxyapatite Synthesis

Previous established methods of wet chemical synthesis, microemulsion and macroemulsion synthesis were used and adapted to synthesis hydroxyapatite (M.J.Phillips *et al.*, 2003; T.Furuzono *et al.*, 2001). Each method of hydroxyapatite synthesis required the use of the following reactants provided by VWR International (UK); analytical grade (AnalaR) $Ca(OH)_2$ and general purpose grade (GPR) H_3PO_4 as the core components and AnalaR grade NH_4OH solution (specific gravity = 0.88) for the pH adjustment of the reaction. In all reactions, deionised water (10 MΩ) was used after production from an USF Elga Option 3 Water Purifier.

All reactions were carried out on an IKA Werke (UK) magnetic stirrer/heater with the experimental set up covered and isolated in a fume cupboard to prevent contamination in addition to health and safety aspects. Scientific laboratory grade glassware and polyethylene covered magnetic stirrer bars were used. Filtering was carried out using a 150 mm Buchner filter in addition to Whatman Glass Microfibre 150 mm filter paper with an average 0.3 μm pore size unless otherwise described. Equipment was cleaned before every experiment by washing with warm water and detergent, rinsing with warm water and then re-rinsing with deionised water before being oven dried. Unless otherwise stated the synthesis reaction was carried out at laboratory room temperature (17 °C).

5.1.1 Wet Chemical Precipitation

Wet chemical precipitation of hydroxyapatite was used to produce a large yield of hydroxyapatite powder as a standard material for a comparative study investigating powder particle size. This method of material synthesis was combined with freeze drying to provide powder with increased surface area.

A 1L solution of 0.3 mol H_3PO_4 was added dropwise into a 1L suspension of 0.5 mol $Ca(OH)_2$ whilst being continually stirred. The pH of the system was maintained at 10.5 by the dropwise addition of NH_4OH. Stirring was stopped after 2 hrs and the system was left to age for 18 hrs. The resulting precipitate was filtered through Whatman standard filter paper (average pore size of 4 μm) and washed with 100 ml H_2O to produce a filtercake for freeze-drying.

Commercial grade 'Plasmabiotal' hydroxyapatite powder and premium grade (phase pure) 'Apatec' hydroxyapatite powder that were produced by methods of wet chemical precipitation and oven dried, were also used within this study in order to optimise the success of the laser surface modification.

5.1.2 Emulsion Synthesis

A "water in oil" (w/o) emulsion system was employed to enhance the precipitation of hydroxyapatite powder with the aim of producing finer powder particles of further increased surface area that would be free-flowing with better packing properties and increased stability during thermal processing and consolidation. This corresponds to the increase in the interfacial area of water when in the form of discrete droplets within an emulsion in comparison to the form of a body of water with equal volume. The aim of precipitation of hydroxyapatite particles within the discrete water droplets is to produce particles of increased surface area due to the restricted area available for reaction. The reactants used in the wet chemical precipitation process formulated the water phase and the reactants used for the oil phase were high performance liquid chromatography (HPLC) grade 2,2,4-trimethylpentane (isooctane) and Sigma Ultra grade sodium salt of dioctyl sulfosuccinate (Na-AOT) as supplied by Sigma-Aldrich (UK).

Throughout emulsion synthesis of hydroxyapatite, 0.1 mol Na-AOT and 6 mol of isooctane were measured out prior to stirring together for 30 minutes in a 3000 ml glass beaker to allow the Na-AOT to dissolve in the isooctane developing the oil phase.

5.1.3 Emulsion Characterisation

As established in Section 3.3, a particular emulsion system can categorically be defined as a microemulsion or macroemulsion according to the following characteristics:

A microemulsion is typically transparent and thermodynamically stable due to minimal volume of the water phase in the oil phase.

A macroemulsion has a cloudy or opaque appearance due to the large volume of the water phase dispersed in the oil phase and stability can only be maintained by continual stirring.

This particular system was characterised and described previously by (M.J.Phillips *et al.*, 2003). In that procedure, preparation of an oil phase required 0.01 mol of Na-AOT dissolved in 0.6 mol of isooctane, while continuous stirring was maintained. In the next step, 1 ml of H_2O was added into the reaction mixture using an Eppendorf pipette. The system was observed to allow the return of a transparent state before the next addition of H_2O. The emulsion was transparent when less 10 ml of H_2O was added. The emulsion returned to the transparent state within 120 s when the volume of the individual additions of H_2O was decreased to 0.5 ml. The emulsion system became opaque and stable when 11.5 ml H_2O had been added and continued to demonstrate stability up to the addition of 50 ml H_2O.

The w/o emulsion system employed in this study has previously been defined as being a microemulsion when the water phase is less than 11 % of the overall system volume and a macroemulsion when exceeding the 11 % amount.

5.1.4 Microemulsion Synthesis

The preparation of hydroxyapatite in a microemulsion corresponded to a system where the concentration by volume of water in oil, was 10 % and was carried out by the following procedure:

A 50 ml suspension of 0.05 mol $Ca(OH)_2$ was added to the pre-prepared oil phase and continually stirred to form an emulsion prior to the dropwise addition of a 50 ml solution of 0.03 mol H_3PO_4. The pH was maintained at 10.5 during the addition by the dropwise addition of NH_4OH solution. The microemulsion was covered to prevent contamination and stirred for 24 hrs before the system was allowed to separate and the precipitated components age for a further 24 hrs. The distinctly different phases were then separated to enhance the filtering process. The waste layer (typically clear) was disposed of and the layer containing precipitate (typically white and opaque) was filtered before freeze-drying.

5.1.5 Macroemulsion synthesis

Initially, it was found that the yield of hydroxyapatite produced by microemulsion synthesis was less than 2 g and the length of time (approximately 1 week) required for production of such a small yield made the process inefficient when at least 4.5 g of powder was required to produce sintered HA discs for further study on laser surface microstructuring of HA. As a result macroemulsion synthesis of hydroxyapatite was also performed.

The preparation of hydroxyapatite in a macroemulsion corresponded to a system where the concentration by volume of water in oil, was 25 % and was carried out by the same procedure employing reagent quantities of 125 ml of 0.1 mol $Ca(OH)_2$ and 125 ml of 0.06 mol H_3PO_4.

In order to investigate the effect of temperature on the hydroxyapatite yield and particle size, the procedure was carried out at temperatures of 17 °C, 25 °C and 50 °C.

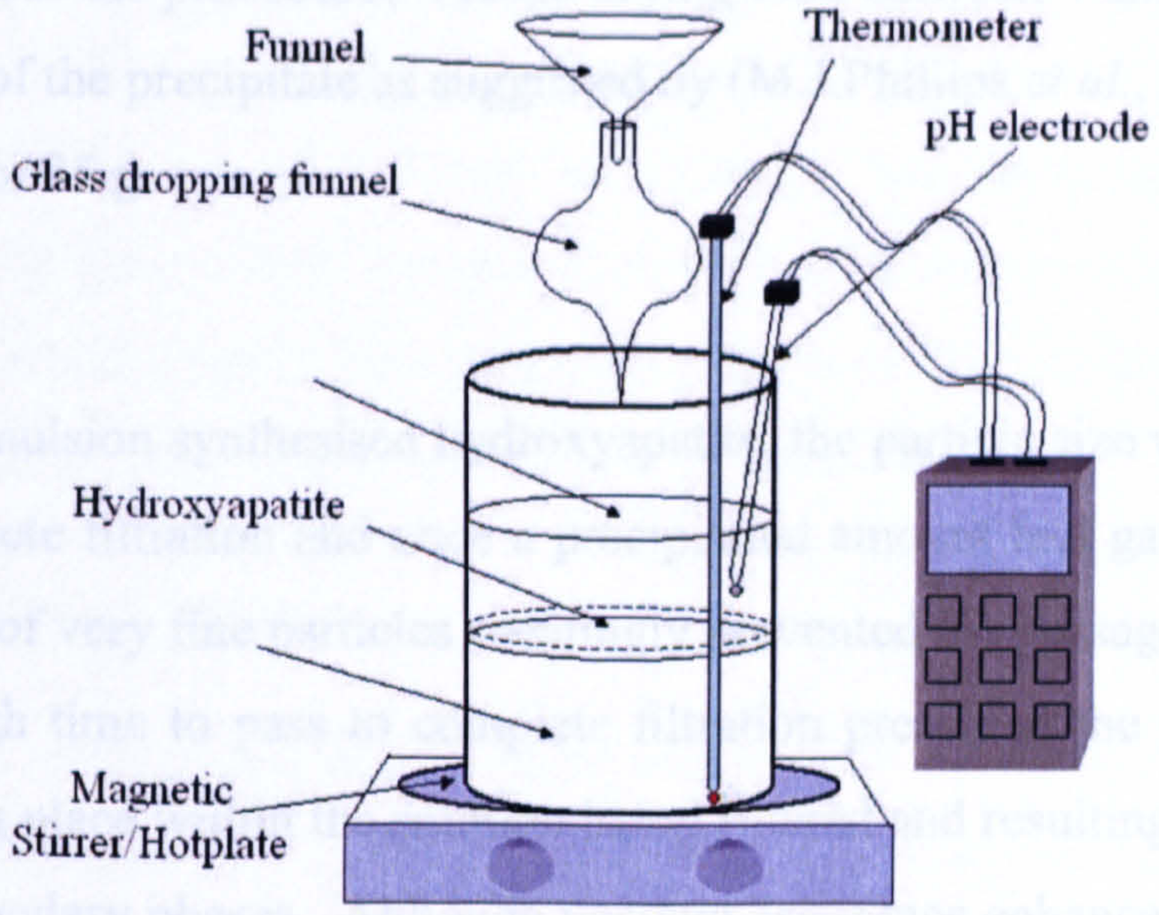

Figure 5.1: Diagram of emulsion set up with separated phases.

5.2 Hydroxyapatite Processing

5.2.1 Freeze-drying

Freeze-drying was performed after the hydroxyapatite precipitate was filtered using a Buchner filter. In the case of the hydroxyapatite synthesised by wet chemical precipitation, freeze-drying was performed in 500 ml flasks using an Edwards 4K Modulyo Freeze Dryer connected to a vacuum pump. The washed and still wet filter cake was removed from the filter paper and spread around the walls of the freeze-drying flask by rolling the flask sealed with laboratory grade parafilm along a surface, in order to increase the surface area being dried and improve the efficiency of the process. Liquid nitrogen was then used to freeze the precipitate while in the flask. Before attachment to the freeze-dryer the apparatus was switched on and the temperature permitted to reach -40 ˚C by refrigeration. The vacuum pump was switched on and the set up was checked to ensure perfect seal allowing a vacuum of 10 Pa to be maintained during freeze-drying. A section of filter paper placed in the attachment adjoining the vacuum flask was used to prevent impurities entering the hydroxyapatite and to prevent the loss of hydroxyapatite into the drying chamber. The entire flask and contents were then attached to the freeze-dryer and the vacuum maintained at above 10 Pa for between 18 and 48 hrs. The flask itself was kept at room temperature to enhance the drying

process throughout the procedure. Freeze-drying took between 4 and 72 hrs depending on the quantity of the precipitate as suggested by (M.J.Phillips *et al.*, 2003) e.g. 4 hrs for 2 g and 72 hrs for 35 g.

In the case of emulsion synthesised hydroxyapatite, the particle size was often too small to ensure complete filtration and once a precipitated amount had gathered on the filter paper, the layer of very fine particles seemingly prevented the passage of water through. Allowing enough time to pass to complete filtration presented the problem of further chemistry taking place within the solution being filtered and resulting in the presence of undesirable secondary phases. Although vacuum assistance enhanced the filtration rate it also prevented accurate filtration by dragging a lot of the very fine particles through the paper and therefore permitted the loss of some quantity of the precipitate. Therefore filtration was performed to produce a slurry (of less than 10 mm thick) that could be freeze-dried in a Virtis® Advantage ES (USA) freeze-dryer within a tray. Once frozen and the condenser cooled to a temperature of -50 °C within a vacuum of under 200 mT the slurry was freeze-dried by the following program (recommended for all ceramic powder slurries):

Step 1 - 35 °C for 120 mins

Step 2 - 25 °C for 840 mins

Step 3 - 20 °C for 120 mins

Step M- 5 °C

The condenser temperature was maintained at below -50°C throughout the process and defrosted with an automatic defrost program after the powder had been freeze-dried and removed.

5.2.2 Disc Pressing

Hydroxyapatite discs were prepared according to the following procedure:

4.5 g of finely ground (using a mortar and pestle) hydroxyapatite powder was placed in between two smoothly polished faced discs in a hardened steel die mould. The a hardened steel plunger was placed into the die mould and the complete apparatus was inserted into a die press where a pressure of 0.59 MPa was placed on the mould and held for 3 - 4 seconds, before being released. Discs of 30 mm diameter and 5.5 mm height were prepared in this manner before being sintered.

5.2.3 Calcination and Sintering

Hydroxyapaptite powder obtained by using any method of chemical synthesis used in this study (wet chemical precipitation or emulsion synthesis) was relatively amorphous and required thermal treatment (calcination) to produce fully crystalline material or fully dense products if processed into shape or form such as discs (via sintering).

The prepared discs were placed on a ceramic plate and sintered in a Carbolite® tube furnace using a regime where the material was heated from 25 °C at a rate of 2.5 °C min^{-1} up to 1200 °C which was maintained for 2 hrs before cooling at a rate of 10 °C min^{-1} back to 30 °C. The resultant discs had dimensions of 21 mm diameter and 4.5 mm height.

All thermally processed materials were stored in an airtight container placed within a desiccator to prevent contamination with atmospheric H_2O and decomposition into any undesirable phases.

5.3 XRD Chemical Characterisation

X-ray powder diffraction (XRD) is a highly developed and documented technique that is widely used to identify crystalline materials. It can provide quantitative information about the chemical composition of a sample, providing proportional data of the different chemicals or phases present. An X-ray incident upon a sample is diffracted in accordance with Bragg's Law (Equation 5.1) formulated by W.L. Bragg in 1912 and described by Cullity (1978).

$$\lambda = 2d\sin\theta$$

(Equation 5.1)

where λ is the x-ray wavelength, d is lattice spacing and θ is the scattering angle.

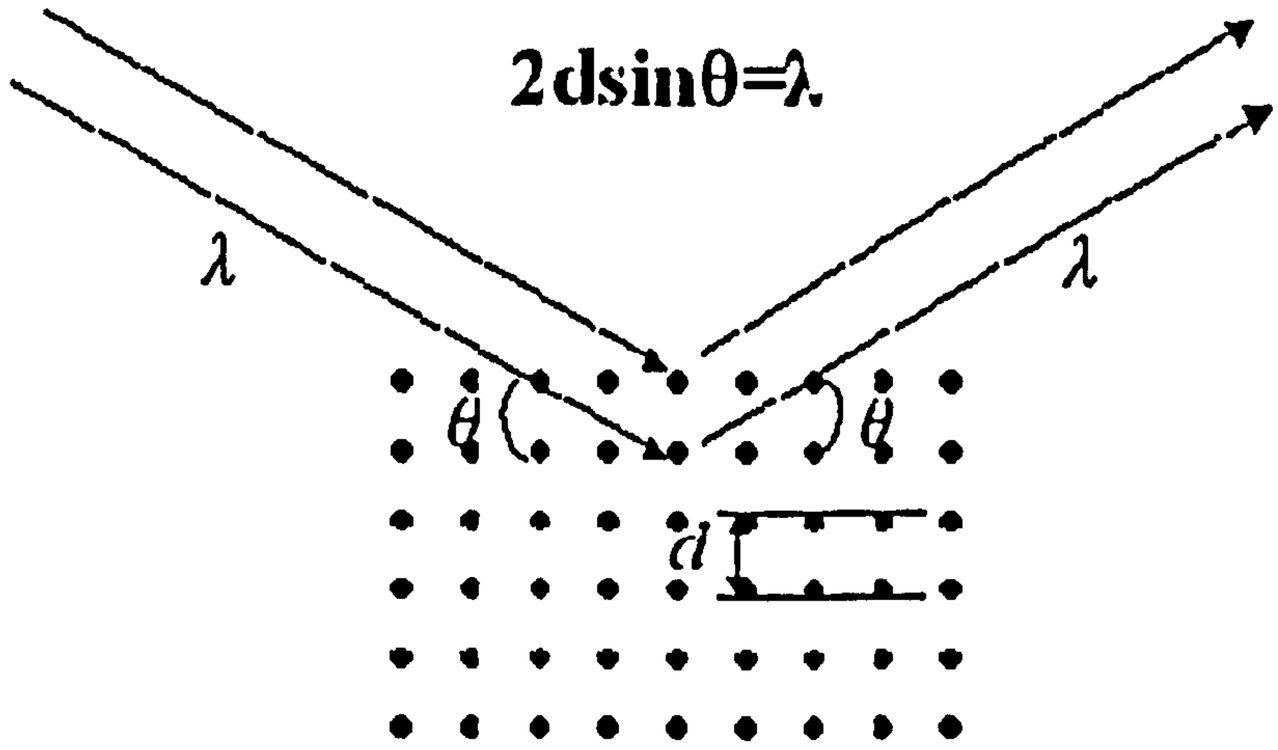

Figure 5.2: Diagram illustrating Bragg's Law

Powder XRD is one of the most widely used X-ray diffraction techniques used for characterising materials with the powdery form describing the random orientation of the crystals in the sample. Upon recording of the two-dimensional diffraction pattern, scattered peaks correspond to the various *d* spacings in the crystal lattice. The positions and intensities of the peaks are used for identifying the underlying structure (or phase) of the material.

XRD data patterns were produced and collected for the as-prepared and sintered powder samples using a Siemens D5000 diffractometer. CuKα radiation was used and the X-ray generator was operated at 40 kV and 4 mA to collect data from the powder attachment across the 2θ range. The powdered samples were fixed at 1° with the detector scanned between 25°-40° using a step size of 0.02° and a count time of 2.5 seconds.

XRD data patterns were collected for the as prepared powder samples in addition to powder samples that had been thermally processed using the program described in Section 5.2 allowing the thermal stability of the powder to be analysed. Identification of the chemical phases present was achieved by the comparison of the produced diffraction patterns against powder diffraction cards present on the ICDD-JCPDS database as shown in Table 5.1

Table 5.1 ICDD-JCPDS reference cards used

Card Number	Phase	Chemical Structure
09-0432	Hydroxyapatite	$Ca_5(PO_4)_3(OH)$
09-0169	Whitlockite (TTCP)	$Ca_3(PO_4)_2$
05-0586	Calcite	$CaCO_3$

5.3.1 Crystal size analysis

The mean crystallite diameter of each powder sample was determined from the linewidth of the X-ray diffraction spectra using the Scherrer formula shown by Equation 5.2.

$$D_{XRD} = \frac{K\lambda}{B\cos\theta}$$

Equation 5.2

From the full width at half maximum, the average grain size for each sample can be estimated from (002) and (211) diffraction peaks in the XRD spectra according to Scherrer's formula where D_{XRD} is the crystallite size; K=0.89, which is the Scherrer constant related to the shape and index (hkl) of the crystals; λ is the wavelength of the X-rays (CuKα, 1.54); θ is the diffraction angle; and B is the measured width at the half height of the diffraction peak (F.Zhang *et al.*, 2004; Z.Wei *et al.*, 2006).

5.4 Surface Area Analysis

Both the as-prepared and sintered powders were subjected to the Brunauer-Emmett-Teller (BET) method to determine the specific surface area of each sample using a Micromeritics Gemini II 2370 surface area analyzer. The specific surface area for each powder sample was used to determine the average particle size of the sample corresponding to the relationship with (BET) specific surface area shown in Equation 6.1 provided in Section 6.1.1.

The powder samples were degassed with helium for 2 hours at 200 °C using a Flow Prep 060 controller prior to analysis relating to the nitrogen adsorption method. This method uses the physical adsorption of a gas on the surface of the powdered solid before measuring the amount of adsorbed gas corresponding to a monomolecular layer

on the surface to determine the specific surface area of the powder. Physical adsorption results from relatively weak intermolecular forces known as van der Waals forces between the adsorbed gas molecules and the adsorbent surface of the test powder. Gravimetric, volumetric or continuous flow procedure can be used to measure the amount of gas adsorbed. The recorded data are then treated according to the Brunauer, Emmett and Teller (BET) adsorption isotherm equations:

$$\frac{P}{V_{ads}(P_o - P)} = \frac{1}{V_m c} + \frac{c-1}{V_m c}\frac{P}{P_o}$$

(Equation 5.3)

where V_{ads} is the volume of gas adsorbed at $^{P}/_{Po}$, P is the partial vapour pressure of adsorbate gas in equilibrium with the surface at -196 °C, P_o is the saturated pressure of adsorbate gas and V_m is the volume of adsorbate for one monolayer of surface coverage whilst c is related to the heat of adsorption in the first and subsequent adsorbed layers. The equation is then used to plot the BET value against $^{P}/_{Po}$, yielding a straight line graph that lies normally in the approximate relative pressure range 0.05 to 0.3. The correlation coefficient (r) of the linear regression must be greater than 0.9975 for the data to be considered acceptable. The following equation is then applied to calculate the specific surface area A_s, in m^2/g:

$$A_s = \frac{V_m}{V_{molecule}} A_{molecule}$$

(Equation 5.4)

where $V_{molecule}$ is the volume of the adsorbate molecule and $A_{molecule}$ is the cross-sectional area of the adsorbate molecule.

5.5 Density

Bulk density and the subsequent percentage of porosity for the sintered discs were calculated as follows:

$$d = \frac{w}{v}$$

(Equation 5.5)

where d is the bulk density (kg/m^3), w is the weight (kg) and v is the volume of the disc (m^3). The volume of each disc was calculated using the simple equation to calculate the volume of a cylinder:

$$v = \pi r^2 h$$

(Equation 5.6)

where r is the radius (m) and h is the height (m).

The percentage of porosity was then calculated according to:

$$P = \left(1 - \frac{d}{g}\right) \times 100\%$$

(Equation 5.7)

where P is the percentage of porosity (%), d is the bulk density as calculated and g is the theoretical density of hydroxyapatite taken as 3160 kg/m^3 (B.Kundu *et al.*, 2004; D.Tadic *et al.*, 2004; K.A.Hing *et al.*, 1999). Of each powder sample used, 6 discs were measured to provide an average figure of density and percentage of porosity.

5.6 Laser Processing of Hydroxyapatite

The base of this study has been taken from the recent fabrication of ordered rows of conical spikes on a Si substrate by etching with a femtosecond pulsed laser in the presence of SF_6 gas (D.Mills *et al.*, 2004). The overall aim is to create similar structures that are both regular in shape and spacing on nanocrystalline HA. In all cases

the laser used for irradiation was a Lambda Physics LPX105 operating on the XeCl excimer (308 nm, ~180 mv or 0.072 J per pulse, 20 ns pulse width). Samples processed were in the sintered disc form and were placed in a specially prepared holder that could be mounted on a precision *xy* stage (Newport MFN25CC) in a vacuum chamber (rotary pumped) where the laser beam was focused by a 500 mm quartz lens. (Figure 5.3) Within the chamber, different types and pressures of gas could be admitted via a valve and pressure gauge controller. The repetition rate of the system was controlled by the regenerative amplifier while the oscillator and pump lasers ran at a fixed rate. All experiments were conducted at room temperature and with normal incidence of the vertically polarized laser beam.

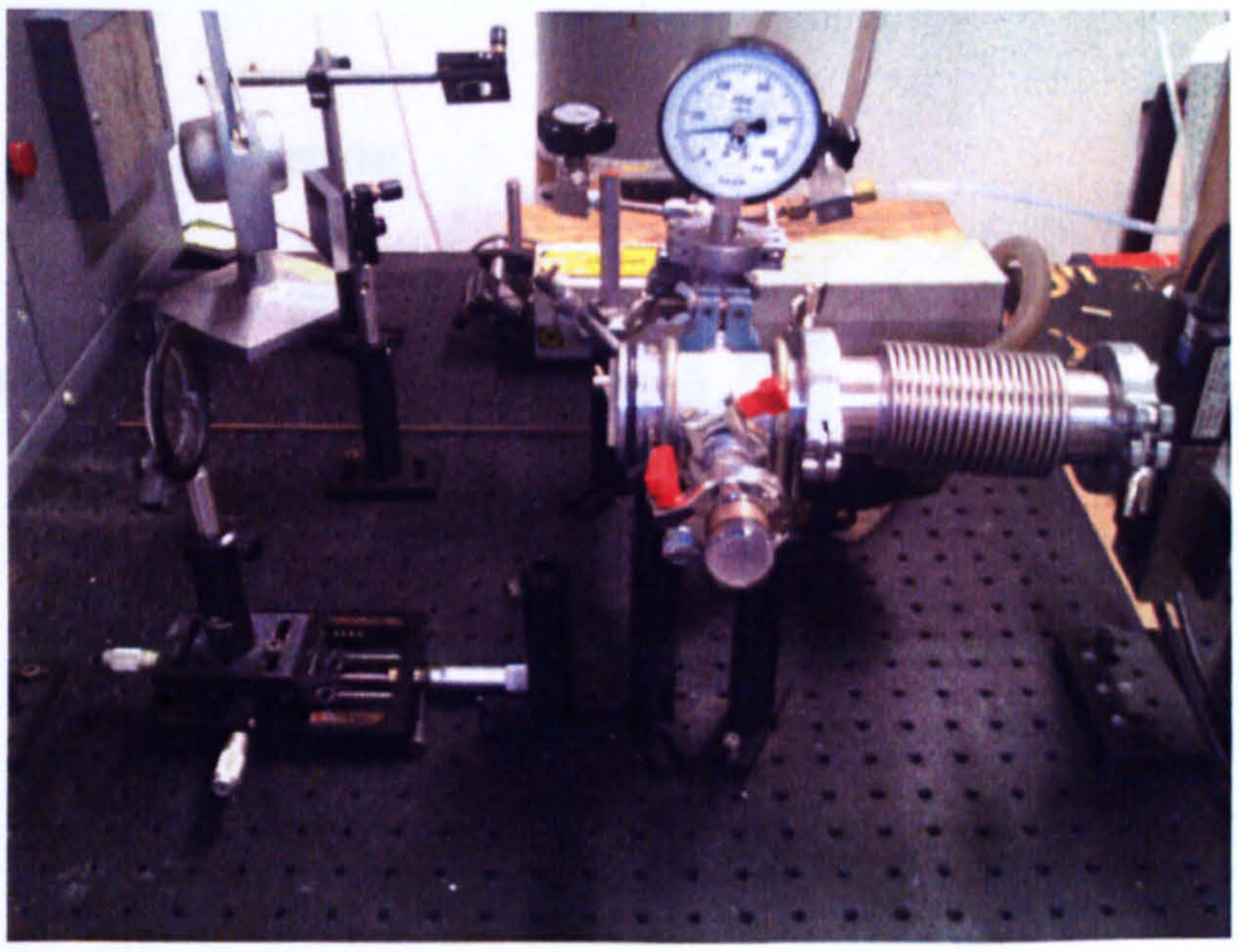

Figure 5.3: Quartz lens and Gas chamber

Different types of gas within the irradiation atmosphere were investigated including SF_6, SF_6 with H_2O and NH_3. The properties of the gases are shown in Table 5.2.

Table 5.2 Properties of Processing Gases

Type of Gas	**SF_6**	**H_2O**	**NH_3**
M_w	146.05	18.015	17.03
Critical Temp. /°C	45.6	373.95	133
Critical Pressure. /kPa – Abs.	3704.138	22064	11425
Boiling Point /°C	-63.0	-	-33.4

A repetition rate of 20 Hz was used in all cases. The HA disc samples were first washed with acetone to remove any surface impurities of carbon debris. The following procedure was then repeated in order to establish the correct irradiation conditions for providing as near a regular surface structure to the HA discs as possible. The samples were mounted within the processing chamber which was then pumped for 15 minutes (p ~0.1 Pa) before a pressure of gas was introduced. The focal length was measured and the laser was initially run to determine the position of the beam on the disc and the spot size of the laser by measurement (after processing) under a light microscope with calibrated measuring facility.

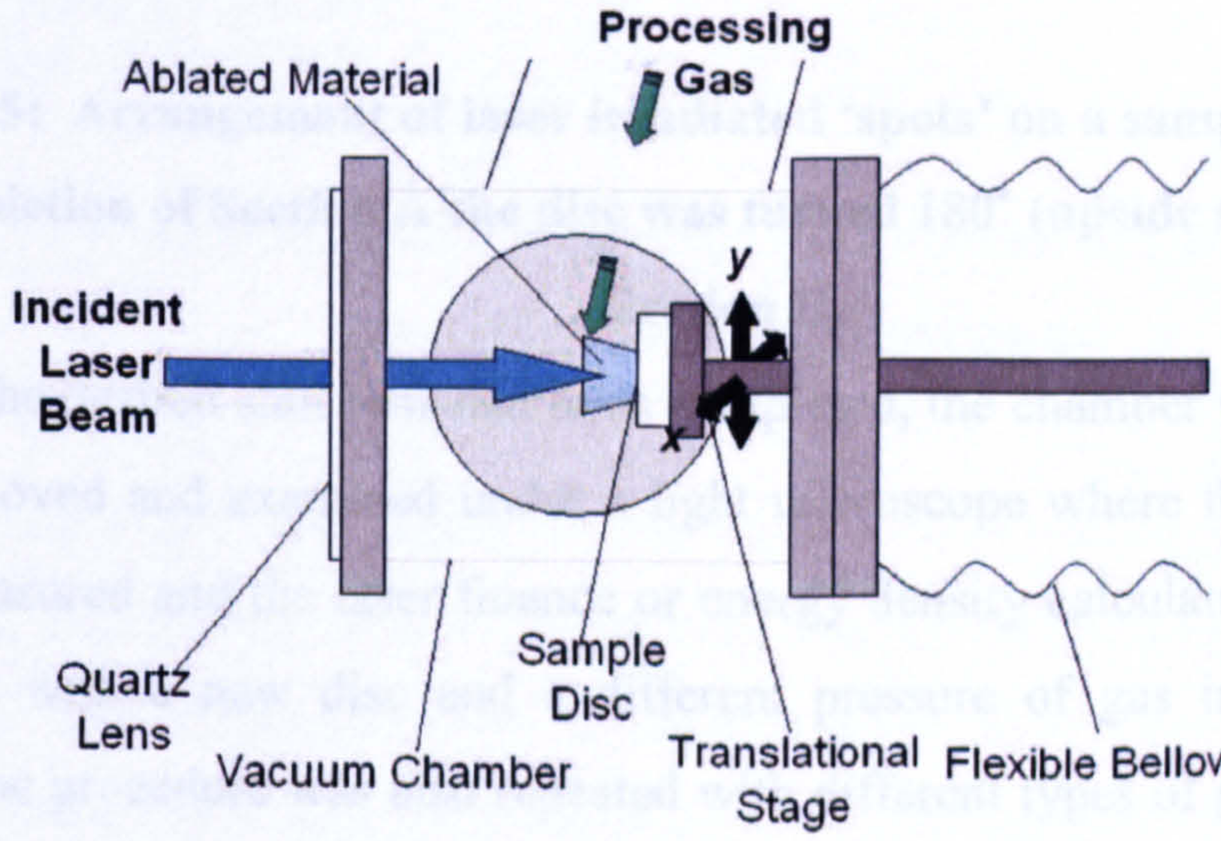

Figure 5.4: Diagram of Laser processing chamber.

The laser was run administering an irradiation dose at a different number of shots that increased between runs until the maximum in order to establish the correct processing conditions that facilitated as close to an organised order of surface structure as possible. Different gas pressures and laser fluencies were investigated. In between laser irradiation, the disc was displaced so that the irradiated areas or 'spots' were separated by 2 mm in the *y* axis and 3 mm in *x* axis.

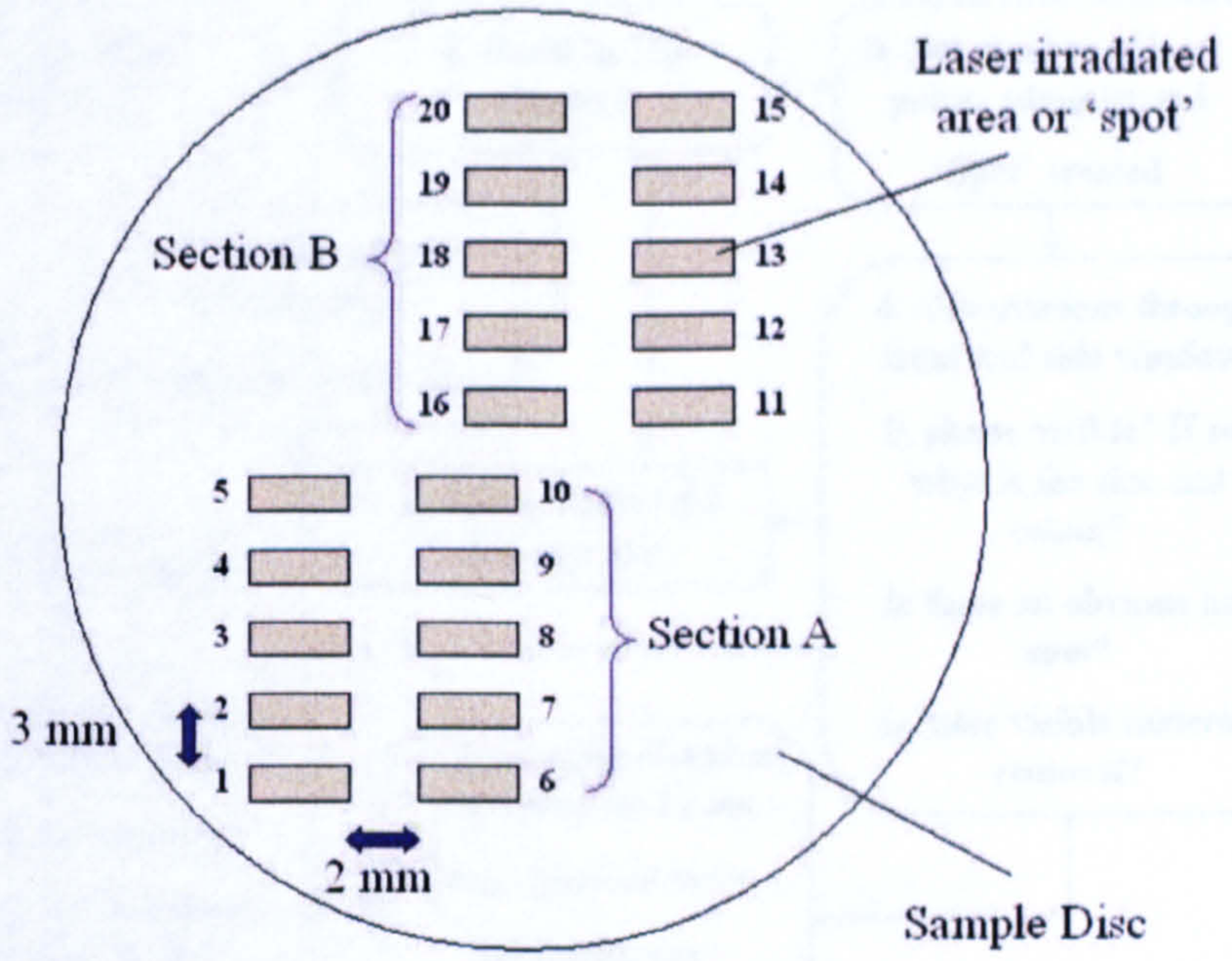

Figure 5.5: Arrangement of laser irradiated 'spots' on a sample disc. After completion of Section A the disc was turned 180° (upside down) to create Section B.

When all of the desired shot runs had been completed, the chamber was vented and the disc was removed and examined under a light microscope where the spot size of the laser was measured and the laser fluence or energy density calculated. The procedure was repeated with a new disc and a different pressure of gas introduced into the chamber. The procedure was also repeated with different types of gas introduced into the processing chamber as previously shown in Table 5.2.

Various observations were made throughout the study such as the colour and size of the laser plume, any charring or change in colour to the material surface. The laser plume appeared large and bright when material removal took place and seemingly structure was created. As a result of this the focal length was also adjusted to a position where a large plume was created. The individual stages of the procedure developed to establish the working conditions that would result in even topographical development on the HA material surface are portrayed in Figure 5.6.

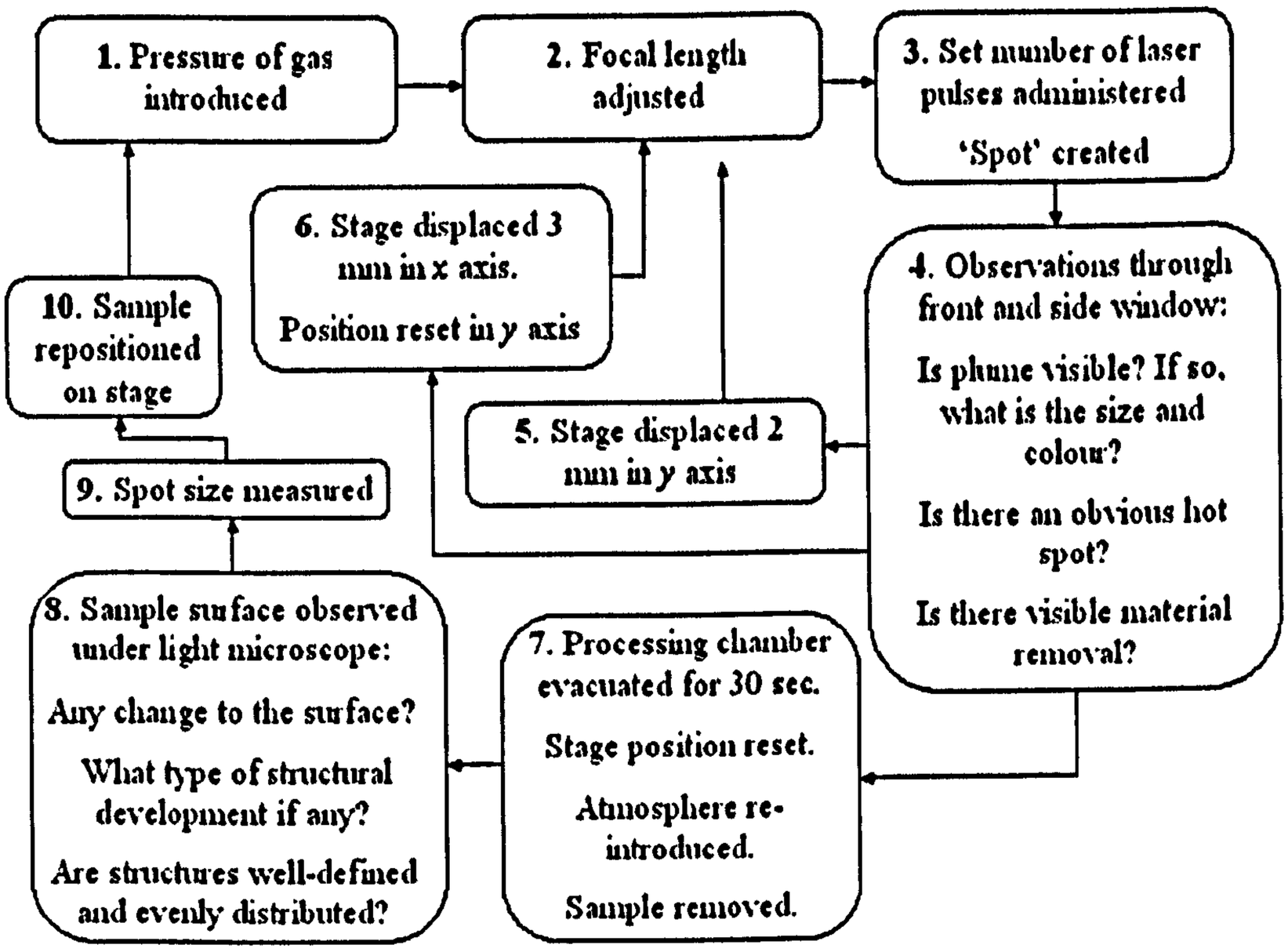

Figure 5.6: Schematic diagram demonstrating the procedure carried out during the initial laser processing study.

When any of the conditions investigated showed the ability to develop what appeared under the light microscope to be a desired even and regularly spaced surface structure, the conditions were repeated with irradiation over a 10 mm strip for further investigation using FTIR, Raman, X-ray microdiffraction and SEM/EDS methods. The results of the preliminary investigation used to establish the appropriate working conditions with each gas for the surface microstructuring of bioceramic HA are shown in Tables 6.4, 6.5, 6.6 and 6.7.

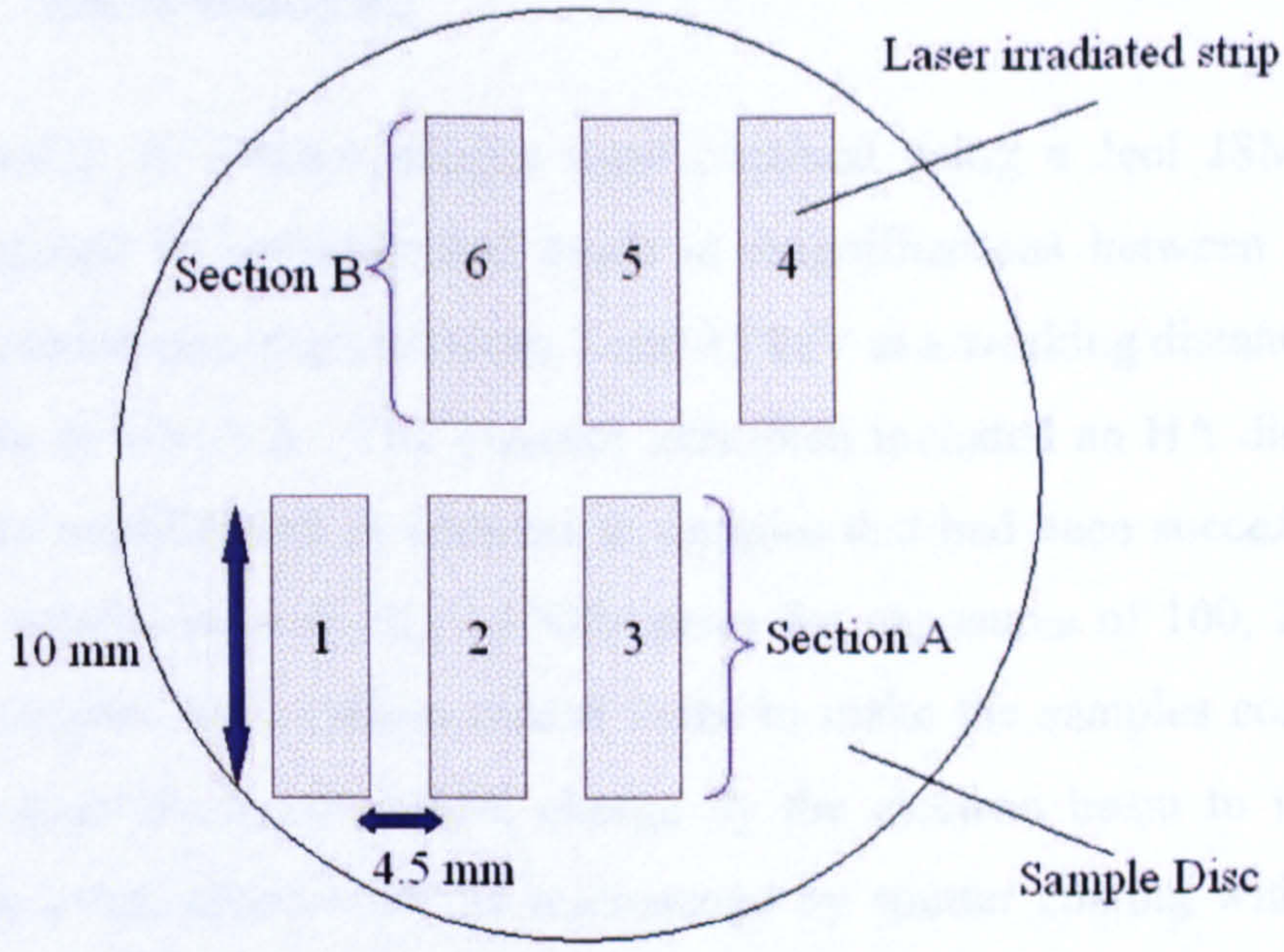

Figure 5.7: Arrangement of laser irradiated strips on a sample disc. After completion of Section A the disc was turned 180° (upside down) to create Section B.

5.7 FTIR Characterisation

All the FTIR spectroscopic studies were performed using a Nicolet 8700 FTIR spectrometer (Thermo Electron Corporation, UK). Typical image collection parameters included a wavelength range of 4000-650 cm^{-1} (mid-infrared region) at 4 cm^{-1} reslotuion, averaging 256 scans. Data processing was carried out by employing Omnic™ software. The samples analysed included an HA disc sample prior to any surface modification in addition to samples that had been processed under laser irradiation with SF_6 or NH_3 gases with successfully produced surface topography

5.8 Raman Characterisation

All the Raman spectroscopic studies were performed using a Nicolet Almega™ XR Dispersive Raman spectrometer (USA) equipped with a 785 nm infrared laser. Typical image collection parameters included a wavelength range of 1250-80 cm^{-1} at a 2 second scan time, averaging 64 scans. Data processing was carried out by employing Omnic™ software. The samples analysed included an HA disc sample prior to any surface modification in addition to samples that had been processed under laser irradiation with SF_6 or NH_3 gases with successfully produced surface topography.

5.9 SEM Imaging

A number of surface images were obtained using a Jeol JSM 6300 (UK) electron microscope in backscattered mode at magnifications between 70x and 1000x using acceleration potentials between 5 and 15 keV at a working distance of 16 mm and probe current of 10-13 A. The samples examined included an HA disc sample prior to any surface modification in addition to samples that had been successfully processed under laser irradiation with SF_6 or NH_3 gases for exposures of 100, 200, 500, 1000 pulses. The samples were carbon coated twice to make the samples conductive and minimise the accumulation of electric charge by the electron beam to improve image quality before examination with the microscope by sputter coating with a BAL-TEC Balzers CED 030 Carbon Evaporator (UK).

A number of images were also gathered after some samples had been cross-sectioned both length and width wise in order to ascertain the processing depth of the laser and height of any structural development. The sections were cut with a water-cooled low speed EXACT diamond band saw (EXACT Technologies Inc., Oklahoma City, OK) before being air-dried and carbon coated ready for SEM analysis (A.K.Bembey *et al.*, 2006; R.De Santis *et al.*, 2000).

5.9.1 Energy dispersive X-ray analysis (EDS)

This technique was used in conjunction with SEM employing an electron beam to strike the surface of a conducting sample. Upon the surface bombardment of the electron beam electrons are ejected from the atoms comprising the sample's surface and the vacancies produced are frequently filled by electrons from higher or outer orbitals that must lose a specific amount of energy (readily predicted by the Laws of Quantum Mechanics) to occupy the vacancies within the closer orbitals/shells. The energy is emitted in the form of X-rays in order to balance the energy difference between the two electrons. Energy dispersive analysis separates and detects X-rays of specific energy and displays them as histograms. The X-rays are characteristic to and labelled by the element producing the X-ray, the shell producing the vacancy, the shells traversed in filling the created vacancy in addition to, the number of electrons producing vacancies. The intensity of the produced X-rays depend on the atomic number of the element, the

ionisation cross section, the fluorescent yield further to the beam current and X-ray absorption and fluorescence. A vacancy created within innermost orbitals will produce characteristic X-rays of the greatest energy but the energy will always be less than that found within the incident beam.

Some of the advantages (particularly over wet chemical analysis) include: (i) X-ray sampling is non-destructive; (ii) the natural heterogeneity of a sample can be retained; (iii) analysis can be conducted on microgram quantities and; (iv) adjacent structures can be directly compared. The imaging of different elements is possible employing energy-dispersive X-ray analysis and can be used to locate the distribution of elements within a sample. Methods representing this produce resultant: (i) line-scans of relative element concentrations along the scanned line; (ii) "dot-maps" (images of presence/absence) at a certain energy level specific to the element under detection and; (iii) cumulative computer maps that can image low resolution maps of different elements at the same time (P.N.de Aza *et al.*, 2003; S.Deb *et al.*, 2005). With reference to all methods of analysis including the basic histogram demonstrating the elemental identification of a sample, the accuracy and resolution of the resultant maps/peaks increases with the count rate and the time over which the data is collected. The technique can provide qualitative and semi-quantitative information (A.Cuneyt Tas *et al.*, 1997; H.Zeng *et al.*, 2000a; Q.Z.Chen *et al.*, 2004; S.Joschek *et al.*, 2000).

With regard to this study, the chemical composition of the ceramic surfaces was investigated by SEM-EDS obtaining semi-quantitative data using the energy dispersive X-ray analyser, EDS (INCA Energy 300 of Oxford Instruments Analytical Ltd UK) fitted to the Jeol JSM 6300 scanning electron microscope. The samples were prepared as for the SEM investigation. The analysis of the chemical composition was carried out with a resolution of approximately 1 μm^2 and an energy source of 10 keV at a working distance of 16 mm and probe current of 8 A. For a semi-quantitative evaluation it was assumed that the peak height is proportional to the mole fraction of an element. Both elemental dot-maps and line scans were obtained for direct chemical comparison in situ of the laser-modified and surrounding unmodified areas.

5.10 X-ray Microdiffraction

Although phase identification and the structural study of solid materials by X-ray diffraction is the most commonly used technique, if the area or the quantity of the sample is small (e.g. micrograms), it may be difficult or impossible to obtain useful XRD data in the lab. The major limiting factor of standard diffraction is the limited spatial resolution resultant of the cross-section of the X-ray beam dwelling in the range between hundreds and several microns (R.Cancedda *et al.*, 2007). The development of X-ray optics that can focus the beam in the sub-micrometer range has led to the use of X-ray microdiffraction, combining the standard X-ray diffraction with X-ray focusing optics to significantly improve spatial resolution. The analysis of non-homogeneous materials gains particular benefit as the structural properties can change on a micrometer scale. The tissue/implant interface of virtually any biomaterial study is one such example (A.Cedola *et al.*, 2004).

X-ray microdiffraction can be performed using a very bright X-ray beam, approximately 2-3 orders of magnitude brighter than a conventional sealed tube and a position sensitive detector. As the beam is significantly bright, it is useful to reduce its size, which is achieved by reducing the pinholes and slits. This allows very small regions of interest to be analysed (micro-diffraction) or small amounts of particles over a larger area to be analysed (dilute micro-diffraction). A curved position sensitive detector is excellent for rapid data collection and, over long data collection times, for detecting weak intensity diffraction peaks (C.Kirk *et al.*, 2004).

In the present research, X-ray microdiffraction was performed at the Department of Mineralogy, Natural History Museum (UK) using a Bede MicroSOURCE and INEL curved position sensitive detector employing $CuK\alpha_1$ radiation and two slits, one horizontal, one vertical to provide a 0.5 mm diameter pinhole. The pinhole served to reduce the beam size sufficiently and focus within the 1 mm laser processed widths upon the sample surfaces. The INEL CPS120 detector collected 120° of data with a step-width of 0.03° in a single snap shot. The samples analysed included a blank

unprocessed HA disc for comparison against processed HA areas with 1000 shots in SF_6 gas and the surrounding unprocessed areas in addition to processed HA areas with 1000 shots of NH_3 gas and the surrounding unprocessed areas.

Chapter 6 Results

6.1 Hydroxyapatite Synthesis

Powdered hydroxyapatite was produced by methods of: (i) conventional wet precipitation; (ii) microemulsion synthesis and; (iii) macroemulsion synthesis. Commercially wet precipitated hydroxyapatite powders, 'Apatec' and 'Plasmabiotal' were also used for comparative study, investigating the specific surface area and grain size of the powdered samples. The produced samples were freeze-dried for initial study against the commercial products to investigate the raw powder qualities and then all samples were thermally treated at 1200°C for 2 hours before further analysis and evaluating chemical stability.

6.1.1 Surface area analysis

Brunauer-Emmett-Teller (BET) surface area analysis of the as-prepared powders and after thermal treatment at 1200 °C for 2 hrs are tabulated in Table 6.1.

Table 6.1 Specific surface area (BET) and particle size of powders produced by different processing routes

HA Powder/Processing Route	Specific surface area +/- 5 /m^2/g	Specific surface area /m^2/g calcined	Average particle size /nm	Average particle size /nm calcined
'Plasmabiotal' HA	15	1	126	1371
'Apatec' HA	72	1	26	1759
Conventionally Precipitated	101	0.04	19	47468
Macroemulsion	148	1	13	1668
Microemulsion	170	1	11	1639

The average particle size for each powder sample corresponds to the relationship with (BET) specific surface area shown in Equation 6.1:

$$t = \frac{6}{(ps)}$$

(Equation 6.1)

where t is the average particle size in μm, p is the density in kg/m^3 and s is the specific surface area in m^2/g.(L.B.Kong *et al.*, 2002) Using the theoretical density of HA of 3.16 kg/m^3, the particle sizes have been calculated for each of the powders and shown in Table 6.1.(B.Kundu *et al.*, 2004; D.Tadic *et al.*, 2004)

The commercial grade 'Plasmabiotal' HA that was produced by 'bulk' wet chemical precipitation and oven dried featured the largest particle size followed by the premium grade 'Apatec' HA produced by the same processing route. The relationship between the average particle sizes produced by the different processing routes has been demonstrated in Figure 6.1.

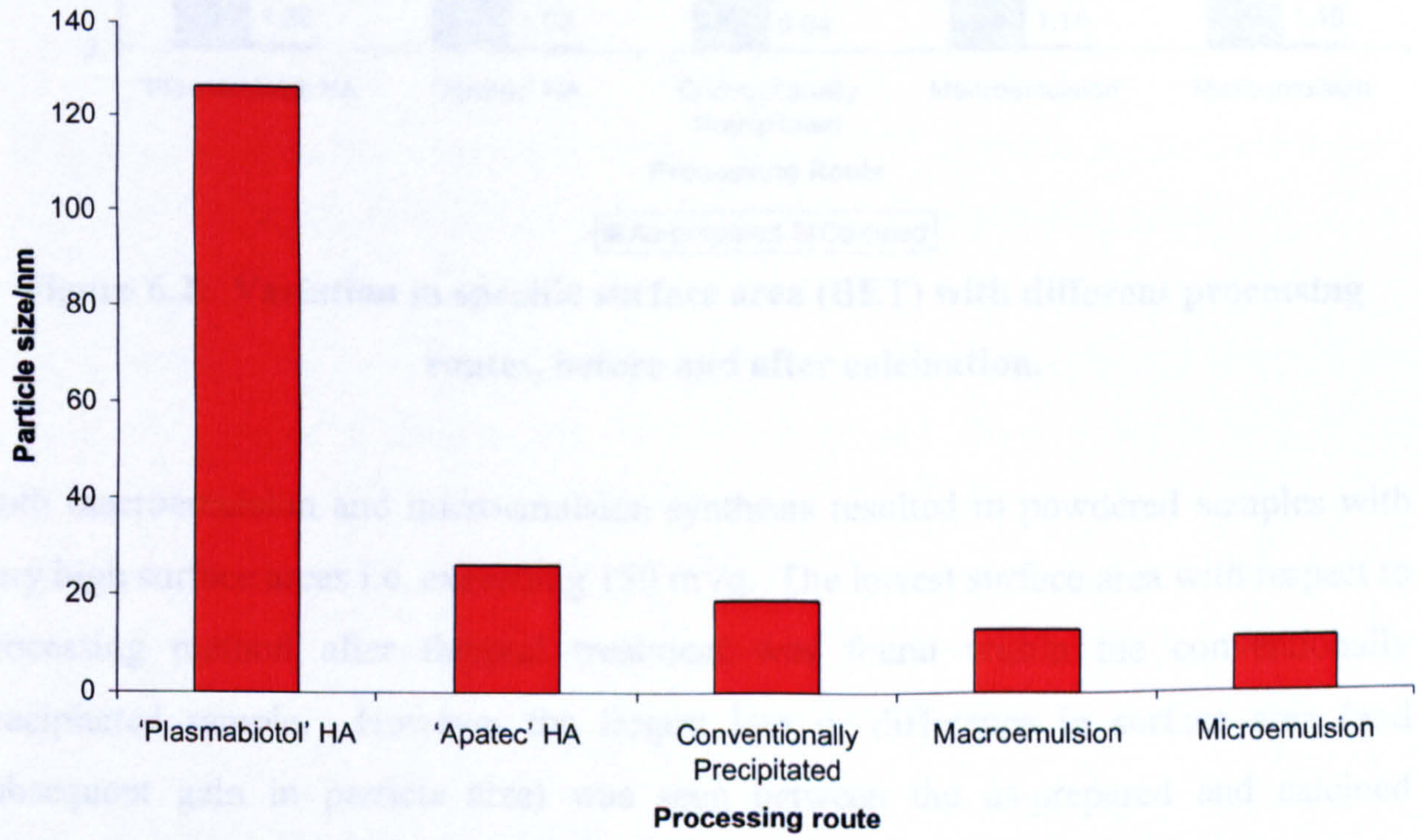

Figure 6.1: Variation in average particle size from different processing routes.

The commercially produced and oven-dried HA powders had much larger primary particle sizes than the produced powders that were freeze-dried reflected with low surface area values. Furthermore, the raw powders produced by emulsion technology had particle sizes far smaller and with greater surface area: volume ratio than the powders produced by wet chemical precipitation methods, depicted by the columnar part of Figure 6.2.

The relationship between the surface area of the as-prepared powders and the reduced surface area of the calcined powders is shown in Figure 6.2.

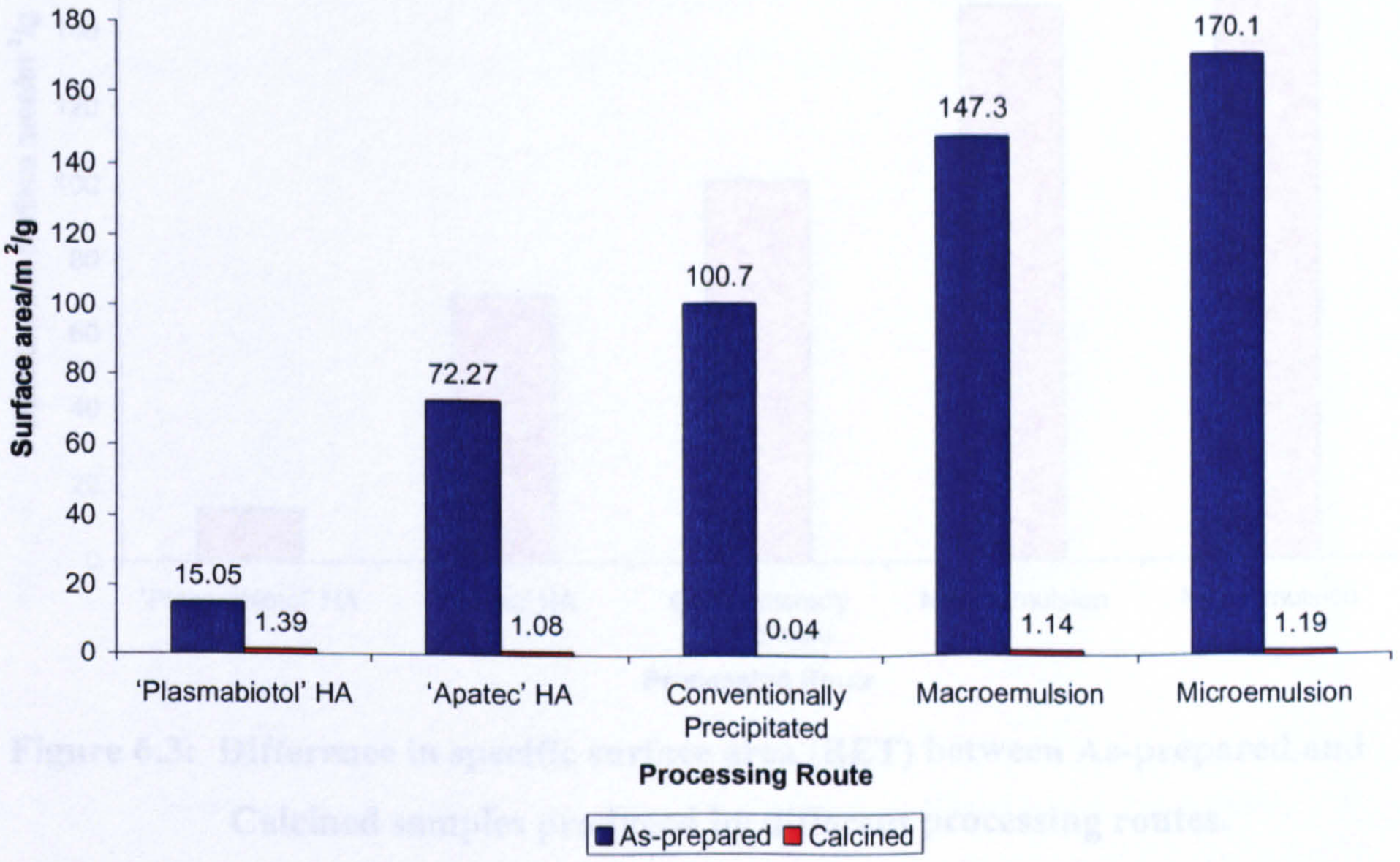

Figure 6.2: Variation in specific surface area (BET) with different processing routes, before and after calcination.

Both macroemulsion and microemulsion synthesis resulted in powdered samples with very high surface areas i.e. exceeding 150 m^2/g. The lowest surface area with respect to processing method after thermal treatment was found within the conventionally precipitated sample. However the largest loss or difference in surface area (and subsequent gain in particle size) was seen between the as-prepared and calcined powdered samples produced by emulsion synthesis as shown in Figure 6.3.

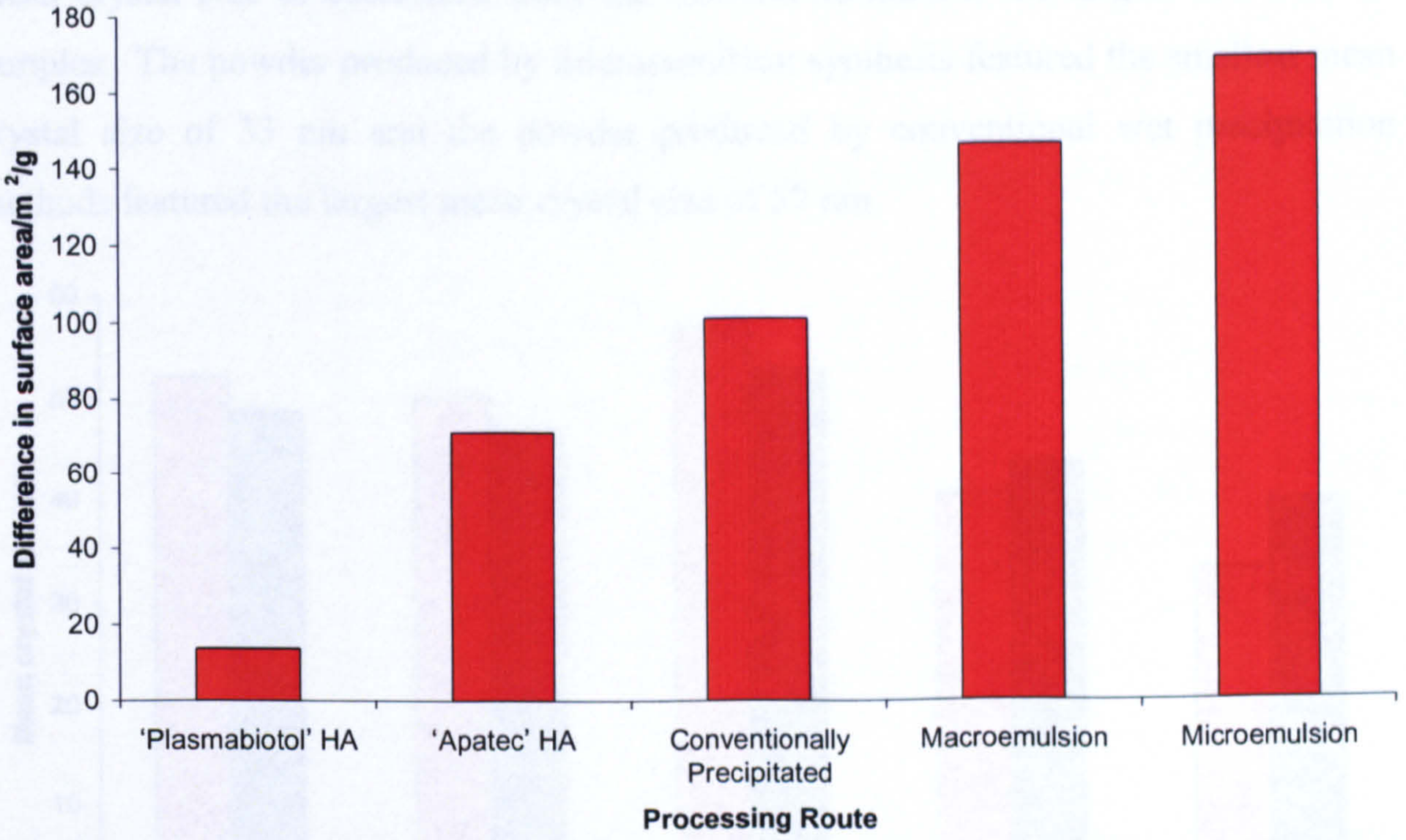

Figure 6.3: Difference in specific surface area (BET) between As-prepared and Calcined samples produced by different processing routes.

Consistent with the trend seen in the surface areas of the as-prepared samples, the pattern of decrease in surface area of the heat-treated samples shows that of the emulsion synthesised powders to be much higher than that of the samples produced by precipitation methods. Despite this the surface areas were still above 1 m^2/g. Interestingly the commercial grade 'Plasmabiotal' HA featured the largest calcined particulate surface area and therefore smallest particle size (Table 6.1).

6.1.2 Determination of crystal size

As previously introduced in Section 5.3.1, the use of Scherrer's formula applied to the X-ray diffraction patterns collected from the calcined HA powder samples synthesised by different routes, provided the calculated mean crystal size of each sample. Both the (002) peak found at 25.88° and the (211) peak found at 31.78° were used in order to improve accuracy. Both sets of data collaborate in the trend found with crystal sizes respective to processing method, although the sizes differ slightly between the two sets of data. Portrayed in Figure 6.4, the results collaborate with the same trend found for the powder particle sizes determined from BET surface area analysis in that the mean crystal sizes of the powders produced by wet chemical precipitation are larger than that of the powders produced by emulsion synthesis. However, whereas the powder particle size of the conventionally precipitated HA is smaller than than those featured in the 'Apatec' and 'Plasmabiotal' samples as determined from BET surface area analysis, the

mean crystal size as calculated from the Scherrer formula is the largest of all of the samples. The powder produced by microemulsion synthesis featured the smallest mean crystal size of 33 nm and the powder produced by conventional wet precipitation methods featured the largest mean crystal size of 57 nm.

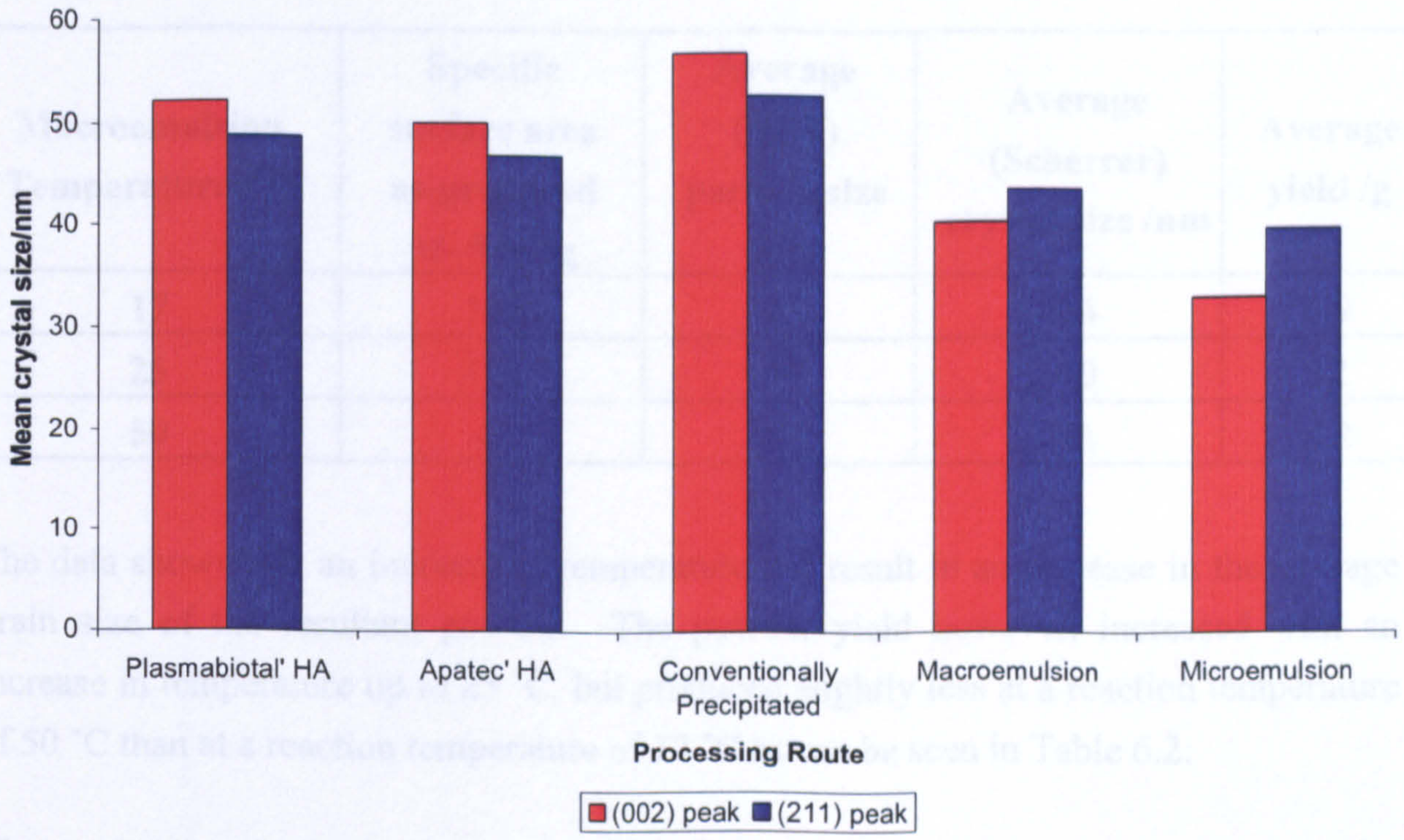

Figure 6.4: Mean crystal size of HA powder synthesised by different routes as calculated with Scherrer formula.

6.1.3 Macroemulsion synthesis (Emulsion technology)

Due to the lengthy production period required for emulsion synthesis of HA, the effect of temperature on macroemulsion synthesis was investigated with respect to the yield of nanocrystalline HA in order to improve the efficiency of the process rather than alter the particle size of the product. The initial microemulsion system that was employed to produce nanocrystalline HA powder produced less than 2 g of final powder in each case, which was not considered enough to award it as a viable or efficient method of production. At least 4 g was required for further experimental work in the processed disc form (Section 5.2.2). Macroemulsion synthesis provided at least twice the amount that microemulsion produced and BET surface area analysis established that the powder grains were nanosized. An ageing step of 24 hrs was introduced to allow the phases to separate improving the accuracy of the filtering step to increase the yield further. Temperatures of 17 °C, 25 °C and 50 °C were then maintained throughout synthesis

until the filtering step (Section 5.1.5) and the slurry products freeze-dried. The specific surface areas were established by BET surface area analysis as shown in Table 6.2:

Table 6.2 Powder properties of macroemulsion synthesised HA at different temperatures

Macroemulsion Temperature /°C	Specific surface area as-prepared +/- 5 m^2/g	Average (BET) particle size /nm	Average (Scherrer) crystal size /nm	Average yield /g
17	148	13	34	6.9
25	118	16	40	12
50	43	45	43	5.2

The data shows that an increase in temperature did result in an increase in the average grain size of the resultant powder. The powder yield however, increased with an increase in temperature up to 25 °C, but produced slightly less at a reaction temperature of 50 °C than at a reaction temperature of 17 °C as can be seen in Table 6.2:

The results suggest that in order to increase the yield of production, the slight gain in the grain size (< 4nm) by production at 25 °C would be acceptable due to the production yield being almost double that of the system maintained at 17 °C reaction temperature.

6.2 XRD Characterisation

The following XRD traces (Figure 6.5) confirmed that in all cases of synthesis phase pure hydroxyapatite (JCPDS pattern 09-0432) was almost exclusively present. A similar result was shown in the XRD traces obtained for commercial grade 'Plasmabiotal' HA and premium grade phase pure 'Apatec' HA powders. However, due to the nano-size of the of the as-prepared powders and the subsequent crystallites formed after freeze-drying, the initial XRD traces obtained featured very broad peaks creating difficulty in the estimation of the exact phase compositions. After calcination in air at 1200 °C for 2 hrs, reproducing a similar state similar to the green body material form, the XRD patterns were more informative due to the increased crystallite size. Collaborative confirmation of phase purity after powder processing into disc form prepared for laser experimentation is provided by the XRD trace (Figure 6.22(c) and 6.24(c)) of a sintered HA disc.

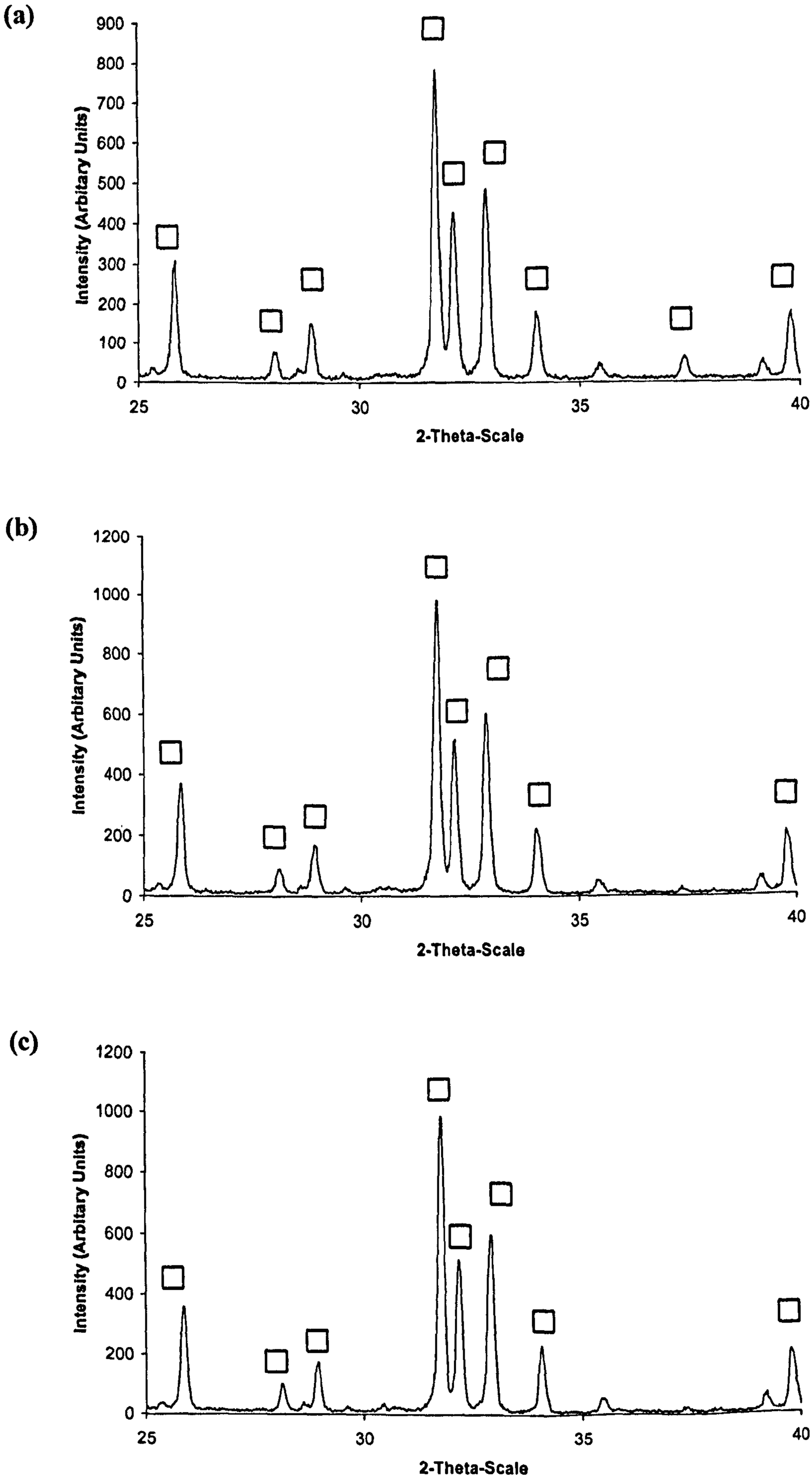

Figure 6.5: XRD traces for HA powders as-prepared and calcined at 1200 °C. (a) Precipitated HA, (b) 'Plasmabiotal' HA, (c) 'Apatec' HA. (Key – □ HA, JCPDS pattern 09-0432)

The sharp intense peaks in all of the patterns showed the powdered samples to be crystalline. No secondary phases were detected demonstrating thermal and chemical stability at the high calcination temperature of 1200 °C.

A small amount of 'Calcite' $CaCO_3$ was detected in the calcined sample produced at 17 °C (Figure 6.6(b)) and a small amount of 'Whitlockite' (TCP) $Ca_3(PO_4)_2$ was detected in the calcined sample produced at 50 °C (Figure 6.6(d)).

(a)

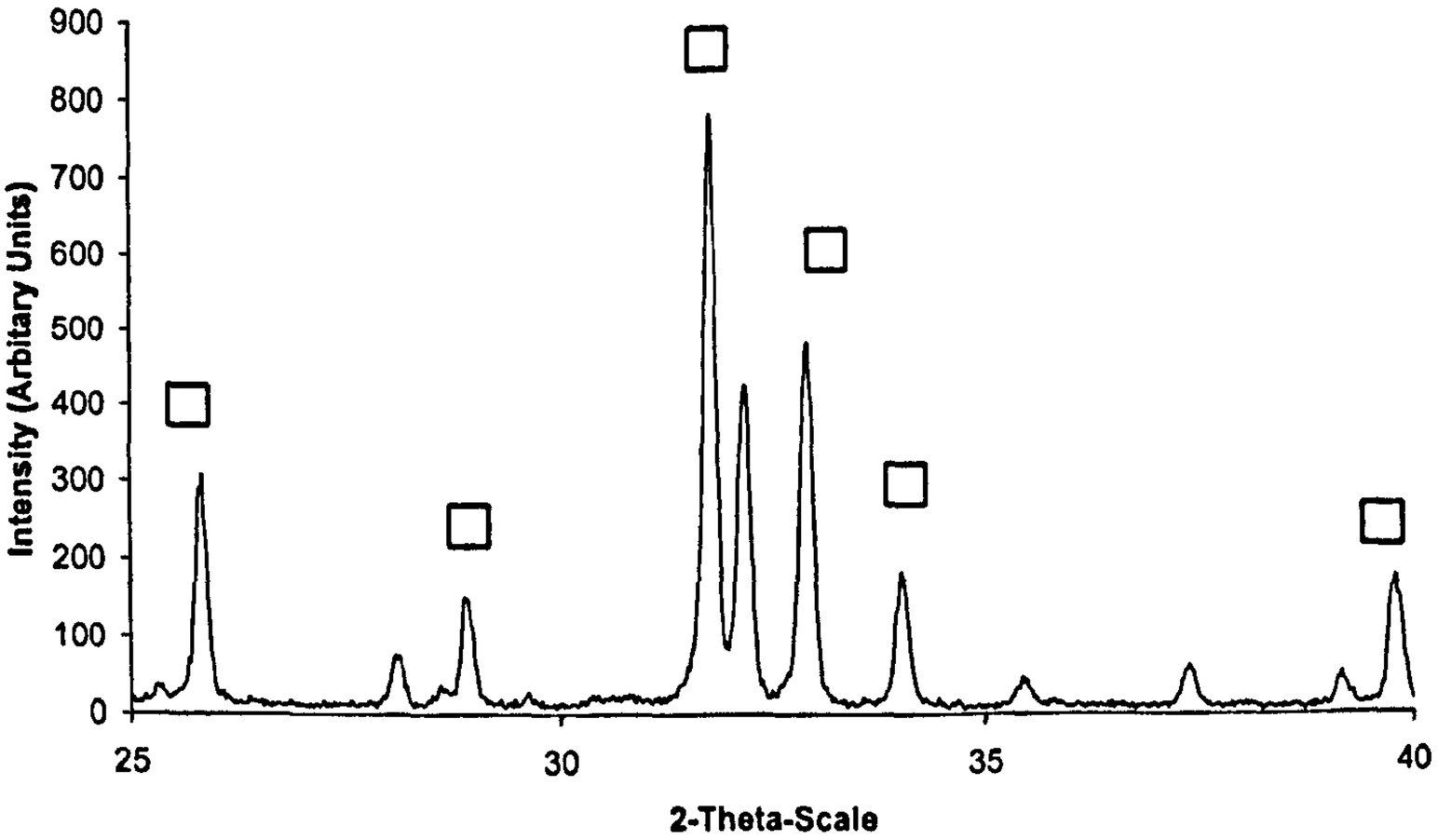

(b)

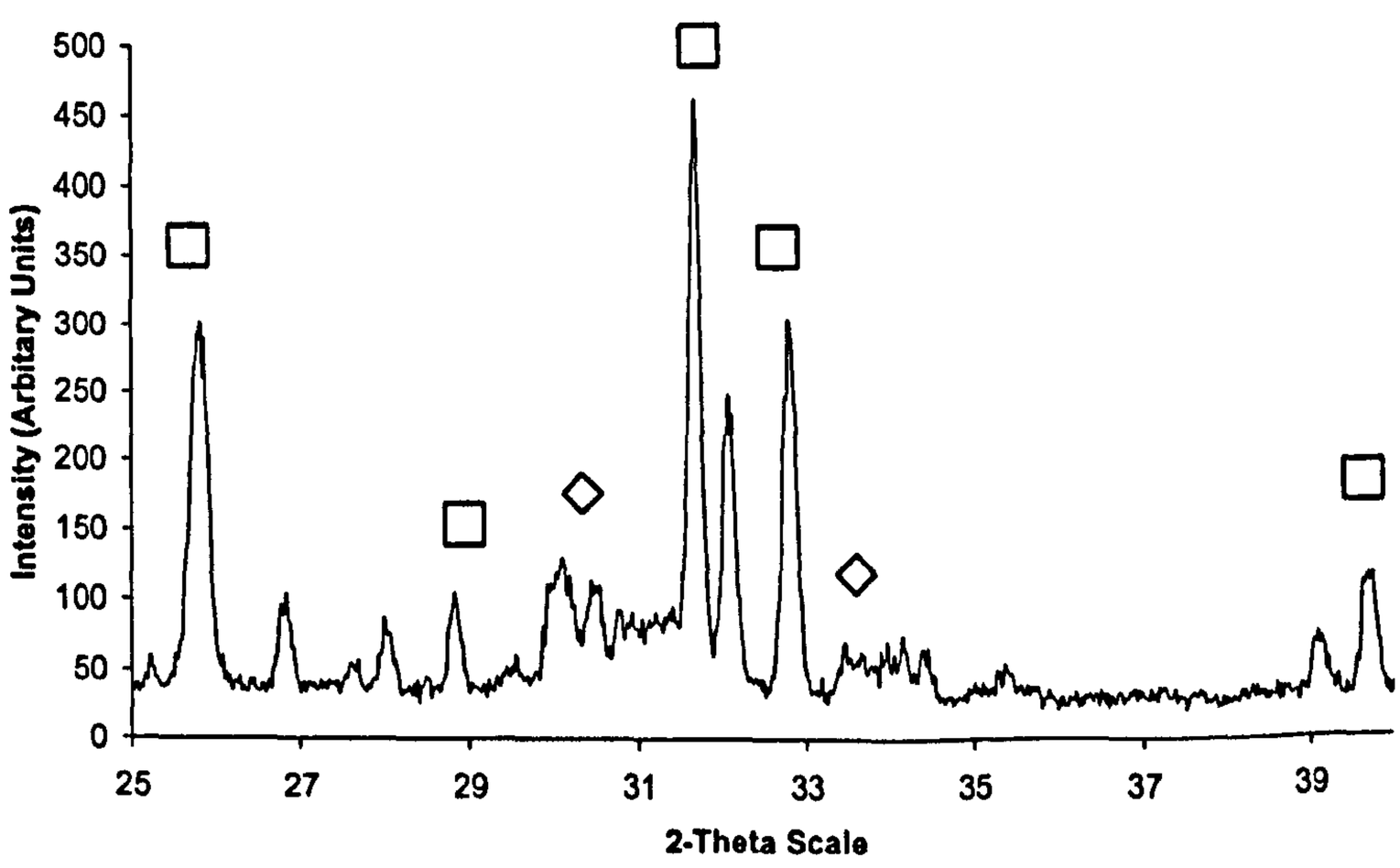

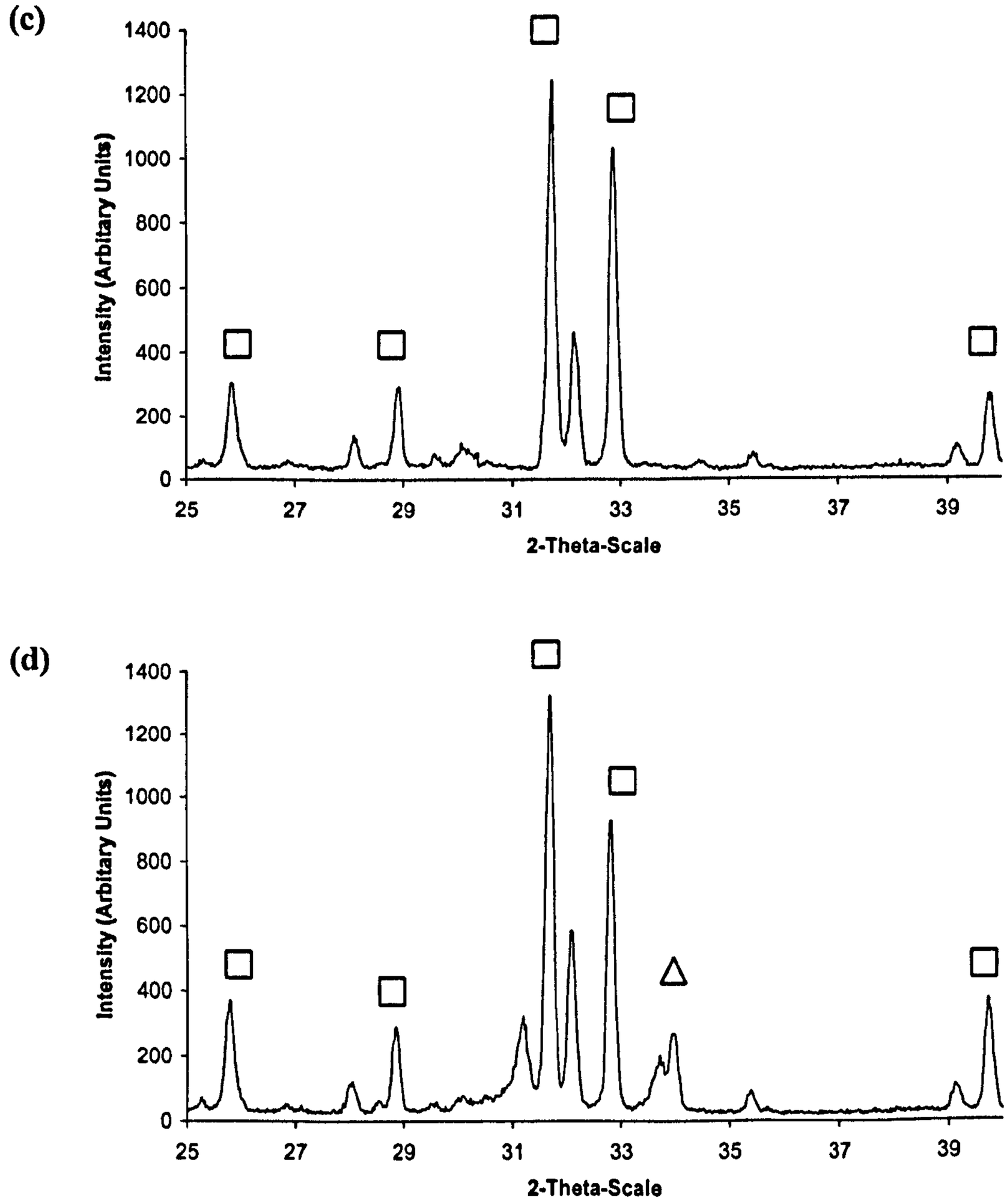

Figure 6.6: XRD traces of emulsion synthesised HA calcined at 1200 °C. (a) Microemulsion, (b) Macroemulsion at 17 °C, (c) Macroemulsion at 25 °C, (d) Macroemulsion at 50 °C. (Key – □ HA, ◇ Calcite and Δ TCP)

However looking at the corresponding uncalcined traces, the phases were apparent prior to calcination and are not a result of thermal decomposition but likely to be resultant of pH fluctuations during the chemical addition into the emulsion system which was approximately pH 9 prior to addition of ammonia solution. Subsequently a greater amount of ammonia was required to maintain a pH < 10.5 in the emulsion systems for HA production than in the conventional precipitation methods. Furthermore, in the case of the macroemulsion at 17 °C the production of calcite could be resultant of an incomplete reaction due to the reaction proceeding at a slower rate corresponding to the

lower temperature when compared to the other systems. The opposite could be therefore suggested for the macroemulsion at 50 °C where the reaction rate may have proceeded at a rate that proved to be too fast for adequate or sufficient control of the pH by the rate of addition of ammonia.

6.3 Density

Sintered discs were produced from commercial HA powders ('Apatec' and 'Plasmabiotal') in addition to conventionally precipitated and macroemulsion synthesised HA powders (Section 5.2.2). The microemulsion system employed did not yield enough HA powder to facilitate disc production and any further investigation. The average density and porosity of 6 discs of each type of HA powder was calculated as shown in Table 6.3. All initially pressed discs prior to sintering had the same dimensions and statistics with particle size being the only obvious differing factor between disc samples.

Table 6.3 Details of density and porosity of prepared discs

	Unsintered 'Plasmabiotal' disc	**'Plasmabiotal'**	**'Apatec'**	**Conventionally Precipitated**	**Macro-emulsion**
Weight/kg	4.5×10^{-3}	4.37×10^{-3}	4.16×10^{-3}	4.14×10^{-3}	4.13×10^{-3}
Volume/m^3	3.89×10^{-6}	1.76×10^{-6}	1.56×10^{-6}	1.32×10^{-6}	1.35×10^{-6}
Density/kg/m^3	1156.81	2482.95	2676.67	3136.36	3059.26
Porosity/%	63.4	21.5	15.5	0.63	3.48

In all cases during the thermal consolidation process, the discs decreased in volume and increased in density (subsequently decreasing in percentage of porosity) as was expected. The porosity of each sample disc demonstrated a corresponding relationship to the particle size of the initial powder as shown when comparing Figure 6.7 (Chart demonstrating the percentage porosity of the sintered discs produced by HA powders processed different processing methods) by with Figure 6.1 (Chart demonstrating the initial particle size of the as-prepared HA powders). The observed trend portrayed that an increase in initial powder particle size can be associated with an increase in percentage porosity in the sintered disc product corresponding with a decrease in sintered disc density and a decrease in the volumetric difference between the unsintered and sintered disc. The sintered product produced with conventionally precipitated HA

powder provided an exception to the observed trend featuring the lowest percentage porosity and highest sintered density despite the initial as-prepared powder featuring a larger particle size than the macroemulsion synthesised powder that produced a sintered product of higher porosity.

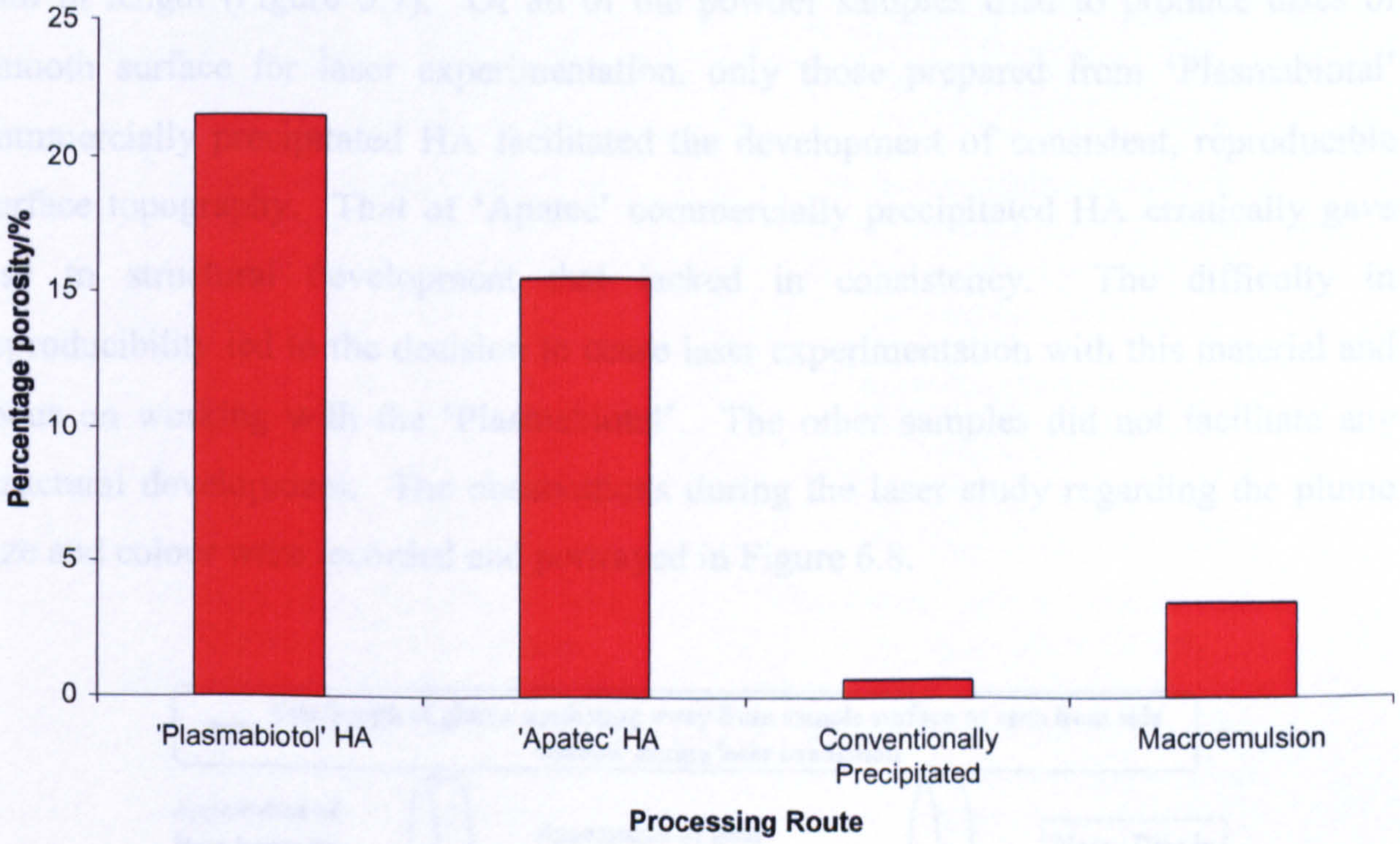

Figure 6.7: Percentage porosity of HA sintered discs.

6.4 Laser processing of hydroxyapatite

6.4.1 Processing parameters

Using a femtosecond XeCl excimer laser (308 nm, ~180 mv or 0.072 J per pulse, 20 ns pulse width) focused onto sintered HA discs, different types of structural topography were created using different laser fluencies in the presence of process gases listed in Table 6.8. The lasing conditions were adapted from previous work resulting in ordered arrays of cones or spikes on single crystal silicon wafers, with the aim of producing similar surface structures of regular order on HA (K.W.Kolasinski, 2004). Images obtained from previous laser surface modification of HA failed to demonstrate the development of completely regular or uniform structures with ordered spacing. In order to provide the conditions used to create structure the energy density or laser fluence has been calculated according to:

$$\frac{\text{beam energy}}{\text{spot size area}} = \text{kJ/m}^2$$

(Equation 6.2)

due to the focal length varying the spot size but the beam energy being constant.

Simple trial and error was used to establish the working conditions and in each successful case, 6 samples were produced and each with 6 modified surface strips of 10 mm in length (Figure 5.7). Of all of the powder samples used to produce discs of smooth surface for laser experimentation, only those prepared from 'Plasmabiotal' commercially precipitated HA facilitated the development of consistent, reproducible surface topography. That of 'Apatec' commercially precipitated HA erratically gave rise to structural development that lacked in consistency. The difficulty in reproducibility led to the decision to cease laser experimentation with this material and focus on working with the 'Plasmabiotal'. The other samples did not facilitate any structural development. The observations during the laser study regarding the plume size and colour were recorded and portrayed in Figure 6.8.

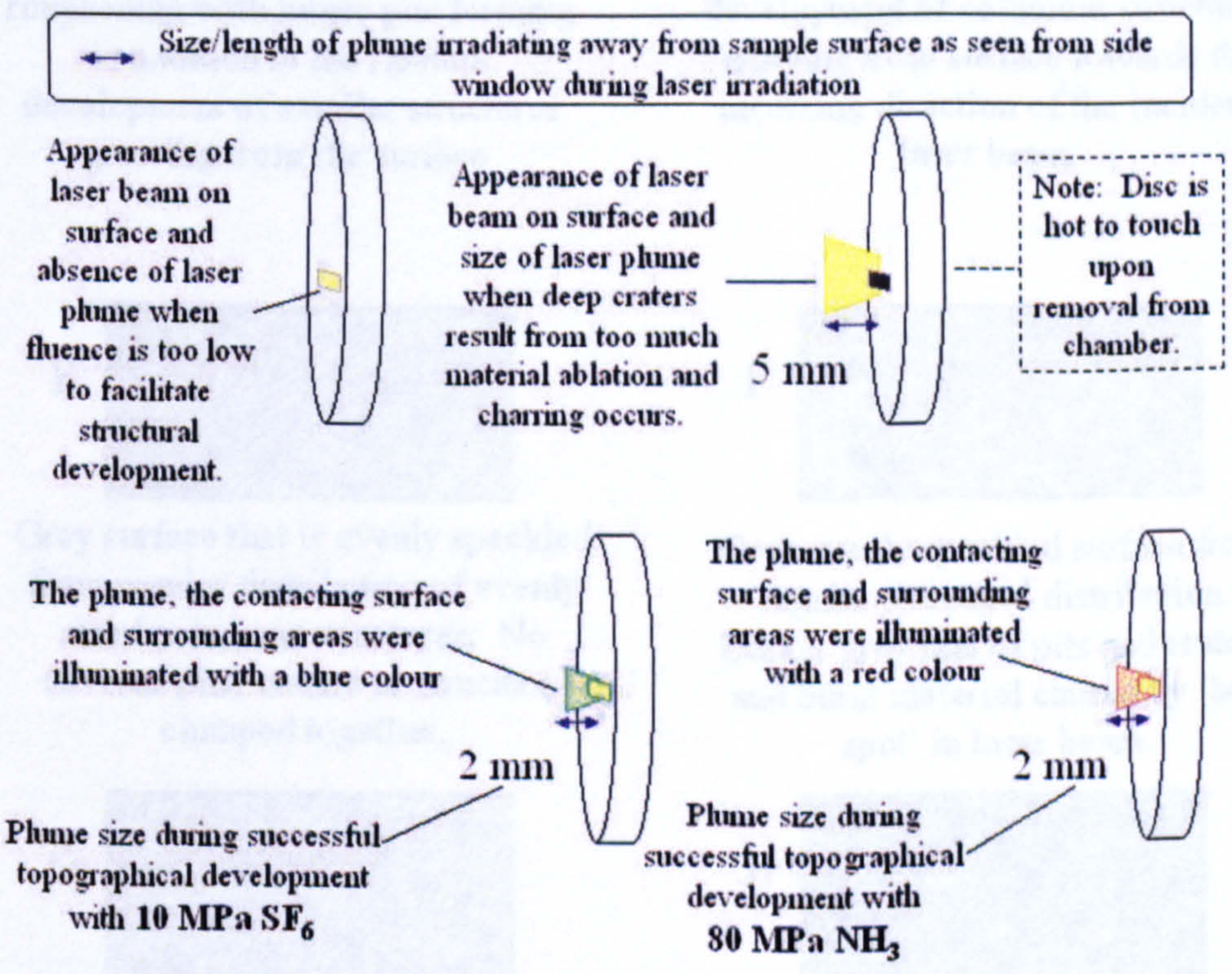

Figure 6.8: Diagram of observations made during the laser study.

Using light microscopy, the appearance of the laser irradiated spots was recorded for each set of working conditions using SF_6 and NH_3 gas. The modified appearance in each case has been recreated and categorised in Figures 6.9 and 6.10 and are referred to in Tables 6.4, 6.5, 6.6 and 6.7. In each case the laser was allowed to administer 1000 pulses whilst observations were made through the side window of the processing chamber. The appearance of the surface after each exposure was used to determine the

gas pressure and focal length required in each case to produce the most uniformly developed and evenly distributed type of surface topography. The recorded details and calculated laser fluencies are displayed in Tables 6.4, 6.5, 6.6 and 6.7.

A 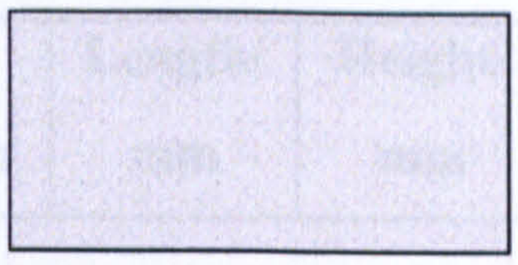

Slight discolouration of original white surface. No visible structural development or change to the surface.

B 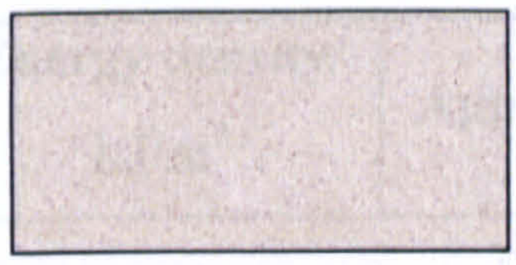

Slight roughening of surface. Change in shade due to presence of random pitting as material is ablated from surface.

C 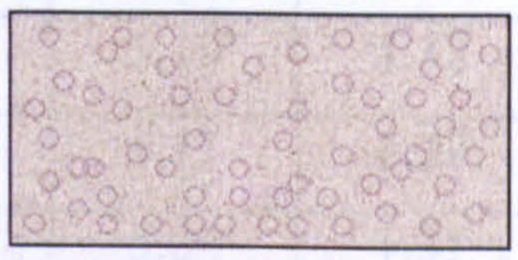

Surface colour slightly grey and speckled. Obvious surface roughening with larger pits forming in addition to the random development of smaller structures growing from the surface.

D 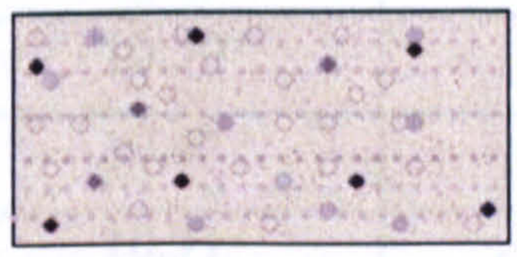

Grey surface colour speckled with darker spots due to further development of columnar structures growing from surface towards the incoming direction of the incident laser beam.

E 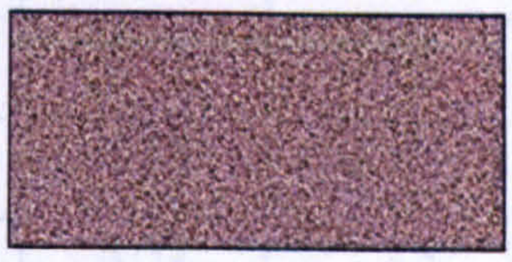

Grey surface that is evenly speckled from regular distribution of evenly sized columnar structures. No obvious pits, craters or structures clumped together.

F 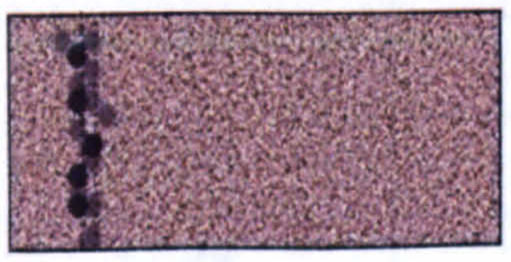

Grey evenly speckled surface from regular structural distribution. Darker grey line of pits and craters and burnt material caused by 'hot spot' in laser beam.

G 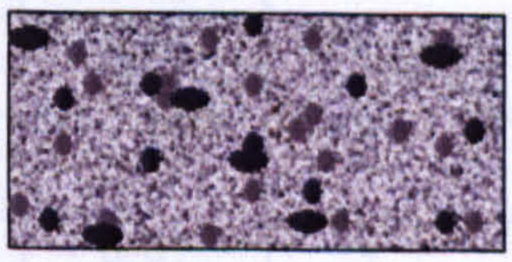

Grey surface with irregular placement of darker pits and craters due to too much material removal. Clumping of columnar structures in places from melting of surface.

H 

Dark grey surface uneven in texture and colour. Deep craters scattered randomly across from too much material removal. No visible columnar structures. Surrounding area appears charred and black.

Figure 6.9: Categorised appearance of laser irradiated 'spots' during preliminary investigation with SF_6.

The first set of results gathered from the initial studies using SF_6 gas are shown in Table 6.4. From the post irradiated surface appearance it became apparent that the lower gas

pressures facilitated the development of surface topography and so the second part of the study focused on gas pressures below 25 MPa as shown in Table 6.5.

Table 6.4 First set of results from preliminary laser study with SF_6

Focal length/mm	Length/ mm	Height/ mm	Spot size area/mm^2	Energy density/ kJ/m^2	Appearance
Initial stage					
Pressure/MPa			**80**		
22	5.35	1.34	7.17	10.04	A
21	5.27	1.33	7.01	10.27	A
20	5.19	1.32	6.85	10.50	A
19	5.11	1.32	6.75	10.67	A
18	5.04	1.31	6.6	10.91	A
17	4.98	1.31	6.52	11.04	A
16	4.9	1.3	6.37	11.30	A
15	4.84	1.3	6.29	11.44	A
14	4.77	1.3	6.2	11.61	A
13	4.71	1.29	6.08	11.85	A
12	4.65	1.29	6	12.00	A
11	4.59	1.28	5.88	12.25	A
10	4.52	1.28	5.79	12.44	A
Pressure/MPa			**70**		
22	5.23	1.32	6.9	10.43	A
21	5.15	1.31	6.75	10.67	A
20	5.08	1.31	6.65	10.82	A
19	4.99	1.31	6.54	11.01	A
18	4.92	1.3	6.4	11.26	A
17	4.85	1.3	6.31	11.42	A
16	4.77	1.29	6.15	11.70	A
15	4.7	1.29	6.06	11.88	A
14	4.64	1.28	5.94	12.12	A
13	4.58	1.28	5.86	12.28	A
12	4.52	1.28	5.79	12.44	A
11	4.46	1.27	5.66	12.71	A

10	4.4	1.27	5.59	12.88	A
Pressure/MPa			**60**		
22	5.14	1.31	6.73	10.69	A
21	5.08	1.3	6.6	10.90	A
20	4.99	1.3	6.49	11.1	A
19	4.92	1.29	6.35	11.34	A
18	4.84	1.29	6.24	11.53	A
17	4.77	1.28	6.11	11.79	A
16	4.71	1.28	6.03	11.94	A
15	4.66	1.27	5.92	12.17	A
14	4.58	1.27	5.82	12.38	A
13	4.52	1.27	5.74	12.54	A
12	4.45	1.26	5.61	12.84	A
11	4.39	1.26	5.53	13.01	A
10	4.33	1.25	5.41	13.30	A
Pressure/MPa			**50**		
22	5.04	1.3	6.55	10.99	A
21	4.97	1.3	6.46	11.14	A
20	4.89	1.29	6.31	11.41	A
19	4.81	1.28	6.16	11.69	A
18	4.72	1.28	6.04	11.92	A
17	4.66	1.28	5.96	12.07	A
16	4.6	1.27	5.84	12.32	A
15	4.53	1.27	5.75	12.51	A
14	4.48	1.26	5.64	12.76	A
13	4.4	1.26	5.54	12.99	A
12	4.32	1.26	5.44	13.23	A
11	4.26	1.25	5.33	13.52	A
10	4.2	1.25	5.25	13.71	B
Pressure/MPa			**40**		
22	4.86	1.29	6.27	11.48	A
21	4.81	1.28	6.16	11.69	A
20	4.75	1.28	6.08	11.84	A
19	4.7	1.27	5.97	12.06	A

18	4.62	1.27	5.87	12.27	A
17	4.57	1.27	5.8	12.40	A
16	4.51	1.26	5.68	12.67	A
15	4.47	1.26	5.63	12.78	A
14	4.43	1.25	5.54	13.00	A
13	4.39	1.25	5.49	13.12	B
12	4.35	1.24	5.39	13.35	B
11	4.3	1.24	5.33	13.50	B
10	4.24	1.24	5.26	13.69	B
Pressure/MPa			**30**		
22	4.74	1.28	6.07	11.87	A
21	4.69	1.27	5.96	12.09	A
20	4.63	1.27	5.88	12.24	A
19	4.58	1.26	5.77	12.48	B
18	4.52	1.26	5.7	12.64	B
17	4.44	1.26	5.59	12.87	B
16	4.38	1.25	5.48	13.15	B
15	4.31	1.25	5.39	13.36	B
14	4.24	1.24	5.26	13.69	C
13	4.19	1.24	5.2	13.86	C
12	4.13	1.23	5.08	14.17	C
11	4.08	1.23	5.02	14.35	C
10	4.03	1.22	4.92	14.64	D
Pressure/MPa			**20**		
22	4.6	1.26	5.8	12.42	B
21	4.54	1.25	5.68	12.69	C
20	4.49	1.25	5.61	12.83	C
19	4.42	1.24	5.48	13.14	C
18	4.38	1.24	5.43	13.26	C
17	4.33	1.23	5.33	13.52	C
16	4.24	1.23	5.22	13.81	C
15	4.17	1.22	5.09	14.15	D
14	4.11	1.22	5.01	14.36	D
13	4.06	1.21	4.91	14.67	D

12	4	1.21	4.84	14.88	D
11	3.93	1.2	4.72	15.27	F
10	3.88	1.2	4.66	15.46	F
Pressure/MPa			**10**		
22	4.34	1.24	5.38	13.38	D
21	4.28	1.24	5.3	13.57	D
20	4.23	1.23	5.2	13.84	D
19	4.19	1.22	5.11	14.09	D
18	4.16	1.22	5.08	14.19	D
17	4.12	1.21	4.99	14.44	D
16	4.05	1.2	4.86	14.81	E
15	3.97	1.19	4.72	15.24	F
14	3.92	1.19	4.66	15.43	G
13	3.87	1.18	4.57	15.77	G
12	3.83	1.17	4.48	16.07	H
11	3.79	1.17	4.43	16.24	H
10	3.75	1.16	4.35	16.55	H

For the second and final stages of the preliminary study using SF_6 gas, the focal length was adjusted by 0.5 mm increments so as to evaluate smaller changes in the energy density or laser fluence and improve accuracy in establishing the range of laser fluencies over which surface structural formation would take place.

Table 6.5 Second set of results from preliminary laser study with SF_6

Focal length/mm	Length/ mm	Height/ mm	Spot size area/mm^2	Energy density/ kJ/m^2	Appearance
Second stage					
Pressure/MPa			**25**		
18	4.45	1.25	5.56	12.94	B
17.5	4.42	1.25	5.52	13.03	B
17	4.4	1.24	5.46	13.2	B
16.5	4.37	1.24	5.42	13.29	B
16	4.32	1.24	5.36	13.44	C
15.5	4.3	1.23	5.29	13.61	C

15	4.28	1.23	5.26	13.68	C
Pressure/MPa			**20**		
18	4.38	1.24	5.43	13.26	C
17.5	4.35	1.24	5.39	13.35	C
17	4.33	1.23	5.33	13.52	C
16.5	4.29	1.23	5.28	13.64	C
16	4.24	1.23	5.22	13.81	C
15.5	4.21	1.22	5.14	14.02	C
15	4.17	1.22	5.09	14.15	D
Pressure/MPa			**15**		
18	4.25	1.23	5.23	13.77	C
17.5	4.23	1.22	5.16	13.95	C
17	4.2	1.22	5.12	14.05	C
16.5	4.17	1.22	5.09	14.15	D
16	4.17	1.21	5.05	14.27	D
15.5	4.15	1.21	5.02	14.34	D
15	4.12	1.21	4.99	14.44	D
Pressure/MPa			**10**		
18	4.16	1.22	5.08	14.19	D
17.5	4.14	1.21	5	14.37	D
17	4.12	1.21	4.99	14.44	D
16.5	4.09	1.21	4.95	14.55	E
16	4.05	1.2	4.86	14.81	E
15.5	4	1.2	4.8	15.00	E
15	3.97	1.19	4.72	15.24	F
Pressure/MPa			**7.5**		
18	4.1	1.2	4.92	14.63	D
17.5	4.07	1.2	4.88	14.74	D
17	4.04	1.19	4.81	14.98	F
16.5	4	1.19	4.76	15.13	G
16	3.96	1.19	4.71	15.28	G
15.5	3.9	1.18	4.6	15.65	G
15	3.87	1.17	4.53	15.90	H
Pressure/MPa			**5**		

18	4.03	1.19	4.79	15.01	G
17.5	4.01	1.19	4.77	15.09	G
17	3.96	1.18	4.67	15.41	G
16.5	3.92	1.18	4.63	15.57	G
16	3.87	1.17	4.53	15.92	H
15.5	3.82	1.17	4.47	16.11	H
15	3.75	1.16	4.35	16.55	H
Final stage					
Pressure/MPa			**12.5**		
16.5	4.21	1.23	5.18	13.90	D
16	4.17	1.22	5.09	14.15	D
15.5	4.14	1.22	5.05	14.26	D
15	4	1.21	4.8	14.88	D
Pressure/MPa			**10**		
16.5	4.09	1.21	4.95	14.55	E
16	4.05	1.2	4.86	14.81	E
15.5	4	1.2	4.8	15.00	E
15	3.97	1.19	4.72	15.24	F
Pressure/MPa			**7.5**		
16.5	4	1.19	4.76	15.13	G
16	3.96	1.19	4.71	15.28	G
15.5	3.9	1.18	4.6	15.65	G
15	3.87	1.17	4.53	15.90	H

From the results shown in Table 6.5 it was determined that the development of surface topography took place using 10 MPa SF_6 gas at laser fluencies within the range of 14.50 to 15.20 MPa. The most uniformly developed surface topography was observed after laser irradiation at an energy density of 14.81 kJ/m^2 as summarised in Table 6.8.

The first set of results gathered from the initial studies using NH_3 gas are shown in Table 6.6. From the post irradiated surface appearance it became apparent that high gas pressures facilitated the development of surface topography and so the second part of the study focused on gas pressures above 65 MPa as shown in Table 6.7.

A 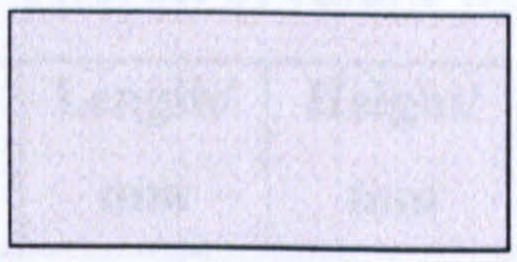

Slight discolouration of original white surface. No visible structural development or change to the surface.

B 

Slight roughening of surface. Change in shade due to presence of random pitting as material is ablated from surface.

C 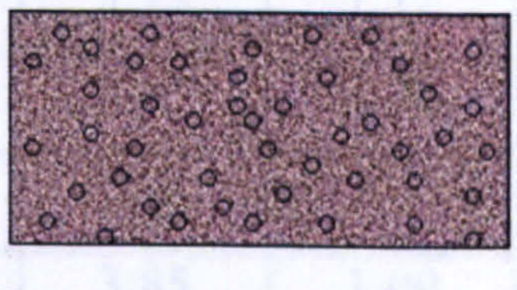

Surface colour grey and speckled. Obvious surface roughening with larger pits forming in addition to the random development of smaller structures growing from the surface.

D 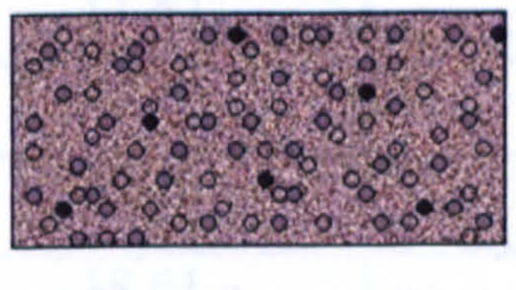

Grey surface colour speckled with darker spots due to further development of porous structures growing from surface towards the incoming direction of the incident laser beam.

E 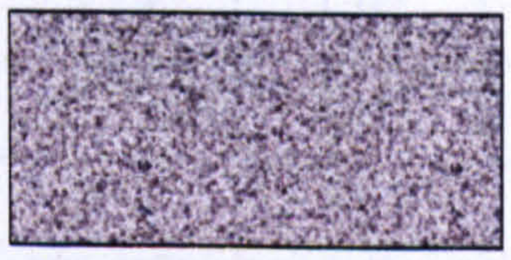

Grey surface that is evenly speckled from regular distribution of evenly sized porous boulder-like structures. No obvious structures clumped together or enlarged pores and craters.

F 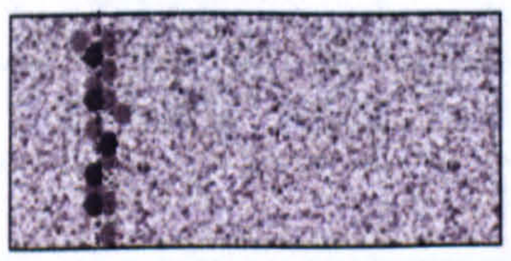

Grey evenly speckled surface from regular structural distribution. Darker grey line of pits and craters and burnt material caused by 'hot spot' in laser beam.

G 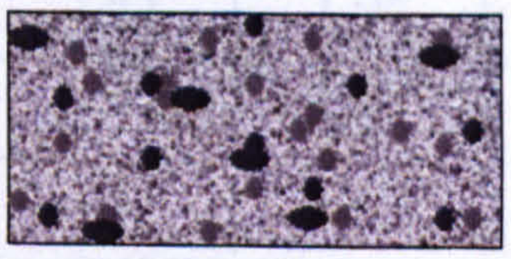

Grey surface with irregular placement of large darker pits and craters due to too much material removal. Clusters of boulder-like structures in places from melting of surface.

H 

Dark grey surface uneven in texture and colour. Deep craters scattered randomly across from too much material removal. No visible structures. Surrounding area appears charred and black.

Figure 6.10: Categorised appearance of laser irradiated 'spots' during preliminary investigation with NH_3.

The irradiated surfaces produced with NH_3 were distinctly different in texture and feature to those produced using SF_6 gas when observed under a light microscope as described in Figure 6.10.

Table 6.6 First set of results from preliminary laser study with NH_3

Focal length/mm	Length/ mm	Height/ mm	Spot size area/mm^2	Energy density/ kJ/m^2	Appearance
Initial stage					
Pressure/MPa			**80**		
22	3.78	1.13	4.27	16.86	D
21	3.73	1.12	4.18	17.23	D
20	3.68	1.11	4.08	17.63	D
19	3.6	1.1	3.96	18.18	E
18	3.55	1.09	3.87	18.61	F
17	3.49	1.09	3.80	18.93	F
16	3.42	1.08	3.69	19.49	G
15	3.36	1.08	3.63	19.84	G
14	3.3	1.07	3.53	20.39	G
13	3.24	1.07	3.47	20.77	G
12	3.19	1.06	3.38	21.29	G
11	3.12	1.05	3.28	21.98	H
10	3.07	1.05	3.22	22.34	H
Pressure/MPa			**70**		
22	3.48	1.09	3.79	18.98	H
21	3.43	1.08	3.7	19.44	H
20	3.38	1.08	3.65	19.72	H
19	3.33	1.07	3.56	20.21	H
18	3.29	1.06	3.49	20.65	H
17	3.22	1.06	3.41	21.09	H
16	3.15	1.05	3.31	21.77	H
15	3.09	1.05	3.24	22.19	H
14	3.03	1.04	3.15	22.85	H
13	2.97	1.03	3.06	23.54	H
12	2.9	1.03	2.99	24.10	H
11	2.84	1.02	2.9	24.86	H
10	2.78	1.02	2.84	25.39	H
Pressure/MPa			**60**		
22	3.23	1.06	3.42	21.03	H

21	3.17	1.06	3.36	21.42	H
20	3.11	1.05	3.27	22.05	H
19	3.05	1.05	3.2	22.48	H
18	2.98	1.04	3.1	23.23	H
17	2.9	1.04	3.02	23.87	H
16	2.84	1.03	2.93	24.61	H
15	2.77	1.03	2.85	25.24	H
14	2.7	1.02	2.75	26.14	H
13	2.63	1.01	2.66	27.11	H
12	2.57	1.01	2.6	27.74	H
11	2.51	1	2.51	28.69	H
10	2.46	1	2.46	29.27	H
Pressure/MPa			**50**		
22	2.89	1.04	3.01	23.96	H
21	2.81	1.04	2.92	24.64	H
20	2.75	1.03	2.83	25.42	H
19	2.69	1.03	2.77	25.99	H
18	2.62	1.02	2.67	26.94	H
17	2.55	1.01	2.58	27.96	H
16	2.48	1.01	2.5	28.74	H
15	2.4	1	2.4	30.00	H
14	2.34	1	2.34	30.77	H
13	2.28	0.99	2.26	31.9	H
12	2.22	0.98	2.18	33.09	H
11	2.15	0.98	2.11	34.17	H
10	2.09	0.97	2.03	35.52	H
Pressure/MPa			**40**		
22	2.57	1.02	2.62	27.47	H
21	2.51	1.02	2.56	28.12	H
20	2.44	1.01	2.46	29.22	H
19	2.38	1.01	2.40	29.95	H
18	2.32	1.01	2.34	30.73	H
17	2.25	1	2.25	32.00	H
16	2.19	1	219	32.88	H

15	2.13	0.99	2.11	34.14	H
14	2.06	0.99	2.04	35.30	H
13	1.99	0.98	1.95	36.92	H
12	1.92	0.98	1.88	38.27	H
11	1.86	0.97	1.80	39.91	H
10	1.79	0.97	1.74	41.47	H
Pressure/MPa			**30**		
22	2.29	1.02	2.34	30.82	H
21	2.23	1.02	2.27	31.65	H
20	2.16	1.02	2.20	32.68	H
19	2.1	1.01	2.12	33.95	H
18	2.05	1.01	2.07	34.77	H
17	1.98	1.01	2	36.00	G
16	1.91	1	1.91	37.7	G
15	1.85	1	1.85	38.92	G
14	1.79	0.99	1.77	40.63	G
13	1.73	0.99	1.71	42.04	G
12	1.67	0.98	1.64	43.99	G
11	1.6	0.98	1.57	45.92	G
10	1.52	0.97	1.47	48.83	G
Pressure/MPa			**20**		
22	1.98	1.01	2	36.00	G
21	1.92	1.01	1.94	37.13	G
20	1.85	1	1.85	38.92	G
19	1.79	1	1.79	40.22	G
18	1.73	1	1.73	41.62	G
17	1.67	0.99	1.83	43.55	G
16	1.61	0.99	1.59	45.17	G
15	1.55	0.98	1.52	47.4	D
14	1.47	0.98	1.44	49.98	D
13	1.4	0.98	1.37	52.48	D
12	1.32	0.97	1.28	56.23	D
11	1.23	0.97	1.19	60.35	C
10	1.18	0.96	1.13	63.56	C

Pressure/MPa			10		
22	1.68	1	1.68	42.86	G
21	1.61	1	1.61	44.72	D
20	1.56	0.99	1.54	46.62	D
19	1.48	0.99	1.47	49.14	D
18	1.4	0.98	1.37	52.48	C
17	1.33	0.98	1.30	55.24	C
16	1.25	0.97	1.21	59.38	C
15	1.18	0.97	1.14	62.90	B
14	1.1	0.96	1.06	68.18	B
13	1.03	0.95	0.98	73.58	B
12	0.98	0.95	0.93	77.34	B
11	0.9	0.94	0.85	85.11	A
10	0.85	0.94	0.8	90.11	A

For the second and final stages of the preliminary study using NH_3 gas, the focal length was adjusted by 0.5 mm increments so as to evaluate smaller changes in the energy density or laser fluence and improve accuracy in establishing the range of laser fluencies over which surface structural formation would take place. The focal length required to produce surface topography focused the laser beam further from the HA surface to provide a larger spot size area and subsequently a higher laser fluence when compared to the study carried out with SF_6 gas.

Table 6.7 Second set of results from preliminary laser study with NH_3

Focal length/mm	Length/ mm	Height/ mm	Spot size area/mm^2	Energy density/ kJ/m^2	Appearance
Second stage					
Pressure/MPa			**80**		
22	3.78	1.13	4.27	16.86	D
21.5	3.76	1.13	4.25	16.95	D
21	3.73	1.12	4.18	17.23	D
20.5	3.71	1.11	4.12	17.48	D
20	3.68	1.11	4.08	17.63	D
19.5	3.63	1.1	4	18.03	E

19	3.6	1.1	3.96	18.18	E
18.5	3.58	1.09	3.9	18.45	E
18	3.55	1.09	3.87	18.61	F
Pressure/MPa			**75**		
22	3.61	1.11	4.01	17.97	F
21.5	3.58	1.1	3.94	18.28	F
21	3.56	1.1	3.92	18.39	G
20.5	3.52	1.1	3.87	18.6	G
20	3.49	1.09	3.8	18.93	G
19.5	3.47	1.09	3.78	19.04	G
19	3.44	1.09	3.75	19.20	G
18.5	3.41	1.08	3.68	19.55	H
18	3.37	1.08	3.64	19.78	H
Pressure/MPa			**70**		
22	3.48	1.09	3.79	18.98	G
21.5	3.46	1.09	3.77	19.09	G
21	3.43	1.08	3.7	19.44	H
20.5	3.41	1.08	3.68	19.55	H
20	3.38	1.08	3.65	19.72	H
19.5	3.36	1.07	3.6	20.03	H
19	3.33	1.07	3.56	20.21	H
18.5	3.31	1.06	3.51	20.52	H
18	3.29	1.06	3.49	20.65	H
Pressure/MPa			**65**		
22	3.38	1.07	3.62	19.91	H
21.5	3.35	1.07	3.58	20.09	H
21	3.33	1.06	3.53	20.4	H
20.5	3.3	1.06	3.5	20.58	H
20	3.28	1.06	3.48	20.71	H
19.5	3.26	1.05	3.42	21.03	H
19	3.23	1.05	3.39	21.23	H
18.5	3.2	1.05	3.36	21.43	H
18	3.18	1.04	3.31	21.77	H

Final stage					
Pressure/MPa			**80**		
20	3.68	1.11	4.08	17.63	D
19.5	3.63	1.1	4	18.03	E
19	3.6	1.1	3.96	18.18	E
18.5	3.58	1.09	3.9	18.45	E
18	3.55	1.09	3.87	18.61	F
Pressure/MPa			**77.5**		
20	3.59	1.11	3.98	18.07	F
19.5	3.56	1.11	3.95	18.22	G
19	3.52	1.1	3.87	18.6	G
18.5	3.49	1.1	3.83	18.75	G
18	3.46	1.1	3.81	18.92	G
Pressure/MPa			**75**		
20	3.49	1.09	3.8	18.93	G
19.5	3.47	1.09	3.78	19.04	G
19	3.44	1.09	3.75	19.20	G
18.5	3.41	1.08	3.68	19.55	H
18	3.37	1.08	3.64	19.78	H

From the results shown in Table 6.7 it was determined that the development of surface topography took place using 80 MPa NH_3 gas at laser fluencies within the range of 17.17 to 18.50 MPa. The most uniformly developed surface topography was observed after laser irradiation at an energy density of 18.18 kJ/m^2 as summarised in Table 6.8.

Table 6.8 Details of processing conditions resulting in HA surface topography

Process Gas	Pressure / MPa	Repetition rate/Hz	Number of pulses	Focal length / mm	Spot size area/mm^2	Laser fluence/ kJ/m^2	Range/ kJ/m^2
SF_6	10	20	1000-1100	20	4.86	14.81	14.50-15.20
NH_3	80	20	1000	19	3.96	18.18	17.70-18.50
SF_6 / H_2O	5 / 1.8-2	20	1500	20	6.92	10.41	-

In order to determine the number of shots the height of the beam spot was measured, (Y-L) as portrayed in Figure 6.11;

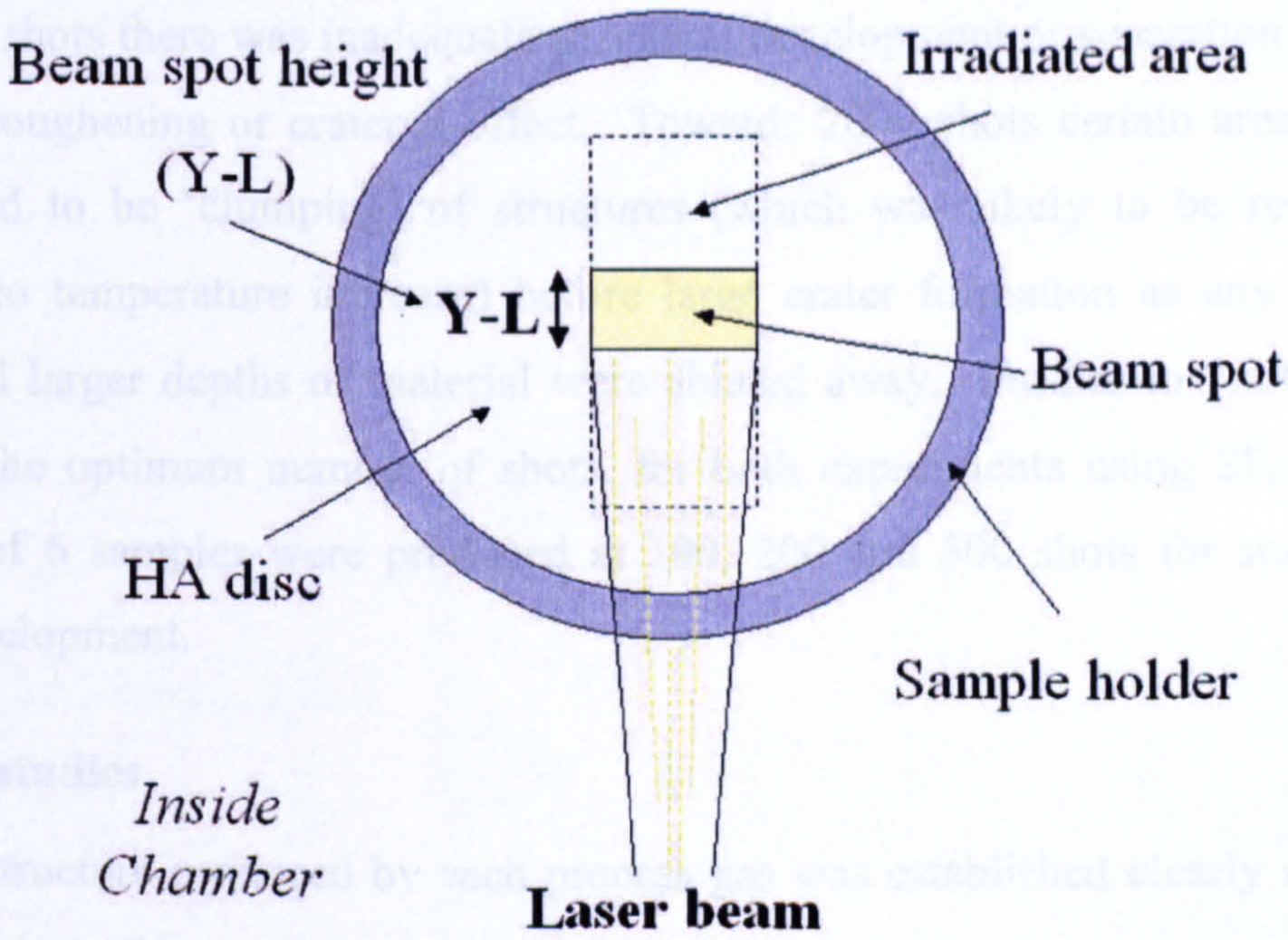

Figure 6.11: Diagram demonstrating the calculation of the laser beam height

Using the equation:

$$\frac{\text{Number of shots}}{\text{Repetition rate}} = \text{time(t)}$$

(Equation 6.3)

The beam height (Y-L) is translated into time (t) to provide a uniform number of shots over the given area using:

$$\text{Speed} = \frac{\text{distance (mm)}}{\text{time (t)}}$$

$$\text{Speed} = \frac{\text{(Rep-rate x (Y-L))}}{\text{N° of shots}}$$

(Equation 6.4)

$$\text{N° of shots} = \frac{\text{Rep-rate x (Y-L)}}{\text{Speed}}$$

(Equation 6.5)

Between 1000 and 1500 pulses were required to create structures of adequate clarity. Prior to 1000 shots there was inadequate structural development or separation and more of a surface roughening or cratered effect. Towards 2000 shots certain areas showed what appeared to be 'clumping' of structures (which was likely to be resultant of melting due to temperature increase) before large crater formation as any structural formation and larger depths of material were ablated away. Further to the 6 samples produced at the optimum number of shots, for both experiments using SF_6 and NH_3 gases, a set of 6 samples were produced at 100, 200 and 500 shots for study of the structural development.

6.4.2 SEM studies

The type of structure produced by each process gas was established clearly with SEM imaging (Figure 6.12).

The structures produced in the presence of 10 MPa SF_6 were of roughly columnar shape and fairly evenly sized as opposed to the topography produced in the presence of 80 MPa NH_3 that was 'globular' or hillock-like in appearance and more irregular in height and size.

During a trial experiment the presence of gaseous phase water in combination with SF_6 gas had little effect on the type of morphological structure created but resulted in structures of a much smaller size, however SEM images could not be obtained of any significant quality.

In all cases other than those working with ammonia gas, the structural modification was obtained at lower gas pressures and reactivity decreased with an increase in process gas pressure.

(a) Unmodified HA disc

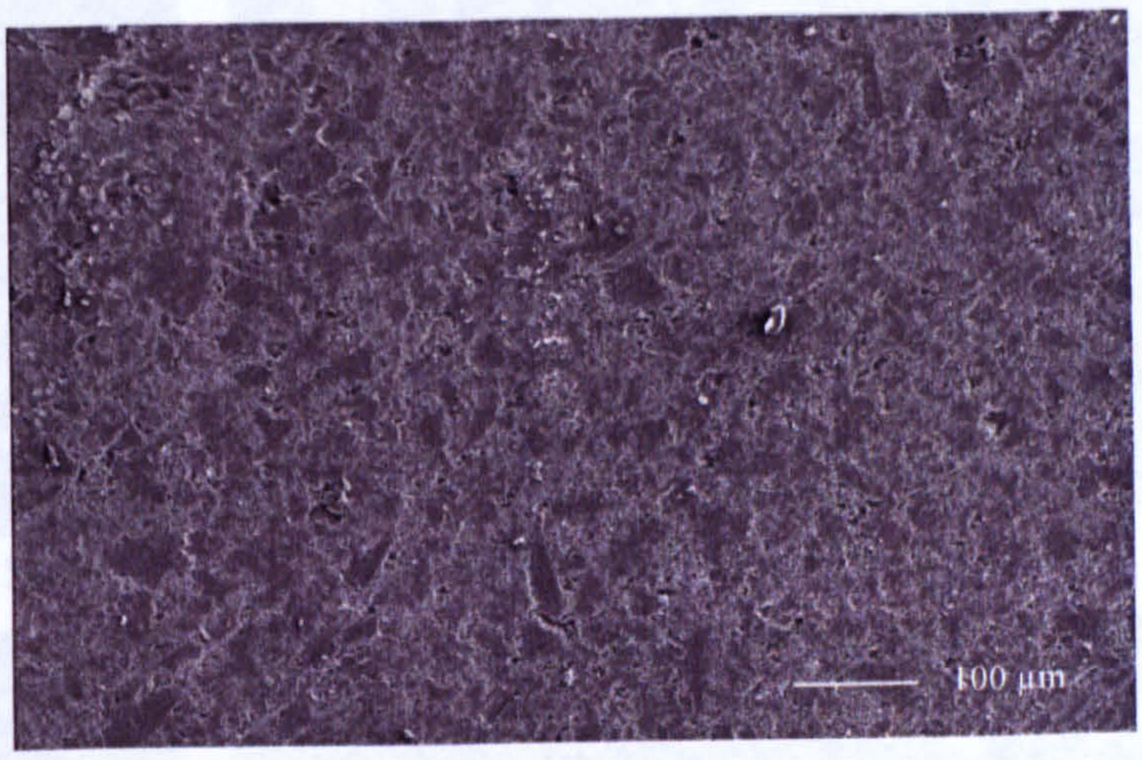

(b) 80 MPa NH_3 processed disc

(c) 10 MPa SF_6 processed disc

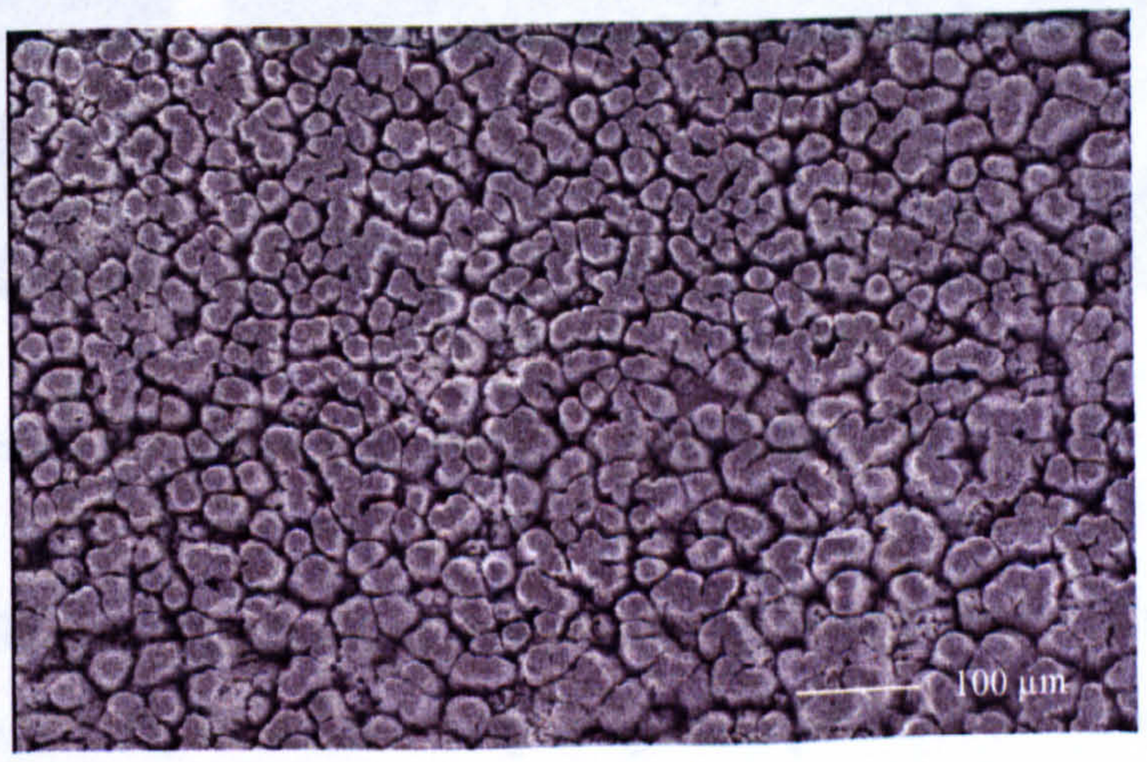

Figure 6.12: SEM images of HA discs before/after 1000 laser shots. (Mag x 70)

Further differences between the types of structural development resultant of the type of process gas were ascertained at higher magnifications.

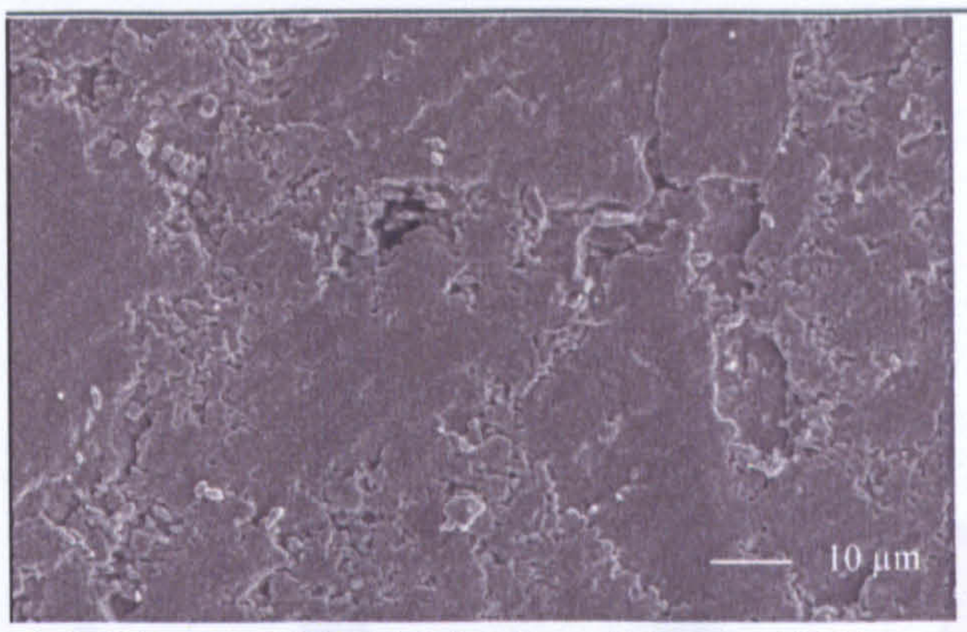

(a) Unmodified HA disc (Mag x 500)

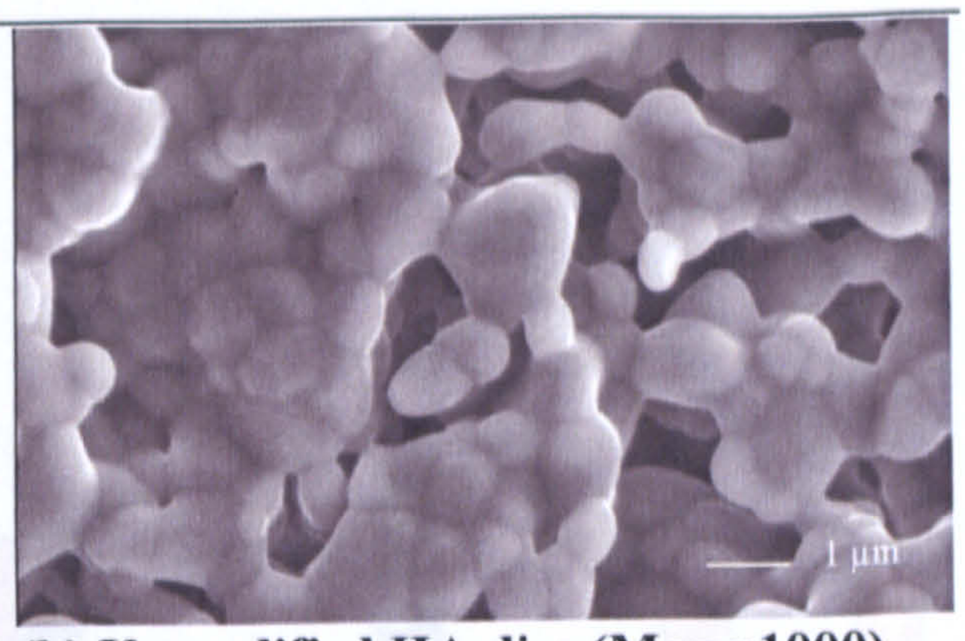

(b) Unmodified HA disc (Mag x1000)

(c) 80 MPa NH_3 (Mag x 500)

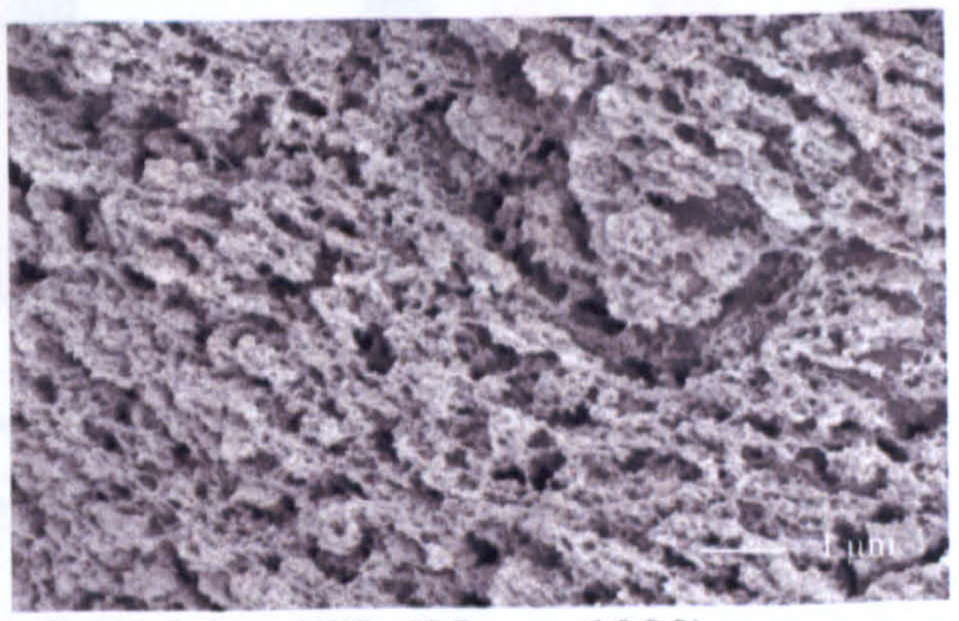

(d) 80 MPa NH_3 (Mag x 1000)

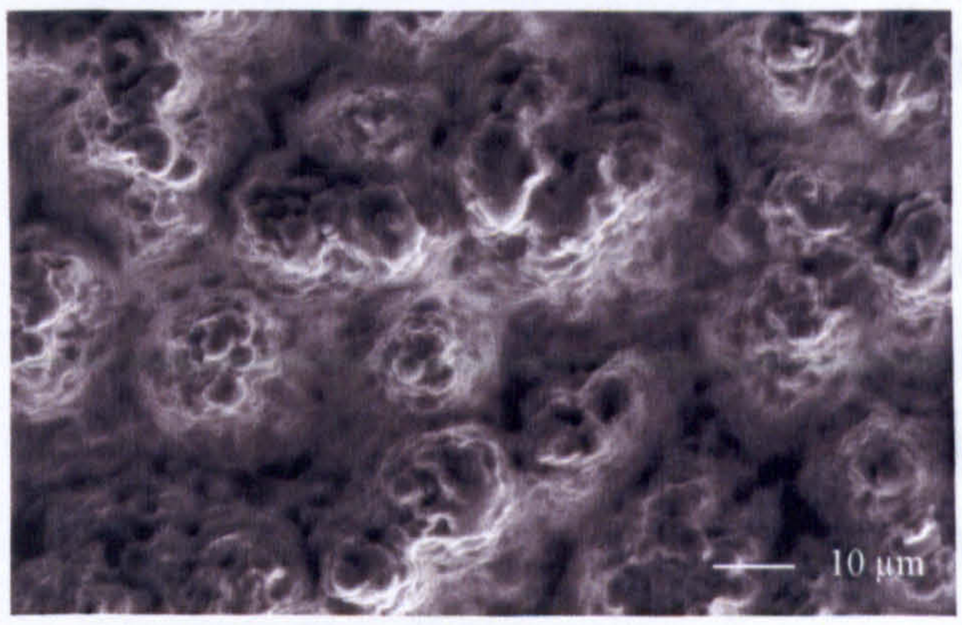

(e) 10 MPa SF_6 (Mag x 500)

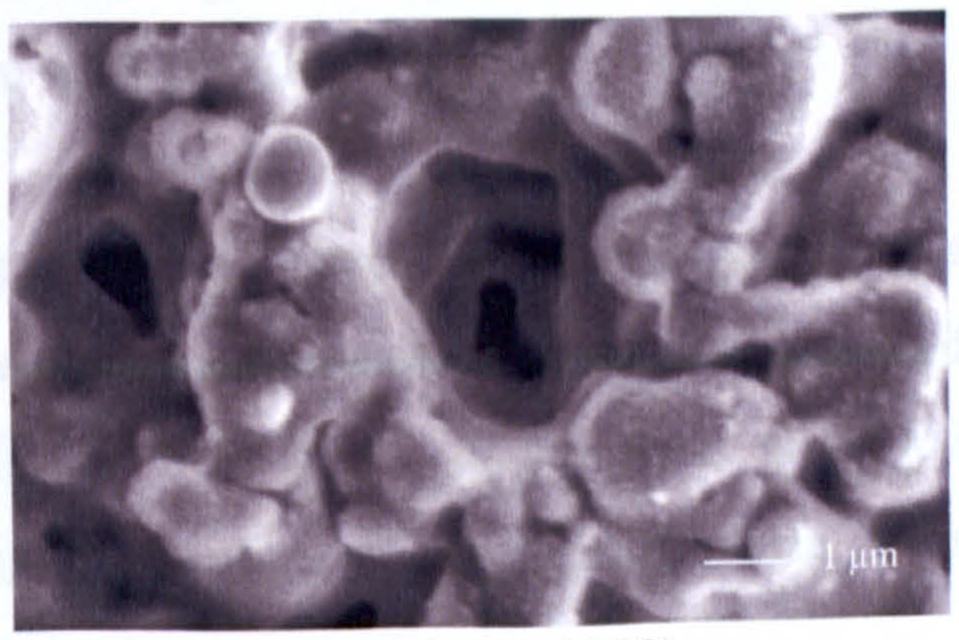

(f) 10 MPa SF_6 (Mag x 1000)

Figure 6.13: SEM images of HA discs before/after 1000 laser shots.

At greater maginification the difference in structure was vastly more apparent. The material processed in the presence of NH_3 featured a very rough and porous crater-like surface whilst that processed with SF_6 demonstrated smoother features but with fewer and larger pores. During laser processing with NH_3 the material became very hot and had a greater tendency to burn. The colours present within the laser plume also differed between the two process gases. During laser irradiation with SF_6, the plume featured a blue tint as opposed to that formed with NH_3 present that had red hues and showed greater intensity with increasing temperature upon the sample surface. In each case, the greatest reactivity and quality of structural development was observed after processing when the plume was large and bright.

The development of the each type of topography was identified by SEM imaging at incremental exposures to calculated pulses of laser irradiation at the established fluence.

10 MPa SF_6

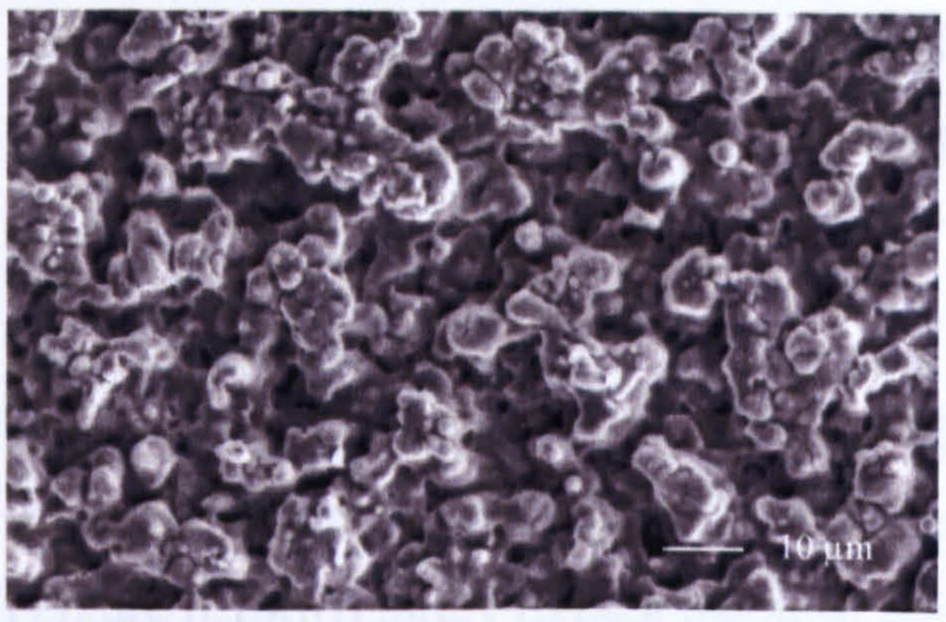

(a) 100 pulses

80 MPa NH_3

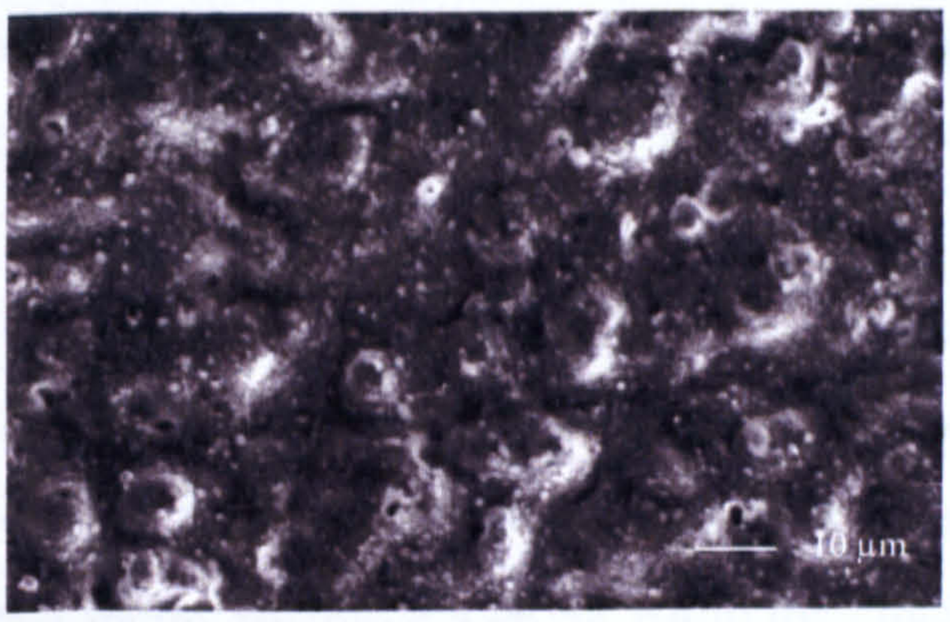

(b) 100 pulses

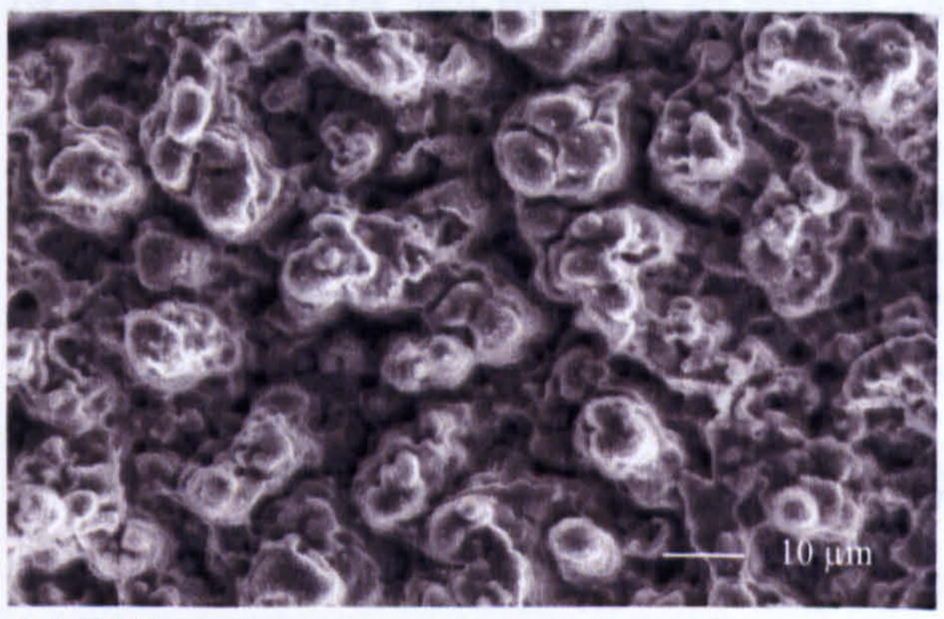

(c) 200 pulses

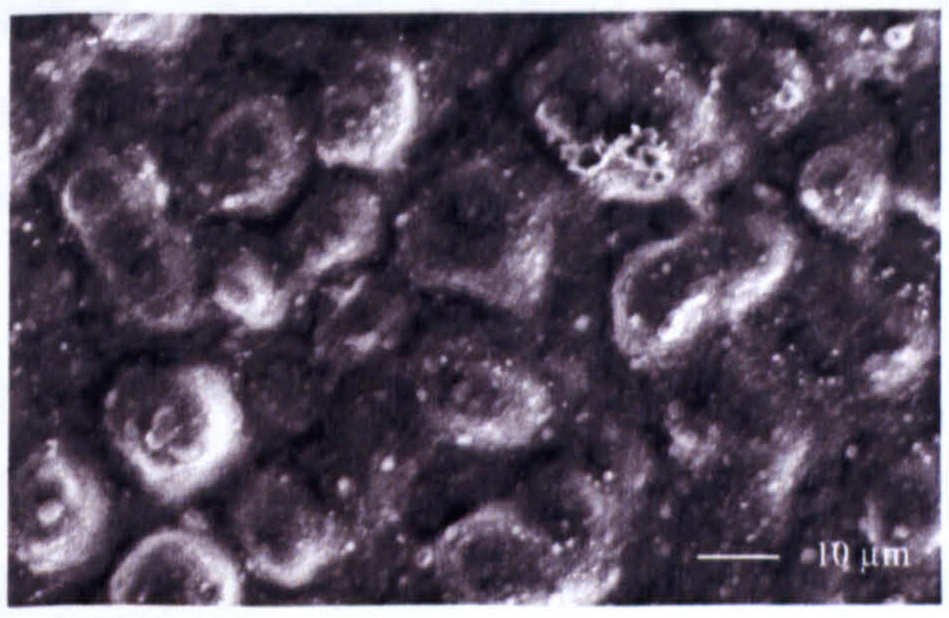

(d) 200 pulses

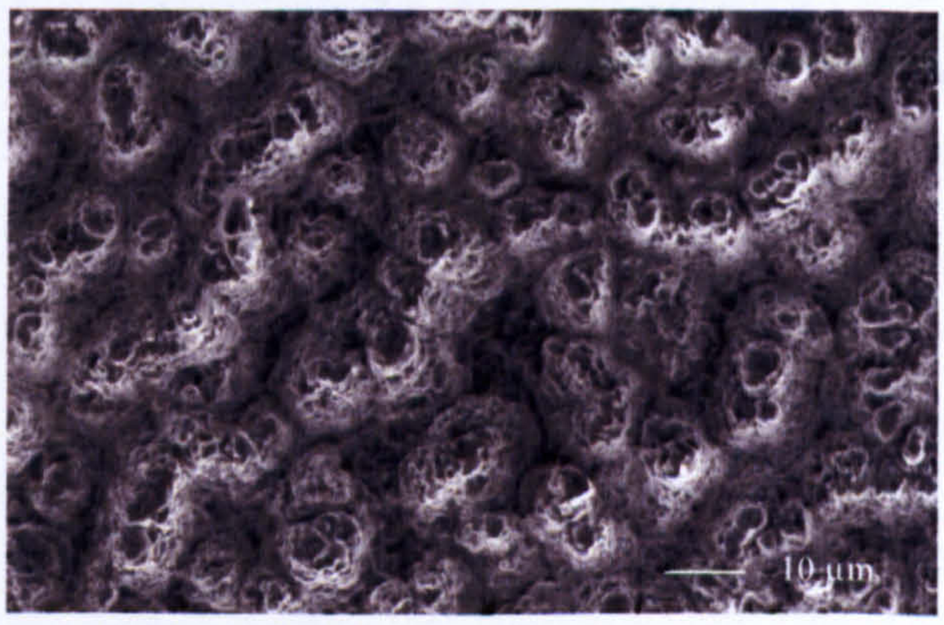

(e) 500 pulses

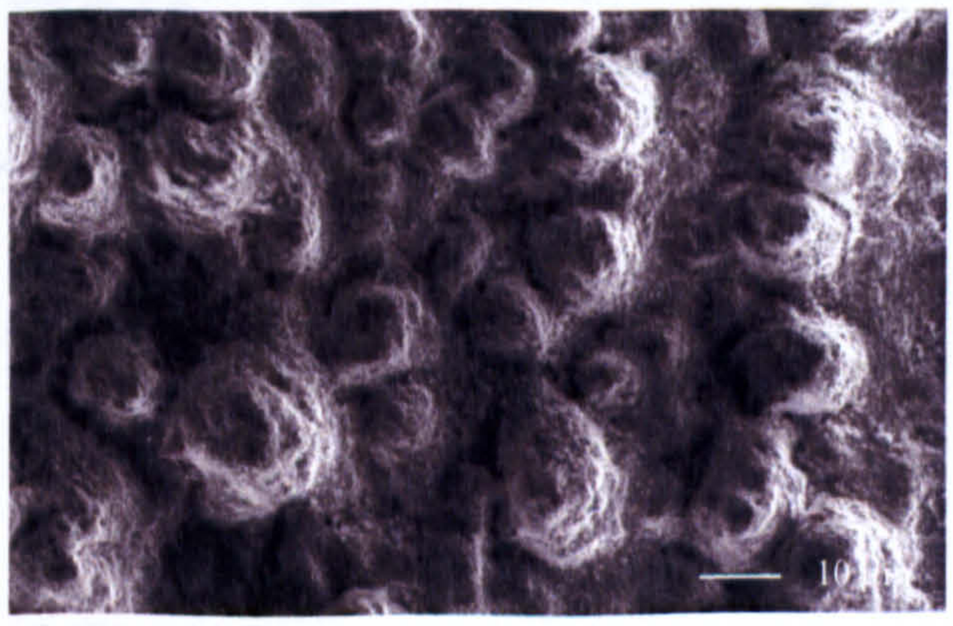

(f) 500 pulses

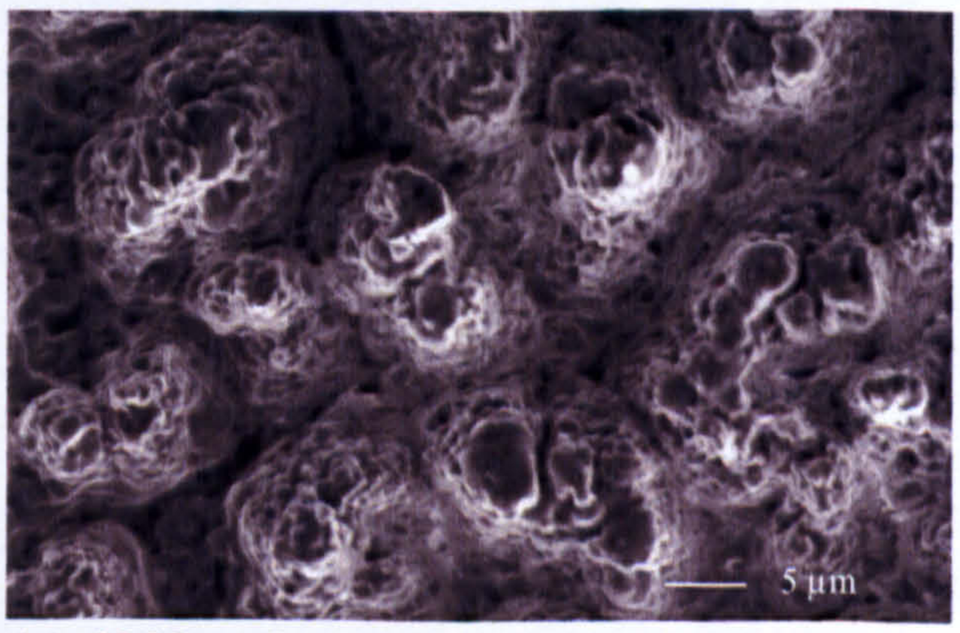

(g) 1000 pulses

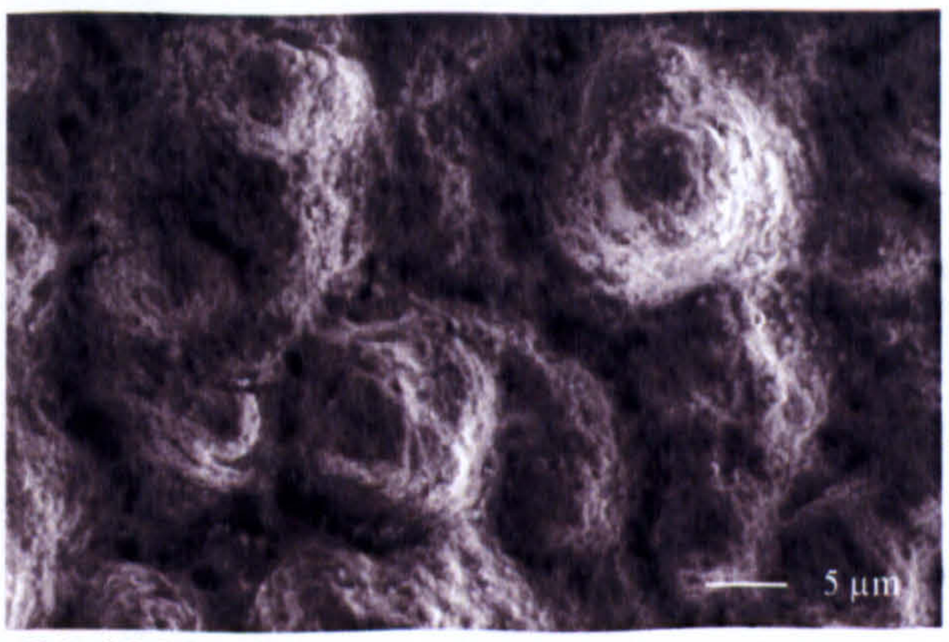

(h) 1000 pulses

Figure 6.14: SEM images of topographical development with increasing exposure to laser irradiation. (Mag x 1000)

Whilst surface roughening and structural differences could be observed from 100-200 laser pulses in each case, clear development of structural development became apparent after 500 shots. The approximate depth/height of the surface features was established by SEM imaging of diamond-saw cut sections of modified material tilted at varying angles and rotated until clear structural profiles could be brought into focus (Figure 6.15).

Interestingly, the immediate surrounding HA surface to the laser irradiated areas displayed surface structural differences to that of the unprocessed HA disc surfaces (Figure 6.15(h)) likely to be a result of the laser plume spanning a larger width than that of the laser beam and the area of initial interaction. Observation during laser irradiation determined a plume that spanned up to 2 mm either side of the beam width such that 4.5 mm spaces were allowed between the laser-processed strips.

Measurements taken during imaging at 45° angular positioning established the height of the structural features to be within the range of 10-20 μm and the range of width to be within 8-12 μm. Images of similar quality could not be obtained for the samples irradiated in the presence of NH_3 due to charging regardless of the carbon coating. The irregularity of the structures that ranged greatly in size and height prevented the determination of any useful measurements of the structural features.

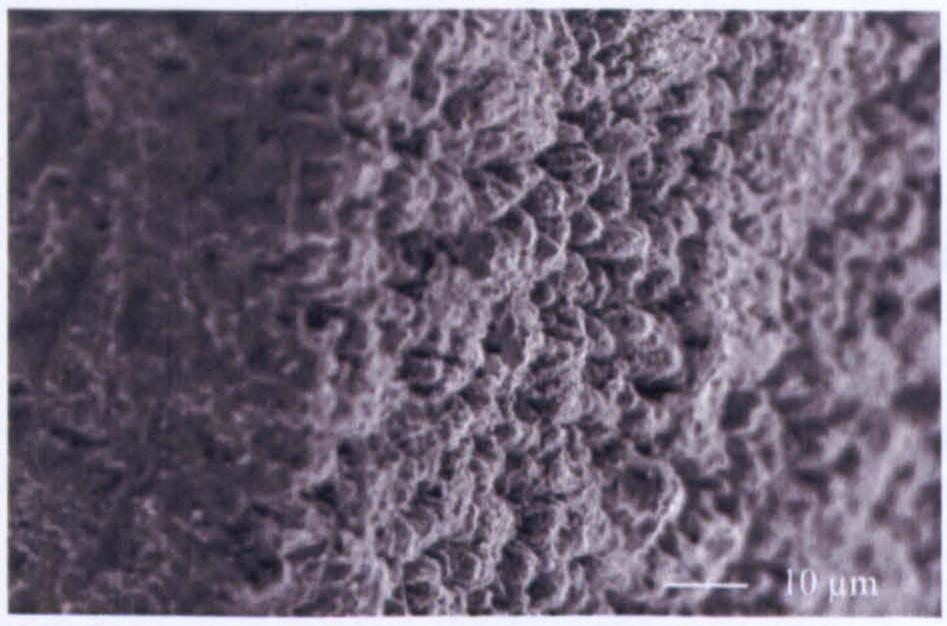

(a) Lateral cross-section (Mag x 180)

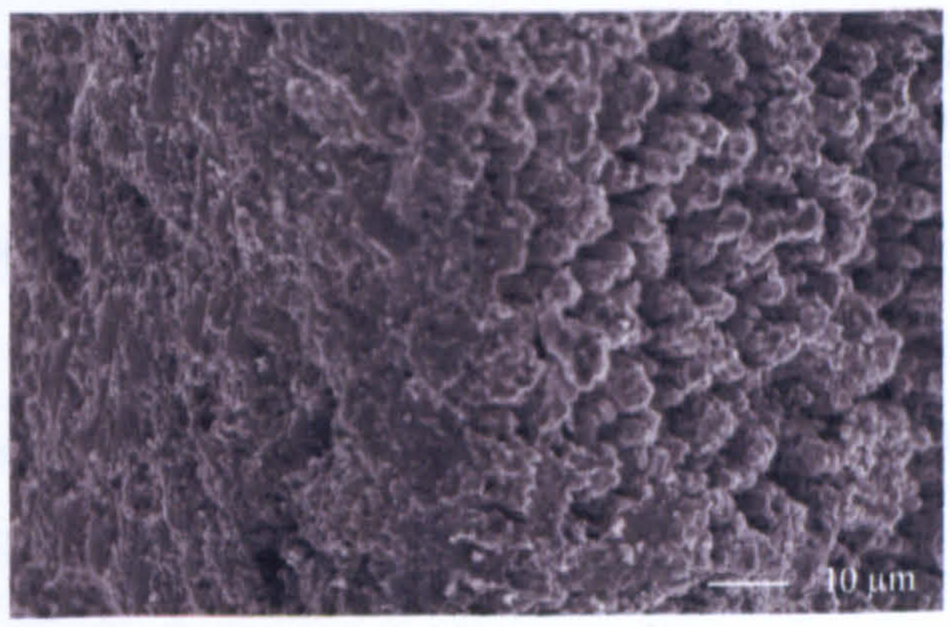

(b) Longitudinal cross-section (Mag x 180)

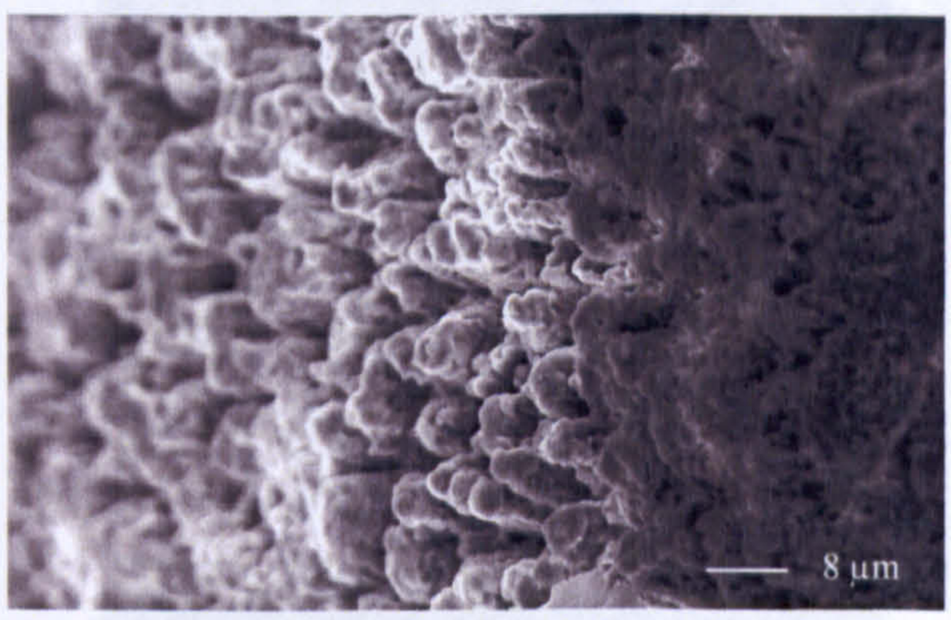

(d) Lateral cross-section (Mag x 300)

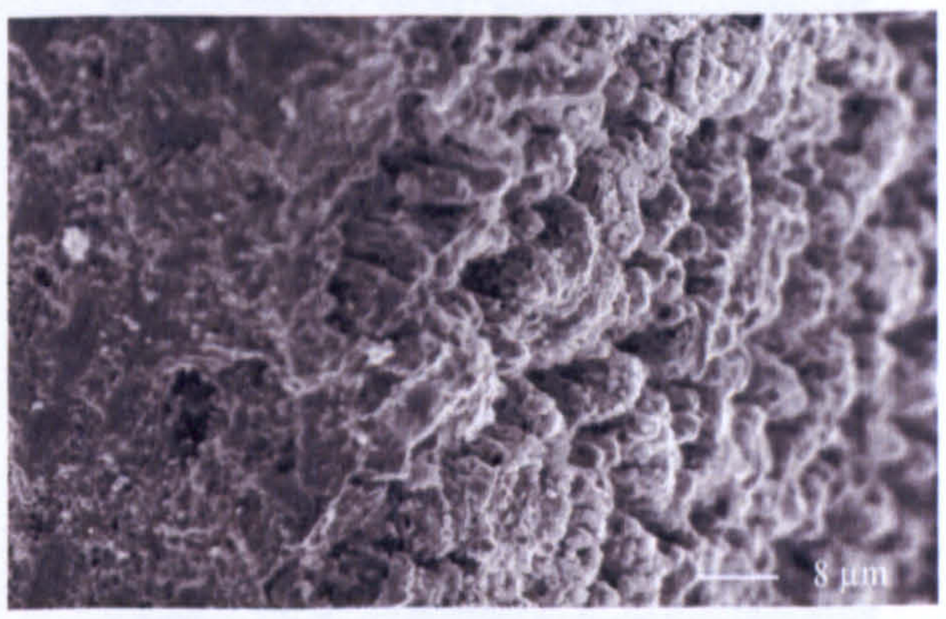

(e) Longitudinal cross-section (Mag x 300)

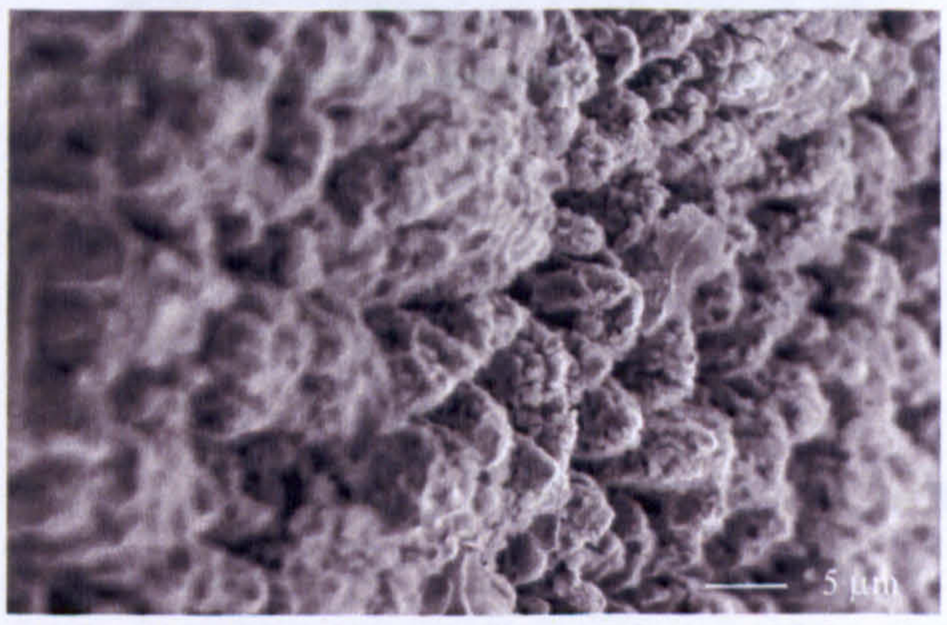

(e) Lateral cross-section (Mag x 500)

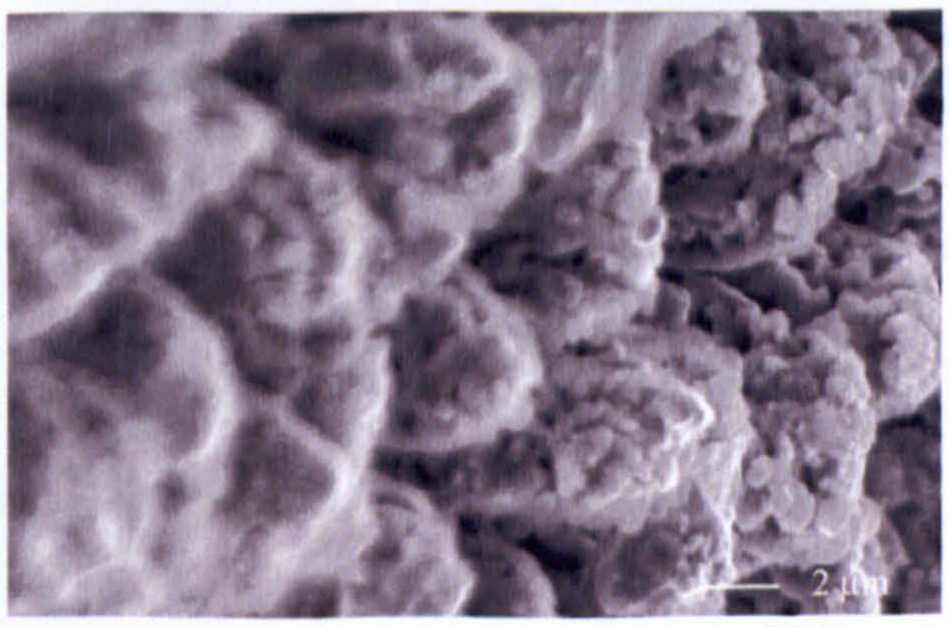

(f) Lateral cross-section (Mag x 800)

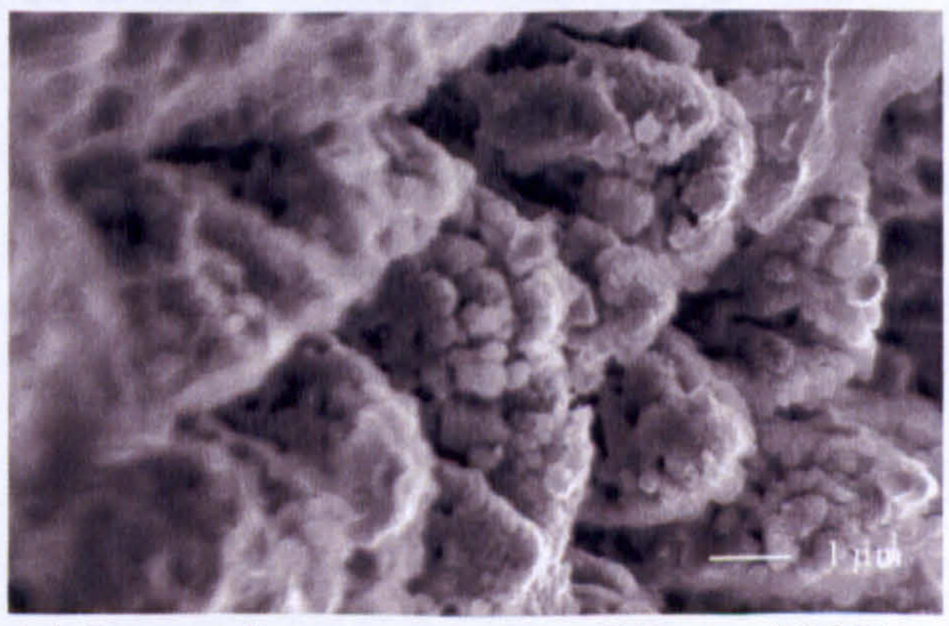

(g) Lateral cross-section (Mag x 1000)

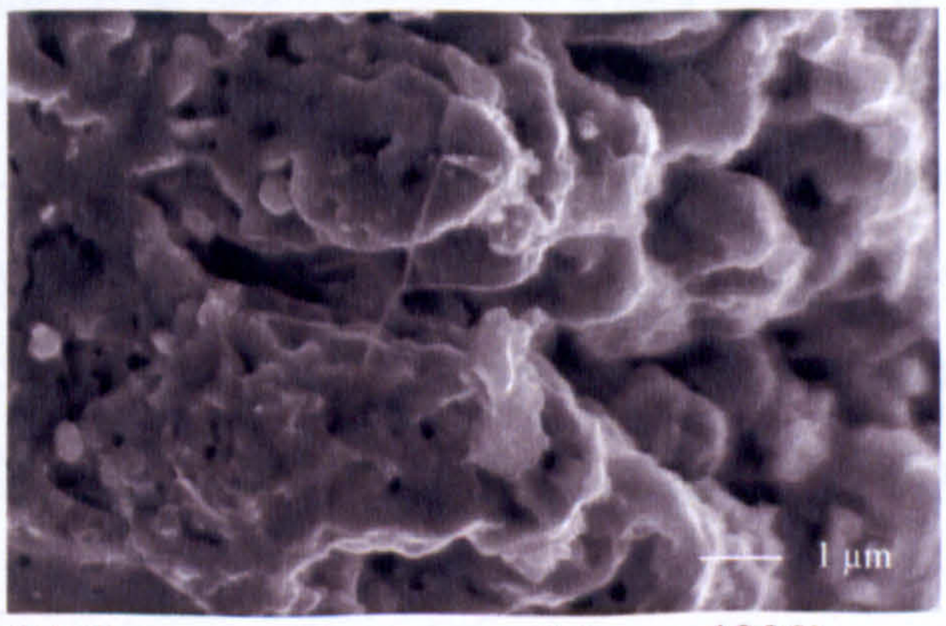

(h) Surrounding area (Mag x 1000)

Figure 6.15: SEM images of various cross-sections of 10 MPa SF_6 laser processed HA after 1000 pulses and adjacent HA surface.

6.4.3 Energy dispersive X-ray analysis (EDS)

SEM in combination with energy dispersive X-ray analysis or SEM-EDS was used to identify the surface chemistry of the HA discs before and after (including the surrounding non-irradiated areas) laser experimentation.

Initial images of the unprocessed 'Plasmabiotal' disc showed an even surface with even map distribution of calcium, phosphorous and oxygen.

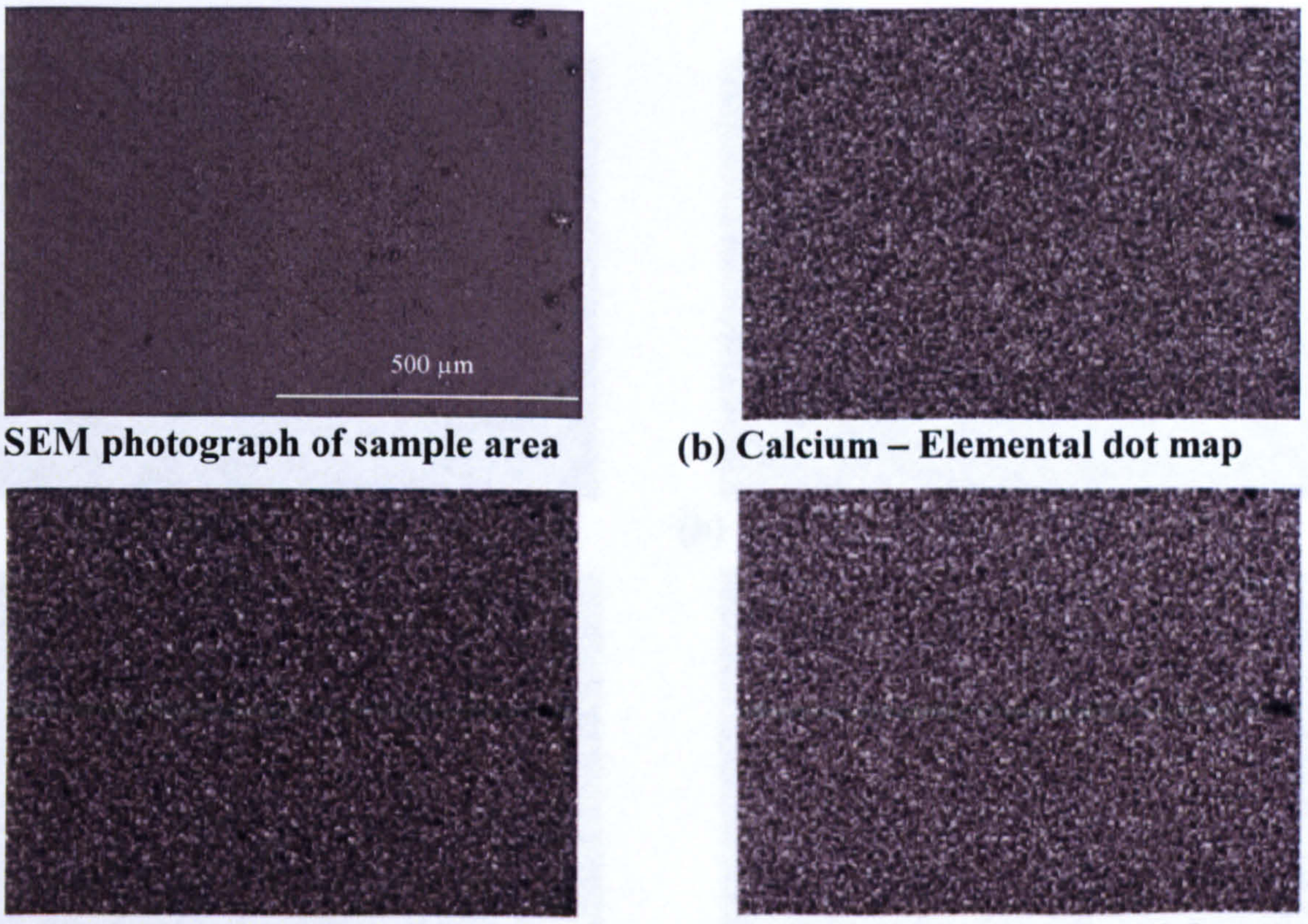

(a) SEM photograph of sample area

(b) Calcium – Elemental dot map

(c) Oxygen – Elemental dot map

(d) Phosphorous – Elemental dot map

Figure 6.16: SEM–EDS analysis/Elemental dot maps of 'Plasmabiotal' HA disc.

Elemental dot maps obtained of samples laser irradiated with 10 MPa SF_6 process gas showed an abundance of fluorine throughout the irradiated surface and less concentration of phosphorous and oxygen. This finding correlates well with previous studies that have demonstrated that the apatite structure is ready to accept negatively charged F^- ions by replacing the OH^- ions within the structure, such that the oxygen content would be less in the fluorinated area shown clearly in Figure 6.18(c) (S.Kannan *et al.*, 2006).

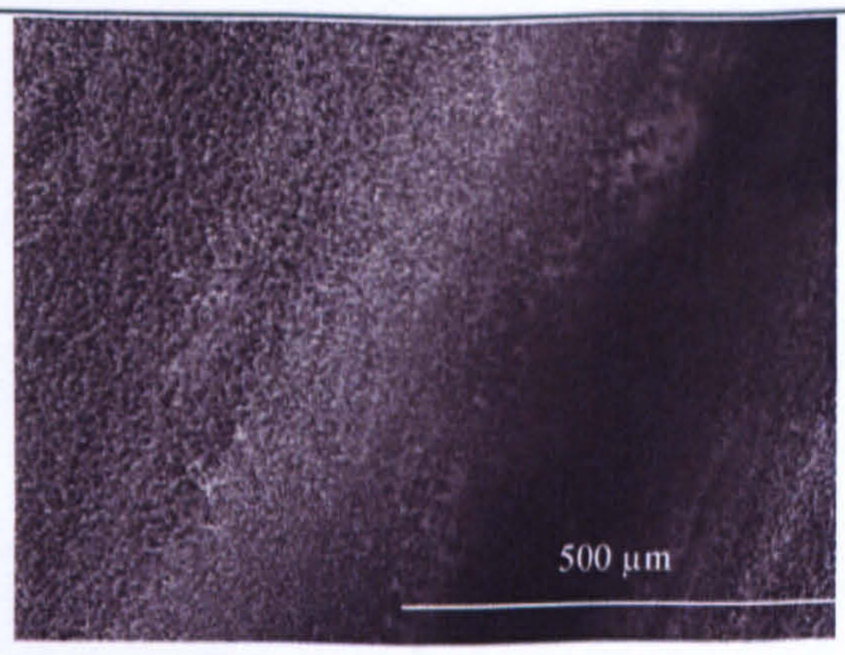

Figure 6.17: SEM photograph of SF_6 modified sample area

(a) Fluorine – Elemental dot map

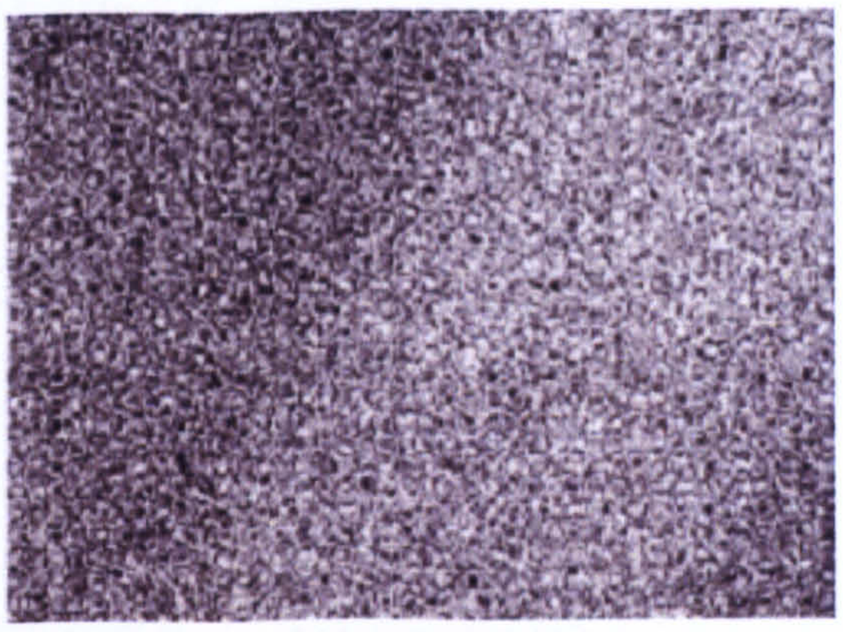

(b) Calcium – Elemental dot map

(c) Oxygen – Elemental dot map

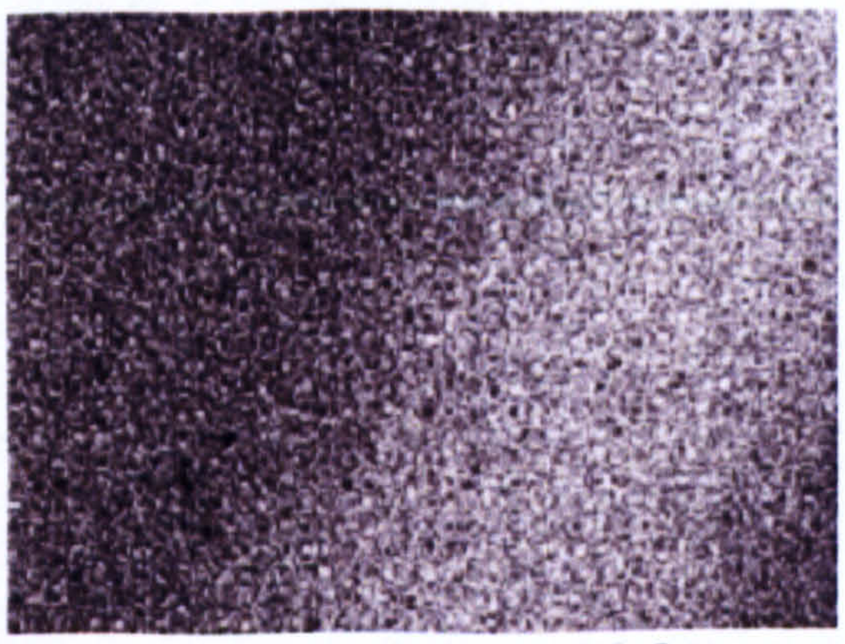

(d) Phosphorous – Elemental dot map

Figure 6.18: SEM–EDS analysis/Elemental dot maps of 10 MPa SF_6 (1000 shots) laser processed HA disc.

For semi-quantitative evaluation it was assumed that the peak height is proportional to the mole fraction of an element. From the data obtained and portrayed in chart format (Figure 6.19), the trend seen with regards to surface fluorine content was an increase corresponding to an increase in the number of laser irradiation pulses in the presence of of 10 MPa SF_6 with a respective decrease in the concentration of oxygen and phosphorous. The calcium content was also found to increase in compositional fraction.

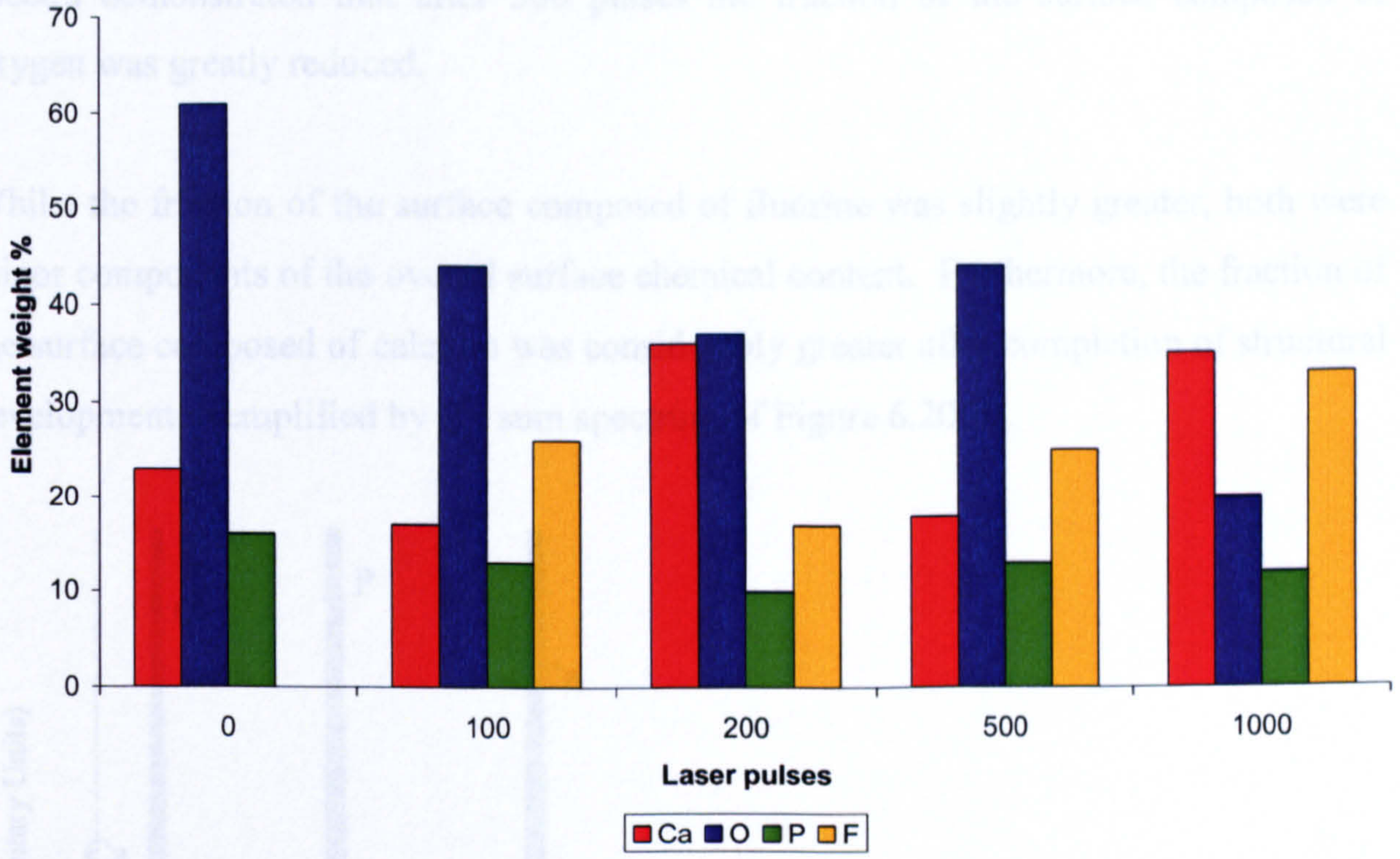

Figure 6.19: SEM–EDS analysis of elemental weight % after increasing pulses of laser irradiation with 10 MPa SF_6.

Similar elemental concentrations were found after 100 and 500 laser pulses with a deviation in the general elemental wt % pattern after 200 pulses, likely to be resultant of plume chemistry, laser deposition and ablation before subsequent structural development shown by SEM images (Figure 6.14) to predominantly occur after exposure to 500 shots or more.

The SEM-EDS spectra taken of the SF_6 irradiated HA sample are distinctly different to the spectra taken of the original 'Plasmabiotal' HA as portrayed in Figure 6.20. Spectra obtained after gradual exposure to the lasing conditions corroborate well with the elemental dot maps (Figure 6.18) that the presence of fluorine is accommodated on the surface by an exchange of oxygen and phosphorous which decrease in compositional fraction.

The calcium composition of the surface increased in content with an increase in the number of lasing pulses further substantiating the dot map analysis. Interestingly, at 500 pulses when the structures are initially apparent but not well defined, a greater percentage of the surface is composed of fluorine than when the structures are fully established and defined in height and spacing at approximately 1000 pulses. The

spectra demonstrated that after 500 pulses the fraction of the surface composed of oxygen was greatly reduced.

Whilst the fraction of the surface composed of fluorine was slightly greater, both were minor components of the overall surface chemical content. Furthermore, the fraction of the surface composed of calcium was considerably greater after completion of structural development exemplified by the sum spectrum of Figure 6.20(d).

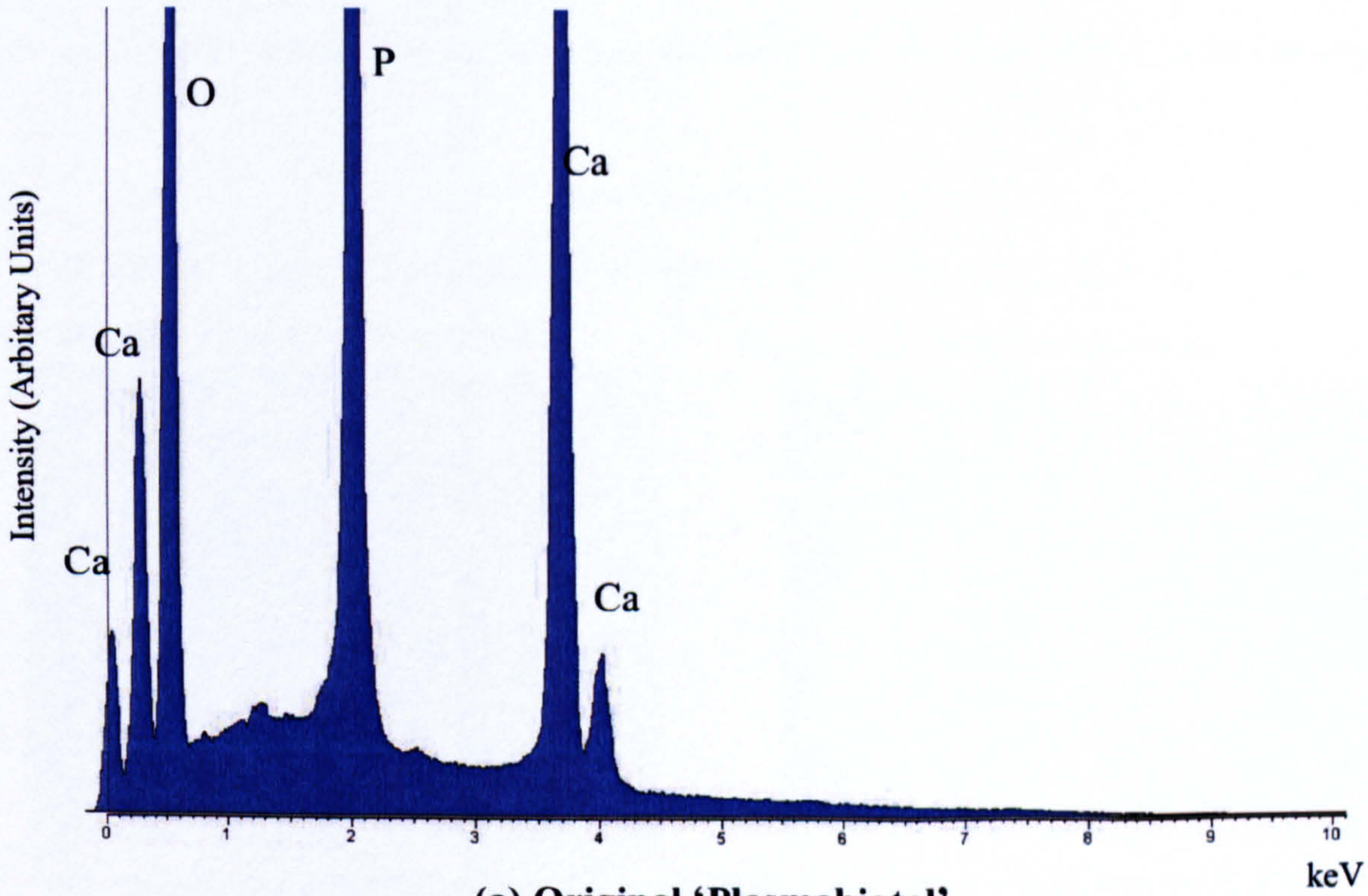

(a) Original 'Plasmabiotal'

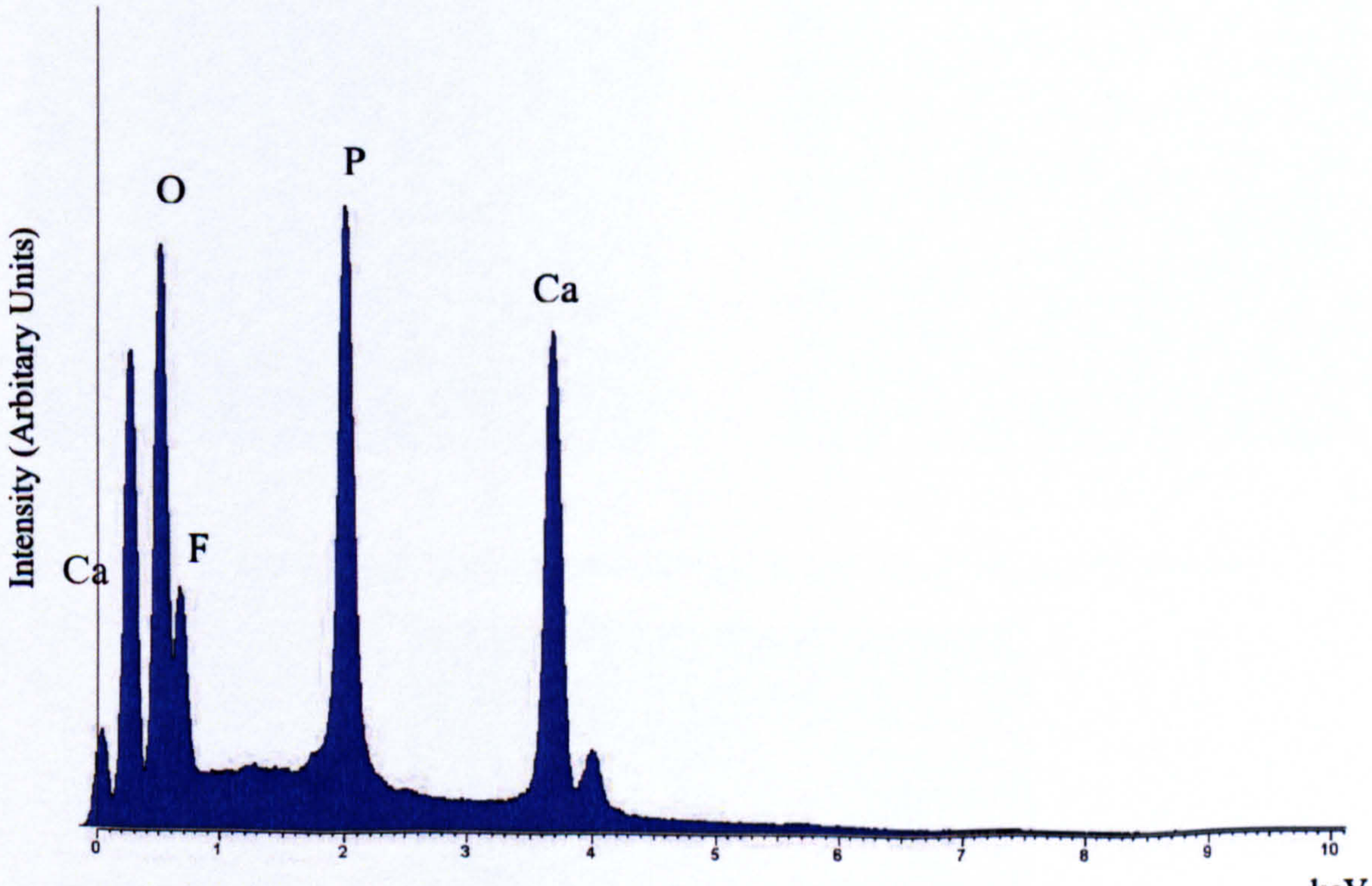

(b) 100 pulses

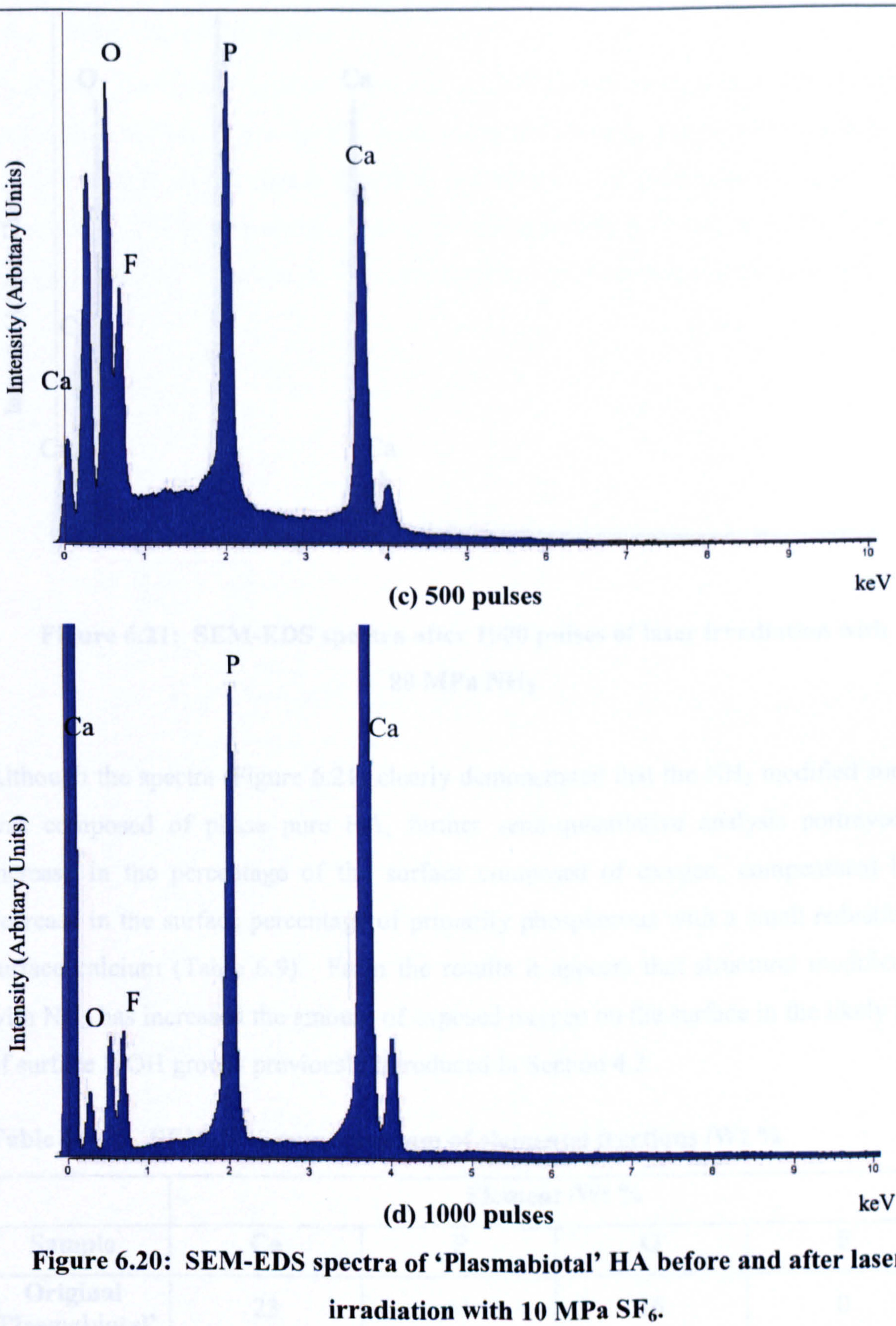

Figure 6.20: SEM-EDS spectra of 'Plasmabiotal' HA before and after laser irradiation with 10 MPa SF_6.

With regard to the samples irradiated in the presence of 80 MPa NH_3, no apparent variation was found in the elemental composition of the surfaces suggesting that the surface chemistry was unaffected by the structural changes (Figure 6.21).

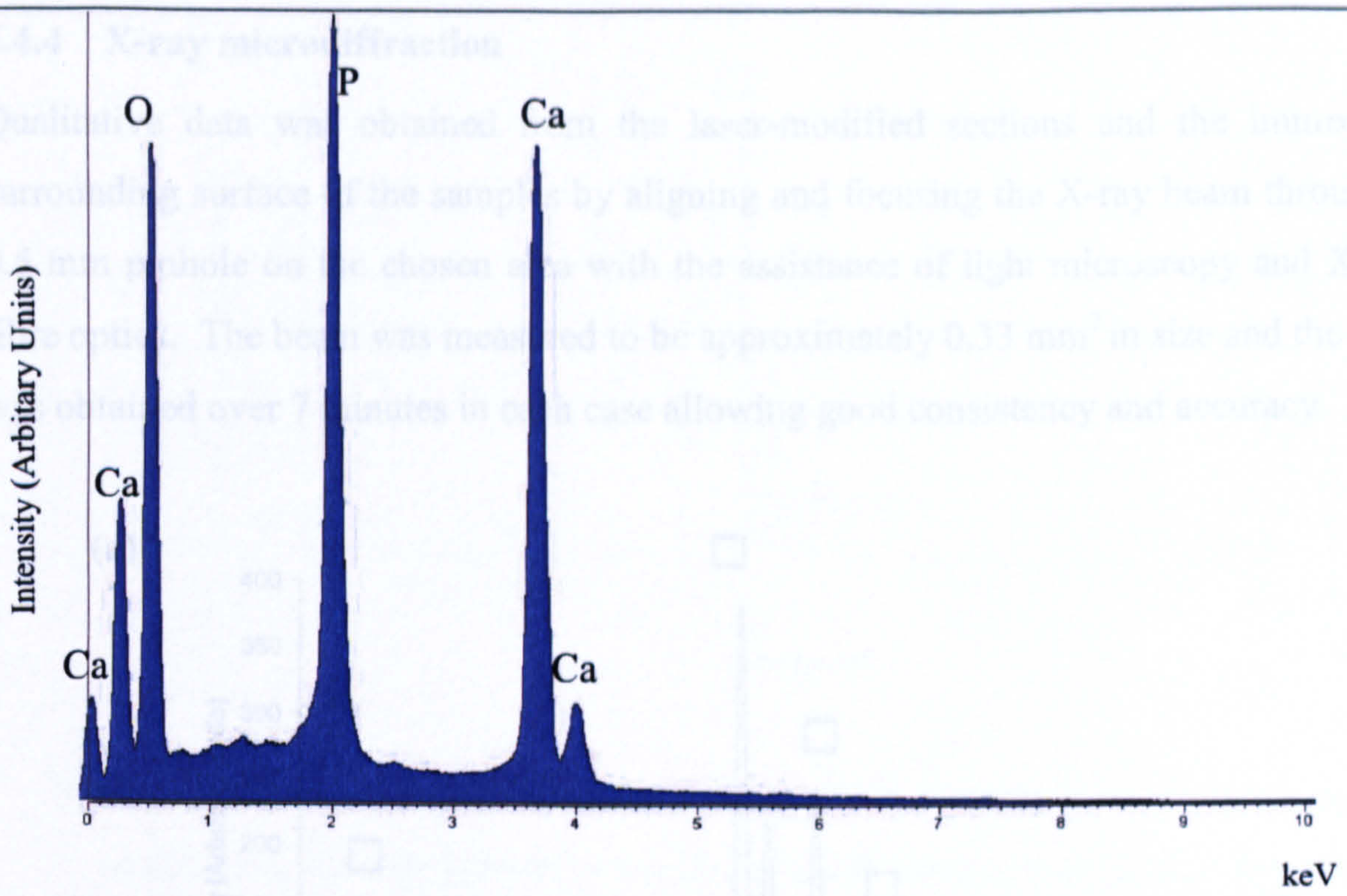

Figure 6.21: SEM-EDS spectra after 1000 pulses of laser irradiation with 80 MPa NH_3.

Although the spectra (Figure 6.21) clearly demonstrated that the NH_3 modified surface was composed of phase pure HA, further semi-quantitative analysis portrayed an increase in the percentage of the surface composed of oxygen, compensated by a decrease in the surface percentage of primarily phosphorous with a small reduction in surface calcium (Table 6.9). From the results it appears that structural modification with NH_3 has increased the amount of exposed oxygen on the surface in the likely form of surface P-OH groups previously introduced in Section 4.2.

Table 6.9 SEM-EDS sum spectrum of elemental fractions /Wt %

	Element /Wt %			
Sample	**Ca**	**P**	**O**	**F**
Original 'Plasmabiotal'	23	61	16	0
10 MPa SF_6 (1000 pulses)	35	20	12	33
80 MPa NH_3 (1000 pulses)	12	11	77	0

6.4.4 X-ray microdiffraction

Qualitative data was obtained from the laser-modified sections and the immediate surrounding surface of the samples by aligning and focusing the X-ray beam through a 0.5 mm pinhole on the chosen area with the assistance of light microscopy and X-ray fibre optics. The beam was measured to be approximately 0.33 mm^2 in size and the data was obtained over 7 minutes in each case allowing good consistency and accuracy.

(a)

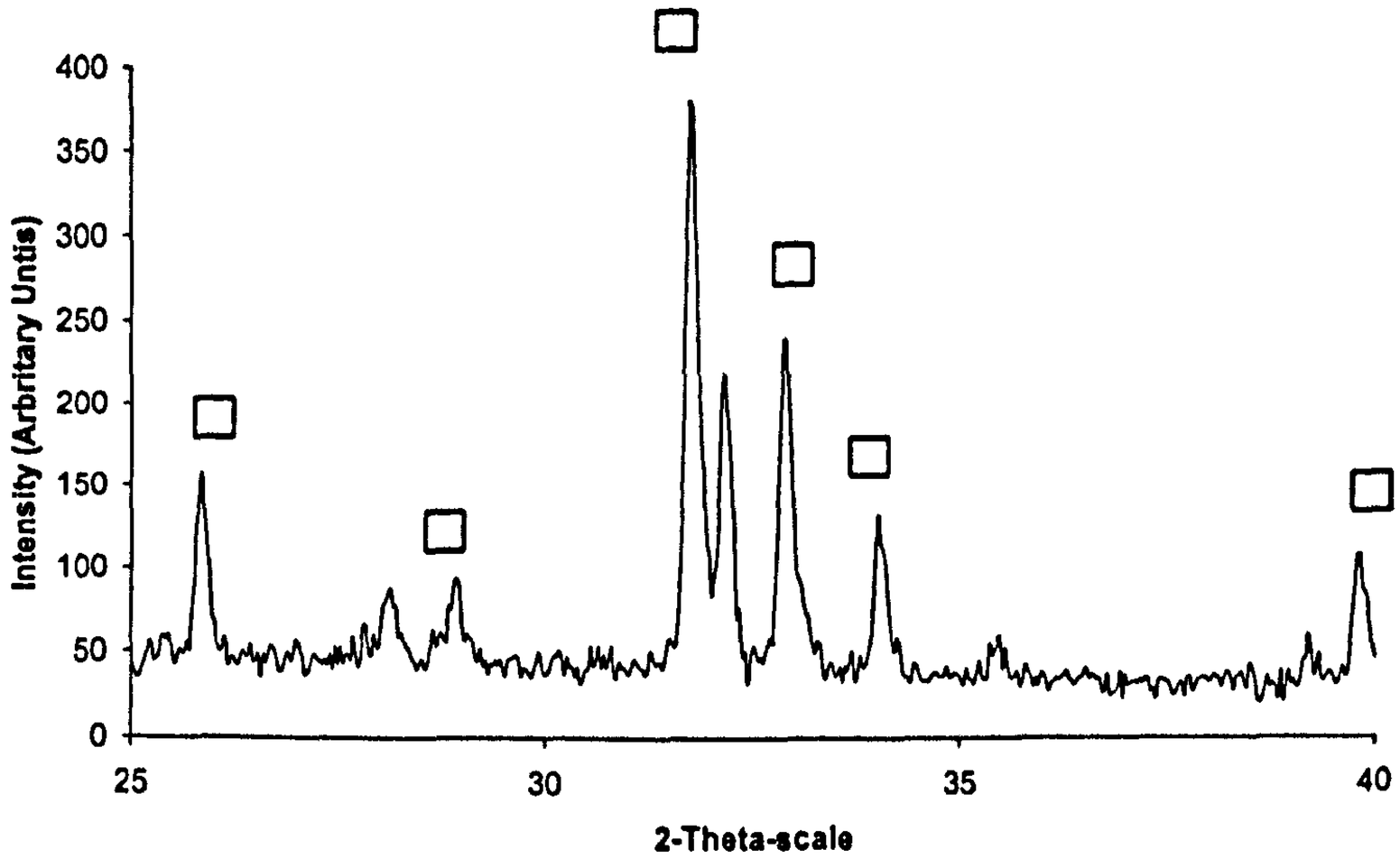

(b)

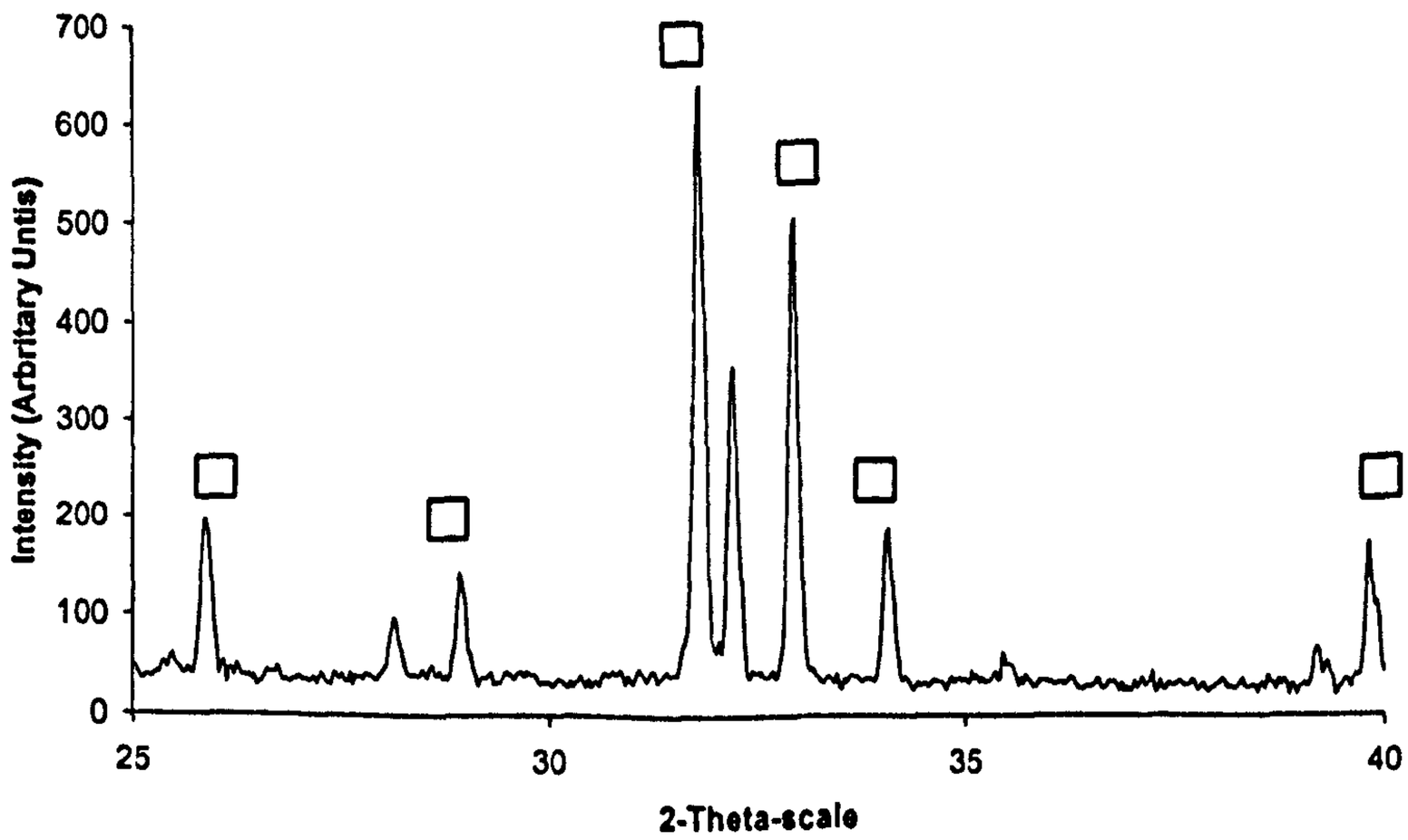

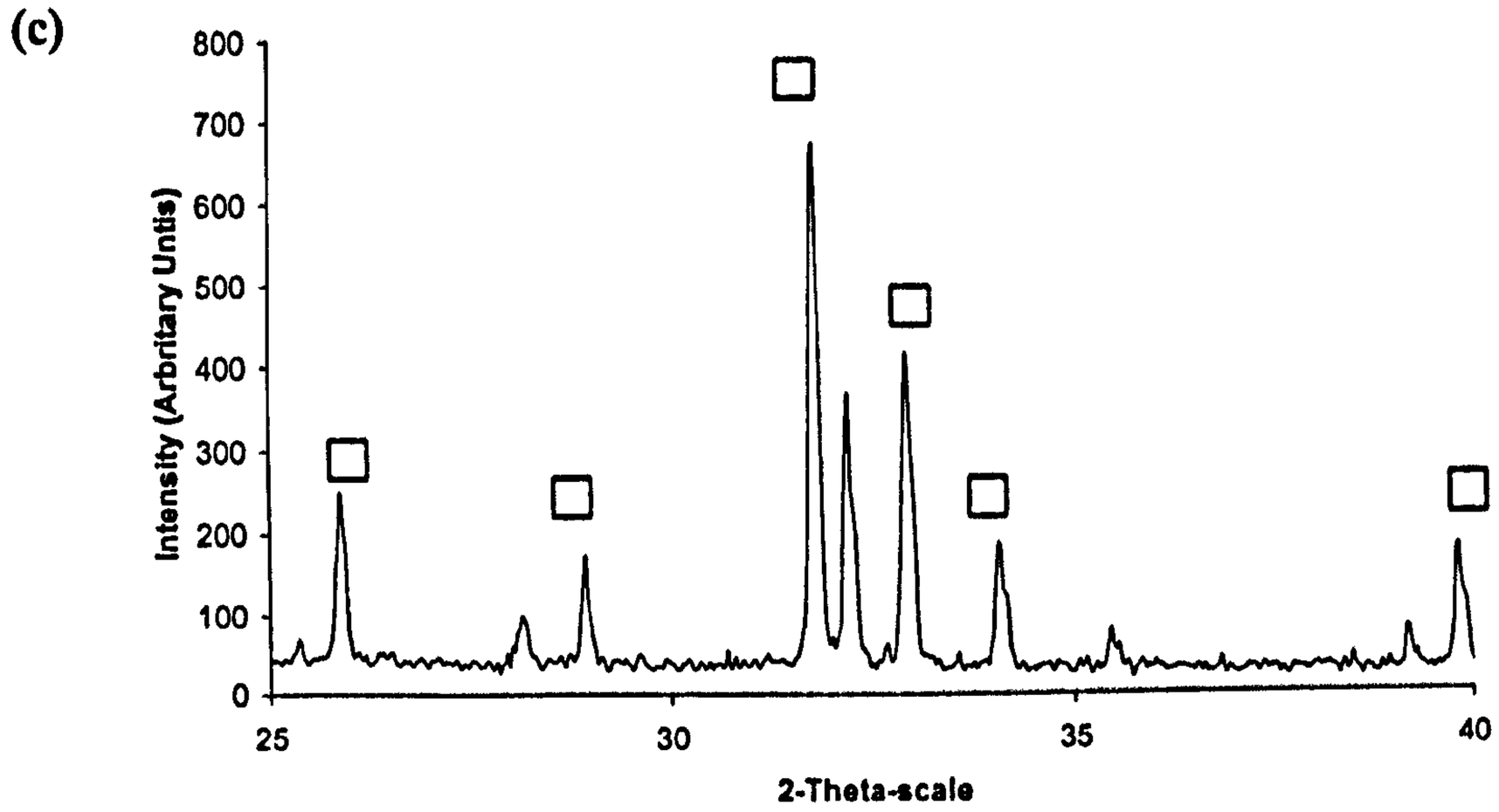

Figure 6.22: X-ray microdiffraction traces of HA samples before/after laser irradiation with 10 MPa SF_6. (a) 10 MPa SF_6 modified area; (b) Immediate surrounding unmodified area; (c) 'Plasmabiotal' original disc. (Key – □ HA, JCPDS pattern 09-0432)

In all cases data obtained from exposed material or material surrounding the laser-modified sections showed the sections to be more crystalline by the XRD traces featuring sharp, narrow and well defined peaks. (Figures 6.22(b),(c) and 6.23(b),(c))

The laser ablated areas were found to be less crystalline with the increased surface roughness causing an increase in noise content during analysis, demonstrated by the slightly shorter, wider peaks during comparison of the XRD traces. (Figures 6.22(a) and 6.23(a))

In all but one case, the broad range X-ray microdiffraction data found the surface composition to be hydroxyapatite with no other phase detected and that laser processing of the surface in either process gas did not cause decomposition or chemical modification to the bulk composition.

However, with regard to the 10 MPa SF_6 laser-modified sample, short range X-ray microdiffraction data demonstrated a gradual merging of (211) and (112) peaks at 31.8° and 32.2° respectively with exposure to laser irradiation in SF_6 (Figure 6.23). While comparing with previously reported studies, peaks (211) and (112) merge with each

other, as fluorine content increases in fluorine substituted hydroxyapatite (H.Qu *et al.*, 2005a; I.Manjubala *et al.*, 2001).

Similarly, the (300) reflection peak (normally located between 32.5° and 33.5°) for the irradiated sample was shifted toward a higher 2 0 relative to that of hydroxyapatite further to appearing much broader or enlarged, showing (smaller d-spacings) a decrease in the *a*-axis length of the HA lattice cell. The finding collaborates well with previous studies where the substitution of fluorine in HA lattice has been analysed from the shift of the HA peaks (H.Qu *et al.*, 2005b; H.Zhang *et al.*, 2006; M.Wei *et al.*, 2003; S.Barinov *et al.*, 2004).

(a)

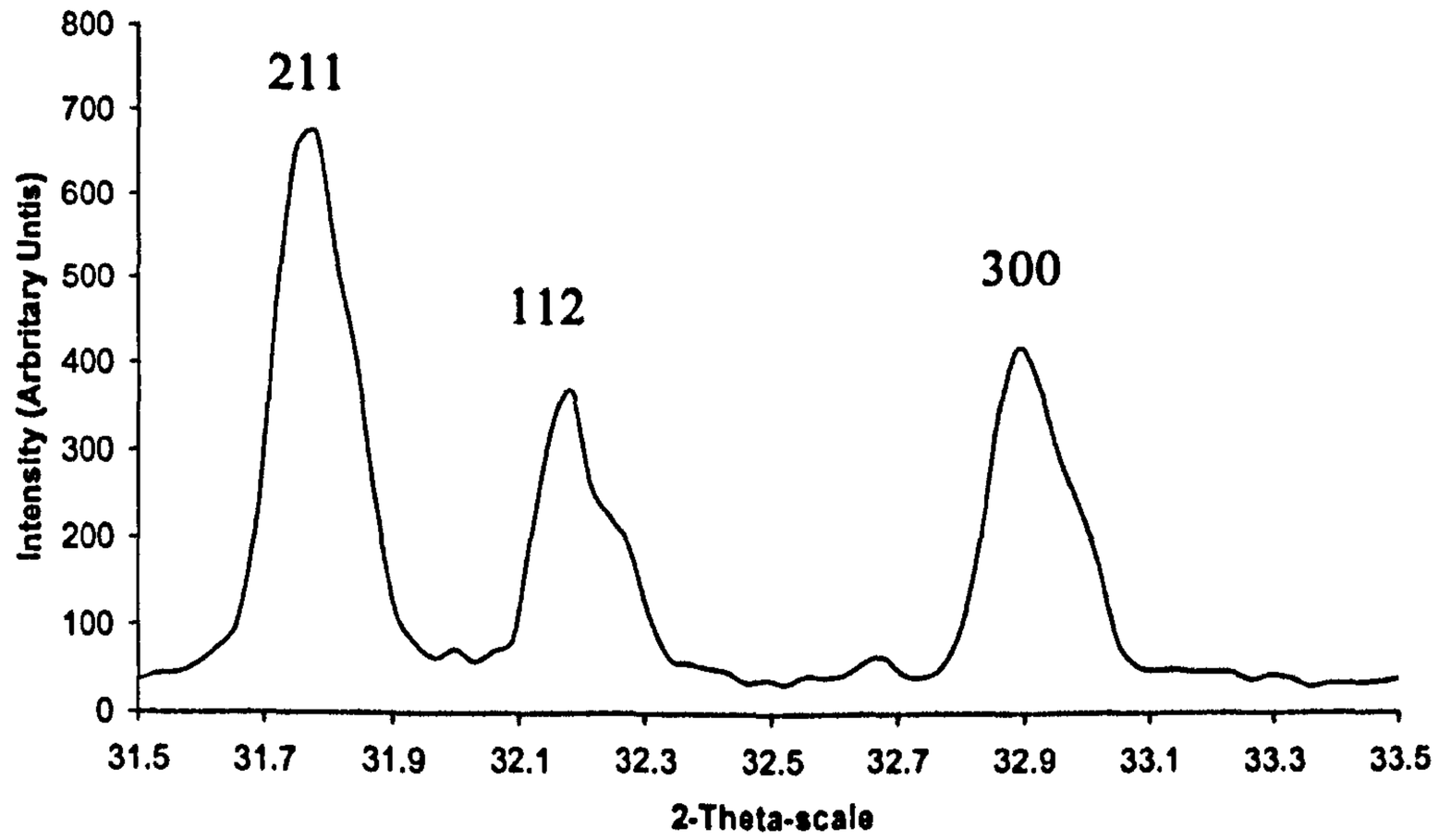

(b)

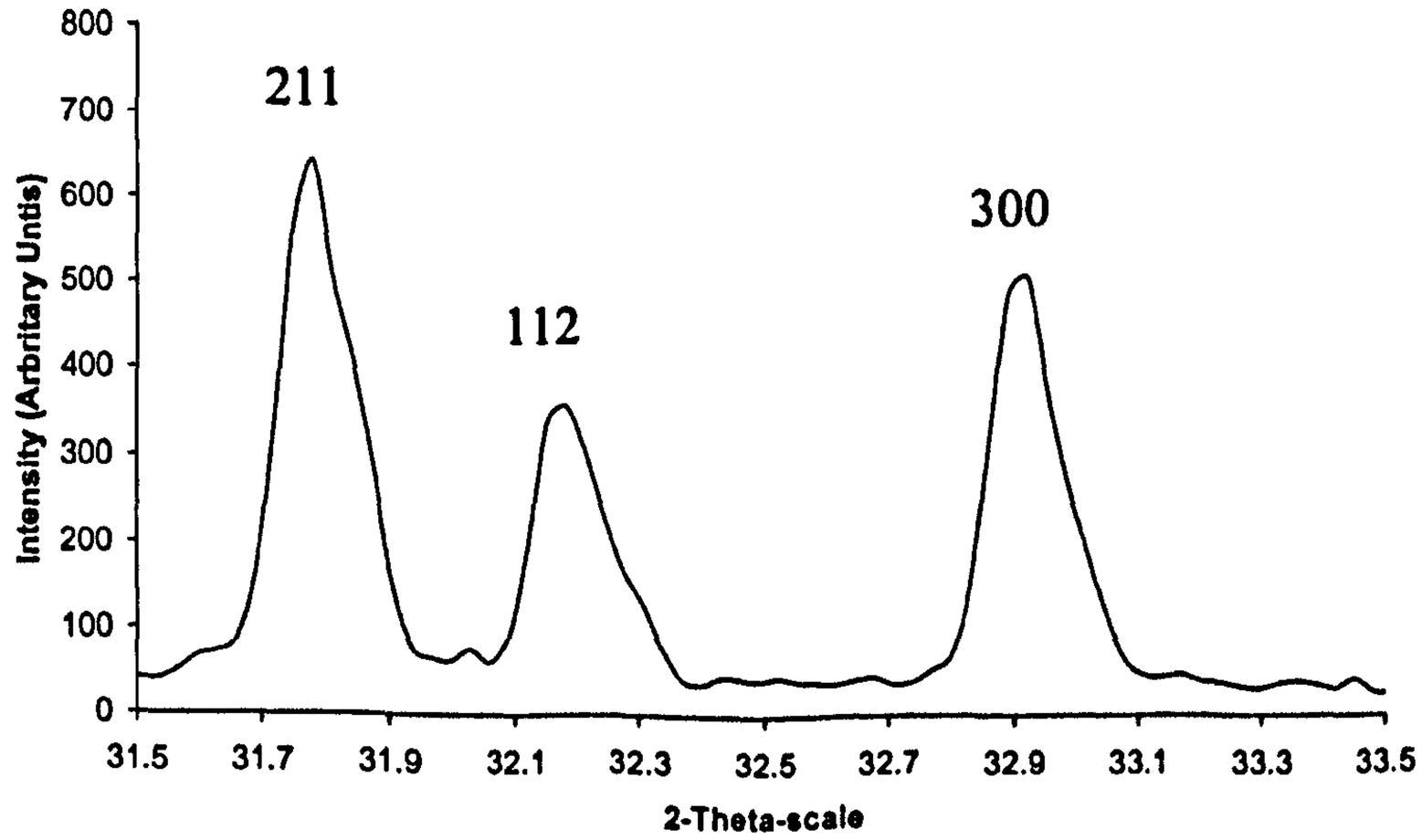

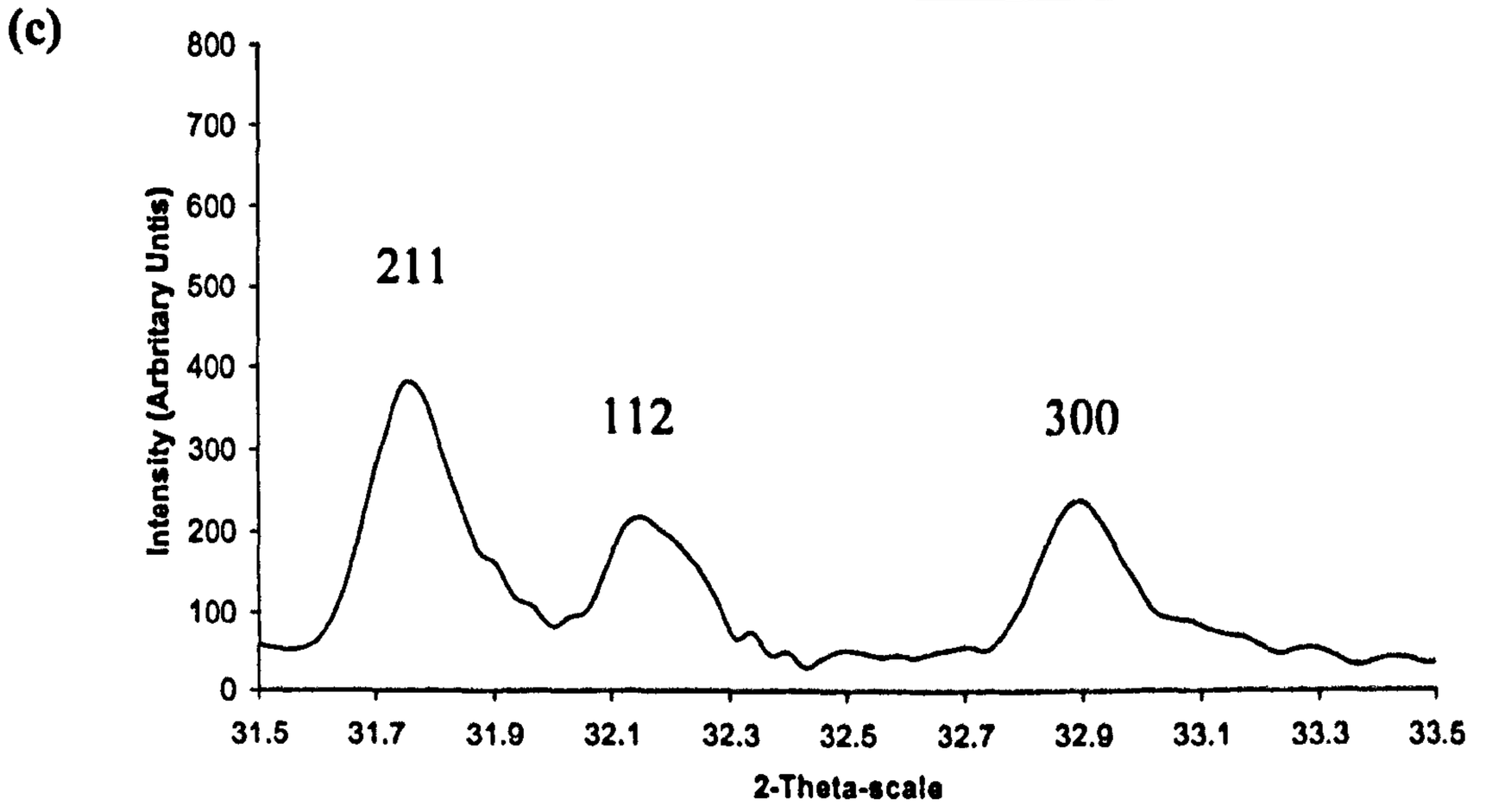

Figure 6.23: Expanded X-ray microdiffraction patterns in the region of (211), (112) and (300) peak. (a) 'Plasmabiotal' original disc; (b) Immediate surrounding unmodified area; (c) 10 MPa SF_6 modified area.

In addition, the enlarged, broader peaks of decreased intensity not only demonstrate a decrease in crystallinity of the irradiated sample but could also due to the formation (particularly with regard to the (300) peak) be convolution of the peaks from fluorinated hydroxyapatite (FA) and hydroxyapatite as opposed to merely fluorine substituted hydroxyapatite (FHA) (H.Qu *et al.*, 2005a).

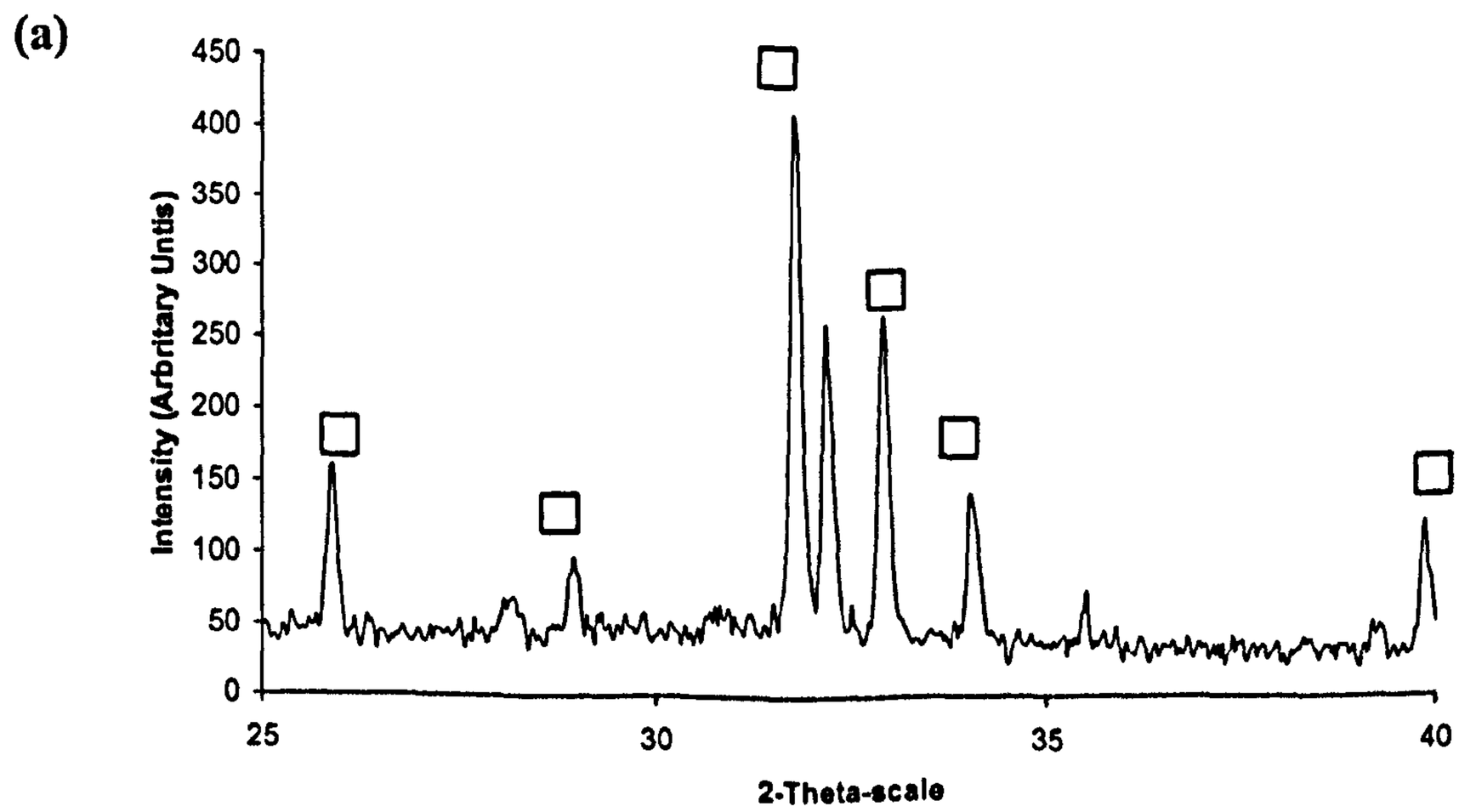

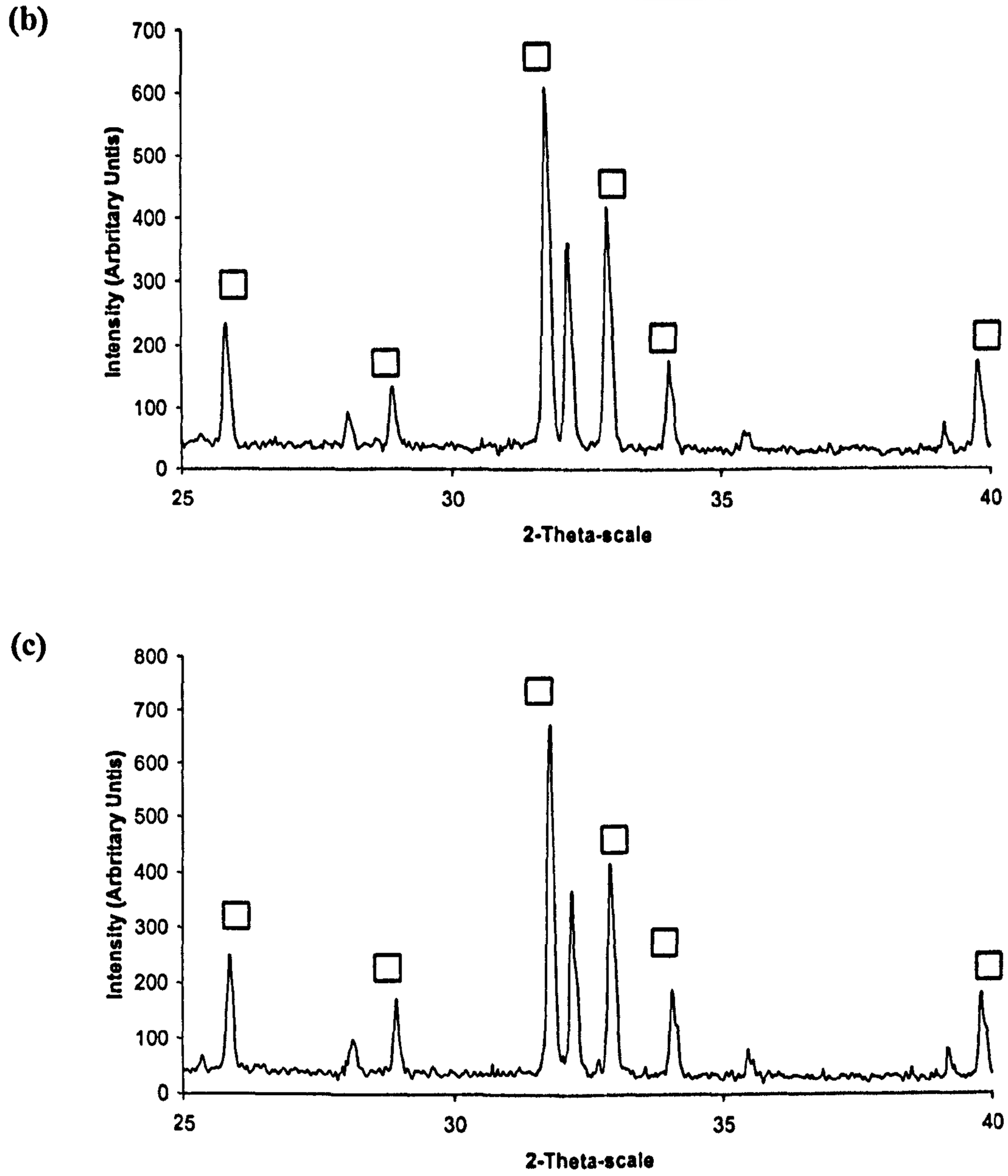

Figure 6.24: X-ray microdiffraction traces of HA samples before/after laser irradiation with 80 MPa NH_3. (a) 80 MPa NH_3 modified area; (b) Immediate surrounding unmodified area; (c) 'Plasmabiotal' original disc. (Key – □ HA, JCPDS pattern 09-0432)

The small amount of FHA featured by the XRD trace when compared to the larger quantity found by EDS analysis (Figure 6.18) would be due to the X-ray microdiffraction technique providing analytical information from below the immediate surface and further into the bulk composition than SEM-EDS analysis. Moreover, it has been shown in a number of previous studies that the XRD patterns of HA and FHA are of greater similarity than of comparative patterns of HA and FA, therefore the likelihood is for the surface chemical composition to be FHA as opposed to FA (M.Wei *et al.*, 2003; N.Rameshbabu *et al.*, 2006).

6.4.5 Raman analysis

The Raman spectra of the samples shown in Figures 6.25 and 6.26 were found to correspond with the Raman spectrum of HA and labelled accordingly. HA was confirmed as the major phase in the bulk composition by the presence of the strongest Raman active band of ν_1PO_4 mode defined in the spectra by the sharp, narrow peak at 962 cm^{-1} (M.R.Saeri *et al.*, 2003). Phosphate ions theoretically have four vibrational modes (ν_1-ν_4) that are all infrared and Raman active.

Of the four theoretical carbonate ion vibrational modes (ν_1-ν_4) only two can be seen in the Raman spectrum. The very low intensity carbonate ν_4 bands are rarely seen in the infrared spectra whilst appearing strong in the Raman spectra in addition to the ν_1 vibrational bands (I.R.Gibson *et al.*, 2000).

In the region of ν_2PO_4 bending mode two distinguishable peaks appeared at 430 and 450 cm^{-1}. The medium bands at 1047 and 1075 cm^{-1} were assigned to the stretching mode of ν_3PO_4. The stronger bands seen at 582, 590 and 609 cm^{-1} were assigned to factor group components of ν_4PO_4 bending mode (A.Antonakos *et al.*, 2007; L.Pramatarova *et al.*, 2004; M.R.Saeri *et al.*, 2003; M.Wei *et al.*, 2003). A further band has been previously reported appearing at 617 cm^{-1} that was not seen in this study (G.Penel *et al.*, 1997).

The majority of information relevant to the HA Raman spectrum is found below 1200 cm^{-1}. A band of medium intensity appearing at 3570 cm^{-1} has been previously assigned by others to the OH vibrational mode within the HA Raman spectrum. The information that can be provided by the O-H peak relates to peak intensity. Formerly de-Aza *et. al* (1997) reported that the intensity directly depends on the crystallinity of the sample (M.R.Saeri *et al.*, 2003).

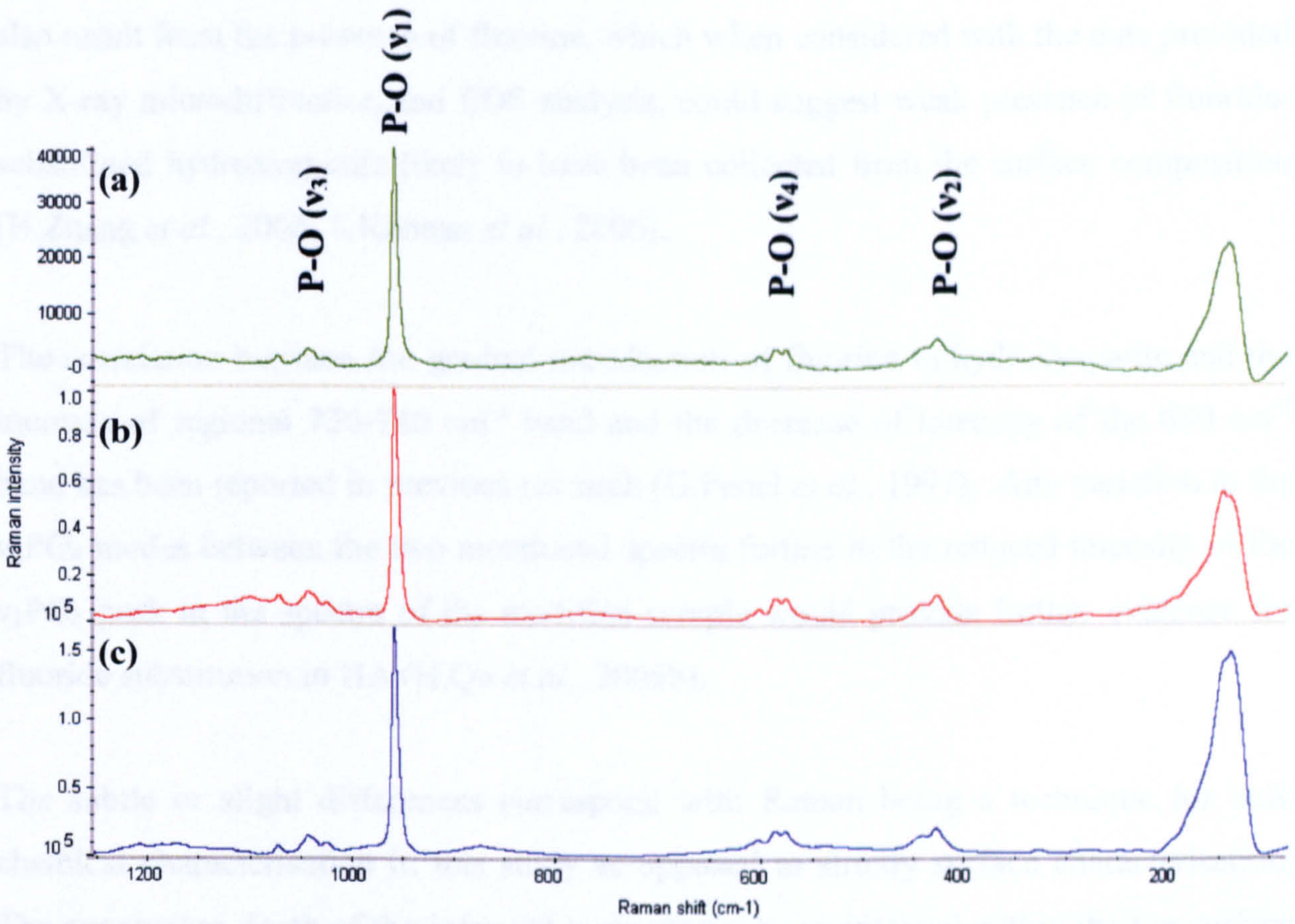

Figure 6.25: Raman spectra of HA samples before/after laser irradiation with 10 MPa SF_6. (a) 10 MPa SF_6 modified area; (b) Immediate surrounding unmodified area; (c) 'Plasmabiotal' original disc.

With regard to the spectra obtained for the laser irradiated sample with SF_6, in comparison to that obtained from plain unmodified HA, (Figures 6.25(a) and 6.25(c)) the vibrational/bending mode of the OH^- chain found at 630 cm^{-1} has a minimal peak resolution if any, suggesting a possible partial replacement of OH group with substituted F^- anions. It is known that the ν_2 vibration mode remains constant throughout the substitution range of hydroxyl by fluoride ions. Any shift in band frequency is identical to resolution and subsequently insignificant.

However, as the fluoride content increases the first and last of the ν_4 vibration mode bands have been found to decrease accordingly such that upon complete substitution, Fluoroapatite displays only two major bands around 608 and 591 cm^{-1} (G.Penel *et al.*, 1997). Despite the last of the ν_4 vibration mode bands not being clear in any of the spectra, the SF_6 laser irradiated sample shows a clear reduction in the intensity of the ν_4 vibration mode bands.

The further development of bands or a shoulder around the region at 730 cm^{-1} could also result from the presence of fluorine, which when considered with the data provided by X-ray microdiffraction and EDS analysis, could suggest weak presence of fluoride-substituted hydroxyapatite likely to have been collected from the surface composition (H.Zhang *et al.*, 2006; S.Kannan *et al.*, 2006).

The correlation between the gradual introduction of fluorine in hydroxyapatite and the increase of regional 720-740 cm^{-1} band and the decrease of intensity of the 630 cm^{-1} band has been reported in previous research (G.Penel *et al.*, 1997). Any variation in the ν_3PO_4 modes between the two mentioned spectra further to the reduced intensity of the ν_1PO_4 peak in the spectra of the modified sample would provide further evidence for fluoride substitution in HA (H.Qu *et al.*, 2005b).

The subtle or slight differences correspond with Raman being a technique for bulk chemical characterisation in this study as opposed to strictly surface characterisation. The penetration depth of the infra-red laser cannot be maintained within the top surface layers of dense opaque HA samples and so whilst X-ray microdiffraction and SEM-EDS techniques definitively established a fluoride-substituted surface, Raman could only provide partial surface chemical information with the majority applying to the bulk material.

Therefore, it can be assumed that the use of 10 MPa SF_6 at laser fluencies in the range of 14.50 to 15.20 kJ/m^2 is sufficient to provide a unique chemically enhanced surface topography composed of fluoride-substituted hydroxyapatite without altering the bulk chemistry of hydroxyapatite.

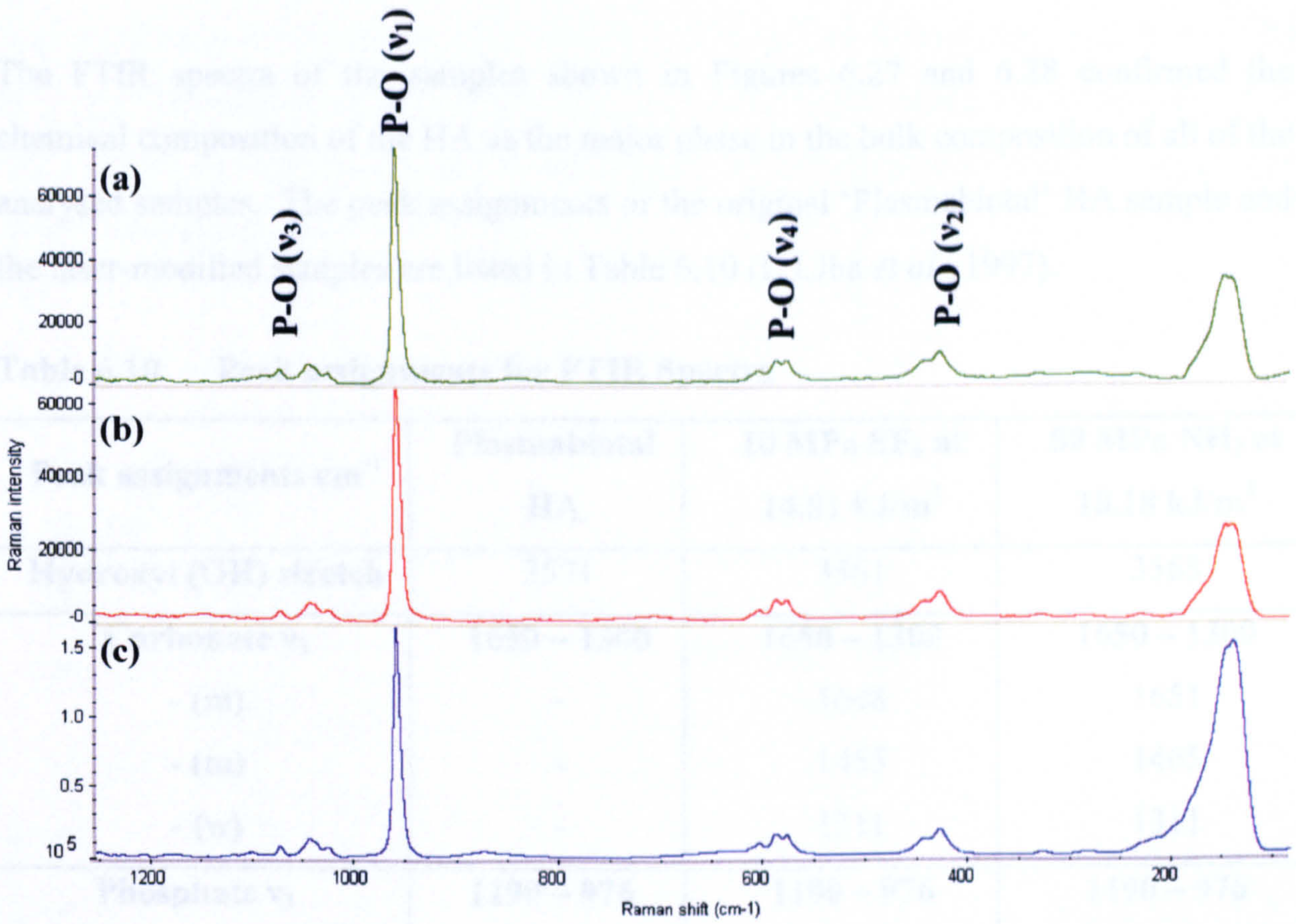

Figure 6.26: Raman spectra of HA samples before/after laser irradiation with with 80 MPa NH_3. (a) 80 MPa NH_3 modified area; (b) Immediate surrounding unmodified area; (c) 'Plasmabiotal' original disc.

With respect to the sample subjected to laser irradiation in the presence of NH_3 process gas, no other chemical phase other than hydroxyapatite was detected by Raman analysis (Figure 6.26). The result provides further evidence to the SEM-EDS and X-ray microdiffraction data for supporting the supposition that the use of 80 MPa NH_3 gas at laser fluencies in the range of 17.70 to 18.50 kJ/m^2 is sufficient to produce a unique surface topography upon sintered hydroxyapatite without altering the surface or bulk chemistry of the material. Structural modification however is accompanied by an increase in exposed surface hydroxyl groups.

6.4.6 FTIR Analysis

FTIR analysis is a technique for bulk material chemical characterisation as opposed to strictly surface characterisation as the penetration depth of the infra-red laser in the reflectance mode of this FTIR analysis could not be maintained within the top surface layers of dense opaque HA samples. Subsequently the FTIR analysis could only

provide partial surface chemical information with the peaks both from the surface and the bulk of the HA sample.

The FTIR spectra of the samples shown in Figures 6.27 and 6.28 confirmed the chemical composition of the HA as the major phase in the bulk composition of all of the analysed samples. The peak assignments of the original 'Plasmabiotal' HA sample and the laser-modified samples are listed in Table 6.10 (L.J.Jha *et al.*, 1997).

Table 6.10 Peak assignments for FTIR Spectra

Peak assignments cm^{-1}	Plasmabiotal HA	10 MPa SF_6 at 14.81 kJ/m^2	80 MPa NH_3 at 18.18 kJ/m^2
Hydroxyl (OH) stretch	3571	3561	3568
Carbonate ν_3	1650 – 1300	1650 – 1300	1650 – 1300
- (m)	-	1648	1651
- (m)	-	1455	1465
- (w)	-	1311	1311
Phosphate ν_3	1190 – 976	1190 – 976	1190 – 976
- (vs)	1190	1190	1190
- (vs)	-	1178	1091(w)
- (vs)	-	1091	-
Phosphate ν_1 – (m)	-	972	972
Carbonate ν_2 – (ms)	-	877	877
Phosphate ν_4	660 – 520	660 – 520	660 – 520
- (m)	-	-	-
- (vs)	-	-	-
- (vs)	-	-	-
Phosphate ν_2 – (w)	-	-	-

As previously mentioned, of the four theoretical carbonate ion vibrational modes (ν_1-ν_4) only three can be observed in the infrared spectrum. ν_2 and ν_3 vibrational modes are observed in the infrared spectra. The distribution of the carbonate ν_3 peaks depends on the maturation and formation of apatite crystals. Occupancy depends on competition between the phosphate and carbonate ions whilst occupancy of the ν_2 sites depends on competition between the OH^- and carbonate groups of the growing crystal.(I.R.Gibson *et al.*, 2000) Of the two sites occupied by carbonate ions the ν_3 vibrational mode

carbonate ion showing peaks in the 1650-1300 cm^{-1} region were observed split into three peaks at 1648, 1455 and 1311 cm^{-1} in the spectrum acquired for the 10 MPa SF_6 laser-modified sample and at 1651, 1465 and 1311 cm^{-1} in the spectrum acquired for the 80 MPa NH_3 laser-modified sample. In both cases, ν_2CO_3 mode was observed at 877 cm^{-1}. In the spectrum acquired for the original HA sample neither ν_2 or ν_3 vibrational modes were apparent.

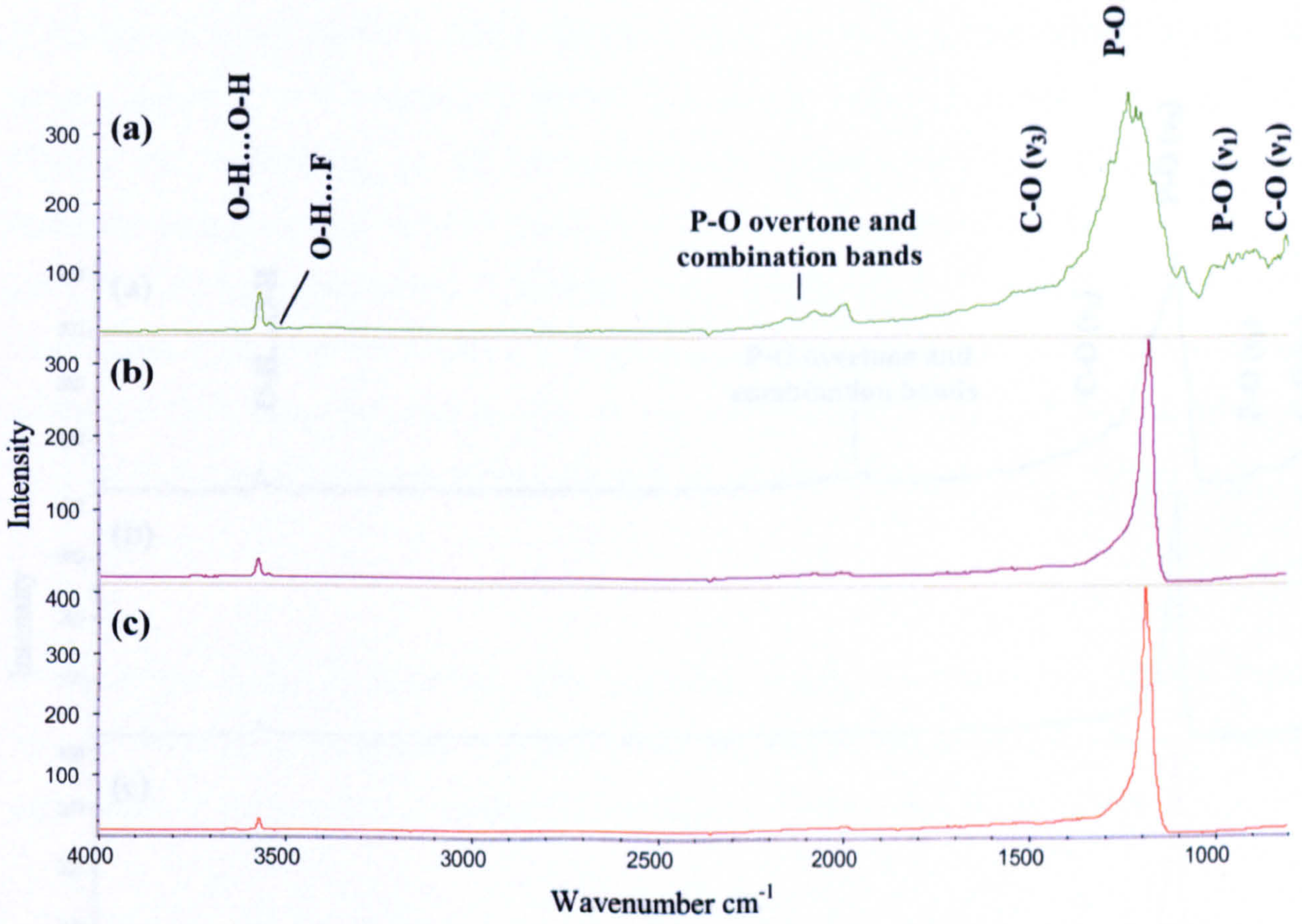

Figure 6.27: FTIR spectra of HA samples before/after laser irradiation with 10 MPa SF_6. (a) 10 MPa SF_6 modified area; (b) Immediate surrounding unmodified area; (c) 'Plasmabiotal' original disc.

Regarding the four phosphate vibrational modes (ν_1-ν_4) that are all infrared active, the ν_3 vibrational mode clearly defined at 1190 cm^{-1} in the spectrum of the original HA sample appeared somewhat higher than in previous reports (M.J.Phillips *et al.*, 2003). Reported observations of the ν_2PO_4 band at 440 and approximately 475 cm^{-1} are not in the wavelength range measured as is the case for the phosphate ν_4 bands reportedly present in the region of 633, 602 and 567 cm^{-1} (I.Rehman *et al.*, 1997). With respect to the laser-modified HA samples, (Figure 6.27(a) and Figure 6.28(a)) the ν_3 PO_4 mode was also seen both at 1178 (in the case of the 10 MPa SF_6 laser-modified sample) and 1091 cm^{-1}. The variation in position, intensity and appearance of the phosphate vibrational

mode ν_3 seen in the spectrum obtained for the 10 MPa SF_6 laser-modified sample can be attributed to the substitution of fluoride into the HA lattice (C.Silwood *et al.*, 2005; G.Penel *et al.*, 1997; M.Wei *et al.*, 2003). The phosphate ν_3 bands being of such high intensity are suggested to mask the carbonate ν_1 bands. The phosphate combination and overtone bands seen at approximately 2000 cm^{-1} appeared with greater intensity in comparison to the other spectra as did the presence of the carbonate ν_3 bands in the range of 1650 – 1300 cm^{-1} (C.Silwood *et al.*, 2005; H.Tanaka *et al.*, 2004).

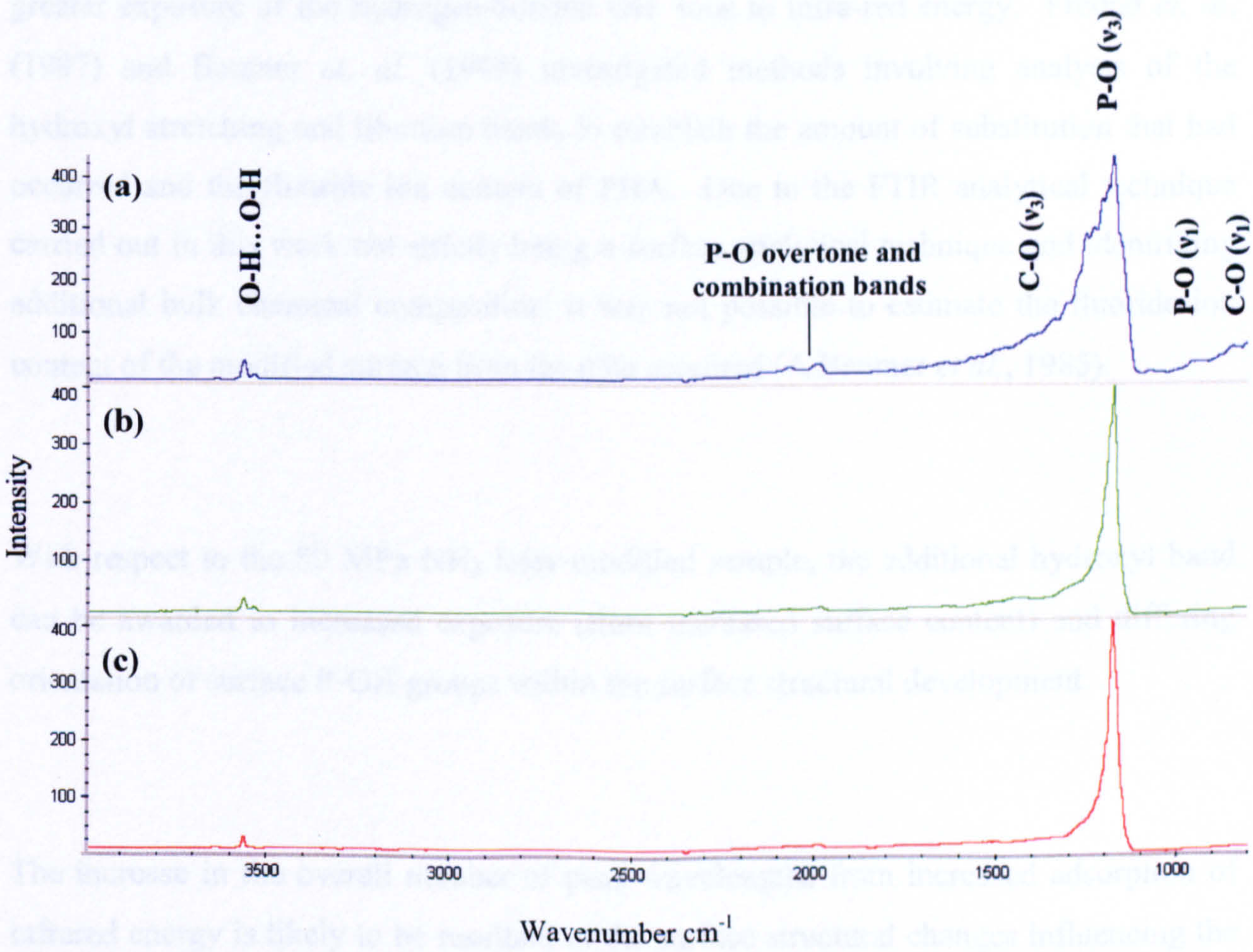

Figure 6.28: FTIR spectra of HA samples before/after laser irradiation with 80 MPa NH_3. (a) 80 MPa NH_3 modified area; (b) Immediate surrounding unmodified area; (c) 'Plasmabiotal' original disc.

For both spectra obtained from the successfully laser microstructured samples an additional weak hydroxyl stretching peak was observed at 3548 cm^{-1} in addition to the major hydroxyl peak appearing at 3568 cm^{-1} for the 80 MPa NH_3 laser-modified sample and in the shifted position at 3561 cm^{-1} for the 10 MPa SF_6 laser-modified sample. With respect to the 10 MPa SF_6 laser-modified sample (Figure 6.27(a)), fluorine substitution into the HA lattice is known to shift the hydroxyl stretching and libration

bands and furthermore split them into several bands. The peak assigments at 3561 cm^{-1} and 3548 cm^{-1} collaborate with previous reports to be the stretching mode of hydrogen-bonded OH^- ions (OH-OH and OH-F, respectively) (F.Freund *et al.*, 1997; G.Penel *et al.*, 1997; N.Rameshbabu *et al.*, 2006). Upon full and complete fluoride substitution for the hydroxyl group and the production of fluoroapatite (FA), the hydroxyl bands are completely absent from the FTIR spectrum (S.Kannan *et al.*, 2006). As fluorine subsitution increases the peak intensity is considered to decrease. However, in terms of this study the peak remained constant or increased slightly due to the bulk HA composition being detected further to the surface structural modification resulting in greater exposure of the hydrogen-bonded OH^- ions to infra-red energy. Freund *et. al.* (1997) and Baumer *et. al.* (1998) investigated methods involving analysis of the hydroxyl stretching and libration bands to establish the amount of substitution that had occurred and the fluoride ion content of FHA. Due to the FTIR analytical technique carried out in this work not strictly being a surface analytical technique and identifying additional bulk chemical composition, it was not possible to estimate the fluoride ion content of the modified surface from the data acquired (A.Baumer *et al.*, 1985).

With respect to the 80 MPa NH_3 laser-modified sample, the additional hydroxyl band can be awarded to increased exposure (from increased surface content) and differing orientation of surface P-OH groups within the surface structural development.

The increase in the overall number of peak wavelengths from increased adsorption of infrared energy is likely to be resultant of the surface structural changes influencing the positioning (length and orientation) and exposure of the bonded molecules within the structure, further to the high temperatures achieved during laser treatment resulting in a material surface with increased crystallographic symmetry. The temperature of the HA surface during laser processing (particularly during re-melting) can reach up to 3000 °C (C.Chen *et al.*, 2005).

The FTIR analysis corroborates with the previous data supporting the assumption that the use of 10 MPa SF_6 at a laser fluence of 14.81 kJ/m^2 (or in the range of 14.50 to 15.20 kJ/m^2) is sufficient to provide a unique chemically enhanced surface topography

composed of fluoride-substituted hydroxyapatite and that the use of 80 MPa NH_3 gas at a laser fluence of 18.18 kJ/m^2 (or in the range of 17.70 to 18.50 kJ/m^2) is sufficient to produce a unique surface topography upon sintered hydroxyapatite with an increase in exposed surface hydroxyl groups. In both cases the bulk HA composition remains unchanged and in the case of the latter type of surface modification there is no change to the surface chemical composition either.

Chapter 7 Discussion

Overview

The results found within this study are discussed in two main sections giving importance to the separate subject areas of; (i) Hydroxyapatite synthesis and processing and; (ii) Laser surface modification of hydroxyapatite. Both areas are discussed with significance to improving hydroxyapatite as an orthopaedic biomaterial with specific application in osseous tissue replacement. The initial study contains reference for methods and processing variables employed to improve the powder quality required for advanced material mechanical properties, while the following principal section documents the effects of a novel method of laser surface modification aimed to improve the bioactivity of the material through surface chemical composition and microstructuring. Previous research is discussed initialising the study with present results evaluated for relevance to the aim and significance for future work.

7.1-Hydroxyapatite Synthesis and Processing

7.1.1 Particle Morphology

The wet chemical synthesis of hydroxyapatite (HA) otherwise known as "bulk" precipitation, has been previously shown to yield powdered products with large primary particles and wide particle size distributions (Figure 2.2) due to the inability to effectively control flocculation of particles during synthesis and therefore requiring post processing treatments such as ball-milling in order to produce fine, free-flowing particles without agglomeration (M.J.Phillips *et al.*, 2003). Emulsion technology has permitted the synthesis of nanoparticle HA by the chemistry being restricted to within tiny (micro- or even nanosized) droplet reactors that resultantly reduce particle flocculation and limit particle growth. Such "Water in oil" emulsion systems have been shown to increase the interfacial area of the water providing droplet reactors of controlled size and uniform shape that can be utilised in the processing of nanosized, spherical HA particles (G.K.Lim *et al.*, 1997; M.G.S.Murray *et al.*, 1995). The manufacture of free-flowing, spherical (for good packing properties), nanosized HA powders are highly desirable for high strength bone grafts and other load bearing applications that require sufficient replacement of the complex structure and superior

mechanical properties of bone (A.S.Edward *et al.*, 2001; A.Santomaso *et al.*, 2003; E.C.Abdullah *et al.*, 1999; M.G.S.Murray *et al.*, 1995).

Within this study, HA powder was produced by methods of: (i) conventional wet precipitation; (ii) microemulsion technology and; (iii) macroemulsion technology. Commercially wet precipitated hydroxyapatite powders, 'Apatec' and 'Plasmabiotal' were also used for comparative study, investigating the specific surface area and grain size of the powdered samples. Brunauer-Emmett-Teller (BET) surface area analysis of as-prepared powdered samples and after thermal treatment at 1200 °C for 2 hrs, correspond with previous reports and are summarised in Table 6.1 (M.J.Phillips *et al.*, 2003). The commercial grade 'Plasmabiotal HA' and premium grade 'Apatec' HA that were produced by wet chemical "bulk" precipitation methods and oven dried to powder, portrayed surface areas of <100 m^2/g and large particulate size similar to previous reports. The surface areas and of the powders produced by "water in oil" macro- (148 m^2/g) and microemulsion (170 m^2/g) technology were at least double that of the conventionally precipitated powders before undergoing thermal treatment. Similarly the corresponding particle sizes were diminutive (<15 nm using BET surface area analysis), collaborating with previous research to demonstrate emulsion technology as superior to conventional wet precipitation routes in the production of small particulate powders with high surface area (G.K.Lim *et al.*, 1996; G.K.Lim *et al.*, 1997). The mean crystal sizes of the powders as determined by Scherrer formula showed the same trends and confirmed the relevance of the values determined with BET surface area analysis despite the difference in the calculated figures. Figure 6.4 portrays different values to those displayed in Table 6.1 or Figure 6.1 as a result of the two techniques measuring different things. The use of Scherrer formula determines the mean crystal size that is a measure of a coherently diffracting domain. Due to the presence of polycrystalline aggregates or agglommerates, crystal size is not the same as particle size. BET surface area analysis for size determination, measures the particle size rather than the crystal size using the total surface area of a particle including the surface area of the aggregates within the particle. Therefore, the crystal sizes provided from Scherrer's formula are much less in value than the calcined particle sizes provided from BET surface area analysis and can furthermore, provide an indication of the extent of powder agglommeration. The crystal sizes provided from Scherrer's formula are of calcined

powder offering reason for the values being higher than the uncalcined particle sizes provided from BET surface area analysis. Using Table 6.1 and Figure 6.4 it is apparent that the powders showing minimal agglomeration were produced by emulsion methods.

Conventional processing methods produce powders with large primary particles and low surface areas (< 100 m^2/g), with the use of oven drying producing surface areas of typically 55-90 m^2/g (P.Shuk *et al.*, 2001). The use of freeze drying has been reported to provide powders of a smaller mean grain size and narrower grain size distribution that is reflected in a higher surface area value (H.Lu *et al.*, 1998). With regard to the as-prepared powder properties, (Figures 6.1 and 6.2), the commercial grade 'Plasmabiotal' HA that was produced by 'bulk' wet chemical precipitation and oven dried featured the lowest surface area (15 m^2/g) and the largest particle size (126 nm) followed by the premium grade 'Apatec' HA produced by the same processing route corresponding with previous knowledge that particle agglomeration during the prolonged oven drying period gives rise to a larger particle size with a wider particle size distribution. Between the two grades of powdered material a significant difference in surface area and particle size was also observed that could be resultant from a number of variables during the synthesis stage such as reaction time or temperature. However, the conventionally "bulk" precipitated powder that was freeze-dried demonstrated a higher surface area of 101 m^2/g and a reduced particle size of 19 nm, that can be attributed to the superior drying technique. The result corresponds well with previous work where it has been deduced that oven drying of as-prepared HA powders can produce agglomeration through further "ageing" of the product during the prolonged drying period (typically over 24 hrs) that significantly lowers the powder surface area (M.J.Phillips *et al.*, 2003). Freeze-drying techniques involve drying small sections of precipitate in sequential order and less time resulting in little opportunity for particle agglomeration and is subsequently a superior drying technique. However, upon consideration of the mean crystal size calculated by Scherrer's formula after thermal treament that was 57 nm and comparing it to the mean particle size calculated from BET surface area analysis that was 47,468 nm (the largest particle size featured by any of the powder samples), it is clear that a considerable amount of agglomeration has taken place and marginally more so than for any of the other powder samples as demonstrated by Tables 6.1, 6.2 and Figure 6.4. Despite this, the benefits of the freeze-drying technique may be apparent in

the final sintered product as the HA disc produced with this powder after isostatic pressing at a pressure of 0.59 MPa and pressureless sintering at 1200 ˚C for 2 hrs featured a measured density of 3136.36 kg/m^3 and being determined as > 99 % dense would be likely to feature the best compressive strength of all of the sintered products.

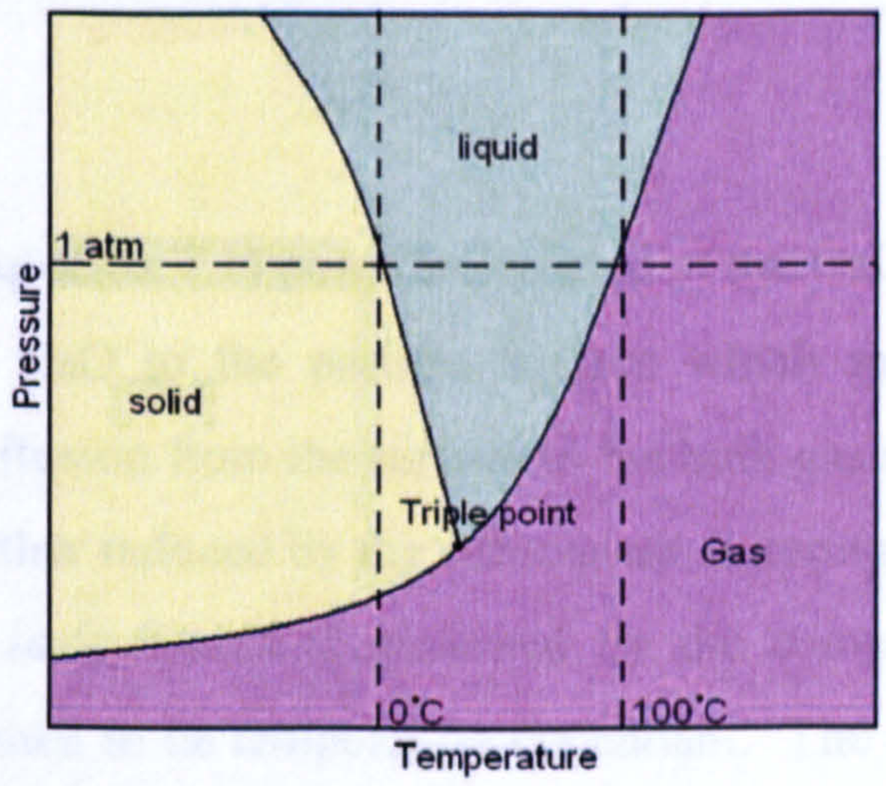

Necessary pressure and temperature values of the different phases of water.

Figure 7.1: Phase diagram of water.

The process occurs by freezing the precipitate material below the eutectic point before reducing the surrounding pressure and adding enough heat to allow the frozen water in the material to sublime directly from the solid phase to gas. The increased powder grain growth demonstrated after thermal treatment (Table 6.1) corresponds to the decreased surface area (BET) (Figure 6.2). As previously introduced (Section 3.4.1), calcination refers to the thermal treatment carried out for modification of the raw (as-prepared) powder to feature properties beneficial for subsequent processing. The recommended temperature for calcination of HA is 900 ˚C for optimal mechanical properties when combined with sintering the green body at 1200-1250 ˚C (H.Juang *et al.*, 1996; M.J.Phillips *et al.*, 2003). The purpose of calcination at the higher temperature of 1200 ˚C was for qualitative analysis of the chemical composition of the materials using XRD techniques in addition to suggesting the particle properties featured in the final product in disc form where processing employs a sintering period of 2 hrs at 1200 ˚C. During calcination of the powdered samples at the high temperature normally used for sintering

pre-calcined and pressed powders it would be likely that both calcination and sintering processes were occurring simultaneously. The simultaneous calcination and sintering of calcium based sorbents such as calcium hydroxide ($CaCO_3$) to calcium oxide (CaO) is employed in the fuel industry during the removal of sulphur from the combustion of coal.

$$CaCO_3(s) \rightarrow CaO(s) + CO_2(g)$$

(Equation 7.1)

During the reaction (Equation 7.1) pores are created at the CaO-$CaCO_3$ interface where CO_2 diffuses through CaO to the particle surface which may initially increase the surface area prior to diffusion from the surface to the bulk gas resulting in the continued loss of surface area further reduced by the subsequent sintering of the calcinate (nascent CaO). The resultant surface area is governed by the comparative rates of the two processes that have shown to be temperature dependant. The sintering rate tends to be higher than the calcination rate but less sensitive to temperature. Therefore the resultant surface area is always much lower (J.Agnew *et al.*, 2000). Similarly during the calcination of HA at 1200 °C, adsorbed moisture, carbonates and chemicals remaining from the synthesis stage, such as ammonia (NH_3) are removed as gaseous products reducing the particulate surface area in accordance with the same shrinking core model where small dispersed particles are assumed to decompose under isothermal conditions, removing heat and mass transfer limiting rates. The gas diffusion and chemical changes facilitate an increase in density and a concurrent increase in crystal size with a decrease in the specific surface area (M.J.Khon *et al.*, 2002).

Previously it has been shown that with decreasing Ca/P ratio of the as-prepared powder an increase in the resultant grain size is accompanied by a drop in the densification ratio after calcination at lower temperatures (S.Raynaud *et al.*, 2002b; S.Raynaud *et al.*, 2002a). Calcination generally tranforms 'finer' populations into 'coarser' populations with increasing temperature resulting in a larger mean particle size and a narrower particle size distribution. At the recommended calcination temperature of 900 °C the distribution is uni-modal. Furthermore the packing efficiency is increased with increased calcination temperature and subsequent agglomerate sizes but despite the

higher green density the sintered density (unless sintered at high temperatures such as 1350 °C which are detrimental to strength due to exaggerated grain growth), does not reach the same amount as for samples calcined at lower temperatures (H.Juang *et al.*, 1996). At high calcination temperatures such as 1200 °C the initial powders undergo more apparent agglomeration and there may be increased particle size distribution which would have been taken into consideration by the BET specific surface area analysis and subsequent results relating to particles size. 'Packing' refers to the re-arrangement of particles towards a reduction of interparticle voidage without affecting the original particle shape and dimension (A.Santomaso *et al.*, 2003).

'Plasmabiotal' HA featured the largest calcined particulate surface area (and therefore smallest particle size) which although beneficial for biomedical application the low surface area (less than 100 m^2/g) of the as-prepared material could facilitate microstructural heterogeneities and differential shrinkage leading to crack-like flaws in the sintered product (A.Afshar *et al.*, 2003; M.J.Phillips *et al.*, 2003). Despite both the macroemulsion and microemulsion synthesised powders featuring very high as-prepared surface areas i.e. exceeding 150 m^2/g, thermal treatment resulted in the largest seen loss or difference in surface area and subsequent gain in particle size (Figure 6.3).

Regarding the emulsion routes employed in this study, in addition to the gain in powder particle size after thermal treatment, the lengthy process with minimal powder yield discouraged use of emulsion technology as an efficient or comparative processing route for bulk synthesis of HA powder. An increase in temperature was investigated in order to improve the efficiency and increase the powder yield of the macroemulsion route. However, it had been previously demonstrated that for both wet chemical precipitation and emulsion synthesis of HA the crystallinity and crystallite size of the HA product particles increase with an increase of reaction temperature in addition to an increase in the ripening or 'ageing' time of the precipitates (A.Osaka *et al.*, 1991; T.Furuzono *et al.*, 2001; Y.X.Pang *et al.*, 2003). At high reaction temperatures it is understood that the rate of particle ripening is high permitting the precipitates to grow large during the allotted time (C.Kothapalli *et al.*, 2004). However unlike wet chemical precipitation where smaller precipitates show the tendency to develop into large agglomerates so as

to minimize surface energy, the emulsion derived small precipitates remained within the nanocrystalline range as indicated within the results (Table 6.2) (C.Kothapalli *et al.*, 2004; I.R.Gibson *et al.*, 2001). Within the emulsion system, individual nanoreactors (Figure 3.3) serve to control precipitate growth and prevent flocculation by containment allowing ease of movement (K.Wei *et al.*, 2005; T.V.Thamaraiselvi *et al.*, 2004). An advantage of these smaller agglomerates can be reflected in sintered density following the physical basis of the Herring law of sintering, where the sintering rate at a given temperature is inversely proportional to the square of the powder particle size. Following this, the smaller the agglomerate size of a powder, greater is the ease to achieve high sintered density at the given sintering temperature. Hence higher surface area powders (above 100 m^2/g) can be sintered at approximately 150 °C lower than powders with a low surface area (C.Kothapalli *et al.*, 2004; I.R.Gibson *et al.*, 2001). A high compacted and sintered density such as that achieved after macroemulsion synthesis in this study (Table 6.3) corresponds with optimum mechanical properties such as biaxial flexural strength desirable for many types of HA orthopaedic application (M.G.S.Murray *et al.*, 1995). The highest sintered density was achieved using the conventionally "bulk" precipitated powder that was freeze-dried. Again this was likely to be resultant of the superior drying technique employed that offers little time for the formation of particle agglomerates and therefore improves sintering properties. The initial grain size was larger than that of the macroemulsion manufactured HA powder (Table 6.1) and could suggest a larger particle size distribution. Therefore despite the achieved higher density, microstructural heterogeneities may exist within the manufactured product that can endorse catastrophic or brittle failure during future application.

Corresponding to previous studies the results documented in Table 6.2, show that an increase in temperature did result in an increase in the average particle size of the resultant powder (K.Sonoda *et al.*, 2002). As desired, the powder yield increased with an increase in temperature up to 25 °C and in order to increase the yield of production, the slight gain in the grain size (< 4nm) would be acceptable due to the production yield being almost double that of the system maintained at the original reaction temperature of 17 °C. Sodium bis(2-ethylhexyl)sulfosuccinate or Na-AOT was the anionic surfactant facilitating the reverse micelles in "water-in-oil" macroemulsions and

research suggests that when reaction temperature rises, the amphiphile molecule gradually decreases its hydrophobicity and the "water-in-oil" emulsion system becomes unstable, resulting in the growth of larger micelles than at lower temperatures and subsequently the growth of larger crystals (K.Sonoda *et al.*, 2002; T.Stoebe *et al.*, 1997). However at a reaction temperature of 25 °C the micelle cavity of the Na-AOT molecule would be stable in the emulsion system because of the hydrophilicity of the surfactant molecules being higher than that over a cloud point typically associated with nonionic surfactants (the temperature at which a solution of a surfactant starts to form micelles or molecular agglomerates, thus becoming cloudy) and so the slight increase in grain size observed with the increase in yield may simply be due to a faster crystal growth rate with the increased temperature from 17 °C (K.Sonoda *et al.*, 2002).

7.1.2 Powder purity

X-ray diffraction was employed to chemically characterise the powdered samples before and after thermal treatment at 1200 °C. The initial small particle size of the as-prepared powders resulted in XRD traces with very broad peaks. The XRD traces after powder calcination featured sharp, distinct peaks of good intensity in all cases allowing accurate chemical identification. Previous research denotes that the greater the intensity of the peaks, the greater the crystallinity within the sample which corresponds with the knowledge that calcination serves to increase the crystallinity of the initial powder (D.R.Villarreal *et al.*, 1998; H.Juang *et al.*, 1996).

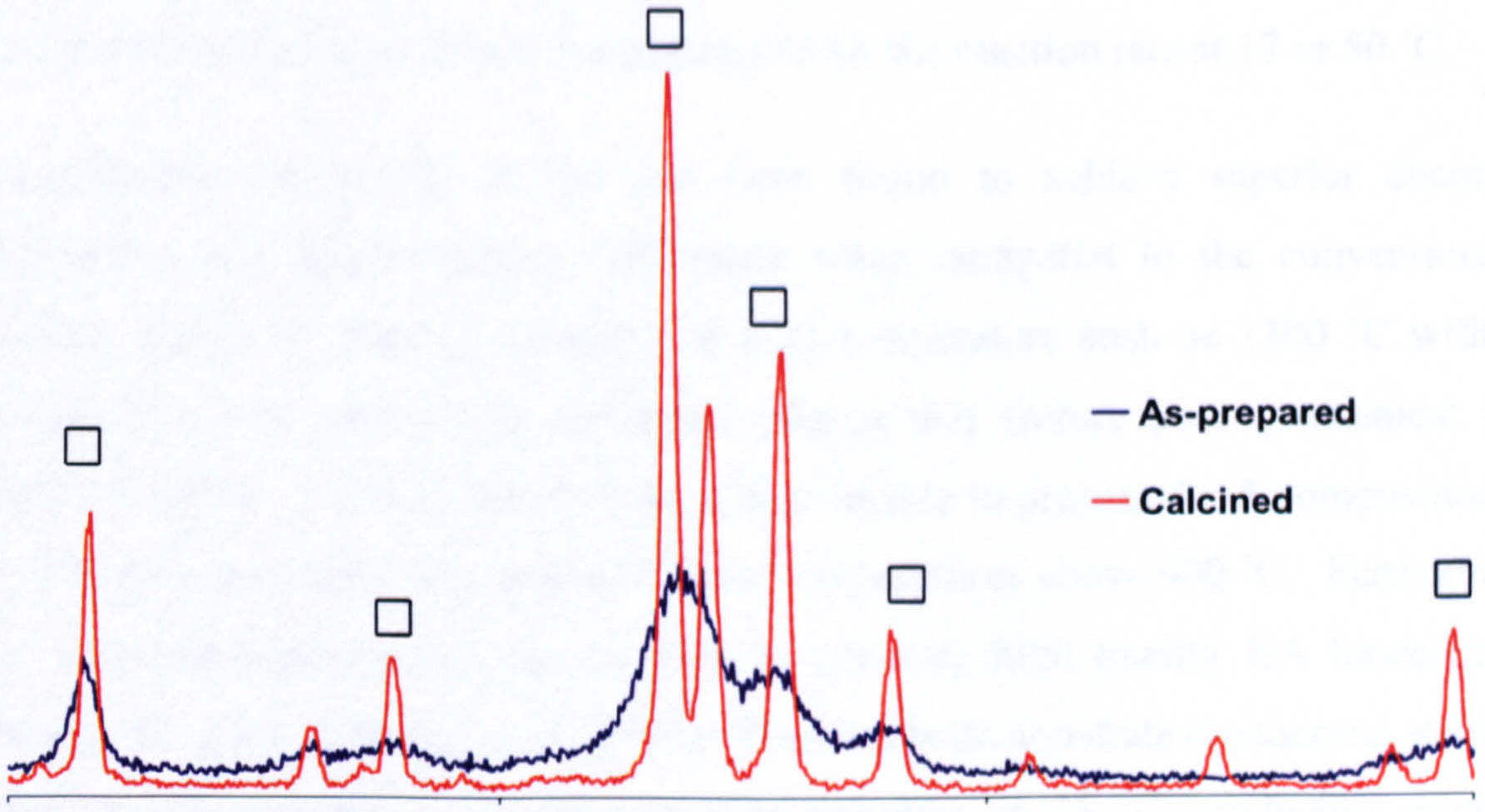

Figure 7.2: XRD trace of precipitated HA powder before and after calcination.

(Key – □ HA, JCPDS pattern 09-0432)

Moreover, physical and chemical defects are known to be detectable by X-ray analysis after treating the specimens at a high temperature of approximately 1200 – 1300 °C (A.Afshar *et al.*, 2003). Secondary minor phases such as calcium hydroxide $Ca(OH)_2$ or β-$Ca_2P_2O_7$ when present in small amounts are no longer masked by the response of the major phase after thermal treatment and can be detected by the presence of CaO or $CaHPO_4$ (S.Raynaud *et al.*, 2002a). During the X-ray diffraction characterisation of the heat-treated powders, all samples were found to be phase pure hydroxyapatite except in the macroemulsion produced powders at 17 and 50 °C where small amounts of 'Calcite' $CaCO_3$ (Figure 6.6(b)) and 'Whitlockite' (TCP) $Ca_3(PO_4)_2$ were found respectively (Figure 6.6(d)). In both cases, the secondary phases were detected by XRD investigation prior to thermal treatment, removing thermal decomposition as grounds for their presence. A likely explanation equates to pH fluctuations within the emulsion systems that were less controllable in comparison to systems employed for conventional wet precipitation, further to an inappropriate rate of reaction occurring during synthesis. Large amounts of ammonia were required to maintain the inherently low pH of the reaction mixture at 10.5. The results suggest that the rate of and amount of ammonia

addition was compatible with the rate of the reaction when carried out at 25 °C to facilitate the precipitation of HA, but unsuitable for the reaction rate at 17 or 50 °C.

Nanocrystalline processing of HA has been found to achieve superior chemical homogeneity and microstructural uniformity when compared to the conventionally processed materials allowing treatment at high temperature such as 1200 °C without decomposition into undesirable secondary phases that feature poor mechanical and chemical stability. Previous methods have been unable to prevent the decomposition of HA powder to tricalcium phosphate (TCP) at temperatures above 900 °C. Furthermore lower sintering temperatures can be used to generate high quality HA bioceramics (E.Ahn *et al.*, 2001; S.Zhang *et al.*, 1997). The results demonstrate the thermal stability of the emulsion synthesised nanocrystalline powders at 25 °C producing calcined powders of comparable phase purity and microstructural uniformity to those presently found in medical usage i.e. 'Apatec' and 'Plasmabiotal' HA powders. In addition the results confirm that there is no compromise in chemical homogeneity or thermal stability by application of microemulsion synthesis to macroemulsion synthesis at 25 °C of nanocrystalline HA, providing a feasible option to increase the product yield.

7.2 Laser Processing of Hydroxyapatite

The unique material interaction of pulsed ultraviolet laser light enables micro-machining and micro-processing of large variety of materials. Highest spatial resolution down to 1 μm is achieved by using short wavelength. The precise ablation of material is achieved due to the high photon energy and high absorption of the ultraviolet light in many materials such as polymer, ceramic and metal materials. Lasers have been used in various fields of medicine and biomedical technology, with significant impact on surgery in dental, dermatology and ocular fields, further to pulsed laser deposition (PLD) providing a method of coating metallic implants with HA so as to take advantage of the bioactivity preserving the mechanical performance of the metallic structure for orthopaedic applications (J.M.Fernandez-Pradas *et al.*, 2003; K.Nakata *et al.*, 2007). Recent developments in laser modification of material have involved the use of laser ablation in the presence of sulphur hexafluoride (SF_6) process gas to create regularly shaped and spaced conical structures on silicon wafers and similar claims of a surface topography consisting of cone-shaped features on the surface of HA material using a

similar excimer laser without the presence of a process gas (A.Queiroz *et al.*, 2004; D.Mills *et al.*, 2004).

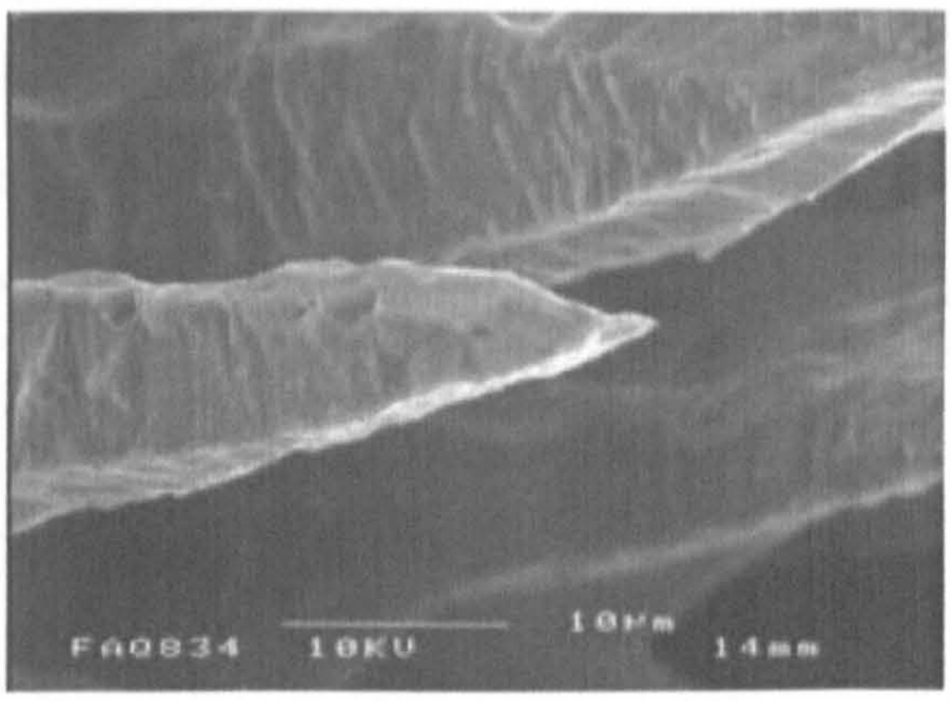

Figure 7.3: Scanning electron micrograph of silicon pillars formed in the presence of SF_6 using nanosecond irradiation (D.Mills *et al.*, 2006; K.W.Kolasinski, 2004).

As discussed, HA is a widely used bioactive ceramic but due to the brittle property inherent to ceramic materials, shaping and machining or surface modification and structuring is difficult. Laser ablation of HA using ultraviolet light has been previously researched, but with the majority relating to laser plume behaviour and thin film coating of hydroxyapatite (K.Nakata *et al.*, 2007). In this study, the fine surface modification intended with micro machining by using a femtosecond XeCl excimer laser (308 nm, ~180 mv or 0.072 J per pulse, 20 ns pulse width) focused onto sintered HA discs has been evaluated using different laser fluences in the presence of SF_6 and NH_3 process gases. The lasing conditions were adapted from previous work resulting in ordered arrays of cones or spikes on single crystal silicon wafers, with the aim of producing similar surface structures of regular order on HA (K.W.Kolasinski, 2004).

The previously investigated HA powders were processed under the same conditions into sintered discs for the laser surface modification evaluation. However only the discs produced with 'Plasmabiotal' HA resulted in reproducible, consistent and defined surface structures when subjected to laser irradiation, suggesting the optimal density of 2482.95 kg/m^3 and 21.5 % porosity for this procedure (Table 6.3). Featuring the largest

particle size of the powders employed, the produced discs had the greatest porosity. The lower sintered density would result from the larger particle size of the powder. As afore mentioned, HA powder consisting of very fine particles has much higher surface area, which is the driving force for solid state sintering and the amount of surface free energy decrease is proportional to the free energy decrease for the sintering reaction (Figure 3.6) (N.Y.Mostafa, 2005; Y.Sung *et al.*, 2004). Serra *et. al.* (1997) state that for lower HA density targets, the ablation rate is higher than for counterparts of higher density.

7.2.1 Surface Microstructuring

The type of surface structure varied with the type of processing gas employed in the lasing chamber, collaborating with results established in previous studies employing silicon (D.Riedel *et al.*, 2004; K.W.Kolasinski, 2004). The use of 10 MPa SF_6 gas at laser fluencies within the range of 14.50-15.20 kJ/m^2 (Table 6.8) permitted the development of a roughly columnar topography, which although lacked placement in regular arrays, demonstrated fairly even sizing. Within this range the most regularly sized and distributed surface structures were formed using a laser fluence of 14.81 kJ/m^2 (Figure 6.12). In contrast the surface topography created through the use of 80 MPa NH_3 gas in the ablating atmosphere at laser fluencies of 17.17-18.50 kJ/m^2 demonstrated irregular shaped hillocks with random size and spacing as depicted clearly in SEM analysis. The most even formation was created using a laser fluence of 18.18 kJ/m^2 (Figure 6.12). Although differing in structural morphology, this finding collaborates well with the previous work carried out on single crystal silicon. The different material properties would explain the difference in the resultant structural developments.

It has been demonstrated a number of times that the repetitive pulsed-laser irradiation of materials at relatively low laser energy densities (>10 kJ/m^2) produces gradual changes in surface topography and the development of 'laser-induced periodic surface structures'. Observed in metals, polymers, semi-conductors and ceramics, the surface modifications are well documented. At higher energy density values (10-50 kJ/m^2) such as those established within this study and typically used for pulsed-laser deposition of

thin films, columnar or conical structures are formed on the laser ablation targets, with the features pointing along the incident laser beam direction.

Pulsed excimer laser irradiation requires an oxidizing atmosphere (containing oxygen or fluorine) to form columns or cones. The shape of the microstructures (straight columns or steeply sloping connected by walls) is governed by the type and concentration of the oxidizing species (D.H.Lowndes *et al.*, 2000).

7.2.2 Structural characterisation

The sectioned SEM images (Figure 6.15) demonstrated the ability of laser treatment to change surface morphology with the advantage of preserving the bulk mechanical integrity of the material. The penetration depth of the laser irradiation has been suggested to be approximately 1 μm for all processing conditions described employing up to 2000 pulses (A.Queiroz *et al.*, 2004). Measurements taken while imaging the samples produced after a 1000 pulses of laser irradiation at fluence of 14.81 kJ/m^2 in the presence of 10 MPa SF_6 found the columnar structures to range between 10- 20 μm in height, from base to tip (Figure 6.15). Between 1000 and 1500-2000 pulses were required to create structures of adequate clarity. Prior to 1000 shots there was inadequate structural development and more of a surface roughening or cratered effect. Towards 2000 shots certain areas showed what appeared to be 'clumping' of structures that were likely to be resultant of melting with the intense temperature reached. The SEM studies confirmed that the base of the structures lay beneath the material surface similar to previous work carried out by lasing single crystal silicon in SF_6 gas (K.W.Kolasinski, 2004). From the sectional SEM images it was ascertained that the laser irradiation created uniform structures of approximate shape and size; there was no detectable difference between longitudinal and latitudinal sections. Approximately 500 pulses were required before clear individual structures could be distinguished from surrounding material. It was previously reported by Queiroz *et. al.* (2004) from a similar study regarding laser ablation of HA that the surface roughness increased with the number of pulses due to the formation of columnar artefacts.

Previous mechanisms for conical or columnar formation on the surfaces of laser ablated materials have been introduced in Section 4.6 and include; (i) liquid flow and material expansion upon solidification such that the structures occur above the original surface (A.J.Pedraza *et al.*, 1999; F.Sanchez *et al.*, 1999; J.Eizenkop *et al.*, 2007), (ii) shadowing due to chemical homogeneity when vaporisation-resistant impurities cause erosional columnar formation by the preferential ablation of the surrounding material (S.R.Foltyn, 1994; X.Y.Chen *et al.*, 1999) and, (iii) shielding due to the reflection of radiation on the lateral walls of nucleated columns concentrating and enhancing ablation in the intercolumnar regions (A.Usoskin *et al.*, 1999; S.R.Foltyn, 1994). In both of the latter cases the top of the structures must be level or below the initial material surface. In the present work Figures 6.12-6.14 reveal some evidence of the melting of the surface layer of HA but no evidence of extensive fluid flow. The structural developments do not occur above the original HA surface excluding the hydrodynamic mechanism as an offered explanation. The observed morphology and results of the structural characterisation are consistent with shadowing mechanism of column growth suggested by Foltyn *et. al* (1994) in addition to the column growth mechanism proposed by Usoskin *et. al.* (1999) whereby further to shielding the laser radiation, ablation from the lateral walls of the structures decreases as the walls are tilted towards the incoming radiation.

The melting of HA during laser irradiation corresponds with recent findings by Nakata *et. al.* (2007) employing irradiation of a XeF excimer laser on a sintered HA surface under atmospheric conditions. The photon energy within the laser (3.5 eV) was lower than the bond energies of major compositional parts of HA resulting in thermal ablation by melting and evaporating the surface to occur dominantly as opposed to photochemical ablation. No structural development was reported (K.Nakata *et al.*, 2007). Regarding this study the photon energy of the XeCl laser was a higher value of 4.02 eV (A.Luches *et al.*, 1993; V.Nassisi *et al.*, 1998). Coupled with the development of columnar surface topography when chemically enhanced with SF_6, the higher energy of the XeCl laser required a much lower fluence (14.81 compared to 91 kJ/m^2) to develop surface structure suggesting that photochemical ablation occurred equally if not dominantly to thermal ablation. Similarly, surface microstructuring with NH_3 required a lower fluence (18.18 kJ/m^2) than reported by Nakata *et. al.* (2007) suggesting that

photochemical ablation was chiefly responsible for structural modification in both cases (Figure 7.4).

With regard to the surface modification carried out with 80 MPa NH_3 at a fluence of 18.18 kJ/m^2, the structures produced after several hundred laser shots were very irregular and randomly arranged on the surface in terms of height, size, shape and placement (Figure 6.13 (c,d)). It was not possible to demonstrate the production of structure on HA under the typical irradiation conditions. The pits, concavities and porosities created may well be of benefit to the material osteoconductivity as discussed further on but there was no indication, as seen with SF_6, that it may have been possible to improve upon the regularity and ordering of the structure. Similar results including the formation of shallow pits have been reported in recent work involving laser processing of silicon in the presence of NH_3 (D.Mills, 2006).

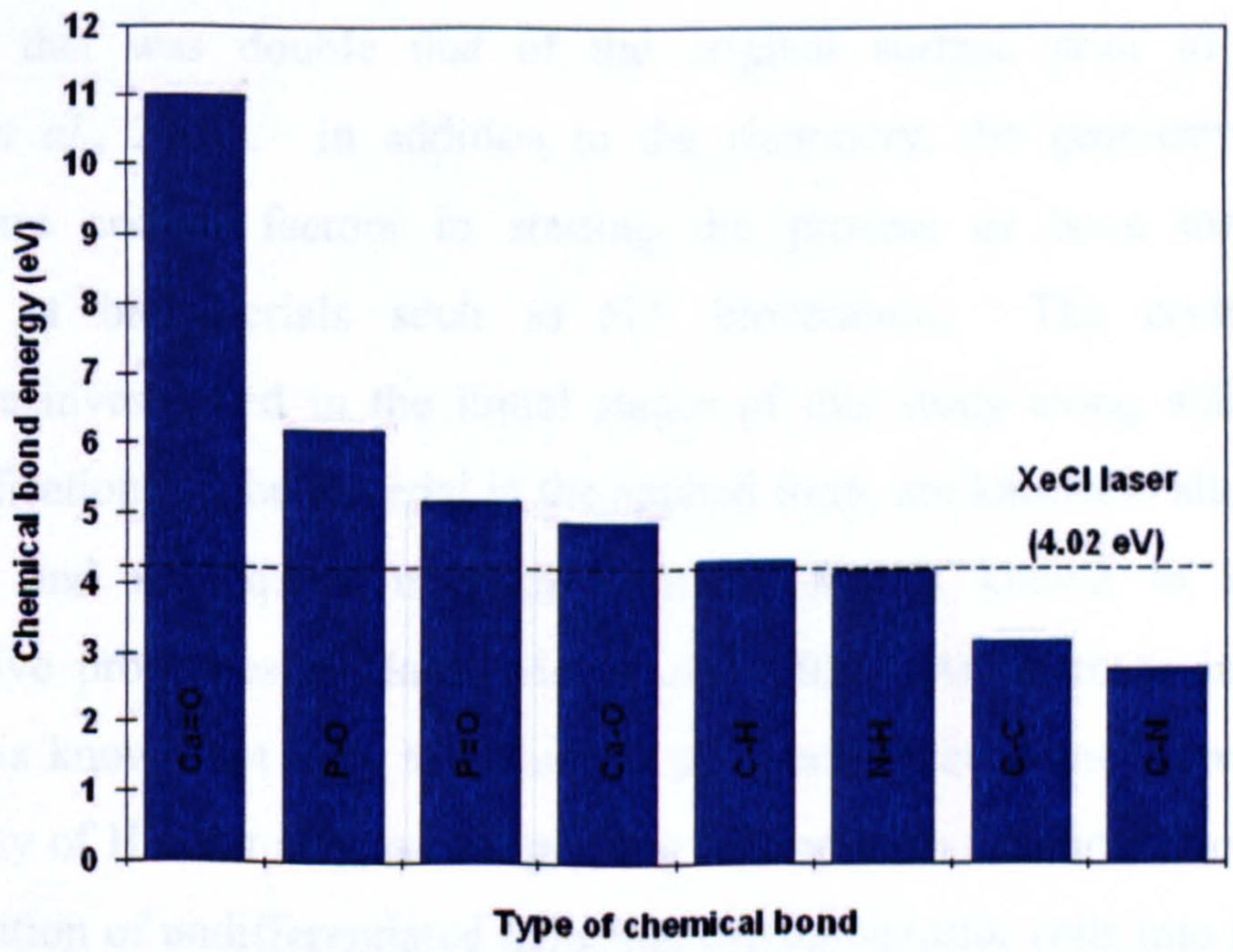

Figure 7.4: Chart of single photon energy level of XeCl laser and chemical bond energies of major components of hydroxyapatite and bone (N.Patel *et al.*, 2003).

The presence of atmospheric conditions within the processing chambers served to increase reactivity particularly when in combination with NH_3 gas where the target demonstrated a tendency to burn. Alternatively, the presence of gaseous phase water in

combination with SF_6 gas had little effect on the type of morphological structure created but resulted in structures of a much smaller size. Further investigation is needed to determine whether the presence of H_2O gas can be used as an implement for regulating structural development. Structural development was achieved at lower gas pressures of SF_6. Increasing the pressure seemingly served to decrease the reactivity with little if any observed physical changes and much smaller plume size, collaborating well with previous findings that the ablation rate of HA is reduced with increased atmospheric pressure (J.L.Arias *et al.*, 2003a). In contrast, structural modification was achieved at higher gas pressures of NH_3. In each case, the greatest reactivity and structural developments were observed after processing when the plume was large and bright.

All images obtained depicted a change in surface morphology that is likely to be accompanied by an increase in surface area. Similar studies have established that 1000 pulses of similar laser irradiation resulting in structural development corresponded to a surface area that was double that of the original surface prior to modification (A.Queiroz *et al.*, 2004). In addition to the chemistry, the geometry and surface topography are critical factors in starting the process of bone induction upon implantation of biomaterials such as HA bioceramic. The crystal size and microstructure investigated in the initial stages of this study along with any further surface modifications of the material in the applied form, are known to alter the specific surface area and subsequent microenvironment that is known to influence the osteoconductive properties (P.Habibovic *et al.*, 2005). An increase in the specific surface area is known not only to influence the mechanical strength and initial bone bonding ability of HA but also exert a positive influence on osteoinduction i.e. causing the differentiation of undifferentiated inducible osteoprogenitor cells into bone-forming cells (D.R.Villarreal *et al.*, 1998; P.Habibovic *et al.*, 2005). Although the exact mechanism of osteoinduction is unknown, a number of studies have indicated some of the parameters necessary for making a biomaterial such as HA osteoinductive.

Crystallinity, porosity (macropores or concavities) and density govern the solubility and dissolution rate controlling the release of calcium and phosphate ions that precedes the precipitation of a biological apatite layer. Precipitation occurs upon the ion

concentration reaching supersaturation level within the material vicinity. For this reason, bone induction takes place within pores and concavities. An increase in the specific surface area is known to increase the dissolution rate and subsequent time in which the biological apatite layer is formed. The laser modification of HA in both types of process gas increased the material surface area that could promote dissolution and moreover provided concavities where subsequent precipitation of biological apatite could be facilitated (C.M.Muller-Mai *et al.*, 1995; D.R.Villarreal *et al.*, 1998; K.A.Hing *et al.*, 1999; M.Bohner, 2000; P.Ducheyne *et al.*, 1999; P.Habibovic *et al.*, 2005).

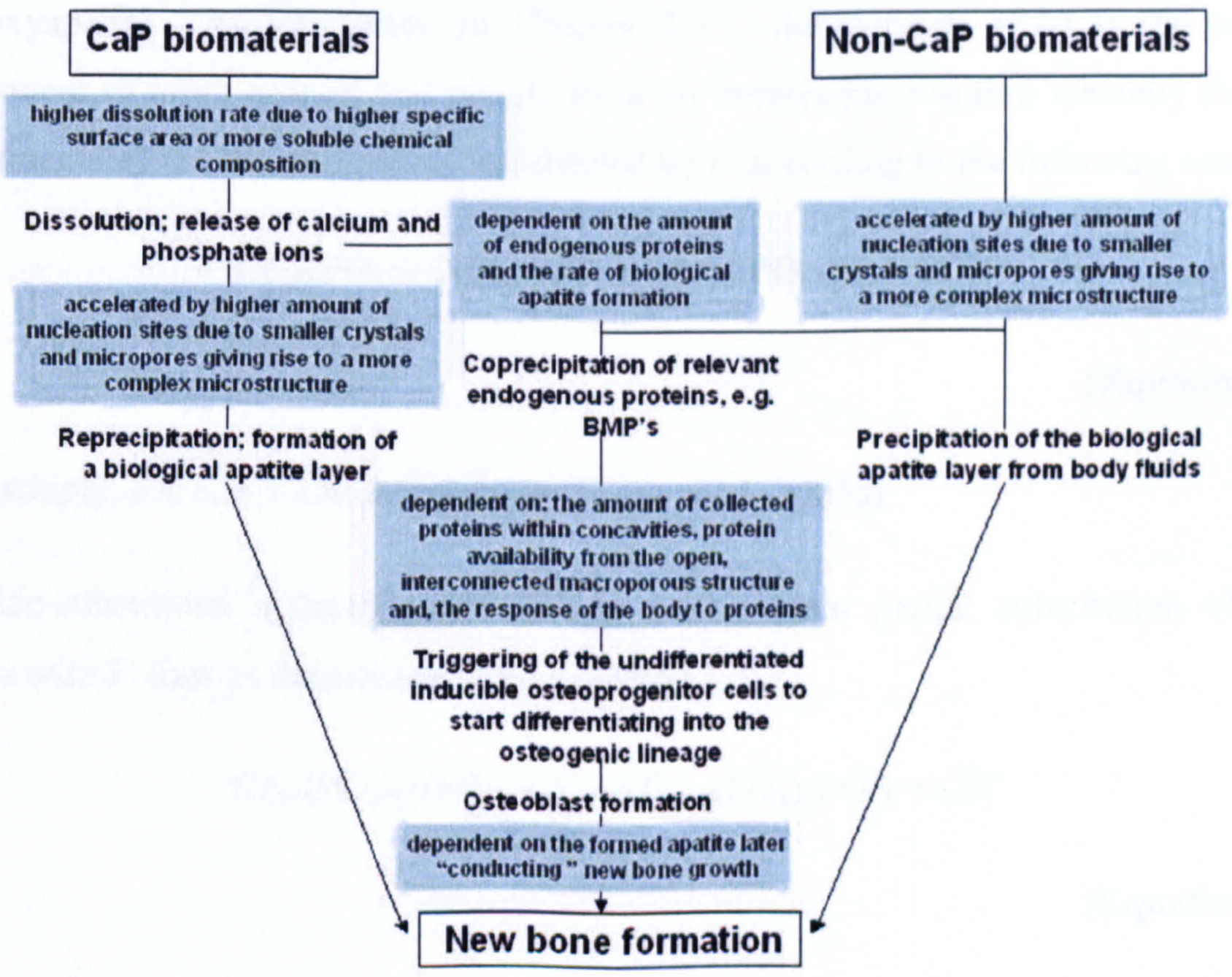

Figure 7.5: Flow chart of the proposed mechanism of osteoinduction by biomaterials (D.Liu, 1997; P.Habibovic *et al.*, 2005).

An optimum specific surface area does however exist and beyond this point degradation occurs too quickly to maintain the shape and stability required for bone formation.

7.2.3 Chemical characterisation

In contrast to the previous study by Queiroz *et. al.* (2004), X-ray microdiffraction, SEM-EDS, FTIR and Raman data confirm that in each case surface structural modification did not result in any chemical decomposition of the HA surface or the bulk composition. There were no undesirable secondary phases present such as α-TCP (A.Queiroz *et al.*, 2004). Combined surface chemical analytical techniques of SEM-EDS and X-ray microdiffraction of the HA surfaces modified with SF_6 confirmed the presence of fluorine within the surface structural features (Figures 6.18, 6.20, 6.23) and collectively determined the microstructured surface to be fluoride-substituted hydroxyapatite. As introduced in Chapter 2.3.3, fluoroapatite (FA) is the mineral component of tooth enamel and results from an irreversible reaction whereby the OH^- components of HA are completely substituted by F^- according to the following reaction:

$$Ca_{10}(PO_4)_6(OH)_2 + 2F^- \rightarrow Ca_{10}(PO_4)_6F_2 + 2OH^-$$

(Equation 7.2)

Interestingly, FA is not osteoconductive.(H.Qu *et al.*, 2005a)

Fluoride-substituted hydroxyapatite (FHA) occurs from partial substitution of OH^- groups with F^- ions as demonstrated by Equation 7.3:

$$Ca_{10}(PO_4)_6(OH)_2 + F^- \rightarrow Ca_{10}(PO_4)_6FOH + OH^-$$

(Equation 7.3)

The Ca:P ratio of the solid remains unchanged in either case as the hydroxyl group is the only affected portion of the molecule (H.McCann, 1953; M.Wei *et al.*, 2003). Whilst stoichiometric FA has a 3.77 wt % fluorine content, the fluorine content of human bone is less than 1 wt % and in order to avoid toxic reactions and severe adverse effects such as osteomalacia, implant materials similarly should not exhibit noticeably higher fluorine concentrations (I.Manjubala *et al.*, 2001). The inclusion of fluoride ions in the HA lattice has been shown to stimulate cells for bone formation and as a partially substituted apatite (FHA) exhibits a lower solubility and degradation rate than both HA and FA (Y.Wang *et al.*, 2007). Advantages of this can be interpreted by more gradual resorption with added benefit of stimulating bone growth leading to improved

osseointegration (K.Bhadang *et al.*, 2004; N.Rameshbabu *et al.*, 2006). The increased stability within the biological environment is awarded to the *a*-axis lattice parameter of FHA being smaller than that for HA (H.Qu *et al.*, 2005a).

In terms of laser interactions with HA, much of the previous studies have offered understanding and explanations for the nature and chemistry of the interaction for the purposes of deposition of material for coatings. Plasma sprayed coatings and pulsed laser deposition of HA material onto other biomaterials, mainly metallic, have featured problems resulting from phase decomposition from incongruent melting of HA and rapid solidification resulting in an amorphous phase producing a combined outcome of chemical inhomogeneity within the coating. The mixture of different phases that result from the combination of high temperatures and fast cooling, are associated with decreased mechanical properties and unequal dissolution rates where the soluble phase parts are released at a quicker rate than the remaining material phases (C.Chen *et al.*, 2005; J.L.Arias *et al.*, 2003b). However in terms of surface modification and surface roughening, the present study collaborates well with the research of others in finding laser processing as a worthy alternative to other methods because it is relatively fast, easily automated and a non-contact process (A.Queiroz *et al.*, 2004; D.Mills *et al.*, 2004; D.Mills *et al.*, 2006; D.Riedel *et al.*, 2004; K.W.Kolasinski, 2004; S.Teixeira *et al.*, 2006).

Earlier research involving the use of excimer laser beams with HA targets have provided explanation and theory for the release of material and the formation of the characteristic plume. Three emitting species are known to occur within the plasma; an atomic component of calcium neutrals and ions (Ca I and Ca II, respectively) with a contribution of oxygen and phosphorous neutrals, a molecular component of calcium oxide of unknown stoichiometry and hot particulates or impurities that arise and expand away from the target (P.Serra *et al.*, 1998). Within a range of laser fluences it has been found that the ablation rate is related to the emission of hot particulates as opposed to the atomic or molecular emissions corresponding to the ablation rate being higher for lower density targets where the atomic and molecular emission is low and the hot particulate emission is high. For targets of higher density (>1700 kg/m^3), the emission

of light species, atoms and molecules is higher but the emission of hot particulates and the overall ablation rate is lower (P.Serra *et al.*, 1997). The 'Plasmabiotal' HA targets that were successfully microstructured by laser ablative methods had a higher density of 2482.95 kg/m^3 (Table 6.3) suggesting that in order to produce structural surface topography by laser irradiation, a low ablation rate is necessary. It is likely that if ablation proceeds too quickly little control is offered over structural development as too much material is removed and too much heat is generated. However, an optimal ablation rate and target density must exist to offer explanation for the lack of structural development or controlled microstructuring upon the other HA targets of higher density still (>2676.67 kg/m^3). Within research carried out by Serra *et. al.* (1998), the use of fast intensified CCD-imaging identified that the emitted species expand into the HA plume as two main emissive components. The first has a hemispherical expansion front and corresponds to the development of a shock wave due to the confinement of some of the ablated species that are mostly neutral oxygen and some calcium. The differences in the degree of confinement between the neutral calcium and oxygen have been attributed to the difference in their atomic size and mass. The second component is much less distinguishable and arises from the backscattering of a fraction of the species in the plume.

Previous work has ascertained that the presence of H_2O gas serves to decrease the velocity of the emissive species from HA targets. Further chemical reaction between emitted neutral calcium and oxygen confined in the front component of the plume and the background water atmosphere lead to the formation of calcium oxide radicals that are again confined to the front component shielding the second component of the plume. The effect of a background water atmosphere has been shown to change the shape and dynamics of the HA laser ablation plume further to the composition of emissive species. Therefore, the presence of H_2O gas may influence the surface chemistry and structure by serving to control subsequent ablation and surface contributions from plume redeposition offering reason for the surface topography of similar structures but of smaller dimensions found in this research when employed with SF_6 gas at a laser fluence of 10.41 kJ/m^2 (P.Serra *et al.*, 1998; P.Serra *et al.*, 1999).

SEM-EDS surface chemical characterisation demonstrated that the SF_6 reactive gas employed contributed to the formation of topography and that the role of the gas is not purely physical (providing influence through heat development or pressure on the developing structures) through the surface structures being comprised of FHA with the F provided by the process gas. Chemical etching results from the interaction of reactive free radicals (electrically neutral species with incomplete outer shells such as F) with the material surface. The accepted mechanism has three elementary steps: (i) adsorption of reactive species on the surface prior to dissociation; (ii) etch products formation (chemical reaction) and; (iii) etch products desorption. Etch plasmas for surface structural modification are mainly F based particularly in plasma etching of silicon (Si) for microelectronic application where fluorinated monomers (CF_4, CHF_3 and SF_6) are commonly used at low gas pressures similar to that employed in this study (H.Tanaka *et al.*, 2006).

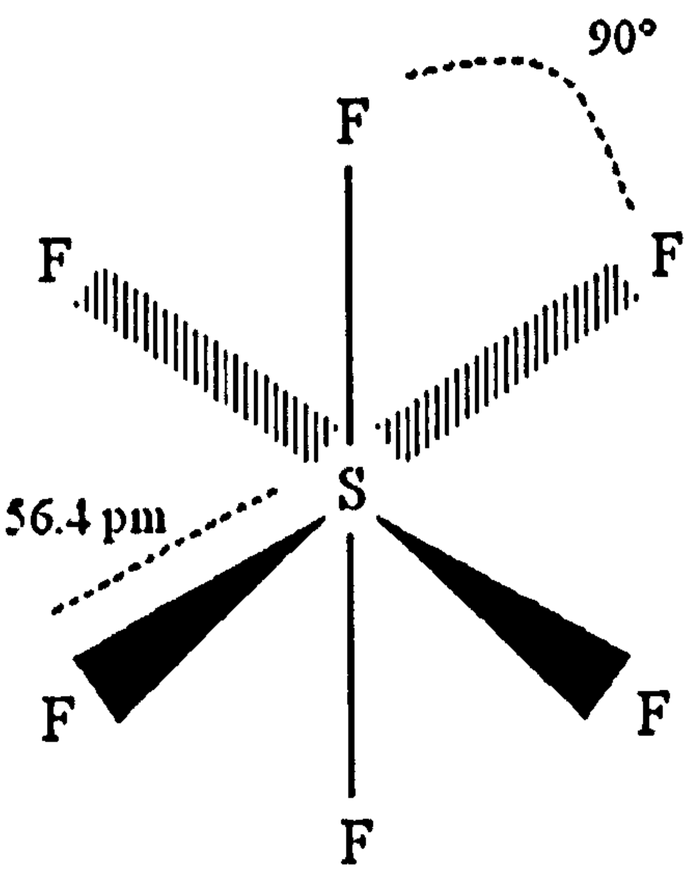

Figure 7.6: Diagram of SF_6 chemical structure

As introduced in Chapter 4.8.1, SF_6 process gas offers high dielectric strength, chemical inertness and extremely low toxicity (P.Brault, 1991; Y.Khairallah *et al.*, 1994). With a high source power SF_6 dissociates into its atomic constituents S and F, by a completely reversible reaction. A higher source power leads to deeper dissociation and more free F^-. In the presence of water vapour, primary and secondary decomposition products hamper the natural recombination of SF_6. A high concentration of water vapour encourages the decomposition products to form highly corrosive hydrogen fluoride (HF) known to vigorously attack glass and porcelain. Fluoride (F) approaching an HA surface can react to produce FA, FHA mixed apatite as found in this work, or calcium

fluoride (CaF_2) such that F^- adsorption cannot be differentiated into a physical or chemical reaction (J.Volker *et al.*, 1940). From solution studies it has been shown that the type of reaction is chiefly dependent on the F concentration in addition to the Ca:P ratio (H.McCann, 1953). In terms of HA solids, if decomposition to form CaF_2 occurs according to the reaction described by Equation 7.4, the Ca:P ratio will change unlike the reaction to FA or FHA, as Ca remaining in the solid whilst the PO_4 is removed will result in increased Ca:P ratio.

$$Ca_{10}(PO_4)_6(OH)_2 + 2OF^- \rightarrow 10CaF_2 + 6PO_4^{\blacksquare} + 2OH^-$$

(Equation 7.4)

However, no decomposition into CaF_2 was found in this laser study. It can be reasoned that the dissociation of SF_6 within the laser plume resulted in reactive free F that reacted according to Equation 7.3 to produce a FHA surface of columnar topography produced by shadowing and shielding (from the lateral walls) mechanisms of columnar growth from photochemical ablation. Initial roughening of the surface by the photochemical ablation would have promoted the initiation of structural development enhanced by the substitution of F^- on the surface. The structural development in itself would enhance the chemical reaction to produce FHA by the creation of porosities that induce a high specific surface area of the surface. Therefore, chemical reactions proceed at a greater rate with the greater number of solid surface atoms which are available for creating volatile species, when compared to atomically flat surfaces (D.H.Lowndes *et al.*, 2000; P.Brault, 1991). Furthermore, preferential ablation of the FHA material within developing crevices would develop the structures further and correspond well with the SEM-EDS semi-quantitative data (Figures 6.19 and 6.20) showing the greatest surface fluorine content to be during structural development as opposed to after when the structures are fully established.

The wettability of a surface is known to depend on the roughness and chemistry such that modification of either can result in affecting the wettability of the original material (D.Szmigiel *et al.*, 2006). Various techniques have been used to increase the surface roughness of implants in order to increase the surface wettability facilitating greater cell adhesion and spreading and subsequently improve the bone tissue integration (L.Hao *et*

al., 2005; R.Narayanan *et al.*, 2006). However research carried out by Qu *et. al.* (2006) report that when F^- replaces the OH^- groups in HA to produce FHA (as shown by Figure 6.18), the negative charges on the surface increase as do contact angle measurements indicating a decrease in surface wettability (M.Kambara *et al.*, 1995). Despite the lack of OH binding sites for protein adsorption (suggested to improve cell attachment and subsequent activity) the release of F^- into the surrounding area has been shown to have greater efficacy in stimulating osteoblastic cell attachment as demonstrated within the same study (G.Rolla *et al.*, 1978; H.Qu *et al.*, 2006). Further investigation involving contact angle measurements could determine the effect that the laser surface modification with SF_6 has had on the wettability of the original material surface and the likely effect on protein adsorption. Past literature considered, it is likely that the microstructured surface with F^- releasing potential will have greater ability to stimulate osteoblastic activities in terms of cell proliferation and differentiation. With all aspects considered, it is likely that the material will be of improved osteoconductivity as desired.

Atomic hydrogen has been reported to etch silicon in much the same way as halogens and fluorinated monomers, therefore, it was hoped that a hydrogen containing gas would have produced similar results when substituted for SF_6 gas (K.W.Kolasinski, 2006a). With regard to the surface modification carried out with 80 MPa NH_3 at a fluence of 18.18 kJ/m^2, no major change to the chemical composition was identified. However, SEM-EDS semi-quantitative analysis identified a vast increase in the amount of surface oxygen as shown in Table 6.9 and Figure 6.20. This is likely to correspond with an increase in the number of surface OH groups introduced previously in Chapter 4.2. The results then suggest that laser modification may have improved the adsorption property of proteins and subsequent cellular response as suggested by previous work establishing that an increase in the number of surface P—OH groups would be likely to influence the adsorption of proteins (H.Tanaka *et al.*, 2004; T.Ishikawa *et al.*, 1989). Cellular adhesion is known to take place by cell-matrix adhesion in which the adhesive proteins of extracellular matrices participate in addition to the physical bond of cell-cell adhesion (M.Ohgaki *et al.*, 2001). Matrix proteins in bone are reported to play a crucial role in hard tissue calcification and reconstruction and attachment of such to implant surfaces by calcium bridging (employing surface calcium) and subsequent binding to

glycosaminoglycans (GAG's – important components of proteoglycans) prior to the electrostatic binding of protein can therefore influence selective cell adhesion and relevant multicellular processes mentioned (D.R.Villarreal *et al.*, 1998).

A major significance of increasing the number of surface P—OH groups relates to the enhanced or improved bonding potential for purposes of chemical coupling to form HA composite materials. The HA-reinforced composite HAPEX™ is a composite of 40 volume % HA in high density polyethylene (HDPE), a non-biodegradable polymer (M.Wang *et al.*, 1998). An advantage of bone tissue being a natural composite of hydroxyaptite in a collagen matrix is reflected through the unique mechanical properties that as of yet have not been matched by any bone substitute material. The HA itself is brittle and collagen serves to minimise the brittle fracture by association with the HA. In HAPEX™ the HA stiffens the PE, and the PE toughens the composite permitted by the covalent bonding of HA to the polymer matrix. Despite the higher mechanical strength of the polymer composite to pure HA constructs, low tensile strength limits the useage to applications with little or no tension such as middle ear implants. Current manufacturing routes produce other composite materials which while exhibiting good characteristics under compression, are less than ideal under extension because of the absence of significant bonding between the HA crystals and the surrounding polymeric support (the ceramic filler is simply trapped inside the polymeric matrix) (A.White *et al.*, 2007; J.D.de Bruijn *et al.*, 1992; M.Ohgaki *et al.*, 2001).

The limited success of previous efforts with respect to the 'Index of Quality' developed by Thompson *et.al.* (1998) are reported in Table 7.1. Using four indicative variables, a materials performance compared to natural bone is defined by a Quality Index value (Iq). The four indicative variables used to calculate this value are; K_{IC} - the fracture toughness (lower), I_b - the bioactivity index value (which depends on how bioactive a material is), Y - the Young's Modulus (GPa) and, UTS - Ultimate Tensile Strength (MPa). The Quality Index value can be calculated according to Equation 7.5.

$$I_q = \frac{(K_{IC} \times I_b \times UTS)}{Y}$$

(Equation 7.5)

A high I_q value of 303 for modified Polysulphone (PS)/Bioglass^{TM} composite (0.4 volume fraction, V_f) has been achieved as a best match to cortical bone to date (I.D.Thompson *et al.*, 1998).

Table 7.1 Comparison of mechanical data and assigned bioactivity indexes for human bone and major commercial bioceramic composite materials

Composite	Polymer	Fracture toughness	Bioactivity index value	Youngs Modulus /GPa	Ultimate Tensile Strength /MPa	Quality Index	Ratio
Abbreviation		K_{1c}	I_b	Y	UTS	I_q	
Cortical bone		6	15	13	100	500	1
Cancellous bone		0.1	1	13	3	8	0.01
Bioglass^{TM}		0.6	35	13	42	9	0.02
HAPEX^{TM}-HA ($0.4V_f$)	PE	3	4	4	23	49	0.1
Bioglass^{TM}($0.4V_f$)	PS	1.2	7	13	52	116	0.23
Bioglass^{TM}($0.4V_f$)	PS*	1.2	5	13	103	303	0.61
Key; PS = Polysulphone and PS* = Modified Polysulphone							

Current methods investigated to improve the bonding between the ceramic filler and the polymeric support include chemical modification of the surface of the filler or the use of bifunctional coupling agents to covalently link the polymeric matrix to the surface of the filler particles (A.Balamurugan *et al.*, 2004). If the surface properties of HA are enhanced by improving the availability of surface reactive (P-OH) groups (that facilitate covalent bonding), coupling will be optimised with a greater number of covalent bonds between ceramic and polymer phases resulting in a biocomposite with improved toughness and strength.

Without any changes to the compositional chemistry of the HA samples the resultant structural modification by laser irradiation may have improved the biocompatibility of

the material from findings established by many scientists that major differences in cellular responses result from different cystallographic structures even though there is no chemical difference between the structures (D.R.Villarreal *et al.*, 1998). The structure and configuration of the functional groups on the surface of hydroxyapatite participates in determining the mode of adsorption that takes place of proteins (including amino acids) and cell varieties (G.Shafei *et al.*, 2001). Further studies involving protein adsorption on the modified HA samples are required to confirm any improved attachment properties.

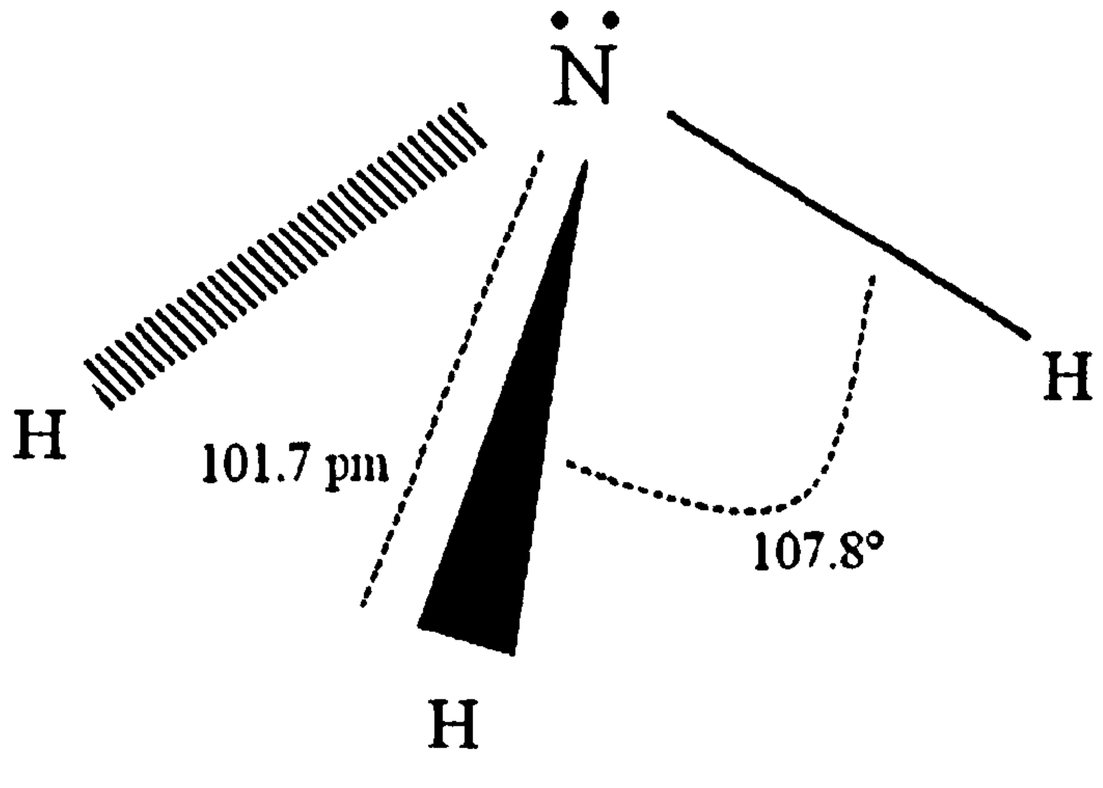

Figure 7.7: Diagram of NH_3 chemical structure

It is known that NH_3 decomposes into flammable hydrogen gas and nitrogen at about 450-500 °C. Decomposition occurs at lower temperatures in the presence of metals and to a lesser extent, catalytic surfaces such as ceramic porcelain. In such cases decomposition begins as low as 300 °C and is complete around 500-600 °C. The reported temperature that the HA surface can reach during laser re-melting is up to 3000 °C (C.Chen *et al.*, 2005). Although no evidence was found in this study of re-melting, the high temperatures reached upon the HA surface during laser microstructuring that are likely to have been in excess of the decompositional temperature of NH_3 resulting in flammable hydrogen gas reacting with the surface offering one explanation for the frequently burnt surface. Furthermore, excimer lasers such as the XeCl laser employed in this study and those used in orthopaedic surgery, have demonstrated very precise cutting because of strong UV absorption of the electronic transitions of virtually all molecules, but are reported to generate a zone of thermal damage of approximately 50

μm. Tissue charring of complex calcified tissues such as bone can result from the excessive heat deposition in the tissue. Influencing factors include the tissue type, pulse duration, pulse energy and wavelength (B.Girard *et al.*, 2007). Subsequently it is most likely that the burnt surface found surrounding the ablated areas was charred HA similar to that witnessed in orthopaedic surgery and probably a result of the high temperatures generated upon the surface in the presence of decomposed NH_3 gas.

Summary

Microemulsion technology combined with freeze-drying techniques were employed to produce an HA powder with increased surface area (>170 m^2/g), finer particle size and distribution in addition to little agglomeration determined by BET surface area analysis. The use of macroemulsion synthesis at a processing temperature of 25 °C served to increase the powder yield with no compromise of powder purity as confirmed by XRD analytical techniques. A slightly lower powder surface area was achieved (148 m^2/g). Freeze-drying methods were employed to produce nanocrystalline (featuring 19 nm particles) conventionally precipitated HA raw powders of increased surface area that were chemically stable at sintering temperatures of 1200 °C. Photochemical ablation methods employing an XeCl excimer laser in the presence of SF_6 and NH_3 gases have been developed to successfully microstructure the surface of sintered HA constructs. The type of surface structure varied with the type of processing gas employed in the lasing chamber. The use of 10 MPa SF_6 gas at laser fluencies within a range of 14.50-15.20 kJ/m^2 permitted the development of a roughly columnar topography. The most regularly formed microstructured surface was created using a laser fluence of 14.81 kJ/m^2. In contrast, the use of 80 MPa NH_3 gas at laser fluencies within the range of 17.17-18.50 kJ/m^2 resulted in an irregularly structured surface of scattered hillocks varying in size and position. The most uniform microstructured surface was created using a laser fluence of 18.18 kJ/m^2. In both cases, the structural development accompanied by the presence of concavities, pits and pores gave rise to a material surface of increased surface area for cellular interaction as determined by SEM evaluation. Whilst Raman and X-ray microdifraction studies identified that the bulk composition of the materials was not modified chemically by the laser microstructuring process, surface chemical analysis through SEM-EDS study established that in the structural development with SF_6 gas produced a fluoride-substituted HA surface and the structural development with NH_3 gas served to increase the number of hydroxyl groups

on the HA surface. Both results are likely to improve the osteoconductivity and bioactivity of the materials.

Conclusions

- Bioceramic phase pure HA powder has been synthesised employing emulsion (micro- and macroemulsion) technology and conventional wet precipitation routes. In all cases the use of a freeze-drying step produced powders of high surface area (>100 m^2/g) that were chemically stable at a high sintering temperature of 1200 °C.

- The use of microemulsion technology facilitated the production of particle agglommerates of an average size of 11 nm, but in very small quantities of 2 g per yield.

- The use of macroemulsion technology facilitated the production of particle agglommerates of an average size of 13 nm, in small quantities of 6.9 g per yield.

- The highest yield of 12 g of HA powder has been achieved through macroemulsion synthesis using a reaction temperature of 25 °C with resultant particulates of 16 nm in size.

- The powders produced by emulsion methods demonstrated the smallest amount of crystal agglommeration within the featured particles.

- The powder produced by macroemulsion synthesis at a reaction temperature of 25 °C produced HA discs that were > 96.5 % dense (3059.26 kg/m^3 measured density) after isostatic pressing with a pressure of 0.59 MPa and pressureless sintering at 1200 °C for 2 hrs.

- The use of freeze-drying with a wet conventional precipitation method facilitated the production of a > 99 % dense (3136.36 kg/m^3 measured density) HA disc after isostatic pressing with a pressure of 0.59 MPa and pressureless

sintering at 1200 °C for 2 hrs, and is considered to be a superior drying technique to oven-drying.

- Successful laser surface microstructuring of bioceramic HA has been achieved using sintered discs of 2482.95 kg/m^3 density and 21.5 % porosity produced with commercially produced 'Plasmabiotal' HA featuring an average as-prepared powder particulate size of 126 nm.

- The creation of surface topography by laser surface microstructuring of bioceramic HA has been determined by SEM imaging and found to be unique to the type of reactive gas employed within the process.

- At least 1000 pulses of XeCl laser energy was required in each case to permit sufficiently established surface topography.

- In all cases of surface structural modification, chemical analysis by X-ray microdiffraction, FTIR and Raman studies has determined that there has been no change to the bulk chemical composition of the HA material.

- The use of 10 MPa SF_6 gas at laser fluencies within a range of 14.50-15.20 kJ/m^2 permitted the development of a roughly columnar topography that was even in size and distribution.. The most regularly formed microstructured surface was created using a laser fluence of 14.81 kJ/m^2. SEM-EDS studies determined the surface topography to be composed of fluoride substituted HA.

- The use of 80 MPa NH_3 gas at laser fluencies within the range of 17.17-18.50 kJ/m^2 resulted in an irregularly structured surface of scattered hillocks varying in size and position. The most uniform microstructured surface was created using a laser fluence of 18.18 kJ/m^2. SEM-EDS analysis determined the surface topography to be composed of HA but featuring an increased number (four times greater) of surface hydroxyl groups in comparision to the original surface.

Suggestions for future work

- The determination of the powder particle morphology using SEM or Transmission electron microscopy (TEM) imaging methods would be valuable in order to evaluate the packing properties and subsequent processing properties of the emulsion synthesised powders.

- For mass production, it would be of interest to improve this further and establish other variables that could influence the time of the lengthy production in addition to the yield of emulsion synthesised HA powders. Variables for possible investigation include the stirring/agitation speed and the use of "Oil in water" emulsions and non-ionic surfactants.

- Mechanical testing is required to determine the compressive and tensile strength of the products with the view to apply bioceramic HA in load-bearing situations. In order to establish the Iq - Quality Index value for comparison against current bone substitute materials, the four indicative variables required from future work are; K_{1C} - the fracture toughness (lower), I_b - the bioactivity index value, Y - the Young's Modulus /GPa and, UTS - Ultimate Tensile Strength /MPa.

- The wettability of a surface can provide indication of affinity for protein and subsequent cellular attachment. Contact angle measurements would be beneficial to establish the wettability of the laser-modified surfaces for comparison .

- Protein studies investigating the adsorption of fibronectin and vitronectin known to promote bone cell attachment would be advantageous in determining the likely biological response to the chemically enhanced and/or microstructured surfaces.

- Cell culture work investigating the cellular response to the emulsion synthesised HA materials in addition to the laser surface modified specimens produced would be beneficial and indicative of the success in orthopaedic applications.

Comparative studies could be undertaken to establish the *in vitro* osteoblast proliferation and long-term functions (as measured by intra- and extra-cellular matrix protein synthesis such as collagen and alkaline phosphatase, as well as calcium-containing mineral deposition) that have been previously determined as enhanced on ceramics with minimal grain sizes. Enhanced osteoclast functions have also been reported with increased formation of resorption pits that should overall increase the bone regeneration and remodelling rate reducing the the length of time required to repair the initial bone defect.

- Solubility and dissolution studies with particular interest to the HA material with the columnar surface topography composed of FHA would be useful to establish the rate and release of fluorine ions into the surrounding medium in addition to the solubility of the surface providing an indication of the possible resorption rate and possible fluorine concentration surrounding the material surface and exposed to cells.

- The coupling and bonding ability of the surface topography produced in the presence of NH_3 gas featuring an increased number of surface P-OH groups would be useful to evaluate for possible production of a biocomposite with improved mechanical stability.

- Further work in the field of laser surface microstructuring of HA could be carried out to determine if other reactive gases can successfully influence the production of other different surface topographies and/or chemically modified apatites.

- Further investigation could be carried out using the conditions established within this study to optimise the regularity or dimensions of the respective surface topographies by varying the optical parameters such as the repetition rate (known to influence the size and spacing of the surface structures).

Bibliography

A.Afshar, M.Ghorbani, N.Ehsani *et al.* Some Important Factors in the Wet Precipitation Process of Hydroxyapatite. Materials and Design. 2003: 24; 197-202.

A.Andersson, F.Backhed, A.von Euler *et al.* Nanoscale Features Influence Epithelial Cell Morphology and Cytokine Production. Biomaterials. 2003a: 24; 3427-3436.

A.Andersson, P.Olsson, U.Lidberg *et al.* The Effects of Continuous and Discontinuous Groove Edges on Cell Shape and Alignment. Experimental Cell Research. 2003b: 288; 177-188.

A.Antonakos, E.Liarokapis, and T.Leventouri. Micro-Raman and FTIR Studies of Synthetic and Natural Apatites. Biomaterials. 2007: 28; 3043-3054.

A.B.Brailovsky, S.V.Gaponov, and V.I.Luchin. Mechanism of Melt Droplets and Solid-Particle Ejection From Target Surface by Pulsed Laser Action. Applied Physics A: Materials Science and Processing. 1995: 61; 81-86.

A.Balamurugan, S.Kannan, V.Trtik *et al.* Development and Spectral Characterisation of Poly(Methyl Methacrylate)/Hydroxyapatite Composite for Biomedical Applications. Trends in Biomaterials and Aritificial Organs. 2004: 18; 41-45.

A.Baumer, W.Klee, and M.Ganteaume. Determination of OH Ions in Hydroxyfluorapatites by Infrared Spectroscopy. Bulletin Mineralogie. 1985: 108; 145-152.

A.Cedola, S.Lagomarsino, V.Komlev *et al.* High Spatial Resolution X-Ray Microdiffraction Applied to Biomaterial Studies and Archeometry. Spectrochimica Acta Part B. 2004: 59; 1557-1564.

A.Cross, Introduction to Practical Infrared Spectroscopy. 1969. 3rd Edition. Butterworths, London. 74-86.

A.Cuneyt Tas, F.Korkusuz, M.Timucin *et al.* An Investigation of the Chemical Synthesis and High-Temperature Sintering Behaviour of Calcium

Hydroxyapatite (HA) and Tricalcium Phosphate (TCP) Bioceramics. Journal of Materials Science: Materials in Medicine. 1997: 8; 91-96.

A.Curtis and C.Wilkinson. Topographical Control of Cells. Biomaterials. 1997: 18; 1573-1583.

A.Filankembo and M.P.Pileni. Is the Template of Self-Colloidal Assemblies the Only Factor That Controls Nanocrystal Shapes? Journal of Physical Chemistry.B. 2000: 104; 5865-5868.

A.Graciaa, J.Lachaise, M.Bourrel *et al.* Differentiation of Continuous and Discontinuous Phases of Water-in-Oil Microemulsions Using Dialysis. Journal of Colloid and Interface Science. 1988: 122; 83-90.

A.Hart, N.Gadegaard, C.Wilkinson *et al.* Osteoprogenitor Response to Low-Adhesion Nanotopographies Originally Fabricated by Electron Beam Lithography. Journal of Materials Science: Materials in Medicine. 2007: 18; 1211-1218.

A.J.Pedraza, J.D.Fowlkes, and D.H.Lowndes. Silicon Microcolumn Arrays Grown by Nanosecond Pulsed-Excimer Laser Irradiation. Applied Physics Letters. 1999: 74; 2322-2324.

A.J.Ruys, M.Wei, C.C.Sorrell *et al.* Sintering Effects on the Strength of Hydroxyapatite. Biomaterials. 1995: 16; 409-415.

A.K.Bembey, A.J.Bushby, A.Boyde *et al.* Hydration Effects on the Micro-Mechanical Properties of Bone. Journal of Materials Research. 2006: 21; 1962-1968.

A.Luches, V.Nassisi, and A.Pecoraro. Generation of Multiply Charged Silicon and Germanium Ions by Excimer Laser Pulses. Applied Physics B: Lasers and Optics. 1993: 57; 163-165.

A.Osaka, Y.Muira, K.Takeuchi *et al.* Calcium Apatite Prepared From Calcium Hydroxide and Orthophosphoric Acid. Journal of Materials Science: Materials in Medicine. 1991: 2; 51-55.

A.Pierres, A.Benoliel, and P.Bongrand. Cell Fitting to Adhesive Surfaces: A Prerequisite to Firm Attachment and Subsequent Events. European Cells and Materials. 2002: 3; 31-45.

A.Queiroz, J.Santos, R.Vilar *et al.* Laser Surface Modification of Hydroxyapatite and Glass-Reinforced Hydroxyapatite. Biomaterials. 2004: 25; 4607-4614.

A.Rosa, M.Beloti, and R.van Noot. Osteoblastic Differentiation of Cultured Rat Bone Marrow Cells on Hydroxyapatite With Different Surface Topography. Dental Materials. 2003: 19; 768-772.

A.S.Edward, N.J.Gleason, A.Nakahira *et al.* Nanostructure Processing of Hydroxyapatite-Based Bioceramics. Nano Letters. 2001: 1; 149-153.

A.S.Posner and R.A.Beebe. The Surface Chemistry of Bone Mineral and Related Calcium Phosphates. Seminars in Arthritis and Rheumatism. 1975: 4; 267-291.

A.Santomaso, P.Lazzaro, and P.Canu. Powder Flowability and Density Ratios: the Impact of Granules Packing. Chemical Engineering Science. 2003: 58; 2857-2874.

A.Tampieri, G.Celotti, F.Szontagh *et al.* Sintering and Characterisation of HA and TCP Bioceramics With Control of Their Strength and Phase Purity. Journal of Materials Science: Materials in Medicine. 1997: 8; 29-37.

A.Usoskin, H.C.Freyhardt, and H.U.Krebs. Influence of Light Scattering on the Development of Laser Induced Ridge-Cone Structure on Target Surfaces. Applied Physics A: Materials Science and Processing. 1999: 69; s823-s826.

A.White and S.M.Best. Hydroxyapatite-Carbon Nanotube Composites for Biomedical Applications: A Review. International Journal of Applied Ceramic Technology. 2007: 4; 1-13.

B.A.Scheven, D.Marshall, and R.M.Aspden. *In Vitro* Behaviour of Human Osteoblasts on Dentin and Bone. Cell Biology International. 2002: 26; 337-346.

B.D.Boyan, T.W.Hummert, D.D.Dean *et al.* Role of Material Surfaces in Regulating Bone and Cartilage Cell Response. Biomaterials. 1996: 17; 137-146.

B.D.Ratner, A.S.Hoffman, F.J.Schoen, and J.E.Lemons, Biomaterials Science, An introduction to materials in medicine. 1996c. 1st Edition. Academic Press Limited, London. 12-13.

B.D.Ratner, A.S.Hoffman, F.J.Schoen, and J.E.Lemons, Biomaterials Science, An introduction to materials in medicine. 1996b. 1st Edition. Academic Press Limited, London. 21-34.

B.D.Ratner, A.S.Hoffman, F.J.Schoen, and J.E.Lemons, Biomaterials Science, An introduction to materials in medicine. 1996a. 1st Edition. Academic Press Limited, London. 75-76.

B.Girard, D.Yu, M.R.Armstrong *et al.* Effects of Femtosecond Laser Irradiation on Osseous Tissues. Lasers in Surgery and Medicine. 2007: 39; 273-285.

B.Ji and H.Gao. Mechanical Properties of Nanostructure of Biological Materials. Journal of the Mechanics and Physics of Solids. 2004: 52; 1963-1990.

B.Kasemo. Biological Surface Science. Surface Science. 2002: 500; 656-677.

B.Kundu, M.K.Sinha, M.K.Mitra *et al.* Fabrication and Characterization of Porous Hydroxyapatite Ocular Implant Followed by an *in Vivo* Study in Dogs. Bulletin of Material Science. 2004: 27; 133-140.

B.M.Tracy and R.H.Doremus. Direct Electron Microscopy Studies of the Bone-Hydroxylapatite Interface. Journal of Biomedical Materials Research. 1984: 18; 719-726.

B.Melde and A.Stein. Periodic Macroporous Hydroxyapatite-Containing Calcium Phosphates. Chemical Materials. 2002: 14; 3326-3331.

C.Chen, D.Wang, Q.Bao *et al.* Influence of Laser Remelting on the Microstructure and Phases Constitution of Plasma Sprayed Hydroxyapatite Coatings. Applied Surface Science. 2005: 250; 98-103.

C.K.Choo, M.Tohara, K.Enomoto *et al.* Pulsed Laser Ablation of Silicon With Low Laser Fluence in a Low-Pressure of Ammonia Ambient. Applied Surface Science. 2004: 228; 120-127.

C.K.Choo, T.Sakamoto, K.Tanaka *et al.* Characterization of Nitrogen Terminated Silicon Nanoparticles on AFI Zeolite With X-Ray and Ultraviolet Photoelectron Spectroscopies. Applied Surface Science. 1999: 148; 116-125.

C.Kirk and G.Cressey. Pushing the Limits of Lab X-Ray (Micro) Diffraction. Acta Crystallographica. 2004: A60; s51-s52.

C.Knabe, R.Gildenhaar, R.Fitzer *et al.* Morphological Evaluation of Osteoblasts Cultured on Different Calcium Phosphate Ceramics. Biomaterials. 1997: 18; 1339-1347.

C.Kothapalli, M.Wei, A.Vasiliev *et al.* Influence of Temperature and Concentration on the Sintering Behaviour and Mechanical Properties of Hydroxyapatite. Acta Materialia. 2004: 52; 5655-5663.

C.M.Muller-Mai, S.I.Stupp, C.Voight *et al.* Nanoapatite and Organoapatite Implants in Bone: Histology and Ultrastructure of the Interface. Journal of Biomedical Materials Research. 1995: 29; 9-18.

C.Nelson. Periprosthetic Fractures of the Femur Following Hip Arthroplasty. The American Journal of Orthopaedics. 2002: 31; 221-223.

C.S.Chai and B.Ben-Nissan. Bioactive Nanocrystalline Sol-Gel Hydroxyapatite Coatings. Journal of Materials Science: Materials in Medicine. 1999: 10; 465-469.

C.Silwood, I.Abrahams, and D.Apperley. Surface Analysis of Novel Hydroxyapatite Bioceramics Containing Titanium (IV) and Fluoride. Journal of Materials Chemistry. 2005: 15; 1626-1636.

Compressed Gas Association, Handbook of compressed gases. 1990. 3rd Edition. Van Nostrand Reinhold Company, New York. 231-252.

D.A.Smith, S.D.Connell, C.Robinson *et al.* Chemical Force Microscopy: Applications in Surface Characterisation of Natural Hydroxyapatite. Analytica Chemica Acta. 2003: 479; 39-57.

D.Bernache-Assollant, A.Ababou, E.Champion *et al.* Sintering of Calcium Phosphate Hydroxyapatite $Ca_{10}(PO_4)_6(OH)_2$ I. Calcination and Particle Growth. Journal of the European Ceramic Society. 2003: 23; 229-241.

D.Castner and B.Ratner. Biomedical Surface Science: Foundations to Frontiers. Surface Science. 2002: 500; 28-60.

D.Deligianni, N.Katsala, P.Koutsoukos *et al.* Effect of Surface Roughness of Hydroxyapatite on Human Bone Marrow, Cell Adhesion, Proliferation and Detachment Strength. Biomaterials. 2001: 22; 87-96.

D.Fang and I.Remedios. Uncemented Hip Replacements in Young Patients. Journal of the Hong Kong Medical Association. 1990: 42; 212-216.

D.Fried, M.Zuerlain, J.Featherstone *et al.* IR Laser Ablation of Dental Enamel: Mechanistic Dependence on the Primary Absorber. Applied Surface Science. 1998: 127-129; 852-856.

D.Fried, N.Ashouri, T.M.Breunig *et al.* Mechanism of Water Augmentation During IR Laser Irradiation of Dental Enamel. Lasers in Surgery and Medicine. 2002: 31; 186-193.

D.H.Lowndes, J.D.Fowlkes, and A.J.Pedraza. Early Stages of Pulsed-Laser Growth of Silicon Microcolumns and Microcones in Air and SF_6. Applied Surface Science. 2000: 154-155; 647-658.

D.Hirsch, R.Azoury, W.J.Landis *et al.* Liposome Interactions With Hydroxyapatite Crystals: A Possible Mechanism in the Calcification of Atherosclerotic Plaques. Calcified Tissue International. 1992: 50; 261-265.

D.Liu. Fabrication of Hydroxyapatite Ceramic With Controlled Porosity. Journal of Materials Science: Materials in Medicine. 1997: 8; 227-232.

D.Mills. Formation and characterisation of silicon meso- and nano-structures. 2006. University of London. 33-56.

D.Mills and K.W.Kolasinski. Laser-Etched Silicon Pillars and Their Porosification. Journal of Vacuum Science and Technology A. 2004: 22; 1647-1651.

D.Mills and K.W.Kolasinski. Solidification Driven Extrusion of Spikes During Laser Melting of Silicon Pillars. Nanotechnology. 2006: 17; 2741-2744.

D.N.Misra. Adsorption of Low Molecular Weight Poly(Acrylic Acid) on Hydroxyapatite: Role of Molecular Association and Apatite Dissolution. Langmuir. 2005: 7; 2422-2424.

D.R.Villarreal, A.Sogal, and J.L.Ong. Protein Adsorption and Osteoblast Responses to Different Calcium Phosphate Surfaces. Journal of Oral Implantology. 1998: 24; 67-73.

D.Riedel, J.L.Hernandez-Poros, R.E.Palmer *et al.* Fabrication of Ordered Arrays of Silicon Cones by Optical Diffraction in Ultrafast Laser Etching With SF_6. Applied Surface Science. 2004: 78; 381-385.

D.Siva Rama Krishna, C.K.Chaitanya, and S.K.Seshadri. Fluorinated Hydroxyapatite by Hydrolysis Under Microwave Irradiation. Trends in Biomaterials and Artificial Organs. 2002: 16; 15-17.

D.Szmigiel, K.Domanski, P.Prokaryn *et al.* The Effect of Fluorine-Based Plasma Treatment on Morphology and Chemical Surface Composition of Biocompatible Silicone Elastomer. Applied Surface Science. 2006: 253; 1506-1511.

D.Tadic, F.Beckmann, K.Schwarz *et al.* A Novel Method to Produce Hydroxyapatite Objects With Interconnecting Porosity That Avoids Sintering. Biomaterials. 2004: 25; 3335-3340.

D.Tadic and M.Epple. Mechanically Stable Implants of Synthetic Bone Mineral by Cold Isostatic Pressing. Biomaterials. 2003: 24; 4565-4571.

E.Ahn, N.Gleason, A.Nakahira *et al.* Nanostructure Processing of Hydroxyapatite-Based Bioceramics. Nano Letters. 2001: 1; 149-153.

E.Bertoni, A.Bigi, G.Cojazzi *et al.* Nanocrystals of Magnesium and Fluoride Substituted Hydroxyapatite. Journal of Inorganic Biochemistry. 1998: 72; 29-35.

E.C.Abdullah and D.Geldart. The Use of Bulk Density Measurements As Flowability Indicators. Powder Technology. 1999: 102; 151-165.

E.Fernandez, J.A.Planell, and S.M.Best. Precipitation of Carbonated Apatite in the Cement System α-$Ca_3(PO_4)$-$Ca(H_2PO_4)_2$-$CaCO_3$. Journal of Biomedical Materials Research. 1999: 47; 466-471.

E.Gogolides, C.Boukouras, G.Kokkoris *et al.* Si Etching in High-Density SF_6 Plasmas for Microfabrication: Surface and Roughness Formation. Microelectronic Engineering. 2004: 73-74; 312-318.

E.Gyorgy, A.Perez del Pino, P.Serra *et al.* Influence of the Ambient Gas in Laser Structuring of the Titanium Surface. Surfaces and Coatings Technology. 2004: 187; 245-249.

E.M.Carlisle. Silicon: A Possible Factor in Bone Calcification. Science. 1970: 167; 279-280.

E.W.Kreutz, R.Weichenhain, R.Wagner *et al.* Microstructuring of SiC by Laser Ablation With Pulse Duration From Ns to Fs Range (LAMP2002). RIKEN Reviews. 2003: 50; 83-87.

E.W.Washburn, H.Ries, and A.L.Day. Report of the Comittee on Definition of the Term "Ceramics". Journal of the American Ceramics Society. 1920: 3; 526-536.

E.Y.Kawachi, C.A.Bertram, and L.T.Kubota. Interface Potential of Calcium Phosphate in Simulated Body Fluid. Biomaterials. 1998: 19; 2329-2333.

F.Balas, J.Perez-Pariente, and M.Vallet-Regi. In Vitro Bioactivity of Silicon-Substituted Hydroxyapatites. Journal of Biomedical Materials Research. 2003: 66A; 364-375.

F.Freund and R.Knobel. Distribution of Fluorine in Hydroxyapatite Studied Be Infrared Spectroscopy. Journal of Chemistry Society.Dalton Transactions. 1997: 1136-1140.

F.Sanchez, J.L.Morenza, R.Aguiar *et al.* Dynamics of the Hydrodynamical Growth of Columns on Silicon Exposed to ArF Excimer-Laser Irradiation. Applied Physics A: Materials Science and Processing. 1998: 66; 83-86.

F.Sanchez, J.L.Morenza, and V.Trtik. Characterisation of the Progressive Growth of Columns by Excimer Laser Irradiation of Silicon. Applied Physics Letters. 1999: 75; 3303-3305.

F.Zhang, S.Yang, W.Wang *et al.* Preparation of Nanocrystalline Ceramic Oxide Powders in the Presence of Anionic Starburst Dendrimer. Materials Letters. 2004: 58; 3285-3289.

G.C.Koumoulidis, A.P.Katsoulidis, A.K.Ladavos *et al.* Preparation of Hydroxyapatite Via Microemulsion Route. Journal of Colloid and Interface Science. 2003: 259; 254-260.

G.Chen, T.Ushida, and T.Tateishi. Development of Biodegradable Porous Scaffolds for Tissue Engineering. Materials Science and Engineering C. 2001: 17; 63-69.

G.Demazeau. Solvothermal Processes: a Route to the Stabilization of New Materials. Journal of Materials Chemistry. 1998: 9; 15-18.

G.K.Lim, J.Wang, S.C.Ng *et al.* Processing of Hydroxyapatite Via Microemulsion and Emulsion Routes. Biomaterials. 1997: 18; 1433-1439.

G.K.Lim, J.Wang, S.C.Ng *et al.* Processing of Fine Hydroxyapatite Powders Via an Inverse Microemulsion Route. Materials Letters. 1996: 28; 431-436.

G.K.Lim, J.Wang, S.C.Ng *et al.* Formation of Nanocrystalline Hydroxyapatite in Nonionic Surfactant Emulsions. Langmuir. 1999a: 15; 7472-7477.

G.K.Lim, S.C.Ng, and L.M.Gan. Nanosized Hydroxyapatite Powders From Microemulsion and Emulsions Stabilised by a Biodegradable Surfactant. Journal of Materials Chemistry. 1999b: 9; 1635-1639.

G.L.Darimont, B.Gilbert, and R.Cloots. Non-Destructive Evaluation of Crystallinity and Chemical Composition by Raman Spectroscopy in Hydroxyapatite-Coated Implants. Materials Letters. 2003: 58; 71-73.

G.M.S.El Shafei and N.A.Moussa. Adsorption of Some Essential Amino Acids on Hydroxyapatite. Journal of Colloid and Interface Science. 2001: 238; 160-166.

G.Penel, G.Leroy, C.Rey *et al.* Infrared and Raman Microspectrometry Study of Fluor-Fluor-Hydroxy and Hydroxy-Apatite Powders. Journal of Materials Science: Materials in Medicine. 1997: 8; 271-276.

G.Rolla and W.H.Bowen. Surface Adsorption of Fluoride and Ionic Exchange Reactions on Hydroxyapatite. Acta Odontology Scandinavia. 1978: 36; 219-224.

G.Shafei and N.Moussa. Adsorption of Some Essential Amino Acids on Hydroxyapatite. Journal of Colloid and Interface Science. 2001: 238; 160-166.

G.Yin, Z.Liu, J.Zhan *et al.* Impacts of the Surface Charge Property on Protein Adsorption on Hydroxyapatite. Chemical Engineering Journal. 2002: 87; 181-186.

H.Benhayounne, E.Jallot, P.Laquerriere *et al.* Integration of Dense HA Rods into Cortical Bone. Biomaterials. 2000: 21; 235-242.

H.Cheung and D.McCarty. Mitogenesis Induced by Calcium Containing Crystal: Role of Intracellular Dissolution. Experimental Cell Research. 1985: 157; 63-70.

H.G.Craighead, C.D.James, and A.M.P.Turner. Chemical and Topographical Patterning for Directed Cell Attachment. Current Opinion in Solid State and Materials Science. 2001: 5; 177-184.

H.Gilman and D.W.Hukins. Seeded Growth of Hydroxyapatite in the Presence of Dissolved Albumin at Constant Composition. Journal of Inorganic Biochemistry. 1994: 55; 31-39.

H.Gilman, D.W.Hukins, and D.S.Hickey. Characterisation of the Morphology of Hydroxyapatite Precipitated in the Presence of Proteins by Texture Analysis of Scanning Electrons Micrographs. Journal of Physics D: Applied Physics. 1991: 24; 127-130.

H.Juang and M.Hon. Effect of Calcination on Sintering of Hydroxyapatite. Biomaterials. 1996: 17; 2059-2064.

H.Lu, Z.Qu, and Y.Zhou. Preparation and Mechanical Properties of Dense Polycrystalline Hydroxyapatite Through Freeze-Drying. Journal of Materials Science: Materials in Medicine. 1998: 9; 583-587.

H.Lubatschowski, A.Heisterkamp, and F.Will. Medical Applications for Ultrafast Laser Pulses. RIKEN Reviews. 2003: 50; 113-118.

H.McCann. Reactions of Fluoride Ion With Hydroxyapatite. Journal of Biological Chemistry. 1953: 201; 247-259.

H.Qu, L.Vasiliev, M.Aindow *et al.* Incorporation of Fluorine Ions into Hydroxyapatite by a PH Cycling Method. Journal of Materials Science: Materials in Medicine. 2005a: 16; 447-453.

H.Qu and M.Wei. Synthesis and Characterization of Fluorine-Containing Hydroxyapatite by a PH-Cycling Method. Journal of Materials Science: Materials in Medicine. 2005b: 16; 129-133.

H.Qu and M.Wei. The Effect of Fluoride Contents in Fluoridated Hydroxyapatite on Osteoblast Behaviour. Acta Biomaterialia. 2006: 2; 113-119.

H.S.Liu, T.S.Chin, L.S.Lai *et al.* Hydroxyapatite Synthesized by a Simplified Hydrothermal Method. Ceramics International. 1997: 23; 19-25.

H.Tanaka, A.Yasukawa, K.Kandori *et al.* Modification of Calcium Hydroxyapatite Using Alkyl Phosphates. Langmuir. 1997a: 13; 821-826.

H.Tanaka, A.Yasukawa, K.Kandori *et al.* Surface Modification of Calcium Hydroxyapatite With Hecyl and Decyl Phosphates. Colloids and Surfaces A: Physicochemical Engineering and Aspects. 1997b: 125; 53-62.

H.Tanaka, M.Futaoka, and R.Hino. Surface Modification of Calcium Hydroxyapatite With Pyrophosphoric Acid. Journal of Colloid and Interface Science. 2004: 269; 358-363.

H.Tanaka, M.Kurihara, J.Xu *et al.* Influence of Ar-H_2-SF_6 Thermal Plasma Treatment of MCMB Powders on the Anode Properties of a Lithium Ion Rechargeable Battery. Thin Solid Films. 2006: 506-507; 311-315.

H.Wennerstrom, O.Soderman, U.Olsson *et al.* Macroemulsions Versus Microemulsions. Colloids and Surfaces A: Physicochemical Engineering and Aspects. 1997: 123-124; 13-26.

H.Zeng and W.Lacefield. XPS, EDX and FTIR Analysis of Pulsed Laser Deposited Calcium Phosphate Bioceramic Coatings: the Effects of Various Process Parameters. Biomaterials. 2000a: 21; 23-30.

H.Zeng, W.R.Lacefield, and S.Mirov. Structural and Morphological Study of Pulsed Laser Deposited Calcium Phosphate Bioceramic Coatings: Influence of Deposition Conditions, Laser Parameters and Target Properties. Journal of Biomedical Materials Research. 2000b: 50; 248-258.

H.Zhang and Q.Zu. Preparation of Fluoride-Substituted Hydroxyapatite by a Molten Salt Synthesis Route. Journal of Materials Science: Materials in Medicine. 2006: 17; 691-695.

I.D.Thompson and L.L.Hench. Mechanical Properties of Bioactive Glasses, Glass-Ceramics and Composites. Processing Insitute of Mechanical Engineering. 1998: 212; 127-136.

I.Degasne, M.F.Basle, V.Dermais *et al.* Effects of Roughness, Fibronectin and Vitronectin on Attachment, Spreading, and Proliferation of Human Osteoblast-Like Cells (Saos-2) on Titanium Surfaces. Calcified Tissue International. 1999: 64; 499-507.

I.Lisiecki, P.Andre, A.Filankembo *et al.* Mesostructured Fluids. 1. Cu(AOT)2-H2O-Isooctane in Oil Rich Regions. Journal of Physical Chemistry.B. 1999: 103; 9168-9175.

I.Manjubala, M.Sivakumar, and S.Najma Nikkath. Synthesis and Characterisation of Hydroxy/Fluoroapatite Solid Solution. Journal of Materials Science. 2001: 36; 5481-5486.

I.R.Gibson, I.Rehman, S.M.Best *et al.* Characterisation of the Transformation From Calcium-Deficient Apatite to B–Tricalcium Phosphate. Journal of Materials Science: Materials in Medicine. 2000: 12; 799-804.

I.R.Gibson, S.Ke, S.M.Best *et al.* Effect of Powder Characteristics on the Sinterability of Hydroxyapatite Powders. Journal of Materials Science. 2001: 12; 163-171.

I.R.Gibson and W.Bonfield. Chemical Characterization of Silicon-Substituted Hydroxyapatite. Journal of Biomedical Materials Research. 1999: 44; 422-428.

I.R.Gibson and W.Bonfield. Novel Synthesis and Characterization of an AB-Type Carbonate- Substituted Hydroxyapatite. Journal of Biomedical Materials Research. 2002: 59; 697-708.

I.Rehman and W.Bonfield. Characterization of Hydroxyapatite and Carbonated Apatite by Photo Acoustic FTIR Spectroscopy. Journal of Materials Science: Materials in Medicine. 1997: 8; 1-4.

J.Agnew, E.Hampartsoumian, J.M.Jones *et al.* The Simultaneous Calcination and Sintering of Calcium Based Sorbents Under a Combustion Atmosphere. Fuel. 2000: 79; 1515-1523.

J.Barralet, S.Best, and W.Bonfield. Carbonate Substitution in Precipitated Hydroxyapatite: An Investigation into the Effects of Reaction Temperature and Bicarbonate Ion Concentration. Journal of Biomedical Materials Research. 1998: 41; 79-86.

J.Barralet, S.Best, and W.Bonfield. Effect of Sintering Parameters on the Density and Microstructure of Carbonate Hydroxyapatite. Journal of Materials Science: Materials in Medicine. 2000: 11; 719-724.

J.C.Anderson, K.D.Leaver, R.D.Rawlings, and J.M.Alexander, Materials Science. 1991. Chapman and Hall, New York. 297,-300.

J.C.Conde, F.Lusquinos, P.Gonzalez *et al.* Finite Element Analysis of the Initial Stages of the Laser Ablation Process. Thin Solid Films. 2004: 453-454; 323-327.

J.C.Elliott, Infrared and Raman spectroscopy of calcified tissues. 1984. 1st Edition. Elsevier Science, Amsterdam. 413-434.

J.C.Elliott, Structure and Chemistry of the Apatites and other Calcium Orthophosphates. 1994. 1st Edition. Elsevier, Amsterdam. 71-85.

J.C.Elliott, Dental Enamel. 1997. 1st Edition. Wiley, Chichester. 54-72.

J.C.Elliott, R.M.Wilson, and S.E.P.Dowker. Apatite Structures. Advances in X-Ray Analysis. 2002: 45; 172-180.

J.D.de Bruijn, C.P.A.T.Klein, K.De Groot *et al.* The Ultrastructure of the Bone-Hydroxyapatite Interface in Vitro. Journal of Biomedical Materials Research. 1992: 26; 1365-1382.

J.Eizenkop, I.Avrutsky, G.Auner *et al.* Single Pulse Excimer Laser Nanostructuring of Thin Silicon Films: Nanosharp Cones Formation and Heat Transfer Problem. Journal of Applied Physics. 2007: 101; 094301-1-094301-7.

J.Gomez-Morales, J.Toreent-Burgues, T.Boix *et al.* Precipitation of Stoichiometric Hyroxyapatite by a Continuous Method. Crystal Research Technology. 2001: 36; 15-26.

J.H.Fitton, B.A.Dalton, G.Johnson *et al.* Surface Topography Can Interfere With Epithelial Tissue Migration. Journal of Biomedical Materials Research. 1998: 42; 245-257.

J.Hu, J.Russell, R.Vagi *et al.* Production and Analysis of Hydroxyapatite From Australian Corals Via Hydrothermal Process. Journal of Materials Science Letters. 2001: 20; 85-88.

J.J.Silber, A.Biasutti, E.Abuin *et al.* Interactions of Small Molecules With Reverse Micelles. Advances in Colloid and Interface Science. 1999: 82; 189-252.

J.L.Arias, M.B.Mayor, J.Pou *et al.* Pulse Repetition Rate Dependence of Hydroxylapatite Deposition by Laser Ablation. Vacuum. 2002: 67; 653-657.

J.L.Arias, M.B.Mayor, J.Pou *et al.* Laser Ablation Rates of Hydroxylapatite in Different Atmospheres. Applied Surface Science. 2003a: 208-209; 57-60.

J.L.Arias, M.B.Mayor, J.Pou *et al.* Micro- and Nano-Testing of Calcium Phosphate Coatings Produced by Pulsed Laser Deposition. Biomaterials. 2003b: 24; 3403-3408.

J.Liu, B.Han, G.Li *et al.* Investigation of Nonionic Surfactant Dynol-604 Based Reversed Microemulsions Formed in Super Critical Carbon Dioxide. Langmuir. 2001: 17; 8040-8043.

J.M.Fernandez-Pradas, G.Sardin, and J.L.Morenza. Inhomogeneity of Calcium Phosphate Coatings Deposited by Laser Ablation at High Deposition Rate. Applied Physics A: Materials Science and Processing. 2003: 76; 251-256.

J.M.Fernandez-Pradas, G.Sardin, P.Serra *et al.* Deposition of Hydroxyapatite Thin Films by Excimer Laser Ablation. Thin Solid Films. 1998: 317; 393-396.

J.M.Fernandez-Pradas, L.Cleries, E.Martinez *et al.* Influence of Thickness on the Properties of Hydroxyapatite Coatings Deposited by KrF Laser Ablation. Biomaterials. 2001: 22; 2171-2175.

J.M.Fernandez-Pradas, L.Cleries, G.Sardin *et al.* Hydroxyapatite Coatings Grown by Pulsed Laser Deposition With a Beam of 355 Nm Wavelength. Journal of Materials Research. 1999: 14; 4715-4719.

J.M.Fernandez-Pradas, M.V.Garcia-Cuenca, L.Cleries *et al.* Influence of the Interface Layer on the Adhesion of Pulsed Laser Deposited Hydroxyapatiite Coatings on Titanium Alloy. Applied Surface Science. 2002: 195; 31-37.

J.Magyar, A.Sklyarov, K.Mikhaylichenko *et al.* Silicon Dioxide Thin Film Removal Using High Power Nanosecond Lasers. Applied Surface Science. 2003: 207; 306-313.

J.Rho, L.Kuhn-Spearing, and P.Zioupos. Mechanical Properties and the Hierarchical Structure of Bone. Medical Engineering and Physics. 1998: 20; 92-102.

J.Sun, Y.Tsuang, W.Chang *et al.* Effect of Hydroxyapatite Particle Size on Myoblasts and Fibroblasts. Biomaterials. 1997: 18; 683-690.

J.Vandiver, D.Dean, N.Patel *et al.* Nanoscale Variation in Surface Charge of Synthetic Hydroxyapatite Detected by Chemically and Spatially Specific High-Resolution Force Spectroscopy. Biomaterials. 2005: 26; 271-283.

J.Volker, H.Carpenter-Hodge, H.Wilson *et al.* The Adsorption of Fluorides by Enamel, Dentin, Bone, and Hydroxyapatite As Shown by the Radioactive Isotope. Journal of Biological Chemistry. 1940: 134; 543-548.

J.Wang and C.Wang. Periprosthetic Fracture of the Femur After Hip Arthroplasty: The Clinical Outcome Using Cortical Strut Allografts. Journal of Orthopaedic Surgery. 2000: 8; 27-31.

K.A.Hing, S.M.Best, and W.Bonfield. Characterisation of Porous Hydroxyapatite. Journal of Materials Science: Materials in Medicine. 1999: 10; 135-145.

K.Anselme. Osteoblast Adhesion on Biomaterials. Biomaterials. 2000: 21; 667-681.

K.Bhadang and K.Gross. Influence of Fluorapatite on the Properties of Thermally Sprayed Hydroxyapatite Coatings. Biomaterials. 2004: 25; 4935-4945.

K.Chittur. Surface Techniques to Examine the Biomaterial-Host Interface: an Introduction to the Papers. Biomaterials. 1998: 19; 301-305.

K.Dee, D.C.Rueger, T.Andersen *et al.* Conditions Which Promote Mineralization at the Bone-Implant Interface: a Model Study. Biomaterials. 1996: 17; 209-215.

K.Kandori, K.Kon-no, and A.Kitahara. Formation of Ionic Water/Oil Microemulsions and Their Application in the Preparation of $CaCO_3$ Particles. Journal of Colloid and Interface Science. 1988: 122; 78-82.

K.Kawasaki, M.Kambar, H.Matsumura *et al.* A Comparison of the Adsorption of Saliva Proteins and Some Typical Proteins Onto the Surface of Hydroxyapatite. Colloids and Surfaces B: Biointerfaces. 2003: 32; 321-334.

K.Nakata, M.Umehara, T *et al.* Excimer Laser Ablation of Sintered Hydroxyapatite. Surface and Coatings Technology. 2007: 201; 4943-4947.

K.Okuyama and I.W.Lenggoro. Preparation of Nanoparticles Via Spray Route. Chemical Engineering Science. 2003: 5; 537-547.

K.Sonoda, T.Furuzono, D.Walsh *et al.* Influence of Emulsion on Crystal Growth of Hydroxyapatite. Solid State Ionics. 2002: 151; 321-327.

K.W.Kolasinski. Laser-Assisted Restructuring Over Nano-, Meso- and Macroscales. Recent Research Developments in Applied Physics. 2004: 7; 267-292.

K.W.Kolasinski, Handbook of Surface Science. 2006a. 1st Edition. Elsevier, Amsterdam. 127-132.

K.W.Kolasinski. Surface Photochemistry in the Vacuum and Extreme Ultraviolet (VUV and XUV): High Harmonic Generation, H_2O and O_2. Journal of Physics: Condensed Matter. 2006b: 18; s1655-s1675.

K.Wei, Y.Wang, C.Lai *et al.* Synthesis and Characterisation of Hydroxyapatite Nanobelts and Nanoparticles. Materials Letters. 2005: 59; 220-225.

L.B.Kong, J.Ma, and F.Boey. Nanosized Hydroxyapatite Powders Derived From Coprecipitation Process. Journal of Materials Science: Materials in Medicine. 2002: 37; 1131-1134.

L.Borum-Nicholas and O.C.Wilson. Surface Modification of Hydroxyapatite. Part I. Dodecyl Alcohol. Biomaterials. 2003: 24; 3671-3679.

L.Chow, L.Sun, and B.Hockey. Properties of Nanostructured Hydroxyapatite Prepared by a Spray Drying Technique. Journal of Research of the National Institute of Standards and Technology. 2004: 109; 543-551.

L.D'Alessio, R.Teghil, M.Zaccagnino *et al.* Pulsed Laser Ablation and Deposition of Bioactive Glass As Coating Material for Biomedical Applications. Applied Surface Science. 1999: 138-139; 527-532.

L.Hao, J.Lawrence, and L.Li. Manipulation of the Osteoblast Response to a Ti-6Al-4V Titanium Alloy Using a High Power Diode Laser. Applied Surface Science. 2005: 247; 602-606.

L.J.Jha, S.M.Best, J.C.Knowles *et al.* Preparation and Characterization of Fluoride-Substituted Apatites. Journal of Materials Science: Materials in Medicine. 1997: 8; 185-191.

L.L.Hench. Bioceramics: From Concept to Clinic. Journal of the American Ceramic Society. 1991: 74; 1487-1510.

L.L.Hench. Bioceramics. Journal of the American Ceramic Society. 1998: 81; 1705-1728.

L.L.Hench and J.K.West. The Sol-Gel Process. Chemical Reviews. 1990: 90; 33-72.

L.M.Rodriguez-Lorenzo and M.Vallet-Regi. Controlled Crystallization of Calcium Phosphate Apatites. Chemical Materials. 2000: 12; 2460-2465.

L.Pramatarova, E.Pecheva, T.Petrov *et al.* Ion Beam and Laser Processing for Hydroxyapatite Formation. Vacuum. 2004: 76; 339-342.

L.Qi, J.Ma, H.Cheng *et al.* Microemulsion Mediated Synthesis of Calcium Hydroxyapatite Fine Powders. Journal of Materials Science Letters. 1997: 16; 1779-1781.

L.Yubao, J.De Wijn, C.Klein *et al.* Preparation and Characterisation of Nanograde Osteoapatite-Like Rod Crystals. Journal of Materials Science: Materials in Medicine. 1994: 5; 252-255.

M.Ball, S.Downes, C.A.Scotchford *et al.* Osteoblast Growth on Titanium Foils Coated With Hydroxyapatite by Pulsed Laser Ablation. Biomaterials. 2001: 22; 337-347.

M.Bohner. Calcium Orthophosphates in Medicine: From Ceramics to Calcium Phosphate Cements. Injury, International Journal of the Care of the Injured. 2000: 31; 37-47.

M.G.S.Murray, J.Wang, C.B.Ponton *et al.* An Improvement in Processing of Hydroxyapatite Ceramics. Journal of Materials Science. 1995: 30; 3061-3074.

M.Gonzalez, J.A.Banderas, V.Rodriguez *et al.* Particle-Induced X-Ray Emission and Scanning Electron Microscopic Analyses of the Effects of CO_2 Laser Irradtion on Dentinal Structure. Journal of Dentistry. 1999: 27; 595-600.

M.Hsieh, L.Perng, T.Chin *et al.* Phase Purity of Sol-Gel-Derived Hydroxyapatite Ceramic. Biomaterials. 2001: 22; 2601-2607.

M.J.Dalby, L.Di Silvio, G.W.Davies *et al.* Surface Topography and HA Filler Volume Effect on Primary Human Osteoblasts in Vitro. Journal of Materials Science: Materials in Medicine. 2000: 12; 805-810.

M.J.Khon, J.Rakovan, and J.M.Hughes. Phosphates: Geochemical, Geobiological and Materials Importance. Reviews in Mineralogy and Geochemistry. 2002: 48; 1-46.

M.J.Phillips, J.A.Darr, Z.B.Luklinska *et al.* Synthesis and Characterization of Nanobiomaterials With Potential Osteological Applications. Journal of Materials Science: Materials in Medicine. 2003: 14; 875-882.

M.Kambara and W.Norde. Influence of Fluoride Applications on Some Physicochemical Surface Properties of Synthetic Hydroxyapatite and Human Dental Enamel and Its Consequences for Protein Adsorption. Caries Research. 1995: 29; 210-217.

M.Katto, M.Nakamura, T.Tanaka *et al.* Hydroxyapatite Coatings Using Novel Pulsed Laser Ablation Methods. Surface and Coatings Technology. 2003: 169-170; 712-715.

M.Katto, M.Nakamura, T.Tanaka *et al.* Hydroxyapatite Coatings Deposited by Laser-Assisted Laser Ablation Method. Applied Surface Science. 2002: 197-198; 768-771.

M.M.Hoffman, J.S.Young, and J.L.Fulton. Unusual Dysprosium Ceramic Nano-Fiber Growth in a Supercritical Aqueous Solution. Journal of Materials Science. 2000: 35; 4177-4183.

M.M.Seckler, M.Danesse, S.Derenzo *et al.* Influence of Process Conditions on Hydroxyapatite Crystallinity Obtained by Direct Crystallization. Materials Research. 1999: 2; 59-62.

M.Maiss and C.Brenninkmeijer. Atmospheric SF_6: Trends, Sources and Prospects. Environmental Science and Technology. 1998: 32; 3077-3086.

M.Mehmel. The Structure of Apatite. I. Z.Kristallogr.Mineral. 1930: 75; 323-331.

M.N.Rahaman, Ceramic Processing and Sintering. 2003. 2nd Edition. Marcel Dekker, Inc., New York. 425-468.

M.Ohgaki, T.Kizuki, M.Katsura *et al.* Manipulation of Selective Cell Adhesion and Growth by Surface Charges of Electrically Polarized Hydroxyapatite. Journal of Biomedical Materials Research. 2001: 57; 366-373.

M.P.Ginebra, F.C.M.Driessens, and J.A.Planell. Effect of the Particle Size on the Micro and Nanostructural Features of a Calcium Phosphate Cement: a Kinetic Analysis. Biomaterials. 2004: 25; 3453-3462.

M.P.Pileni. Reverse Micelles As Microreactors. Journal of Physical Chemistry. 1993: 97; 6961-6973.

M.P.Pileni. Nanosized Particles Made in Colloidal Assemblies. Langmuir. 1997: 13; 3266-3276.

M.Park, Y.Lee, K.Yang *et al.* Management of Periprosthetic Femoral Fractures. The Journal of Arthroplasty. 2003: 18; 903-906.

M.R.Saeri, A.Afshar, M.Ghorbani *et al.* The Wet Precipitation Process of Hydroxyapatite. Materials Letters. 2003: 57; 4064-4069.

M.Sunny, P.Ramesh, and H.K.Varma. Microstructured Microspheres of Hydroxyapatite Bioceramic. Journal of Materials Science: Materials in Medicine. 2002: 13; 623-632.

M.Tanaka. Surface Modification of Tooth Dentine Irradiated by a 9.45μm CO_2 Laser. Journal of the Japanese Society of Laser Dentistry. 2000: 11; 104-109.

M.Tirrell, E.Kokkoli, and M.Biesalski. The Role of Surface Science in Bioengineered Materials. Surface Science. 2002: 500; 61-83.

M.Vallet-Regi, M.T.Gutierrez-Rios, M.P.Alonso *et al.* Hydroxyapatite Particles Synthesized by Pyrolysis of an Aerosol. Journal of Solid State Chemistry. 1994: 112; 58-64.

M.Wang, R.Joseph, and W.Bonfield. Hydroxyapatite-Polyethylene Composites for Bone Substitution: Effects of Ceramic Particle Size and Morphology. Biomaterials. 1998: 19; 2357-2366.

M.Wei, J.H.Evans, T.Bostrom *et al.* Synthesis and Characterisation of Hydroxyapatite, Fluoride-Substituted Hydroxyapatite and Fluorapatite. Journal of Materials Science: Materials in Medicine. 2003: 14; 311-320.

N.Colthup, L.Daly, and S.Wilberley, Introduction to Infrared and Raman Spectroscopy. 1975. 2nd Edition. Academic Press Inc, New York. 57-89.

N.H.Rizvi. Femtosecond Laser Micromachining: Current Status and Applications. RIKEN Reviews. 2003: 50; 107-112.

N.Patel, E.L.Follon, I.R.Gibson *et al.* Comparison of Sintering and Mechanical Properties of Hydroxyapatite and Silicon-Substituted Hydroxyapatite. Bioceramics 15. 2003: 240-2; 919-922.

N.Rameshbabu, T.S Sampath Kumar, and K.Prasad Rao. Synthesis of Nanocrysralline Fluorinated Hydroxyapatite by Microwave Processing and Its in Vivo Dissolution Study. Bulletin of Material Science. 2006: 29; 611-615.

N.Y.Mostafa. Characterization, Thermal Stability and Sintering of Hydroxyapatite Powders Prepared by Different Routes. Materials Chemistry and Physics. 2005: 94; 333-341.

P.A.Ramires, A.Romito, F.Cosentino *et al.* The Influence of Titania/Hydroxyapatite Composite Coatings on in Vitro Osteoblasts Behaviour. Biomaterials. 2001: 22; 1467-1474.

P.Brault. Fluorine Diffusion in Silicon Under Plasma Treatment. Journal of Physics: Condensed Matter. 1991: 3; 7073-7078.

P.Ducheyne and Q.Qui. Bioactive Ceramics: the Effect of Surface Reactivity on Bone Formation and Bone Cell Function. Biomaterials. 1999: 20; 2287-2303.

P.Habibovic, H.Yuan, C.M.van der Valk *et al.* 3D Microenvironment As Essential Element for Osteoinduction by Biomaterials. Biomaterials. 2005: 26; 3565-3575.

P.J.ter Brugge, S.Dieudonne, and J.Jansen. Initial Interaction of U_2OS Cells With Noncoated and Calcium Phosphate Coated Titanium Substrates. Journal of Biomedical Materials Research. 2002: 61; 399-407.

P.K.Mudhopadhyay, M.B.Alsous, K.Ranganathan *et al.* Characterisation of Laser-Diode End-Pumped Intractivity Frequency Doubled, Passively Q-Switched and Mode-Locked Nd:YVO4. Optics and Laser Technology. 2005: 37; 157-162.

P.Laquerriere, M.Guenounou, P.Frayssinet *et al.* Correlation Between Sintering Temperature of Hydroxyapatite Particles and the Production of Inflammatory Cytokines by Human Monocytes. Colloids and Surfaces B: Biointerfaces. 2003: 30; 207-213.

P.N.de Aza, Z.B.Luklinska, C.Santos *et al.* Mechanism of Bone-Like Formation on a Bioactive Implant in Vivo. Biomaterials. 2003: 24; 1437-1445.

P.Serra and J.L.Morenza. Analysis of Hydroxyapatite Laser Ablation Plumes in a Water Atmosphere. Applied Physics A: Materials Science and Processing. 1998: 67; 289-294.

P.Serra and J.L.Morenza. Evidence of Chemical Reactions in the Hydroxyapatite Laser Ablation Plume With a Water Atmosophere. Journal of Applied Physics. 1999: 85; 3289-3293.

P.Serra, J.M.Fernandez-Pradas, G.Sardin *et al.* Interaction Effects of an Excimer Laser Beam With Hydroxyapatite Targets. Applied Surface Science. 1997: 109/110; 384-388.

P.Shuk, W.L.Suchanek, T.Hao *et al.* Mechanochemical-Hydrothermal Preparation of Crystalline Hydroxyapatite Powders at Room Temperature. Journal of Materials Research. 2001: 16; 1231-1234.

P.Zanchetta and J.Guezennec. Surface Thermodynamics of Osteoblasts: Relation Between Hydrophobicity and Bone Active Biomaterials. Colloids and Surfaces B: Biointerfaces. 2001: 22; 301-307.

P.Zhu, Y.Masuda, and K.Koumoto. The Effect of Surface Charge on Hydroxyapatite Nucleation. Biomaterials. 2004: 25; 3915-3921.

Q.Z.Chen, C.T.Wong, W.W.Lu *et al.* Strenghtening Mechanisms of Bone Bonding to Crystalline Hydroxyapatite in Vivo. Biomaterials. 2004: 25; 4234-4254.

R.Barbucci, D.Pasqui, A.Wirsen *et al.* Micro and Nano-Structured Surfaces. Journal of Materials Science: Materials in Medicine. 2003: 14; 721-725.

R.Barbucci, S.Lamponi, A.Magnani *et al.* Micropatterned Surfaces for the Control of Endothelial Cell Behaviour. Biomolecular Engineering. 2002: 19; 161-170.

R.Cancedda, A.Cedola, A.Guiliani *et al.* Bulk and Interface Investigations of Scaffolds and Tissue-Engineered Bones by X-Ray Microtomography and X-Ray Microdiffraction. Biomaterials. 2007: 28; 2505-2524.

R.De Santis, P.Anderson, K.E.Tanner *et al.* Bone Fracture Analysis on the Short Rod Chevron-Notch Specimens Using the X-Ray Computer Micro-Tomography. Journal of Materials Science: Materials in Medicine. 2000: 11; 629-636.

R.E.Riman, W.L.Suchanek, K.Byrappa *et al.* Solution Synthesis of Hydroxyapatite Designer Particulates. Solid State Ionics. 2002: 151; 393-402.

R.G.Flemming, C.J.Murphy, G.A.Abrams *et al.* Effects of Synthetic Micro- and Nano-Structured Surfaces on Cell Behaviour. Biomaterials. 1999: 20; 573-588.

R.J.Exton and R.J.Balla. ArF Laser Excitation, Collisional Transfer, and Quench-Free Fluorescence in I2/Foreign Gas Mixtures. Journal of Quantitative Spectroscopy and Radiative Transfer. 2004: 86; 267-286.

R.Lange, F.Luthen, U.Beck *et al.* Cell-Extracellular Matrix Interaction and Physico-Chemical Characteristics of Titanium Surfaces Depend on the Roughness of the Material. Biomolecular Engineering. 2002: 19; 255-261.

R.M.Wilson, J.C.Elliott, and S.E.P.Dowker. Rietveld Refinement of the Crystallographic Structure of Human Dental Enamel Apatites. American Mineralogist. 1999: 84; 1406-1414.

R.Marr and T.Gamse. Use of Supercritical Fluids for Different Processes Including New Developments-a Review. Chemical Engineering and Processing. 2000: 39; 19-28.

R.Murugan and S.Ramakrishna. Aqueous Mediated Synthesis of Bioresorbable Nanocrystalline Hydroxyapatite. Journal of Crystal Growth. 2005: 274; 209-213.

R.Narayanan, S.Dutta, and S.Seshadri. Hydroxyapatite Coatings on Ti-6Al-4V From Seashell. Surface and Coatings Technology. 2006: 200; 4720-4730.

R.Noyori. Supercritical Fluids: Introduction. Chemical Reviews. 1999: 99; 353-354.

R.Petit. The Use of Hydroxyapatite in Orthopaedic Surgery: a Ten-Year Review. European Journal of Orthopaedic Surgery and Traumatology. 2007: 71-74.

S.Barinov, L.Shorneva, D.Ferro *et al.* Solid Solution Formation at the Sintering of Hydroxyapatite-Fluorapatite Ceramics. Science and Technology of Advanced Materials. 2004: 5; 537-541.

S.Bose and S.K.Saha. Synthesis and Characterization of Hydroxyapatite Nanopowders by Emulsion Technique. Chemistry of Materials. 2003: 15; 4464-4469.

S.D.Ross, Inorganic Infrared and Raman Spectra. 1972. 1st Edition. McGraw-Hill Book Company Limited, London. 71-88.

S.Deb, L.Aiyathurai, J.A.Roether *et al.* Development of High-Viscosity, Two-Paste Bioactive Bone Cements. Biomaterials. 2005: 26; 3713-3718.

S.Joschek, B.Nies, R.Krotz *et al.* Chemical and Physicochemical Characterisation of Porous Hydroxyapatite Ceramics Made of Natural Bone. Biomaterials. 2000: 21; 1645-1658.

S.Kannan, A.Rebelo, and J.M.F.Ferreira. Novel Synthesis and Structural Characterization of Fluorine and Chlorine O-Substituted Hydroxyapatites. Journal of Inorganic Biochemistry. 2006: 100; 1692-1697.

S.Liste, J.Serra, P.Gonzalez *et al.* The Role of the Reactive Atmosphere in Pulsed Laser Deposition of Bioactive Glass Films. Thin Solid Films. 2004: 453-454; 224-228.

S.M.Best, A.E.Porter, and W.Bonfield. Ultrastructural Characterisation of Hydroxyapatite and Silicon- Substituted Hydroxyapatite. Bioceramics 15. 2003: 240-2; 505-508.

S.Naray-Szabo. The Structure of Apatite, $Ca(F)Ca_4(PO_4)_3$. Z.Kristallogr.Mineral. 1930: 75; 387-398.

S.R.Foltyn, Surface modification of materials by cumulative laser irradiation in Pulsed laser deposition of thin films. 1994. 1st Edition. Wiley, New York. pp89-113.

S.R.Kim, J.H.Lee, S.G.Chung *et al.* Synthesis of Si, Mg Substituted Hydroxyapatites and Their Sintering Behaviours. Biomaterials. 2003: 24; 1389-1398.

S.Raynaud, E.Champion, and D.Bernache-Assollant. Calcium Phosphate Apatites With Variable Ca/P Atomic Ratio II. Calcination and Sintering. Biomaterials. 2002a: 23; 1073-1080.

S.Raynaud, E.Champion, D.Bernache-Assollant *et al.* Calcium Phosphate Apatites With Variable Ca/P Atomic Ratio I. Synthesis, Characterisation and Thermal Stability of Powders. Biomaterials. 2002b: 23; 1065-1072.

S.Teixeira, A.C.Queiroz, F.J.Monteiro *et al.* Osteoblast Proliferation and Morphology Analysis on Laser Modified Hydroxyapatite Surfaces: Preliminary Results. Key Engineering Materials. 2006: 309-311; 105-108.

S.Vijayan and H.Varma. Microwave Sintering of Nanosized Hydroxyapatite Powder Compacts. Materials Letters. 2002: 56; 827-831.

S.Zhang and K.E.Gonsalves. Preparation and Characterization of Thermally Stable Nanohydroxyapatite. Journal of Materials Science: Materials in Medicine. 1997: 8; 25-28.

T.A.Czuppon, Ammonia. In: Kirk-Othmer encyclopedia of chemical technology. 1992. 4th Edition. John Wiley and Sons, New York. 638-639.

T.Furuzono, D.Walsh, K.Sato *et al.* Effect of Reaction Temperature on the Morphology and Size of Hydroxyapatite Nanoparticles in an Emulsion System. Journal of Materials Science Letters. 2001: 20; 111-114.

T.Hattori and Y.Iwadate. Sinterability of Hydroxyapatite $Ca_{10}(PO_4)_6(OH)_2$ Prepared From Freeze-Dried Particles. Denki Kagaku. 1988: 56; 1106-1107.

T.Hattori and Y.Iwadate. Hydrothermal Preparation of Calcium Hydroxyapatite Powders. Journal of the American Ceramic Society. 1990: 73; 1803-1805.

T.Hattori, Y.Iwadate, K.Sato *et al.* Preparation of Hydroxyapatite Powder Using a Freeze-Drying Method. Yogyo-Kyokai-Shi. 1987: 95; 825-827.

T.Her, R.Finlay, C.Wu *et al.* Microstructuring of Silicon With Femtosecond Laser Pulses. Applied Physics Letters. 1998: 73; 1673-1675.

T.Hirai, M.Hodono, and I.Komasawa. The Preparation of Spherical Calcium Phosphate Fine Particles Using an Emulsion Liquid Membrane System. Langmuir. 2000: 16; 955-960.

T.Ishikawa, A.Teramachi, H.Tanaka *et al.* Fourier Transform Infrared Spectroscopy Study of Deuteration of Calcium Hydroxyapatite Particles. Langmuir. 2000: 16; 10221-10226.

T.Ishikawa, M.Wakamura, and S.Kondo. Surface Characterisation of Calcium Hydroxylapatite by Fourier Transform Infrared Spectroscopy. Langmuir. 1989: 5; 140-147.

T.M.Di Palma, C.Flamini, S.Orlando *et al.* Reaction of Al With Ammonia by Pulsed Laser Ablation: Optical Analysis and Mass Spectrometry. Nuclear Instruments and Methods in Physics Research B. 1997: 122; 423-426.

T.S Sampath Kumar, I.Manjubala, and J.Gunasekaran. Synthesis of Carbonated Calcium Phosphate Ceramics Using Microwave Irradiation. Biomaterials. 2000: 21; 1623-1629.

T.Stoebe, R.Hill, M.Ward *et al.* Enhanced Spreading of Aqueous Films Containing Ionic Surfactants on Solid Substrates. Langmuir. 1997: 13; 7276-7281.

T.V.Thamaraiselvi and S.Rajeswari. Biological Evaluation of Bioceramic Materials - A Review. Trends in Biomaterials and Artificial Organs. 2004: 18; 9-17.

V N Maller and M S Naidu, Advances in high voltage insulation and arc interruption in SF_6 and vacuum. 1981. 1st Edition. Pergamon Press, New York. 67-82.

V.A.Dubok. Bioceramics- Yesterday, Today, Tomorrow. Powder Metallurgy and Metal Ceramics. 2000: 39; 381-394.

V.Nassisi, A.Beloglazov, E.Giannico *et al.* Emission and Emittance Measurements of Electron Beams Generated From Cu and Diamond Photocathodes. Journal of Applied Physics. 1998: 84; 2268-2271.

V.P.Orlovskii, V.S.Komlev, and S.M.Barinov. Hydroxyapatite and Hydroxyapatite-Based Ceramics. Inorganic Materials. 2002: 38; 973-984.

V.Rusu, C.Ng, M.Wilke *et al.* Size-Controlled Hydroxyapatite Nanoparticles As Self-Organized Organic-Inorganic Composite Materials. Biomaterials. 2005: 26; 5414-5426.

W.Marine, L.Patrone, B.Luk'yanchuk *et al.* Strategy of Nanocluster and Nanostructure Synthesis by Conventional Pulsed Laser Ablation. Applied Surface Science. 2000: 154-155; 345-352.

W.Suchanek and M.Yoshimura. Processing and Properties of Hydroxyapatite-Based Biomaterials for Use As Hard Tissue Replacement Implants. Journal of Materials Research. 1998: 13; 94-117.

W.Suchanek, P.Shuk, K.Byrappa *et al.* Mechanochemical-Hydrothermal Synthesis of Carbonated Apatite Powders at Room Temperature. Biomaterials. 2002: 23; 699-710.

W.T.Lee, M.T.Dove, and E.K.H.Salije. Surface Relaxations in Hydroxyapatite. Journal of Physics: Condensed Matter. 2000: 12; 9829-9841.

X.Deng, J.Hao, and C.Wang. Preparation and Mechanical Properties of Nanocomposites of Poly(D,L-Lactide) With Ca-Deficient Hydroxyaptite Nanocrystals. Biomaterials. 2001: 22; 2867-2873.

X.Y.Chen and Z.G.Liu. Interaction Between Laser Beam and Target in Pulsed Laser Deposition: Laser Fluence and Ambient Gas Effects. Applied Physics A: Materials Science and Processing. 1999: 69; s523-s525.

Y.Ito. Surface Micropatterning to Regulate Cell Functions. Biomaterials. 1999: 20; 2333-2342.

Y.Khairallah, F.Khonsari-Arefi, and J.Amouroux. Decomposition of Gaseous Dielectrics (CF_4, SF_6) by a Non-Equilibrium Plasma. Mechanisms, Kinetics, Mass Spectrometric Studies and Interactions With Polymeric Targets. Pure and Applied Chemistry. 1994: 66; 1353-1362.

Y.Miyamoto, T.Toh, K.Ishikawa *et al.* Effect of Added $NaHCO_3$ on Thebasic Properties of Apatite Cement. Journal of Biomedical Materials Research. 2001: 54; 311-319.

Y.Shin and M.Aoko. Tissue Reactions to Various Percutaneous Materials With Different Surface Properties and Structures. Biomaterials. 1997: 22; 87-96.

Y.Sung, J.Lee, and J.Yang. Crystallization and Sintering Characteristics of Chemically Precipitated Hydroxyapatite Nanopowder. Journal of Crystal Growth. 2004: 262; 467-472.

Y.Wang, S.Zhang, X.Zeng *et al.* Osteoblastic Cell Response on Flupridated Hydroxyapatite Coatings. Acta Biomaterialia. 2007: 3; 191-197.

Y.X.Pang and X.Bao. Influence of Temperature, Ripening Time and Calcination on the Morphology and Crystallinity of Hydroxyapatite Nanoparticles. Journal of the European Ceramic Society. 2003: 23; 1697-1704.

Z.Cheng, A.Yasukawa, K.Kandori *et al.* FTIR Study of Adsorption of CO_2 on Nonstoichiometric Calcium Hydroxyapatite. Langmuir. 1998: 14; 6681-6686.

Z.Wei, P.Yan, W.Feng *et al.* Microstructural Characterization of Ni Nanoparticles Prepared by Anodic Arc Plasma. Materials Characterization. 2006: 57; 176-181.

Appendix I

The images shown in Figure A were used to align the beam prior to X-ray microdiffraction analysis of the laser-modified surfaces. A small row of dots spaced 3 mm apart were placed on the surface of a spare sample with black ink. The beam was then centred and focused onto a dot using fibre optics and optical microscopy and by adjusting the sample position. When the correct samples were ready for analysis, they could be placed into the correct position such that the beam was already aligned and focused onto the area to be analysed.

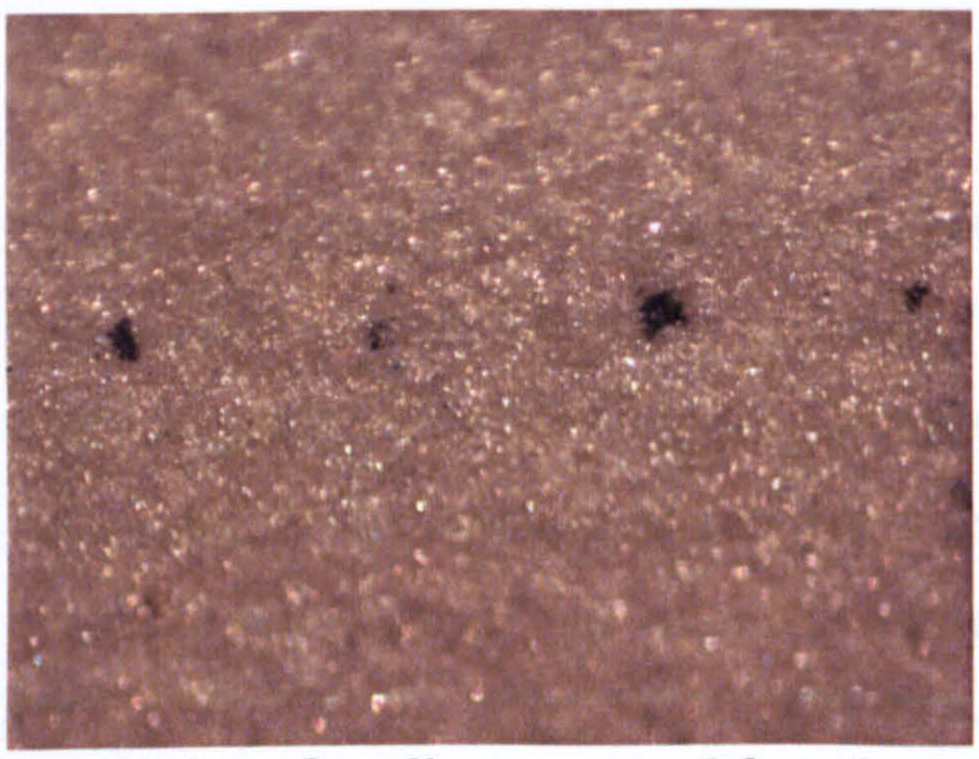

(a) Markers for alignment and focusing

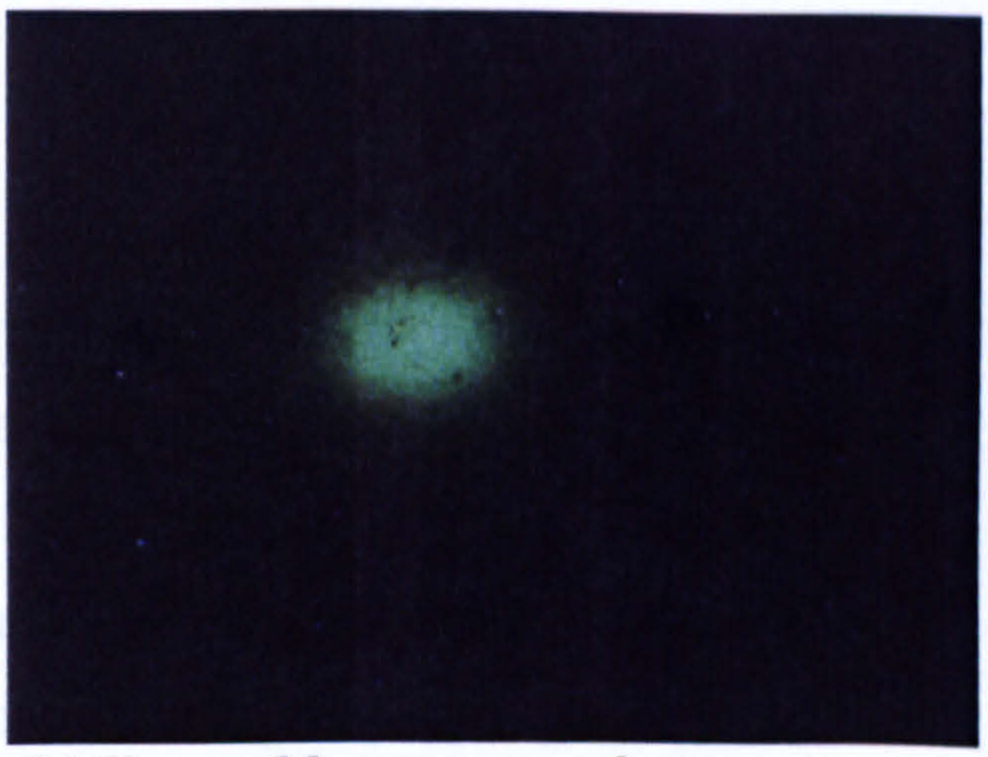

(b) Focused beam on markers

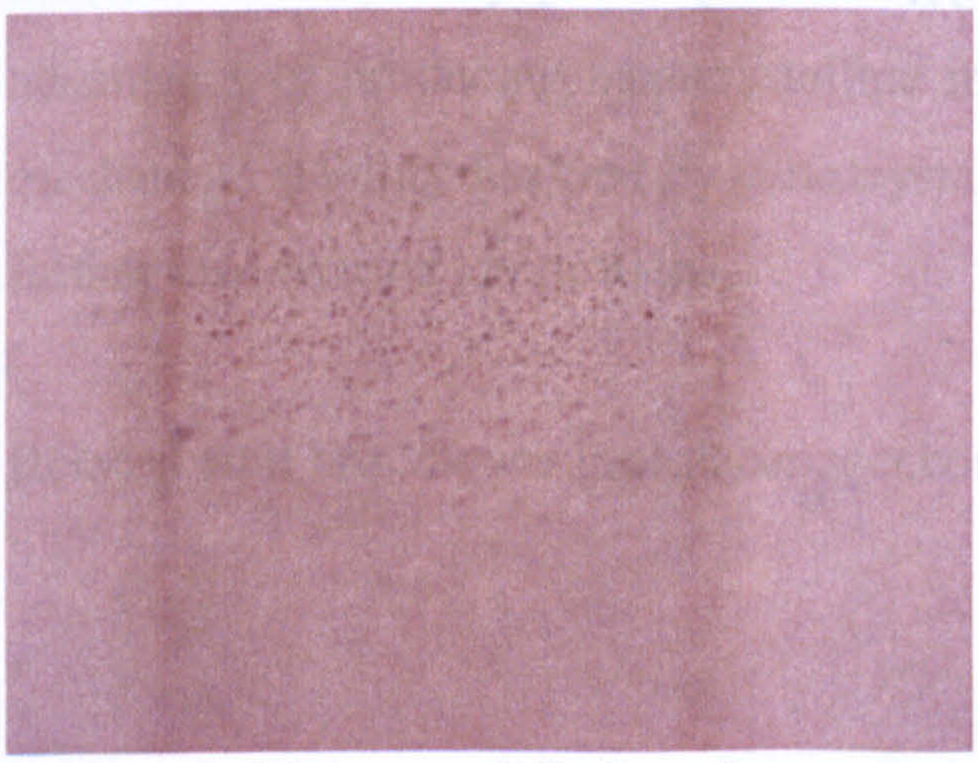

(c) Focused laser modified section

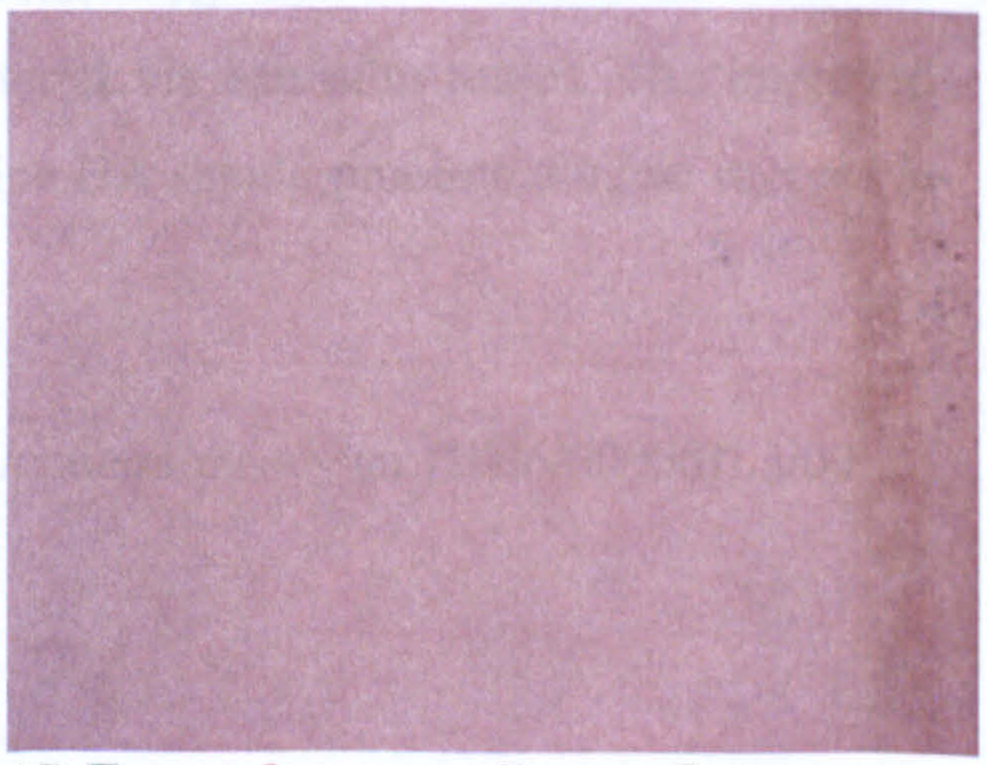

(d) Focused surrounding surface

Figure A: Images employed for the focusing of X-ray beam during X-ray microdiffraction analysis.

Appendix II

Recent Publications

Recent developments in processing and surface modification of hydroxyapatite

Author(s): J. Norton, K.R. Malik, J.A. Darr and I.U. Rehman

Journal: Advances in Applied Ceramics, Volume 105, Number 3, June 2006, pp. 113-139(27)

The present paper reviews the developments in the fields of bioceramic materials and laser surface microstructuring of materials. The clinical success of a bioceramic implant depends largely on the biological response at the implant interface in addition to the sufficiency of the mechanical properties for the application. The use of lasers in the present paper is largely to tailor the topography, surface properties and composition with a view to enhancing the implant biocompatibility. Developments in production methods for hydroxyapatite [HA: $Ca_{10}(PO_4)_6(OH)_2$] are also discussed with the advantages of producing nanocrystalline material via emulsion routes. The improved mechanical stability featured by nanocrystalline HA should promote clinical success in further load bearing applications.

Related site: http://www.ingentaconnect.com/content/maney/aac/2006/00000105/00